



Insights into the 10-100 GeV gamma-ray emission of pulsars from extensive observations of MAGIC

Giovanni Ceribella

Vollständiger Abdruck der von der Fakultät für Physik der Technischen Universität München zur Erlangung des akademischen Grades eines

Doktors der Naturwissenschaften (Dr. rer. nat.)

genehmigten Dissertation.

Vorsitzender:

Prof. Dr. Alejandro Ibarra

Prüfende der Dissertation:

1. Priv.-Doz. Dr. Béla Majorovits
2. Prof. Dr. Laura Fabbietti

Die Dissertation wurde am 04.08.2021 bei der Technischen Universität München eingereicht und durch die Fakultät für Physik am 06.09.2021 angenommen.

Insights into the 10-100 GeV gamma-ray emission of pulsars from extensive observations of MAGIC

Giovanni Ceribella

ABSTRACT

In this doctoral thesis I investigate the very high energy emission of gamma-ray pulsars with the MAGIC Telescopes. Pulsed emission above energies of a few tens of GeV from young rotation-powered pulsars is rare, and its origin is still poorly understood. At the start of my doctoral program, only two pulsars were known to emit at those energies, rendering any comparative study purely speculative. The MAGIC Telescopes recently developed a stereoscopic analog trigger, the Sum-Trigger-II, that greatly improves the performance in the 10 GeV to 100 GeV energy band. I took part in the commissioning and maintenance of this novel hardware component. The enhanced photon collection efficiency achieved by the Sum-Trigger-II makes the MAGIC telescopes the most suited instruments to address the scientific challenge of the search and characterization of new very high energy pulsars. In order to fully profit from the Sum-Trigger-II improvements, the analysis techniques required to be adapted to the dim Cherenkov images of low-energy extensive air showers. I built and validated a modified low-energy data analysis pipeline, and made it available for the MAGIC Collaboration.

I present the results of the observations of two gamma-ray sources: the Crab pulsar (PSR J0534+2200), and Geminga (PSR J0633+1746). Observations of the Crab pulsar, previously detected at the very high energies, aimed to search for a temporal variability of the flux at timescales below one month. I found no significant variability, and derived upper limits for it. Crab observations were used to characterize the novel system and the analysis techniques. My analysis of the Geminga observations led to the discovery of its very high energy pulsed component in the 15 GeV to 75 GeV energy range. At a significance of 6.3σ , Geminga became the third gamma-ray pulsar to be detected with Cherenkov telescopes, and the oldest and only radio-quiet one to date. The very high energy spectrum, a seemingly pure power-law, reveals the presence of a previously undetected inverse Compton component. The classic outer magnetospheric gap emission model allows for such a component, but fails short of reproducing the overall gamma-ray spectrum of Geminga. This indicates that a revision of the theoretical framework of gamma-ray pulsar emission is required to explain the very high energy emission of Geminga. Overall, my doctoral work substantially contributed to make MAGIC a strategic facility for the exploration of the 10 GeV to 100 GeV energy band, and yielded compelling scientific results that bring insights into the extreme processes occurring in pulsars.

ZUSAMMENFASSUNG

In dieser Doktorarbeit untersuche ich die Höchstenergiestrahlung von Gammapulsaren mit den MAGIC-Teleskopen. Gepulste Emission mit Energien von mehr als einigen Zehn GeV wurde von Pulsaren, die ihre Energie aus der Rotation des Neutronensterns beziehen, nur sehr selten beobachtet und ihre Herkunft ist noch unklar. Am Anfang meines Promotionsprojekts waren nur zwei Pulsare gekannt, die in diesem Energiebereich strahlen. Vergleichsstudien auf diesem Forschungsfeld waren darum zwangsweise äußerst spekulativ. Die MAGIC-Teleskope wurden vor kurzem um einen stereoskopischen Analogtrigger erweitert, dem Summentrigger-II, der die Sensibilität der Teleskope im Energiebereich von 10 GeV bis 100 GeV deutlich verbessert. Ich nahm an der Inbetriebsetzung und der Wartung dieser neuen Hardware teil. Der Summentrigger-II erzielt eine höhere Effizienz bei der Detektion von Photonen und macht die MAGIC-Teleskope die am besten geeigneten Instrumente, um die anspruchsvolle Erforschung und Charakterisierung neuer Pulsare bei den höchsten Energien durchzuführen. Um die Verbesserungen des Summentriggers-II auszunutzen, mussten die Datenanalysemethoden für die lichtschwachen Tscherenkowbilder der Luftschauer mit niedriger Energie adaptiert werden. Ich entwickelte und validierte eine modifizierte Analyseketten für die niedrigen Energien und stellte sie der ganzen MAGIC-Kollaboration zur Verfügung.

In dieser Dissertation zeige ich die Ergebnisse der MAGIC-Beobachtungen von zwei Gammastrahlquellen: dem sehr bekannten Krebspulsar (PSR J0534+2200) und dem Geminga-Pulsar (PSR J0633+1746). Die Beobachtungen des Krebspulsars, der bereits in den sehr hohen Energien detektiert wurde, zielten auf die Suche einer möglichen Variabilität des gepulsten Flusses auf Zeitskalen von weniger als einem Monat. Keine erhebliche Zeitvariabilität wurde gefunden, jedoch konnte ich Obergrenzen berechnen. Diese Daten des Krebspulsars wurden genutzt, um das neue System und die Analysemethode zu kalibrieren. Meine Analyse der Geminga-Beobachtungen ermöglichte die Entdeckung seiner sehr hochenergetischen gepulsten Spektralkomponente zwischen 15 GeV und 75 GeV. Mit einer Signifikanz von $6,3 \sigma$ ist Geminga der dritte Gammapulsar, der mit Tscherenkowteleskopen entdeckt wurde. Gleichzeitig ist Geminga der älteste und der einzige Pulsar im höchstenergetischen Energiebereich, der im Radiobereich nur sehr wenig emittiert (engl.: „radio quiet“). Sein Spektrum, das von einem reinen Potenzgesetz gut beschrieben wird, zeigt eine Komponente, die von Inverse-Compton-Prozessen verursacht wird und die bislang nicht bekannt war. Das klassische Emissionsmodell der Lücke der äußeren Magnetosphäre (engl. „outer gap“) kann zwar eine solche Komponente erklären, jedoch nicht das gesamte Gammaskpektrum Gemingas richtig reproduzieren. Dieses Ergebnis zeigt, dass das theoretische Verständnis der Emission von Gammapulsaren unbedingt

eine Revision benötigt, um die Emission Gemingas zufriedenstellend aufzuklären. Insgesamt hat meine Doktorarbeit wesentlich dazu beigetragen, dass die MAGIC-Teleskope weiterhin eine der führenden wissenschaftlichen Einrichtungen zur Erforschung des Gammastrahlenhimmels zwischen 10 GeV und 100 GeV zu sein. Mein Promotionsprojekt brachte bemerkenswerte wissenschaftliche Ergebnisse hervor, die wichtige Einblicke in die extremen Prozesse geben, die in Gammapulsaren stattfinden.

CONTENTS

This thesis is organized as follows. Chapter 1 briefly reviews the physics and open problems of gamma-ray pulsars, introduces pulsar observation methods, and presents the state of the art information on the Crab and Geminga pulsars. Chapter 2 introduces the basics of the imaging atmospheric Cherenkov telescope technique, and provides technical details on the MAGIC telescopes, with special attention to the novel stereoscopic Sum-Trigger-II. Chapter 3 summarizes my technical activities in the commissioning and maintenance of the Sum-Trigger-II system. Chapter 4 describes the data analysis techniques, with a particular focus on the non-standard low-energy methods employed for the pulsar observations. Finally, Chapter 5 and 6 present the results on the Crab and Geminga pulsars, respectively.

1	Gamma-ray Pulsars	11
1.1	Neutron Stars	12
1.1.1	Formation	12
1.1.2	Structure	13
1.2	Pulsar magnetosphere	14
1.3	High-energy emission	20
1.3.1	Gamma-ray emission processes	21
1.3.2	Particle acceleration	23
1.4	Pulsar timing	26
1.4.1	Timing glitches	29
1.4.2	Timing noise	31
1.5	Crab Pulsar	32
1.5.1	Spectrum	33
1.5.2	Phaseogram	34
1.5.3	Variability	35
1.5.4	The Crab Nebula	35
1.6	Geminga Pulsar	38
1.6.1	History and early observations	38
1.6.2	Multi-wavelength studies	40
1.6.3	Pulsar wind nebula	43
1.6.4	TeV Halo	44

2	The MAGIC Telescopes	45
2.1	Extensive Air Showers	45
2.2	IACT Technique	48
2.3	MAGIC Hardware	52
2.3.1	Mechanics	52
2.3.2	Optics	53
2.3.3	Camera	55
2.4	Readout	56
2.4.1	Sampling and Digitization	56
2.4.2	Trigger	57
2.5	Sum-Trigger-II	58
2.5.1	Hardware	60
2.5.2	Software	62
2.6	Observation Strategy	62
3	Technical Results	63
3.1	Calibration procedure	64
3.2	Calibration Stability	67
3.3	Sum-Trigger-II technical shift	70
4	Data Analysis	73
4.1	Raw data analysis	75
4.1.1	Signal Extraction	75
4.1.2	Signal Calibration	76
4.2	Image Cleaning	78
4.2.1	The MaTaJu Cleaning	79
4.3	Image Parametrization	82
4.3.1	Stereoscopic reconstruction	85
4.4	Bright Stars	86
4.5	Physical Parametrization	92
4.5.1	Gamma-Hadron separation	93
4.5.2	<i>Stereo-DISP</i> direction reconstruction	94
4.5.3	Energy Estimation	96
4.6	Pulsar Phases	99
4.6.1	MAGIC TEMPO2 plugin	100
4.7	Source Detection	102
4.7.1	Event selection	102
4.7.2	Standard background estimation	104
4.7.3	Pulsar background	106
4.8	Spectra	108
4.8.1	Effective Time	108
4.8.2	Effective Area	109
4.8.3	Unfolding	110
4.8.4	Lightcurves	111
4.9	Analysis threshold	112
4.10	Tailored Monte-Carlo simulations	114

5 Crab Pulsar	119
5.1 Observations Overview	120
5.2 Data Analysis	123
5.3 Phaseograms	124
5.3.1 Phaseogram morphology	124
5.4 Pulsed Spectra	128
5.4.1 Analysis Threshold	130
5.4.2 Nebula Spectrum	131
5.5 Long-Term Lightcurve	131
5.5.1 Sum-Trigger-II performance stability	137
5.5.2 Variability Upper Limits	138
5.6 Summary	143
6 Geminga Pulsar	145
6.1 Observations overview	146
6.2 Data Analysis	147
6.2.1 <i>Fermi</i> -LAT Analysis	149
6.3 Phaseogram	151
6.3.1 Phaseogram Analysis	154
6.4 Pulsed Spectrum	155
6.4.1 Systematic Effects	156
6.5 Joint MAGIC and <i>Fermi</i> -LAT Spectrum	160
6.5.1 Tests for a Power-Law component	162
6.6 Outer Gap modeling	165
6.6.1 High temperature X-ray component	167
6.7 Summary	168
7 Conclusions	173
A Pulsar Ephemerides	177
A.1 Ephemeris extension	179
A.2 Post-glitch recovery	181
A.3 Cyclic data statistical tests	183
A.4 Segmented ephemerides	184
B Joint parameter distributions	187
B.1 Power-law with a <i>pure</i> exponential cutoff	190
B.2 Power-law with a <i>free</i> exponential cutoff	191
B.3 Overlapping power-law	192
B.4 Overlapping log-parabola	193
B.5 Composite fit	194
C Software repository	195
Bibliography	197
Acknowledgments	225

1

GAMMA-RAY PULSARS

In this introductory chapter I review some basic concepts of pulsar astrophysics and their observation techniques, and I introduce the two sources subject of my studies, the Crab and Geminga pulsars. The pulsars treated in this chapter are the so-called *rotation-powered* ones. These are young neutron stars that dissipate their rotational energy due to electromagnetic emission, and spin down as a result. The complementary class of *accretion-powered* pulsars, is not treated in this thesis. I refer the reader interested in a broad review of pulsar physics to Ghosh (2007).

In Section 1.1, I summarize briefly the formation and basic properties of neutron stars. Section 1.2 contains a compact review of the pulsar magnetosphere, the most probable site of gamma-ray pulsar emission. The physics of this peculiar region, as well as the exact mechanism of the gamma-ray emission, are still being actively investigated. The summary presents the classical Goldreich and Julian (1969) scenario, and introduces the basic features shared also in current emission models. In Section 1.3, I review the gamma-ray production mechanisms and the particle acceleration models currently being considered.

Section 1.4 presents key pulsar observation concepts, such as the rotational phase and the pulsar ephemerides. The production of these, using data of the *Fermi*-LAT experiment, is separately covered in Appendix A.

Finally Sections 1.5 and 1.6 introduce the two objects which are the subject of this thesis: the Crab and Geminga pulsars. The results on them are presented in Chapter 5 and Chapter 6, respectively.

1.1 Neutron Stars

The first pulsar was detected in 1967, when a 1.34 s periodical signal was found during a radio survey originally aimed for quasars (Hewish et al., 1968, based on the work of J. Bell). Due to the shortness of the period, it was immediately recognized as a phenomenon associated with a compact object. Initially thought to be related to the radial pulsation of a white dwarf or neutron star (hence the name “pulsar”), it was soon understood that the periodicity of the emission was caused by the fast rotation of the source (Gold, 1968), similarly to what happens in a lighthouse. This allowed to firmly identify it as a neutron star, as any other object would be disrupted by the centrifugal forces. Since then, 2870 more pulsars have been discovered¹, and about 270 of them have been detected by the *Fermi*–LAT experiment² at energies larger than 100 MeV. Only three pulsars have been confirmed to emit gamma-rays at energies above 50 GeV: the Crab pulsar, the Vela pulsar, and Geminga, whose detection is the primary result of my thesis work (see also Chapter 6).

1.1.1 Formation

Neutron stars form during the gravitational collapse of massive stars ($m \geq 8 M_{\odot}$) and their subsequent explosion as supernovae. In late stages of their evolution, these stars undergo several cycles of expansion and contraction, governed by the succession of thermonuclear reactions with increasingly heavy nuclei in their cores. They also disperse a large fraction of their mass through their stellar wind. The core of lighter stars can eventually achieve a hydrostatic equilibrium in the state of a white dwarf, sustained by the degeneracy pressure of electrons. However, if at that stage its residual mass is larger than the Chandrasekhar limit $M_C \simeq 1.4 M_{\odot}$, the pressure developed by the (relativistic) electrons can not balance the gravitational contraction and the stellar core collapses.

The collapse of the core happens on sub-second timescales. The density and temperature of the core increase up to the point at which the equilibrium of the beta decay and electron capture reactions favors the second one. The neutron decay is inhibited by the fact that the Fermi gas of degenerate electrons already occupies almost all possible energy states, so that little room is left for an extra electron to be emitted. Matter undergoes a process of extensive “neutronization”, accompanied by an emission of neutrinos. The collapse continues further until it is prevented by the degeneracy pressure of non relativistic neutrons and the repulsive strong interactions that they develop at densities higher than the nuclear one. The imploding outer envelope of the progenitor star “bounces” off the surface of the collapsed core. The resulting shock wave ignites thermonuclear reactions in it, which give rise to the supernova explosion, visible in the optical band. A second and larger flash of neutrino emission takes place as the newly formed neutron star contracts to its final radius, dissipating its gravitational potential energy and cooling down by neutrino emission. Such a neutrino flash was directly observed in the case of the notable supernova SN1987A (Hirata et al., 1987; Bionta et al., 1987), which provided a decisive confirmation to the core collapse scenario that has just

¹ ATNF Pulsar Database (<https://www.atnf.csiro.au/people/pulsar/psrcat/>), version 1.64.

² Upcoming third *Fermi*–LAT pulsar catalog (private communication).

been outlined. The formation of a stable neutron star is possible only if the mass of the core is below the Tolman-Oppenheimer-Volkov limit M_{TOV} , analogous in many aspects to the Chandrasekhar one³. The value of M_{TOV} depends sensibly on the equation of state of the neutron star, which is largely unknown (cfr. Section 1.1.2). The recent observation of a gravitational wave signal from a binary neutron star merger (Abbott et al., 2017) and its subsequent analysis (Shibata et al., 2019) led to an estimate of $M_{\text{TOV}} \simeq 2.3 M_{\odot}$. If the core exceeds such limit the collapse can not be stopped and ultimately results in a stellar sized black hole.

Once they have reached their stable state, neutron stars have a radius of the order of 10 km (few times their Schwarzschild radius), and an average densities of the same order as nuclear matter, $\rho_0 = 3 \cdot 10^{17} \text{ kg/m}^3$. Assuming a spherical collapse, the conservation of angular momentum implies that, upon being formed, their rotational frequency must be of the order of 1 kHz. Furthermore, the stellar core progenitor is an excellent conductor, so that the hypotheses of the Alfvén theorem apply and the magnetic flux is also conserved. As a result, the value of the magnetic field at the surface of a typical neutron star is of the order of $B_0 \simeq 10^8 \text{ T}$. The magnetic moment is not necessarily aligned with the rotation axis. Such a rapidly rotating and intensely magnetized object is expected to lose energy and spin down because of the emission of electromagnetic radiation. The measurement of pulsar frequencies ν and the observation of spin-down rates $\dot{\nu}$ compatible with those predicted by this mechanism (cfr. Section 1.2 and 1.4) allows to confirm the theoretical estimates for the magnetic field B_0 .

1.1.2 Structure

The internal structure of a neutron star is an active research topic in theoretical astrophysics. The equation of state of matter at and above the nuclear densities is still unknown, and several competing models for it result in very different scenarios. A very general description usually quotes:

- An **outer crust**, with a depth of few hundred meters, where ionized nuclei form a crystalline structure immersed in a completely degenerate electron Fermi gas. Nuclei are held in the crystal structure by their electrostatic interactions, largely dominant over thermal motion. At the top of the crust an *envelope* (or ocean) of non-crystallized material may be present if the neutron star is accreting matter from a companion star. Moving inwards, nuclei become increasingly more neutron-rich.
- An **inner crust**, extending down to $\sim 1 \text{ km}$. It is separated by the outer crust by the *neutron drip* line. This is the point at which the chemical potential for neutrons in a nucleus equals the mass of the neutron, so that it is energetically favorable to have free neutrons rather than bound ones. Upon reaching densities close to the nuclear one, the interplay between strong and electromagnetic forces may give rise to heavily distorted nuclei in the shape of laces and sheets, usually known as *nuclear pasta*. This is similar to phase transitions in colloidal solutions with strong surface tension (e.g. cellular membranes).

³ In neutron stars, the limiting mass M_{TOV} does not stem from neutrons becoming relativistic, as is for white dwarfs with electrons. Instead, in their general-relativistic regime, the pressure gradient opposing gravity, being itself a component of the stress-energy tensor, becomes a source for gravity itself.

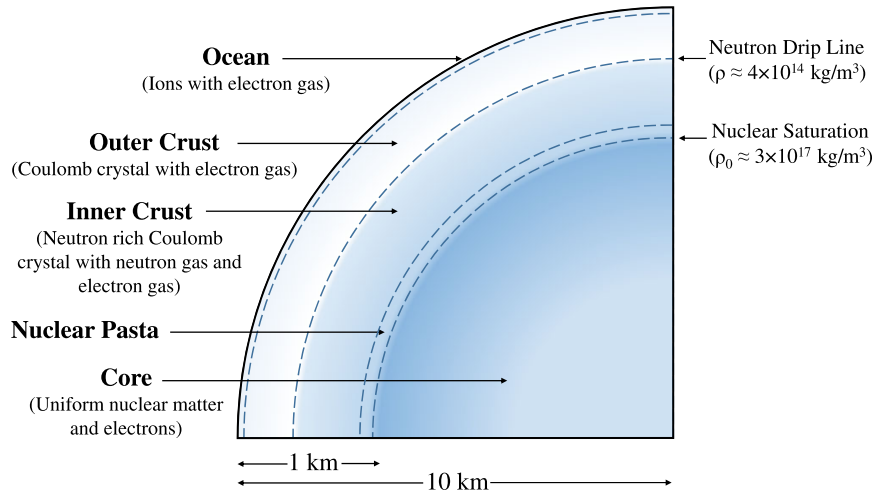


Figure 1.1: Scheme of the interior of a neutron star, from Caplan and Horowitz (2017). The exact structure and properties of the core are unknown.

- The **core** constitutes the remaining inner portion of the star, down to its center at ~ 10 km from the surface. At densities above the nuclear one, it is likely to be composed by uniform nuclear matter. Neutrons are by far the dominant species, but a small fraction of protons and electrons, necessary to keep the β decay equilibrium, is also present. These charged particles make the neutron star an excellent conductor, a fact which is extremely significant to understand the origin of the pulsar phenomenon (cfr. Section 1.2).

The real state of the matter in the core of a neutron star is still debated. Its understanding is required to fully comprehend the physics of these objects. Recent observations of gravitational wave signals from coalescing neutron stars opened a new channel to study their structure and composition.

1.2 Pulsar magnetosphere

The magnetosphere of a pulsar is the vast region surrounding it which is filled with plasma affected by the magnetic field of the neutron star. It is also the region in which pulsed gamma-ray emission is produced. The structure and dynamics of pulsar magnetospheres are still actively investigated, and gamma-ray observations such as the ones of *Fermi*-LAT and MAGIC have decisively contributed to their understanding. Despite its complexity, basic features of the magnetosphere can be illustrated with the seminal model of Goldreich and Julian (1969). This takes several simplifications, assumes that the magnetic field of the star is a simple dipole aligned with the spin axis and ignores both the gravitational and inertial forces acting on the plasma. Its fundamental aspects are summarized in the next paragraphs. I refer the readers interested in a broad review of pulsar magnetospheres to Pétri (2016) and Cerutti and Beloborodov (2017).

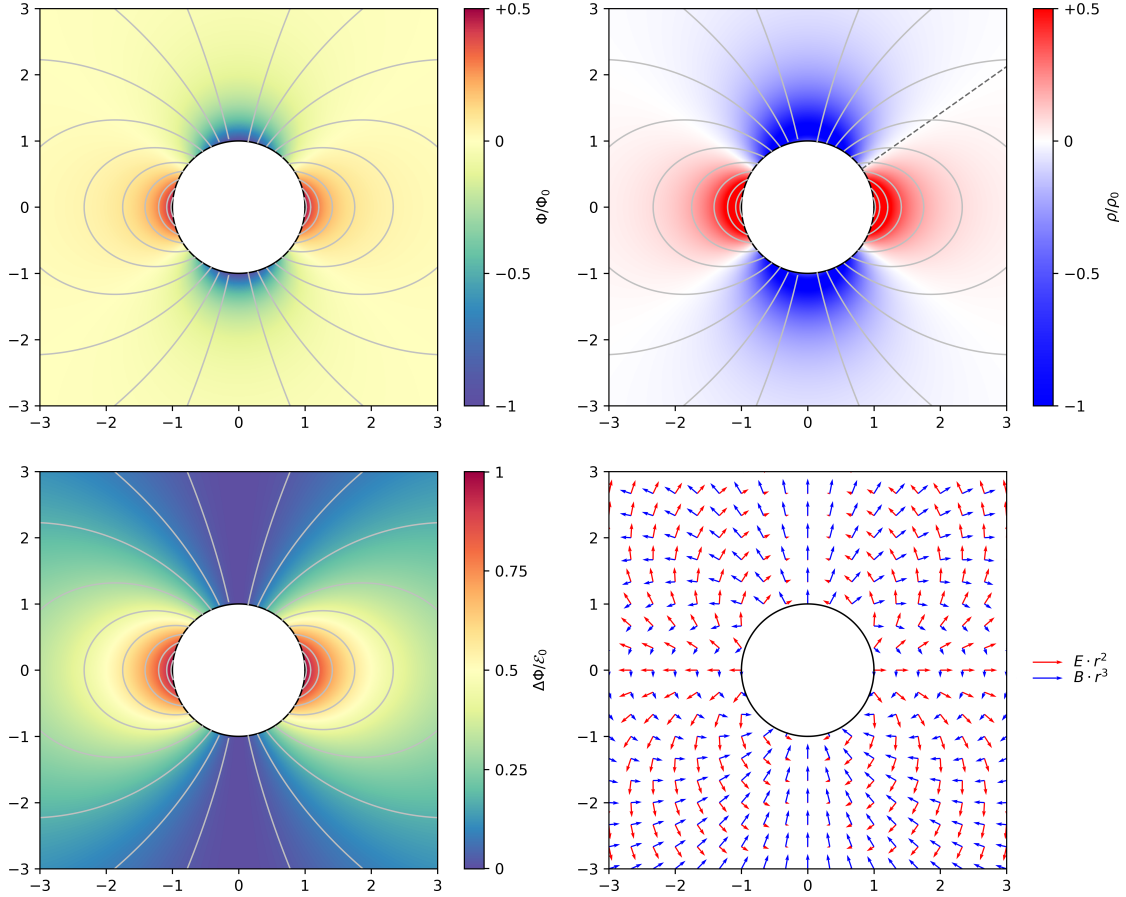


Figure 1.2: Goldreich-Julian potentials and fields in the near zone close to the pulsar, for an aligned rotator. A meridian plane is shown with lengths scaled to the radius of the star.

Upper-left: Electric potential Φ surrounding the neutron-star if it were in a vacuum, in terms of $\Phi_0 \simeq 2 \cdot 10^{16} \text{ V}$ just above the pole. Gray lines show the magnetic field lines.
Upper-right: Spatial charge density ρ_{GJ} , in units of its value at the pole $\rho_0 \simeq 10^{-2} \text{ C/m}^3$. The null surface where $\rho = 0$ forms a double sheeted cone and is evidenced by the dashed line.
Bottom-left: Potential difference with the pole of the star, expressed as a fraction of the drop between the poles and the equator $\mathcal{E}_0 \simeq 3 \cdot 10^{16} \text{ V}$. Magnetic field lines are equipotential.
Bottom-right: Relative intensities of the electric (red) and magnetic fields (blue, poloidal component only), with the radial dependency removed for clarity. The fields are perpendicular and the electric field balances the Lorentz force on charges $q(\mathbf{E} + \mathbf{v} \times \mathbf{B}) = 0$ everywhere (force-free solution).

Pulsar in a vacuum The existence of a plasma surrounding the neutron star can be deduced with simple electrodynamic arguments. A fast rotating and highly magnetized neutron star behaves like a homopolar generator, similarly to a uniformly magnetized spinning conductor⁴. Free charges in the excellently conducting neutron star (cfr. Section 1.1.2) experience a Lorentz force due to their motion in the magnetic field. In a stationary state, they redistribute to produce an electric field \mathbf{E} that globally balances it:

$$\mathbf{E} + (\boldsymbol{\Omega} \times \mathbf{r}) \times \mathbf{B} = 0, \quad (1.1)$$

with $\boldsymbol{\Omega} \times \mathbf{r}$ being the velocity at position \mathbf{r} due to the rigid rotation of the star and \mathbf{B} the dipolar magnetic field due to the magnetic moment $\boldsymbol{\mu}$ of the star. The charge distribution produces an electrostatic potential Φ . If the pulsar were in a vacuum, the external potential would be given by:

$$\Phi(r, \theta) = -\frac{B_0 \Omega R^5}{3r^3} \mathcal{P}_2(\cos \theta), \quad (1.2)$$

with $B_0 \simeq 10^8$ T the value of the magnetic field at the pole of the star, $\Omega \lesssim 1$ Hz its rotational pulsation, $R \simeq 10$ km its radius, θ the meridian angle measured from the pole, and $\mathcal{P}_2(x) = 1/2(3x^2 - 1)$ the second Legendre polynomial. Such potential is plotted with a color code in the upper left panel of Figure 1.2. The corresponding electric field just above a pole would have a strength $E_0 = \Omega R B_0 \simeq 10^{13}$ V/m, and could easily extract electrons from the surface of the neutron star and fill the surrounding space with them. This proves that a pulsar can not be in a vacuum, as in such case, it would immediately develop a magnetosphere with particles ripped away from its surface.

Magnetospheric lepton plasma In this picture, ultra-relativistic particles torn from the surface of the pulsar are accelerated by the large electric field and radiate gamma rays due to curvature and inverse Compton emission (cfr. Section 1.3). In turn, such gamma rays are effectively absorbed via single-photon pair production in the strong magnetic field of the pulsar. This initiates cascades of electron-positron pairs (Sturrock, 1971), which ultimately fill the magnetosphere with a leptonic plasma. The presence of such plasma alters the electromagnetic fields outside the neutron star. It is usually assumed that the production rate of leptons is sufficiently high so that the resulting plasma behaves as an infinitely conducting one. In absence of pressure and inertial forces, this implies that the electric field in it must balance the Lorentz force everywhere, so that:

$$\mathbf{E} + \mathbf{v} \times \mathbf{B} = 0. \quad (1.3)$$

This is formally the same as Equation 1.1, but the plasma velocity field \mathbf{v} is an unknown, and \mathbf{B} and \mathbf{E} are different from the ones in vacuum. Equation 1.3 implies that $\mathbf{E} \cdot \mathbf{B} = 0$, known as the *force-free* condition. It follows that magnetic field lines are also electrostatic equipotential ones, and charges can move freely along them. Ideal magnetohydrodynamics applies to such a plasma, and states that *field lines are frozen in the plasma*, or that *charges are bound to the magnetic field lines* (Alfvén's theorem). The resulting flow of the

⁴ A concise treatment of homopolar induction is given in the classic Landau and Lifchitz (1969) Vol. 8 §49.

plasma is a composition of a rigid co-rotation⁵ with the pulsar at its angular velocity Ω , and a slide motion along the magnetic field lines: $\mathbf{v} = \Omega \times \mathbf{r} + v_{\parallel} \hat{\mathbf{B}}$. In the immediate proximity of the neutron star the magnetic field is similar to an undisturbed dipole (cfr. Figure 1.2), which is a purely poloidal field: $\mathbf{B} \times (\Omega \times \mathbf{r}) = 0$. As a result, particles close to the pulsar are in strict co-rotation with it.

Light Cylinder Clearly, charges can not co-rotate at an arbitrary distance from the star, their velocity being limited by the speed of light. This gives rise to a limit surface, the *light cylinder*, which is centered on the pulsar, aligned with its rotational axis, and defined by the radius at which a co-rotating body would move at the speed of light:

$$R_{\ell} = \frac{c}{\Omega}. \quad (1.4)$$

As the light cylinder is approached, the magnetic field acquires a toroidal component, $\mathbf{B} \times (\Omega \times \mathbf{r}) \neq 0$, and the plasma ceases to co-rotate with the pulsar. The sources of such toroidal field are the currents produced by charged particles sliding along the field lines in the internal magnetosphere. The portion of the magnetosphere inside the light cylinder ($r < R_{\ell}$) is named the *near zone*, whereas the *wind zone* extends outside of it.

Charge density In order for magnetospheric currents to be realized, a space charge density must be present. This can be computed by taking the divergence of Equation 1.3. Close to the neutron star, where the magnetic field is poloidal, its value is given by:

$$\rho_{\text{GJ}} = \frac{-2\varepsilon_0 \Omega \cdot \mathbf{B}}{1 - \left(\frac{\Omega}{c} r \sin \theta\right)^2}, \quad (1.5)$$

which is known as the Goldreich-Julian or co-rotating charge density. The density vanishes where $\Omega \cdot \mathbf{B} = 0$, the *null surface* of the magnetosphere, which separates regions of opposite co-rotating charges. If $\Omega \cdot \boldsymbol{\mu} > 0$, electrons co-rotate at the poles and positrons at the equator, whereas the opposite happens if the sign of \mathbf{B} is reversed. The denominator of Equation 1.5 diverges at the light cylinder, where the assumption of a poloidal-only magnetic field breaks. The value of ρ_{GJ} specifies just the net density required to reach the force-free condition. The same net charge can be achieved equivalently with a completely charge-separated plasma (where positive and negative particles are physically in different regions of space), or with an excess or defect of charges of a certain sign atop a denser and otherwise neutral plasma. It is widely believed that the second case better describes the situation in a real pulsar magnetosphere. Similarly, the magnetospheric currents, required to produce the toroidal magnetic field at R_{ℓ} , arise only when a net imbalance is present between the motion of particles with opposed signs.

⁵ The rigid co-rotation of magnetic field lines is a simple consequence of ideal magnetohydrodynamics, often quoted as *Ferraro's isorotation theorem*. Since all field lines originate on the surface of the pulsar, they are all in co-rotation with it at the same angular velocity Ω .

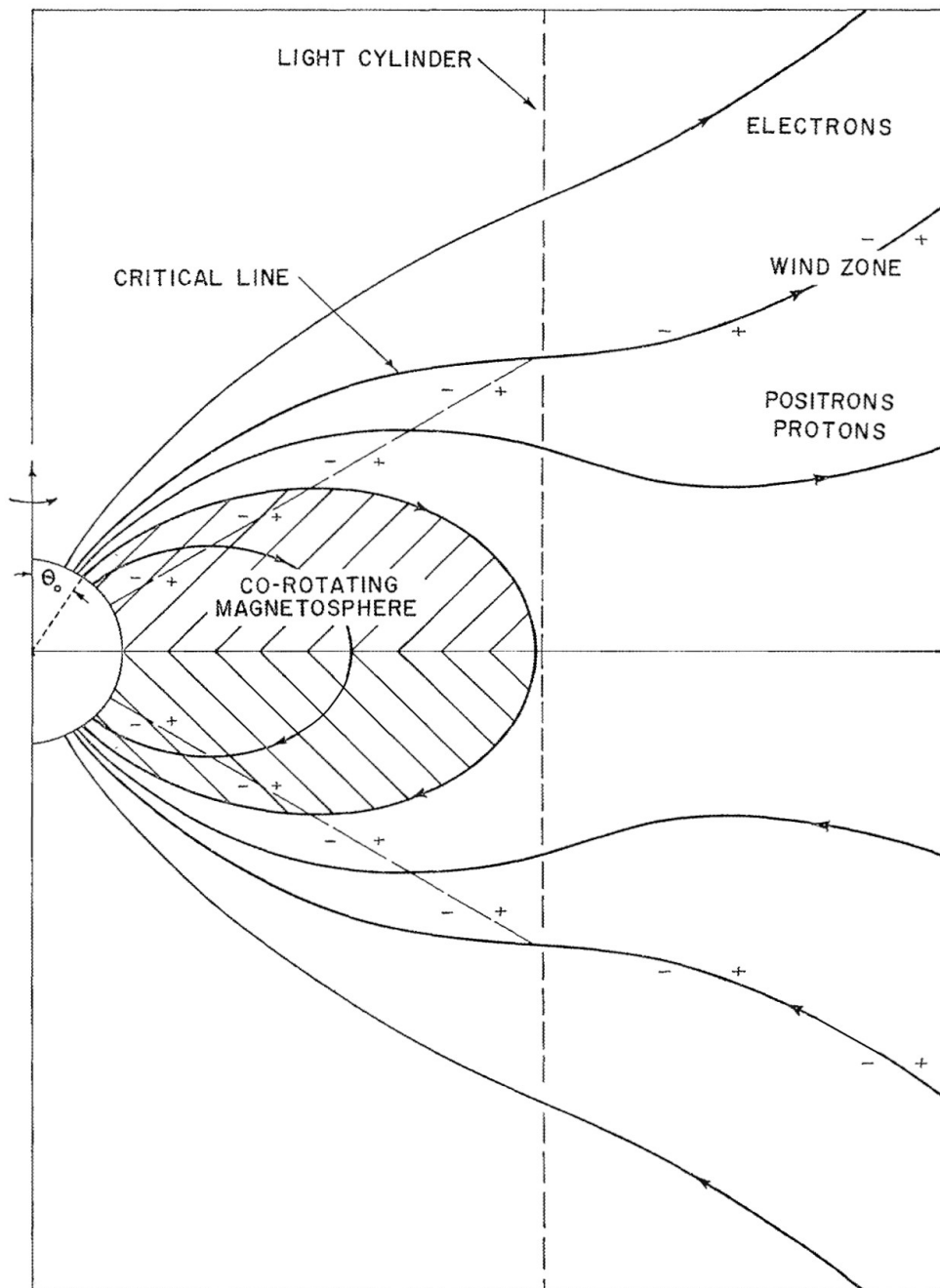


Figure 1.3: Scheme of the pulsar magnetosphere in the near and wind zones, adapted from Goldreich and Julian (1969). Field lines of the poloidal magnetic field are shown as solid lines. In the wind region the toroidal component is dominating, and lines are bent backwards with respect to the rotation (not shown). The signs displayed in the diagram agree with the ones of the co-rotating charge density ρ_{CJ} in the near zone, and with the ones of the out-streaming particles in the wind zone. The latter ones are separated by a *critical line* whose potential is the same as the outer space one.

Open magnetosphere and wind The existence of a light cylinder and the impossibility of co-rotation beyond it has an important consequence: magnetic field lines which cross the light cylinder can not close themselves looping back to the surface of the neutron star⁶. This is one of the most prominent features of a pulsar magnetosphere. Leptons attached on those lines abandon the near zone and ultimately leave the pulsar. Figure 1.3 presents a scheme of the structure of the magnetosphere. In the near zone a roughly dipolar portion exist, the *closed magnetosphere*, in which the magnetic field is purely poloidal. In this zone no net currents flow, and field lines close themselves returning to the pulsar. Conversely, the remaining portion constitutes the *open magnetosphere*. The two sections are separated by the *last closed field line*, which can be assumed to be the dipolar field line that crosses the equatorial plane at $r = R_\ell$. Such line departs from the pulsar surface at an angle θ_0 from the pole, given by:

$$\sin^2 \theta_0 = \frac{R_\star}{R_\ell} = \frac{R_\star \Omega}{c}, \quad (1.6)$$

where R_\star is the radius of the star. For typical values, $\theta_0 \gtrsim 1$ deg. The region defined by $\theta < \theta_0$ and its opposed one form the *polar caps* of the pulsar. Particles originating from there and streaming along field lines eventually leave the neutron star to form the *pulsar wind*. The emission of such a leptonic wind carries away momentum and energy from the star, possibly forming a *pulsar wind nebula* such as the Crab Nebula. In aligned rotator models, where no dipole magnetic braking is possible, this is the main mechanism responsible of the progressive spin-down of the pulsar.

If the neutron star is instead accreting material from a companion object, the inflowing plasma is forced to follow the open magnetic field lines and can reach the pulsar surface only at the polar caps. These represent only a small fraction of the neutron star surface and are heated up to high temperatures. This is the proposed emission mechanism of *accretion-powered pulsars*.

Current structure The net current flowing from the pulsar must be zero, so that the global neutrality of the star is maintained. This implies that the outgoing flux of electrons must be balanced by an equivalent flux of positrons. If the flow of particles of opposed signs is strictly disjoint, between the pole and the last closed field line there must exist a *critical field line*. This is the field line that separates regions of opposite current directions, and touches the star surface at an angle θ_c . The critical line can be equivalently defined as the one having the same potential as the outer space far from the pulsar. If $\mathbf{\Omega} \cdot \boldsymbol{\mu} > 0$, electrons stream away from the pulsar for $0 < \theta < \theta_c$ and positrons do so for $\theta_c < \theta < \theta_0$. Figure 1.3 shows that the sign of the magnetic field is inverted in the northern and southern hemisphere of the magnetosphere. This is a necessary consequence of the solenoidal nature of the magnetic field. When crossing the equatorial plane, the dominant toroidal component of \mathbf{B} experiences a discontinuity. The same holds in the inner magnetosphere along the last closed field line: the toroidal field is zero in the closed portion of the magnetosphere and non-zero in the open one. A poloidal current must flow along these surfaces to sustain such discontinuities. The resulting current pattern takes the name of *equatorial current sheet* of the pulsar. The presence of the sheet violates

⁶ Strictly speaking, since $\nabla \cdot \mathbf{B} = 0$, those lines eventually close themselves far away from the neutron star, where its magnetic field merges with the interstellar one.

the force-free condition $\mathbf{E} \cdot \mathbf{B} = 0$, indicating that the simple and ideal Goldreich-Julian model is not adequate to describe such structures (see Section 1.3.2).

In summary, a pulsar acts as a generator, creating large potential differences due to its magnetic field and fast rotation. In a circuit analogy, *the pulsar wind constitutes the load resistance of the generator*. It flows away removing energy and angular momentum from the star, which spins down. In the more general oblique rotator case, the same happens because of magnetic dipole radiation from the rotating star. The simple Goldreich-Julian model succeeds in outlining the basic concepts of a pulsar magnetosphere, but produces several inconsistencies. Among these, the most evident one is that the force-free condition $\mathbf{E} \cdot \mathbf{B} = 0$ implies that no particle acceleration is possible. If this was the case, no leptonic plasma could be produced in the first place and no high energy gamma-ray emission would be expected. This means that particles can only be accelerated if a “defect” in the force-free plasma is present. This consideration is at the base of several models for the gamma-ray emission of pulsars, which will be reviewed in the next section. Attempts to analytically solve the structure of the pulsar magnetosphere even for the simplest cases have failed. The aligned dipole force-free solution was only obtained numerically in Contopoulos et al. (1999). In recent years extensive numerical simulations have been leading the research on the topic, highlighting the importance of both non-ideal conditions and time-dependent phenomena. Despite these efforts, a complete or even consistent picture of pulsar magnetospheres has not been reached yet. Gamma-ray observations are a powerful tool to probe their physics, and obtain a better understanding of the phenomena taking place in such extreme environment.

1.3 High-energy emission

Pulsars are observed to emit in the whole range of the electromagnetic spectrum, and possibly different mechanisms are responsible for the emission at different energies. In the case of gamma-ray pulsars, two basic processes are thought to be responsible for the emission: *curvature radiation* and *inverse Compton scattering*. Both of them rely on the presence of accelerated leptons in the pulsar magnetosphere. As discussed in the previous section, this is possible only if localized “defects” to the ideality of the plasma or its force-free condition are present. Different models identify different acceleration sites in the pulsar magnetosphere, and these affect the expected spectral shape of the radiation. The measurement of the gamma-ray spectrum of a pulsar is therefore a tool to probe the emission mechanism in its magnetosphere.

Following conventions in gamma-ray astronomy, throughout this thesis I will indicate as the *differential flux* or *spectrum* of gamma-rays from a source the quantity:

$$\mathcal{F}(E) = \frac{dN}{dE dA dt}, \quad (1.7)$$

representing the number dN of photons with energy between E and $E + dE$ received in a time interval dt on a surface dA . As pulsars are point-like sources, the dependence

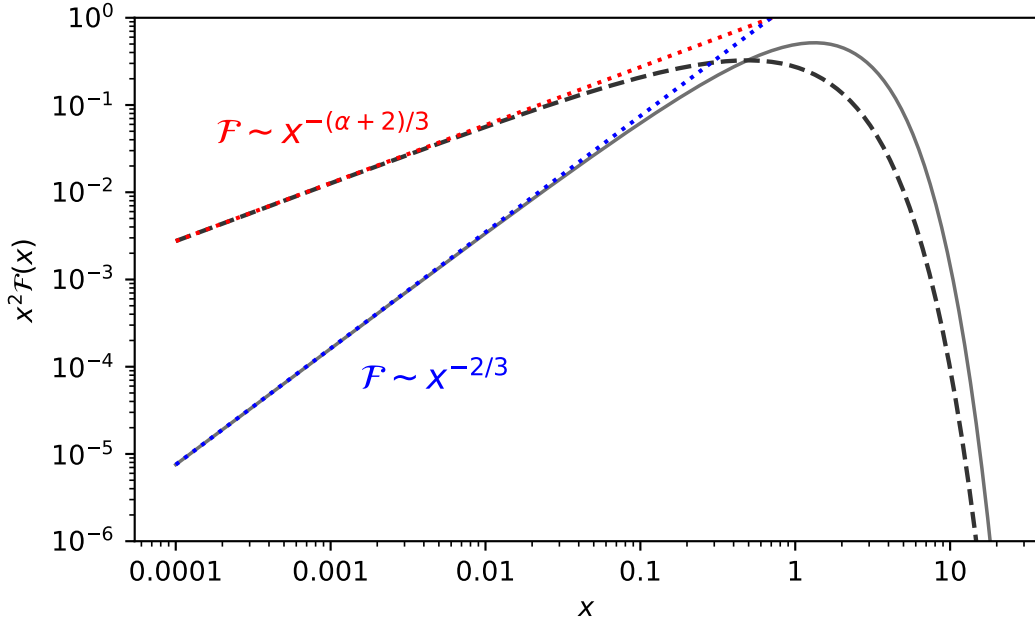


Figure 1.4: Sample curvature radiation spectra. Solid line: spectral energy distribution of a mono-energetic population of particles, as a function of $x = E/E_c$ (cfr. Equation 1.8). Dashed line: same with a particle population whose energy is distributed as a power-law with spectral index $\alpha = 2$. Curves are normalized so that the total emitted energy is the same in both cases.

on the radiation pencil $d\Omega$ is superfluous and the area dA is supposed to be perpendicular to the direction of the source. Since gamma-ray spectra span several orders of magnitude in energy, in many situations it is more useful to obtain this quantity in logarithmic units of energy. The logarithmic differential flux is $E \mathcal{F}(E) = E dN/dE/dA/dt = dN/d \log(E)/dA/dt$. This is formally the same as the power density, the amount of energy emitted or received in photons of a given energy E . Its logarithmic version, the *Spectral Energy Distribution*, given by $E^2 \mathcal{F}(E) = E^2 dN/dE/dA/dt = E dN/d \log(E)/dA/dt$, is the quantity most commonly employed to represent spectra. A source radiating the same power in all logarithmic intervals has a flat spectral energy distribution and corresponds to a power-law spectrum $\mathcal{F}(E) \propto E^{-\Gamma}$ with a spectral index $\Gamma = 2$.

1.3.1 Gamma-ray emission processes

The bulk of the gamma-ray emission of pulsars is well described as a kind of *curvature radiation* due to the motion of high energy leptons in the magnetosphere of the neutron star. This is analogous to synchrotron radiation, with the curved motion of charged particles being provided by the magnetohydrodynamic requirement that they follow curved magnetic field lines. The spectrum of synchrotron emission from a mono-energetic population of particles with Lorentz factor γ resembles a power-law function with an exponential cut-off at higher energies. A critical energy can be defined in terms of the curvature radius r_c and γ :

$$E_c = \frac{3 \hbar c}{2 r_c} \gamma^3. \quad (1.8)$$

In the standard synchrotron scenario, the curvature radius equals the gyro-radius $r_g \propto \gamma$, resulting in a $E_c \propto \gamma^2$ dependence. In the case of curvature radiation, r_c is instead a geometrical parameter and $E_c \propto \gamma^3$. The spectrum of the radiated photons $\mathcal{F}(E)$ can be approximated as:

$$\mathcal{F}(E) \propto \begin{cases} E^{-2/3} & (E < E_c) \\ E^{-1/2} \exp(-E/E_c) & (E > E_c) \end{cases} .$$

The exponential factor introduces a sharp energy cut-off at energies larger than E_c and the corresponding spectral energy distribution is very peaked, with roughly 90% of the power being emitted between $0.1 E_c$ and $4 E_c$. In a realistic case, the radiating particles do not share a common γ , but follow instead a distribution $\mathcal{N}(\gamma) = dN_{e^\pm}/d\gamma$ determined by the particle acceleration mechanism. If this can be described by a power-law $\mathcal{N}(\gamma) \propto \gamma^{-\alpha}$ up to some value γ_0 , the resulting gamma-ray spectrum also follows a power-law $\mathcal{F}(E) \propto E^{-\Gamma}$ with a cut-off at $E > E_c(\gamma_0)$. The spectral indices α and Γ are related by:

$$\begin{aligned} \Gamma_{\text{SYNC}} &= (\alpha + 1)/2 && (\text{synchrotron}) \\ \Gamma_{\text{CURV}} &= (\alpha + 2)/3 && (\text{curvature}) \end{aligned} \quad ,$$

with the difference being justified by the different dependence of E_c upon γ in the two cases ⁷. Figure 1.4 presents the functional form for such spectra. Curvature radiation can easily account for exponentially cut-off power-law trends, which are ubiquitous in the spectra of gamma-ray pulsars between 100 MeV and 10 GeV. Using the typical 1 GeV peak value of the spectral energy distribution and a light cylinder radius $R_\ell \sim 1000$ km as estimates for E_c and R , the cutoff Lorentz factor of the radiating electrons is $\gamma_0 \sim 10^7$.

By contrast, very high energy spectra including a power-law component at energies above several tens of GeV can not be explained by synchro-curvature emission, and *inverse Compton scattering* is usually invoked to account for their presence (VERITAS Collaboration et al., 2011; Aleksić et al., 2012). This requires both accelerated leptons and a softer photon field (typically in the X-ray domain) to coexist in the pulsar magnetosphere. Since the scattering leptons are ultra-relativistic, their kinetic energy is much larger than the energy of the seed photon, and the relativistic limit of the Klein-Nishina cross-section can be taken. In these assumptions, if the scattering electrons have an average energy $E_e = \gamma m_e c^2$, the average energy of the inverse-Compton photons is simply $E_\gamma = E_e/2$. Similarly to the case of synchro-curvature radiation, if the spectrum of the electrons follows a power-law, the resulting gamma-ray spectrum is also a power-law with a spectral index:

$$\Gamma_{\text{IC}} = \alpha - 1$$

Therefore, assuming an electron population with $\gamma = 10^7$ and $E_e \sim 5$ TeV, the inverse Compton mechanism can justify very high energy photons with energies above tens of GeV and a power-law like spectrum. The seed soft photons can be of external origin (for instance, the thermal ones from the surface of the star) or result from the synchrotron emission of the same electron population up-scattering them. In this latter case, the process takes the name of *synchrotron self Compton*. Leptonic synchrotron self

⁷ These results are often formulated in terms of the spectral indices of the power density $E\mathcal{F}(E)$. These are $(\alpha - 1)/2$ and $(\alpha - 1)/3$ for synchrotron and curvature radiation, respectively.

Compton emission is invoked to explain the very high energy emission of many astrophysical sources (e.g. active galactic nuclei, pulsar wind nebulae). Inverse Compton emission has been confirmed to occur in the magnetosphere of the young Crab Pulsar (Ansoldi et al., 2016), where it is responsible for the emission of pulsed gamma rays up to TeV energies, with a power-law spectrum. This is briefly discussed in Section 1.5 and more extensively in Chapter 5, in light of the results presented in this thesis. In Chapter 6, I show that the much older Geminga pulsar also seems to possess an inverse Compton power-law component above 15 GeV and up to 75 GeV. The detection of very high energy emission associated with inverse Compton scattering allows to set constraints on the possible accelerator geometries and to better understand the structure and processes operating in pulsar magnetospheres. The comparison of the spectra of different pulsars is a promising research topic, that may yield viable information on the evolution of these objects.

1.3.2 Particle acceleration

Both the synchro-curvature and the inverse Compton scattering mechanisms require the presence of ultrarelativistic accelerated particles in the pulsar magnetosphere. In Section 1.2 it was shown that, in an ideal magnetosphere, the charges are free to move along the magnetic field lines, but also that the electric field is everywhere perpendicular to them, implying that no acceleration of the electrons can take place. The mechanisms responsible for the acceleration are bound to the existence of zones in the magnetosphere where the solution departs significantly from the ideal case. Such “defects” correspond to dissipative regions of the magnetospheric plasma. Diverse theoretical models have been proposed to explain the formation and dynamics of these accelerating regions. Their locations in the magnetosphere have profound implications for the gamma-ray emission (see Figure 1.5). In particular, different classes of models predict different functional behaviors of the gamma-ray spectrum at its higher end. This can be modeled with a power-law with a *generalized exponential cutoff* in energy:

$$\mathcal{F}(E) = (E/E_0)^{-\Gamma} \exp \left[- (E/E_{\text{cut}})^\beta \right], \quad (1.9)$$

where β is the cutoff index and E_{cut} is the cutoff energy. A short list of the basic models follows. The reader is addressed to referred publications for more details on them.

The **polar cap** was historically the first region where a possible acceleration region has been considered (Ruderman and Sutherland, 1975; Daugherty and Harding, 1996). A charge density depletion in that region, or a so called *vacuum gap*, would make available the large accelerating potential that was calculated in Formula 1.2. However, the strong magnetic field in the proximity of the poles would cause any very high energy gamma ray emission to be quickly re-absorbed due to photo-production of electron-positron couples. This would in turn produce a *super exponential cutoff* in the spectra of pulsars, represented in Formula 1.9 by $\beta > 1$, with a cutoff energy $1 \text{ GeV} < E_{\text{cut}} < 10 \text{ GeV}$. The first MAGIC detection of the Crab pulsar above 25 GeV (Aliu et al., 2008) proved that this was not the case, and its emission above 100 GeV (VERITAS Collaboration et al., 2011; Aleksić et al., 2012) was impossible to reconcile with the polar cap model. Furthermore, most *Fermi*–LAT pulsars can be described well by a power-law function with an *exponential*

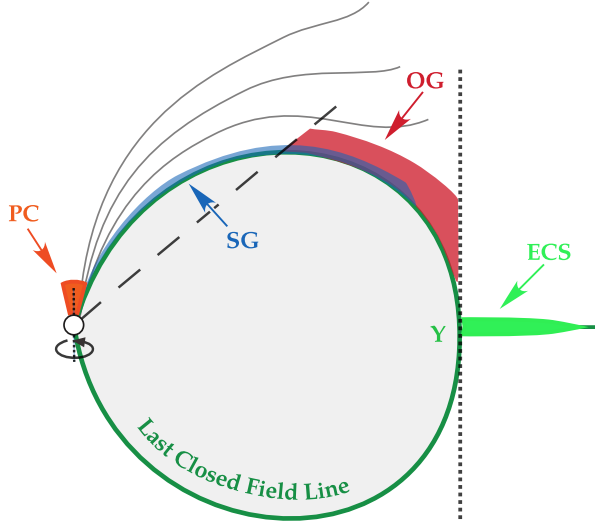


Figure 1.5: Possible regions of particle acceleration in the inner magnetosphere, modified from Hirotani (2011). The pulsar rotates along the vertical axis and the magnetic dipole moment is aligned with it. The last closed field line (dark green), intersects the light cylinder (dotted line) in the equatorial plane, at the Y point. **PC:** polar cap; **SG:** slot gap along the last closed field line; **OG:** outer gap spanning from the null surface (dashed line) to the light cylinder; **ECS:** equatorial current sheet, originating from the Y point and extending outside the light cylinder.

($\beta = 1$) or *sub-exponential* ($\beta < 1$) cutoff (Abdo et al., 2010b, 2013). The polar cap model has therefore been abandoned in favor of scenarios in which the gamma-ray emission is produced farther out in the magnetosphere.

The **outer gap** model represents one of such scenarios. This is another region where a non-ideal magnetosphere could lead to the acceleration of particles (Cheng et al., 1986). Such a gap is proposed to originate from the null surface (cfr. Section 1.2), and to extend along the last closed field line up to the light cylinder. A charge depletion there would lead to a large component of the electric field parallel to the magnetic one ($\mathbf{E} \cdot \mathbf{B} \neq 0$), so that particles could be accelerated to the ultra-relativistic velocities required to radiate gamma-rays by curvature emission. This class of models has proven to reproduce the exponential energy cut-off ($\beta = 1$) in the spectra of several gamma-ray pulsars (Romani, 1996), and has traditionally been invoked to explain the spectra of *Fermi*-LAT pulsars (Abdo et al., 2010c,a,d). A similar model, the **Slot gap**, has also been frequently considered (Harding, 2007). This is proposed to extend as a thin slot along the last closed field line. However, subsequent work has shown that the slot model can not reproduce the observed pulsar flux intensities (Hirotani, 2008). Extensions of the outer gap model Lyutikov (2013) and Hirotani (2013) were proposed to explain the very high energy emission of the Crab pulsar detected by MAGIC and VERITAS (Aliu et al., 2015; Ansoldi et al., 2016), see also Section 1.5. In Section 6.6 I present an application of a similar model to the very high energy emission of the Geminga pulsar, that was detected for the first time during my doctoral work. The outer gap model does not reproduce consistently the spectrum. This either implies that the emission mechanism for very high energy pulsars varies among different objects, or that the theoretical model needs a revision.

The **equatorial current sheet** scenarios are a novel class of models based on extensive Monte-Carlo simulations of the pulsar magnetosphere. These simulations employ well-established numerical techniques of plasma Physics, such as the Particle-In-Cell schemes (Kalapotharakos et al., 2018; Guépin et al., 2020). Results show that if the supply of charged particles is sufficiently large, the pulsar magnetosphere is not dramatically dif-

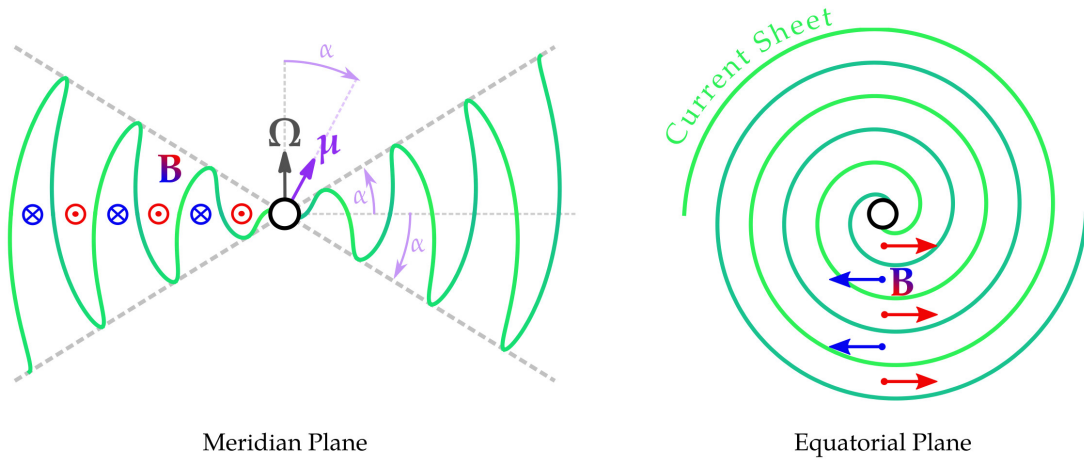


Figure 1.6: Scheme of the striped pulsar wind. **(Left)** The magnetic moment μ of the neutron star is misaligned with the rotational frequency Ω by an angle α . During a rotation period the magnetic equator oscillates in a $\pm\alpha$ zone centered on the rotational equator. The current sheet (green) swipes across the equatorial plane delimiting stripes of opposed magnetic field B (red and blue, respectively). **(Right)** On the rotational equatorial plane, the sheet surface cuts spiral shaped regions (stripes) with opposed toroidal magnetic field signs. Different fronts of the current sheet have been colorized with two shades to highlight the spiral structure. Based on a figure in Mochol (2017).

ferent from the ideal force-free one, with the notable exception of the equatorial current sheet. In the aligned rotator case, the current sheet merges with the last closed field line at the light cylinder, forming a triple reconnection point known as *Y point* (see Figure 1.5). At the *Y point* a large electric field develops, and accelerate charged particles flowing away along the equatorial current sheet. Interestingly, in this scenario the maximum energy reached by positive and negative particles differs, with positrons reaching much larger energies if $\Omega \cdot \mu > 0$, and electrons in the opposite case (Brambilla et al., 2018). Similarly to the outer gap model, the lower energy component observed by *Fermi*-LAT is modeled as curvature radiation from accelerated leptons, with the very high energy one resulting instead from inverse Compton scattering, possibly extending up to TeV energies (Harding et al., 2018).

The wind region has also been considered a candidate site for particle acceleration. In the more general oblique rotator case, the equatorial current sheet is expected to assume a more complex morphology. As the pulsar rotates, the current sheet sweeps an oscillatory pattern in both the northern and southern hemisphere of the outer magnetosphere, with the amplitude of the oscillations increasing linearly with the distance from the pulsar. Such surface intersects the equatorial plane in an Archimedean spiral pattern separating stripes with opposed directions of magnetic field (cfr. Figure 1.6). Mochol and Petri (2015) propose that particles are accelerated in the current sheet of such a **striped wind**, and that gamma-ray radiation is produced via synchro-curvature and synchrotron-self Compton emission processes. The morphology of the pulse profile is interpreted as the intersection of the line of sight with the current sheet surface. Nu-

merical simulations with the wind model predict a hardening of the spectrum at the very high energies followed by a cutoff in the $\gtrsim 1$, TeV domain, compatible with MAGIC observations of the Crab pulsar (Ansoldi et al., 2016). In this scope, further characterization of the very high energy spectrum of the Crab pulsar (cfr. Section 5) and its measurement at larger energies may contribute to confirm or rule out the proposed emission scenario.

Finally, an alternative picture is proposed by **magneto-centrifugal** models. In these, rather than due to the action of an electric field, particle acceleration is considered to be caused by inertial forces in the pulsar magnetosphere. Leptons are bound to the rigidly rotating magnetic field lines by the ideal magnetohydrodynamic requirements. As these approach the limit of the light cylinder, the centrifugal forces are expected to become very large, and kinetic energy is transferred to the particles, in analogy with a centrifugal pump. These scenarios have found application in the modeling of the very high energy emission of the Crab (Osmanov and Rieger, 2017) and Vela (Osmanov and Rieger, 2019) pulsars. In both cases, the model predicts a pulsed inverse-Compton component reaching TeV energies and following a power-law spectrum.

In summary, different theoretical frameworks for the acceleration of leptons in the pulsar magnetosphere exist. It is not clear which one best represents reality, or whether the very high energy emission of pulsars has to be interpreted as a superposition of different and simultaneously active emission regions. Such an approach is proposed in light of *Fermi*-LAT measurements, as well as existing MAGIC and VERITAS data in Yeung (2020). The presence or absence of certain acceleration processes imprints a signature in the gamma-ray spectra of pulsars. Further observations of known very high energy pulsars (cfr. Chapter 5) and the discovery of new ones (cfr. Chapter 6) are the primary strategies to obtain more information on their physics, and to reach a unified description of them.

1.4 Pulsar timing

Given the periodical nature of pulsar emission, it is interesting to study it in the time domain. For intense signals, such as those obtained in the radio band, this allows one to characterize how the rotation of the pulsar evolves in time, and to derive sensible estimates on its physical properties. It also permits to identify the averaged *pulse profile*, the intrinsic wave-form of the pulsar. This acts as a signature for a certain pulsar and conveys information on its physical parameters (e.g. the inclination of the magnetic dipole axis). However, it depends as well on purely geometrical variables (e.g. the pulsar viewing angle) and it typically varies with the observed energy band.

In very high energy gamma-ray observations, a precise model of the pulsar rotation is needed beforehand in order to be able to obtain the pulse profile. This is because the low photon counts need to be integrated over a long period of time for the signal to be detected, and the concurrent evolution of the pulsar rotation is not negligible. Such a model of the rotation is known as a *pulsar ephemeris*. It is most typically given as a Taylor expansion of the rotational frequency ν of the pulsar:

$$\nu(t) = \nu_0 + \dot{\nu}_0(t - t_0) + \frac{\ddot{\nu}_0}{2}(t - t_0)^2 + \frac{\dddot{\nu}_0}{6}(t - t_0)^3 + \dots \quad (1.10)$$

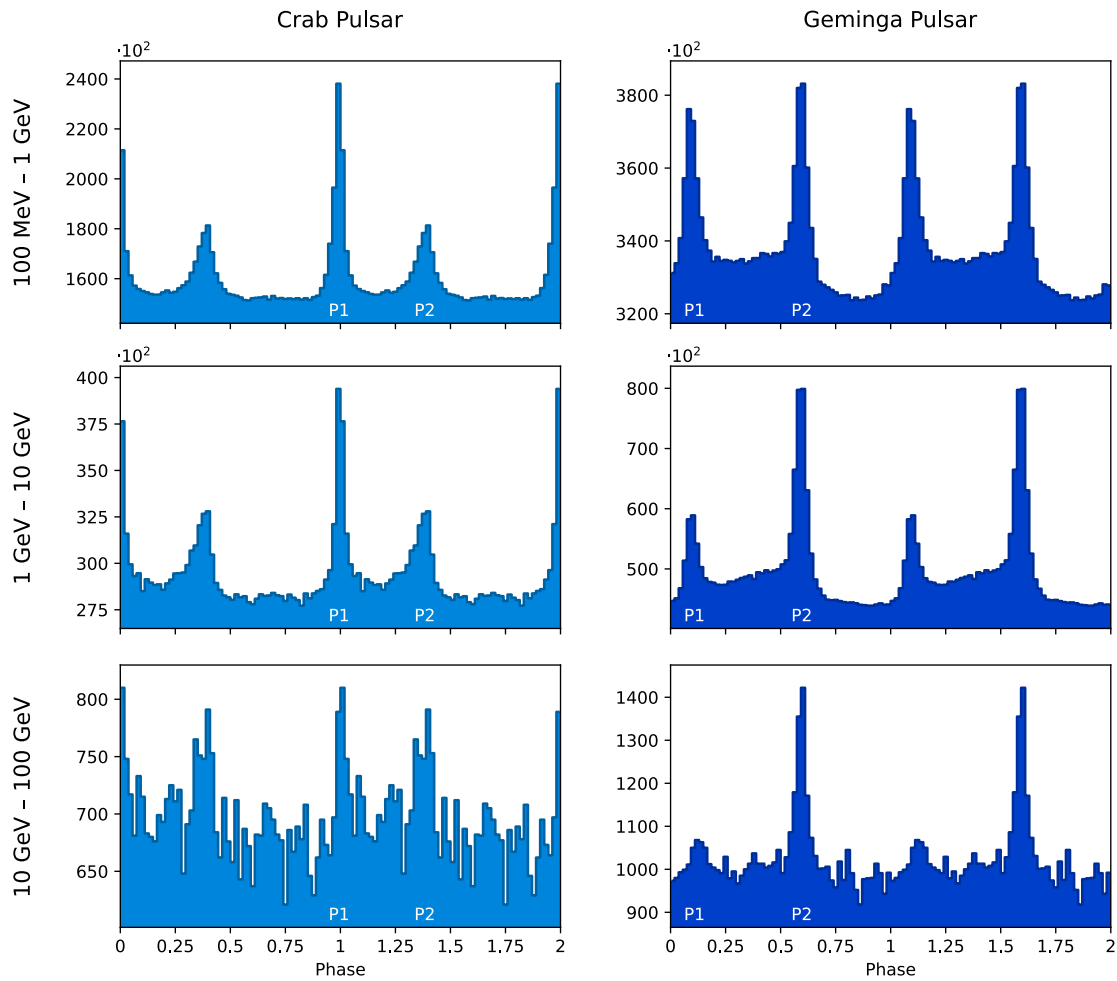


Figure 1.7: Sample *phase diagrams* or *phaseograms*, depicting the gamma-ray pulse profiles of the Crab pulsar (left) and the Geminga pulsar (right), with *Fermi*-LAT data in different energy ranges. The pulse profile of each of them is shown twice (phase ranging from 0 to 2). The shape of the profile depends on the pulsar and varies with energy. Both pulsars have two pulses per period (labeled P1 and P2), but the separation of the two pulses is not necessarily half a turn. Even larger variations happen when considering multiwavelength observations of these two objects (cfr. Figure 1.14).

The number of turns completed by the pulsar from the reference time t_0 is the pulsar *phase* Φ . The fractional part of the pulsar phase at a certain time bears information on the pulsar orientation at that time. Throughout the text I will refer to the fractional part of phase Φ simply as the ‘phase’ and label it with φ . Events with the same fractional phase are emitted when the pulsar has the same orientation with respect to the viewer. Details on how phase is associated to each event are given in Section 4.6. The production of pulsar ephemerides is covered in Appendix A.

The attribution of a phase to each event recorded by the detector allows one to produce a phase diagram or *phaseogram*. This is a histogram grouping events versus their phase and representing the pulse profile. Sample phaseograms are shown in Figure 1.7. The profiles typically present one or multiple *pulses*, commonly labeled as $P1$, $P2$, etc., but broader features such as a *bridge* connecting different pulses can also be observed. Both pulse profiles in Figure 1.7 present two pulses per period; the bottom one presents also a prominent bridge emission between $P1$ and $P2$. Not all pulsars exhibit two pulses per period. In those who do, $P1$ and $P2$ are not necessarily separated by exactly half a turn ($\Delta\varphi = 0.5$).

The dissipation of the rotational energy of the pulsar progressively causes it to spin down. A diagram relating the period P and its time derivative \dot{P} for a population of pulsars is known as the $P - \dot{P}$ *diagram*. Such diagram allows one to classify pulsars, similarly to a Hertzsprung-Russel diagram for regular stars. It is customary to model the spin-down rate of a pulsar as a power-law function of the rotational frequency:

$$\dot{\nu} = -k\nu^n, \quad (1.11)$$

with k a proportionality constant. This defines the *braking index* n of the pulsar. Such index differs for different possible spin-down mechanisms. Both the magnetic dipole radiation from an oblique rotator and the torque exerted by the particle wind result in a braking relation with $n = 3$. This allows to estimate the *characteristic age* τ of the pulsar from the integration of Equation 1.11:

$$\tau = -\frac{\nu}{2\dot{\nu}}, \quad (1.12)$$

where the limit $\nu_0 \gg \nu$ has been taken for the initial rotation frequency ν_0 at the time of the formation of the neutron star. In a similar way, a characteristic magnetic field value \mathfrak{B} can be obtained by assuming the whole rotational energy loss to be caused entirely by magnetic dipole radiation. This is done by considering the moment of inertia \mathcal{I} of the neutron star to be constant, so that the kinetic energy loss can be written as $\dot{K} = \mathcal{I}\omega\dot{\omega}$, with $\omega = 2\pi\nu$. The value of \dot{K} estimated in this way is commonly known as the *spin-down luminosity* of the pulsar. On the other hand, the energy loss must be equal to the total power \mathcal{P} radiated by the rotating magnetic dipole:

$$\mathcal{P} = \frac{\mu_0\omega^4}{6\pi c^3}m^2 \sin^2 \alpha, \quad (1.13)$$

where m is the magnetic moment of the neutron star and α is its inclination with respect to the rotation axis. The characteristic magnetic field \mathfrak{B} is defined as the polar field that

the pulsar would have if its magnetic axis were perpendicular to the rotational one:

$$\mathfrak{B} = \frac{\mu_0 m}{2\pi R_\star^3}, \quad (1.14)$$

with R_\star the radius of the pulsar. The substitution in Equation 1.13 yields:

$$\mathfrak{B}^2 = \frac{3\mu_0 c^3}{8\pi^3 R_\star^6} \mathcal{I} \frac{\dot{\nu}}{\nu^3} \quad (1.15)$$

The characteristic age τ and magnetic field \mathfrak{B} are thus related to the rotation frequency ν and its time derivative $\dot{\nu}$, or equivalently to the rotation period P and the spin-down \dot{P} :

$$\begin{aligned} \tau &\propto \nu/\dot{\nu} &&\propto P/\dot{P} \\ \mathfrak{B} &\propto \sqrt{\dot{\nu}/\nu^3} &&\propto \sqrt{P\dot{P}} \end{aligned} \quad (1.16)$$

Therefore, the position of a pulsar in the $P - \dot{P}$ diagram conveys information on both its age and the strength of its magnetic field. Figure 1.8 shows a $P - \dot{P}$ diagram obtained with data from the ATNF Pulsar Catalogue⁸. Pulsars begin as young spin-powered pulsars (short period, large magnetic field) in the upper part of the diagram and progressively evolve to longer periods and weaker magnetic fields. Those in a binary system may at some point accrete material from the companion star, gaining angular momentum and spinning up again. These old *recycled pulsars* are easily identified by their extremely short period $P \sim 1$ ms and their very weak magnetic field. For these objects, τ is not representative of the real age. Due to the short periods, they are also commonly named *millisecond pulsars*.

1.4.1 Timing glitches

Some pulsars exhibit sudden variations in their rotation frequency, known as *timing glitches*. These events break the usual rotation model given by the Taylor expansion of Equation 1.10. A pulsar glitch consists in an increase of the spin frequency ν characterized by an impulsive nature. The relative change of the frequency has a typical value of 10^{-9} , but strong glitches with $\delta\nu/\nu \geq 10^{-6}$ exist as well⁹. The spin-down rate also typically experiences an acceleration, so that the pulsar loses energy faster after the glitch than it did before. The phenomenon is usually followed by an exponential relaxation process of $\dot{\nu}$, with a typical scale of several days, after which values of the spin-down rate closer to those before the glitch are recovered and the polynomial behavior is reinstated. Glitches are believed to be caused by processes happening in the interior of the pulsar, and leading to a sudden momentum transfer from the inner core to the crust of the neutron star (Espinoza et al., 2011). However, these processes are very poorly understood and involve the unknown state of matter of the neutron star core. Almost all glitching pulsars are young and middle aged spin-powered pulsars.

Glitches disturb the production of a timing solution (ephemeris) for pulsars. After a glitch, the pulsar ephemeris needs to be updated. This often requires several days, due

⁸ ATNF Pulsar Catalogue: <https://www.atnf.csiro.au/research/pulsar/psrcat/>.

⁹ Glitch catalog: <http://www.jb.man.ac.uk/pulsar/glitches.html>

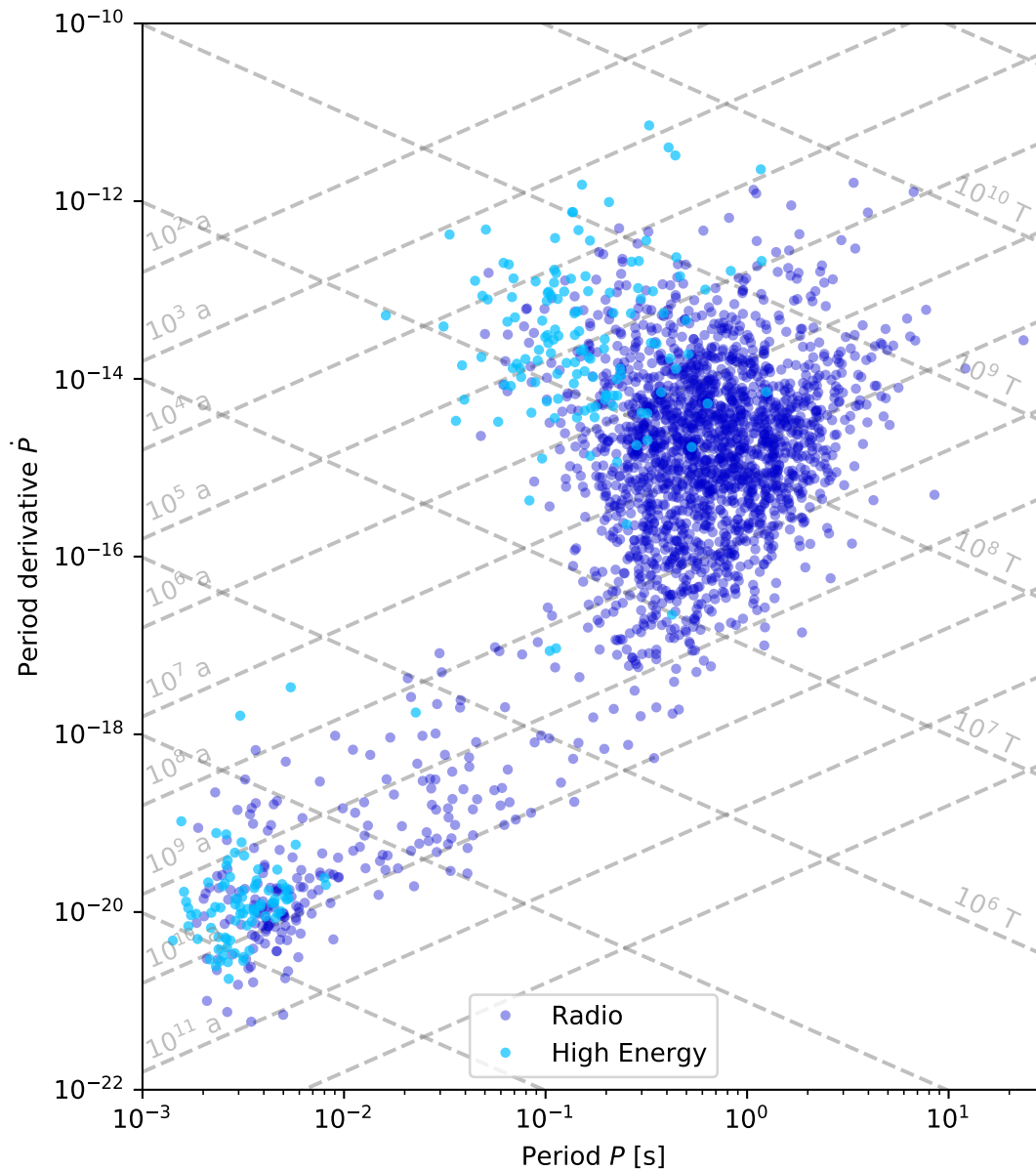


Figure 1.8: Pulsar $P - \dot{P}$ diagram. Pulsars are subdivided in two classes: radio pulsars (deep blue) and ‘high-energy’ ones (light blue), which in this context means pulsars with significant emission above radio frequencies. Diagonal dashed lines represent loci of constant characteristic age τ and characteristic magnetic field \mathfrak{B} . Young spin-powered pulsars have large magnetic field and short spinning periods. They are located in the upper central part of the diagram. As they age, they move diagonally towards the bottom-right. Few of these old pulsars emit beyond the radio band. In the bottom left corner, there exist a population of pulsars with very short periods, but low spin-down rates and low magnetic field. These are *recycled pulsars*, which have spun up again by accreting material from a companion object. They are commonly known as *millisecond pulsars*.

Only rotation-powered pulsars are shown in the diagram. Anomalous X-ray Pulsars (AXP) and Soft Gamma-ray Repeaters (SGR), which are both associated with magnetars, as well as Rotating Radio Transients (RRAT) are not included.

to the time required to collect enough data to assess the new rotation parameters. Section A.2 provides a simple method to do that, based on *Fermi*–LAT data. The Crab pulsar is known to frequently glitch (Shaw et al., 2018), but it is also a young and bright radio-loud pulsar, simplifying the production of post-glitch ephemerides. On the other hand, the Geminga pulsar is an older radio-quiet pulsar, but it has been observed to incur in a minor glitch only once, in 1996 (Jackson et al., 2002).

1.4.2 Timing noise

Besides the sudden glitches, pulsars present a longer quasi-periodical wandering of their timing solutions. This behavior is known as *timing noise* and can be caused by several phenomena, such as the precession of the neutron star or an orbiting planet. As opposed to timing disturbances caused by an improper ephemeris, timing noise is an intrinsic characteristic of a pulsar. It is in general very difficult to decouple these two sources (Coles et al., 2011). In the scope of gamma-ray observations, the timing noise of a pulsar needs to be properly modeled to obtain a precise ephemeris for it, but it is not relevant to identify the intrinsic contributions. This allows to use a simpler technique to produce a rotation model, such as the one discussed in Section A.4.

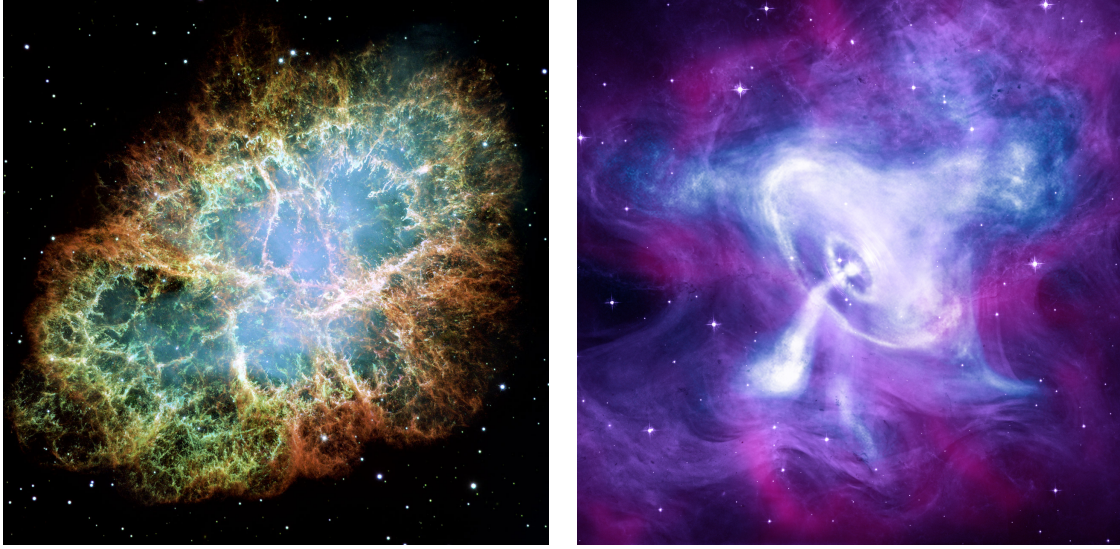


Figure 1.9: Composite images of the Crab pulsar and nebula. **(Left)** Optical image of the Crab nebula (HST), evidencing the gas expelled by the supernova (outer shells, orange, green), and the synchrotron emission from the pulsar wind nebula (blue glow). The image is 6.41 arcmin wide. Credit: NASA, ESA and Allison Loll/Jeff Hester (Arizona State University). Acknowledgment: Davide De Martin (ESA/Hubble). **(Right)** Composite infrared (magenta, Spitzer), optical (purple, HST) and X-ray (blue, Chandra) image of the crab pulsar wind nebula. The image scale is roughly one half of the previous image. The bright dot at the center is the Crab pulsar. Credits: X-ray: NASA/CXC/SAO; Optical: NASA/STScI; Infrared: NASA-JPL-Caltech.

1.5 Crab Pulsar

The Crab pulsar (PSR J0534+2200) and nebula (M1) are the remnants of a supernova occurred in 1054 CE, and recorded in historical Chinese, Japanese (Duyvendak, 1942), and Arabic (Brecher, 1978) documents. As such, they are among the few objects of their kind for which a precise determination of the age is possible ($\tau = 967$ a). Their estimated distance is ~ 2000 pc (Trimble, 1973). As of 2021, the pulsar has a period $P \simeq 33.78$ ms, corresponding to a frequency of $\nu \simeq 29.6$ Hz, and a first frequency derivative $\dot{\nu} \simeq -3.7 \cdot 10^{-10}$ Hz². The frequency has decreased by ~ 0.4 Hz since the beginning of regular radio observations, in 1987. With an associated spin-down luminosity $\dot{K} \sim 4 \cdot 10^{31}$ W and a characteristic magnetic field $\mathfrak{B} \sim 4 \cdot 10^8$ T, it is among the most energetic young pulsars. Its discovery and association with the Crab nebula (Lovelace et al., 1968) provided a decisive confirmation that pulsars are rapidly spinning neutron stars (Gold, 1969). The Crab supernova remnant is among the most studied celestial sources, and used as a standard candle and flux unit of measurement in several branches of high-energy astronomy. Its emission has been detected in the whole electromagnetic spectrum, up to very high energy gamma rays. In this section I briefly review the status of the gamma-ray observations of the Crab pulsar and nebula, and point to the open questions.

1.5.1 Spectrum

The intense pulsed gamma-ray emission of the Crab pulsar was first measured few years after the discovery of pulsars, with the observations of the SAS-2 satellite (Kniffen et al., 1974; Fichtel et al., 1975). These early results evidenced the presence of two emission pulses, P1 and P2, in phase with the radio and X-ray ones. Detected up to 1 GeV, the radiation followed a power-law spectrum. These findings were later confirmed by observations of the COS-B (Clear et al., 1987) and EGRET telescope (Nolan et al., 1993). Phase-resolved spectra were measured up to 10 GeV, with a phase-averaged spectral index consistent with $\Gamma \simeq 2$ and no evidence for a cutoff (Kuiper et al., 2001). This was interpreted as synchro-curvature radiation originated in the magnetosphere of the pulsar, with different particle acceleration models predicting various cutoffs at energies larger than 10 GeV (cfr. Section 1.3). The apparent absence of pulsed emission in the results of early Cherenkov telescopes, probed down to an energy of 60 GeV (de Naurois et al., 2002), seemed to confirm this hypothesis.

After many attempts with ground-based gamma-ray instruments, the first MAGIC telescope finally detected the Crab pulsed emission above 25 GeV (Aliu et al., 2008). The measured flux was significantly lower than the extrapolation of the EGRET power-law, confirming the presence of a spectral break. However, the measurement was several times larger than the super-exponential cutoff predicted by the polar-cap emission model, and incompatible with it. The MAGIC detection ruled out such scenario, previously considered the preferred one, and pointed to a particle acceleration mechanism in the outer magnetosphere. This major breakthrough in the field of gamma-ray pulsars was made possible by a low-energy trigger of novel concept, the Sum-Trigger, which served as prototype for the current stereoscopic Sum-Trigger-II (cfr. Section 2.5). With the launch of *Fermi*-LAT, a rich statistic measurement of the spectral break between 1 GeV and 10 GeV became possible (Abdo et al., 2010c). A deviation from the power-law of EGRET was clearly evidenced, and best modeled as an exponential break with a cutoff energy $E_{\text{cut}} \sim 5.8$ GeV. This result was in turn challenged by the detection of pulsed emission above 100 GeV by VERITAS (VERITAS Collaboration et al., 2011) and up to 100 GeV by MAGIC (Aleksić et al., 2011). Both results reported a strong preference for a power-law like spectrum without an energy break, and hinted at a possible inverse-Compton emission mechanism. Following MAGIC results further reinforced this claim, with the detection of pulsation up to 400 GeV (Aleksić et al., 2012) and the detection of the bridge emission between the P1 and P2 pulses (Aleksić et al., 2014). Finally, MAGIC detected the pulsed emission from the P2 pulse beyond 1 TeV energies (Ansoldi et al., 2016), strongly supporting the inverse-Compton origin of the emission. The particle acceleration mechanism responsible for such teraelectronvolt emission is still being investigated. Several competing models have been proposed to explain its presence. Among these, a possible extension of the outer gap model involving a two-stage cascade process was advocated in Ansoldi et al. (2016). This postulates that particles accelerated by the gap up-scatter a soft field of infrared photons via inverse-Compton process. These primary gamma-rays can not propagate outside the pulsar magnetosphere, as they are efficiently re-absorbed via pair production by the same soft photon field. They generate secondary electron/positron pairs in the 1 TeV energy domain, which propagate in the outer magnetosphere, where the density of the photon field is lower.

There, a second stage of inverse-Compton scattering can produce further teraelectronvolt photons, which are not re-absorbed and are instead radiated away. Besides this double inverse-Compton model, the equatorial current sheet scenario (Harding et al., 2018), the striped wind one (Mochol and Petri, 2015), and also the magneto-centrifugal one (Osmanov and Rieger, 2017) have all been proposed as alternative explanations for the teraelectronvolt emission. Further observations with the current and next generation of imaging atmospheric Cherenkov telescopes will help to disentangle these models and clarify the origin of the inverse-Compton component.

1.5.2 Phaseogram

The phaseogram of the Crab pulsar is dominated at all wavelengths by two prominent pulses, separated by a phase difference of $\Delta\varphi \sim 0.4$, and labeled P1 and P2 (see Figure 1.7). The morphology of such pulses is strongly dependent on the energy, but their agreement in phase is respected in different bands. In some of these, a bridge emission between P1 and P2 is present, and connects the trailing edge of the first one with the rising slope of the second one. An analogous emission between P2 and P1 is not observed. A major feature of the Crab pulsar phaseogram is the energy-varying ratio of the P2 to P1 emission (see Figure 1.10). The P1 pulse is dominant up to hard X-rays at around 100 keV. In these ranges, P1 is known as the main pulse, and P2 is usually referred to as the interpulse. Above 100 keV, the P2 emission becomes more prominent. The pulse ratio peaks at energies close to ~ 1 MeV with $P2/P1 \sim 2$. However, at larger energies P1 rapidly recovers its prominence, with a flat $P2/P1 \sim 0.5$ trend between 50 MeV and 2 GeV (Kuiper et al., 2001). P2 slowly becomes dominant again at energies above 20 GeV and the ratio increases further in the energy range of Cherenkov telescopes (Aleksić et al., 2014). In the same band, a progressive sharpening of the pulses is observed

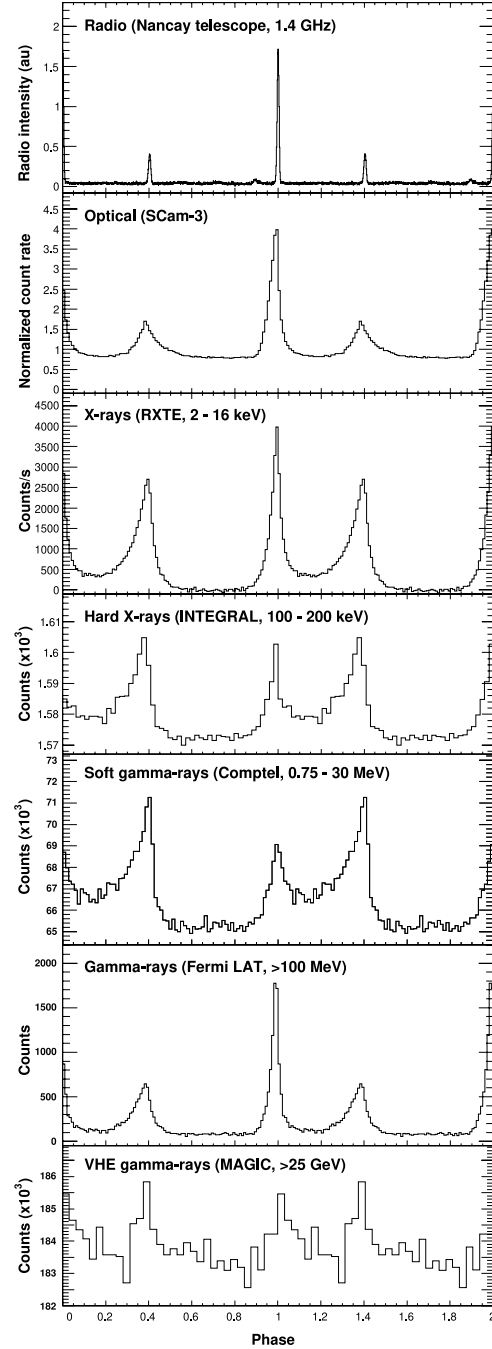


Figure 1.10: Variation of the Crab pulsar pulse profile in a broad energy range, from Abdo et al. (2010c). The MAGIC phaseogram presented here, for $E > 25$ GeV, was the first detection of the Crab pulsar with Cherenkov telescopes (Aliu et al., 2008).

(Aleksić et al., 2012). This complex behavior is a key signature that can be exploited to constrain the emission models, but its origin has not been cleared yet. In Section 5.3, I present an analysis of recent MAGIC data, reporting the increase of the P2/P1 ratio and the reduction of the pulse width between 30 GeV and 200 GeV.

1.5.3 Variability

The possibility of a temporal variability of the pulsed flux was also subject of investigation. In the energy range below 10 GeV, the gamma-ray emission of the Crab pulsar is stable. A claim of a cyclic variation of the pulse ratio, from an early analysis of COS-B and EGRET data (Clear et al., 1987; Nolan et al., 1993), was discarded by following EGRET observations (Kuiper et al., 2001). Since the launch of *Fermi*-LAT in 2008, a practically continuous coverage of the Crab pulsar has been available. These observations showed no sign for variability at energies below 10 GeV. This is in contrast with radio observations of the Crab, where giant radio pulses are frequently observed. Above such threshold, the statistics of *Fermi*-LAT is too low to assess possible variability on time scales shorter than a month. Since at least one gamma-ray pulsar is known to be variable (Allafort et al., 2013), further search for temporal variability at larger energies is still an open topic. This is particularly meaningful in connection with the occasional glitches of the Crab pulsar and with the flares of the Crab nebula, discussed in the next paragraphs. In Section 5.5, I present a proof-of-concept study, aiming to search for variability in the energy range from 30 GeV to 200 GeV on time scales shorter than a month. The improved gamma-ray detection efficiency provided by the Sum-Trigger-II system (cfr. Section 2.5) allows the MAGIC Telescopes to proficiently contribute to this research field.

1.5.4 The Crab Nebula

The wind of the Crab pulsar powers the Crab pulsar wind nebula, the strongest steady gamma-ray source of the entire sky. Detected in the whole electromagnetic spectrum, the emission of the Crab nebula originates at the shock front of the pulsar wind, at a distance of $\sim 4 \cdot 10^{12}$ km (~ 5 light-months) from the pulsar. There, electrons and positrons originating from it are re-accelerated by a first order Fermi mechanism, and emit via synchrotron and synchrotron self-Compton processes. The global structure of the spectrum of the Crab nebula supports this hypothesis. A first very broad spectral component peaks in the ultraviolet range, and extends from radio up to 1 GeV gamma-rays. This broad component corresponds to synchrotron radiation. A second higher energy bump, roughly consistent with a log-parabola spectral shape, peaks in the 100 GeV domain and results from inverse-Compton emission. Extensive studies at all wavelengths have provided a very accurate description of the spectrum of the Crab nebula. Because of this, the source is commonly used as standard candle in several branches of astrophysics (Meyer et al., 2010). The MAGIC telescopes extensively observed the Crab nebula and used its emission as a performance reference (Albert et al., 2008; Aleksić et al., 2015, 2016a). Recently, MAGIC detected the Crab nebula up to 100 TeV (Acciari et al., 2020). Such result, together with similar ones by the HAWC (Abeysekara et al., 2019) and TIBET (Amenomori et al., 2019) Collaborations, suggests that the emission of the Crab nebula could continue up to the PeV regime.

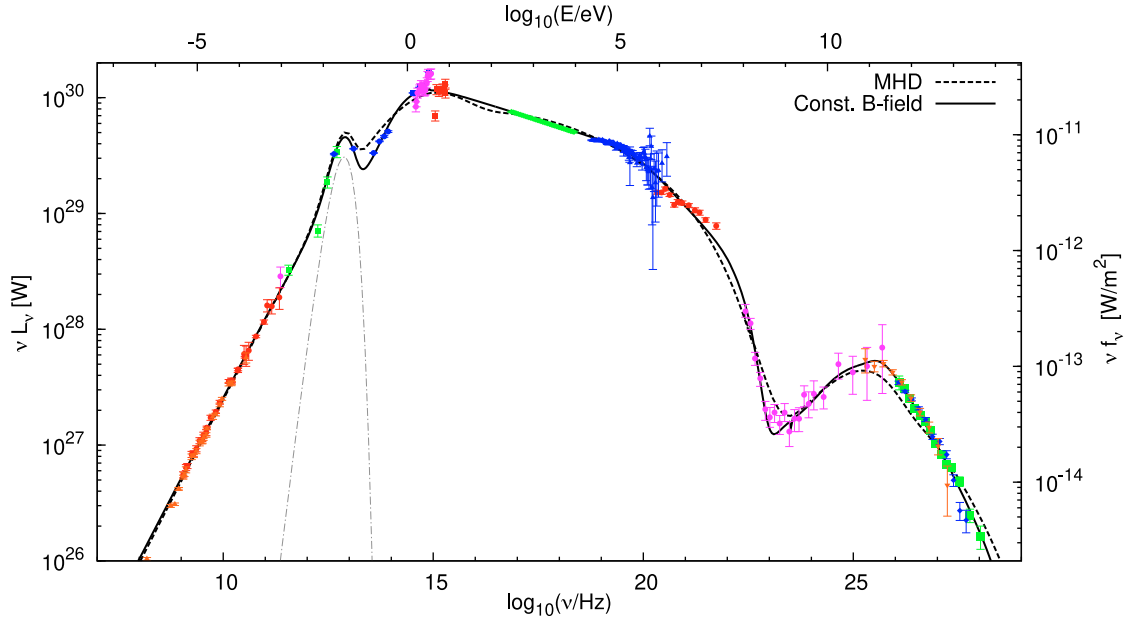


Figure 1.11: Board-band spectral energy distribution of the Crab nebula, from Meyer et al. (2010). Colors represent different instruments, and lines present two possible fits. The y -axes have been uniformed to SI units.

Flare period	<i>Fermi</i> -LAT	AGILE
May 2019	Cheung (2019)	—
October 2018	Cheung et al. (2018)	Bulgarelli et al. (2018b) Cardillo et al. (2018) Lucarelli et al. (2018)
March 2018	Valverde et al. (2018)	Bulgarelli et al. (2018a)
October 2016	Cheung (2016)	Munar-Adrover et al. (2016) Bulgarelli et al. (2016)
August 2014	Becerra et al. (2014)	—
March 2014	Gasparrini and Buehl (2014)	—
October 2013	Buson et al. (2013)	Verrecchia et al. (2013a)
March 2013	Ojha et al. (2013)	Striani et al. (2013a) Verrecchia et al. (2013b)
July 2012	Ojha et al. (2012)	—
April 2012	Buehler et al. (2011)	Striani et al. (2011) Tavani et al. (2011a)
September 2010	Buehler et al. (2010)	Tavani et al. (2010)

Table 1.1: List of the Crab nebula flares for which an ATEL (www.astronomerstelegram.org) was issued. Some minor flares were detected by *Fermi*-LAT and not by AGILE.

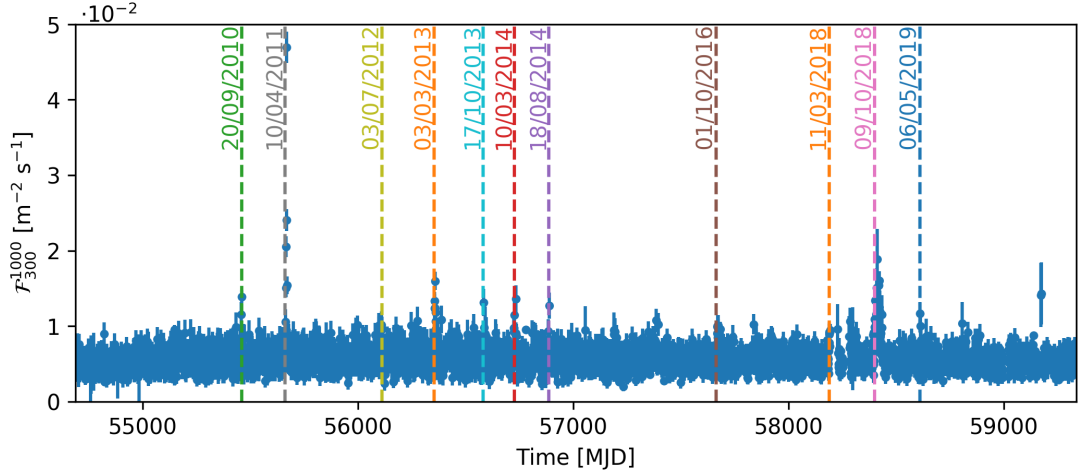


Figure 1.12: *Fermi*–LAT flares of the Crab nebula, in the energy band $300 \text{ MeV} < E < 1 \text{ GeV}$. The plot was produced using the daily *Fermi*–LAT Crab monitoring lightcurve (https://fermi.gsfc.nasa.gov/ssc/data/access/lat/ms1_1c/). Flares for which an ATEL was issued (cfr. Table 1.1) are marked with dashed lines.

Nebula flares

Being considered a standard candle, it came as a surprise when a flare of the Crab nebula was independently detected by the AGILE and *Fermi*–LAT telescopes in September 2010. Since then, ten more such flares were detected (see Table 1.1 and Figure 1.12). These sudden and unpredictable rises in the flux affect the highest energy portion of the synchrotron emission, between tens of MeV and 1 GeV. In such band, the flux during the flaring state can rise up to a factor of 30, but no correlated variability was found at any other wavelength. The typical timescale of one of such flares span from few days to few weeks. Searches for a mirrored variability at the highest end of the inverse-Compton component are on-going (van Scherpenberg et al., 2019), challenging the low available statistics at energies $E \gtrsim 100 \text{ TeV}$.

The cause of the nebular flares is still not understood. The flaring synchrotron emission is produced by the highest energy electrons available at the termination shock. This questions whether a link should be searched with the activity in the highest energy gamma-rays of the pulsar, where the wind is produced. A possible correlation between a putative variability of the pulsar and the flares in the nebula would need to account for the light travel time of 5 months from the pulsar to the termination shock. To assess whether a pulsed variability is present, and if it correlates with the nebula, a monitoring program with a sub-month resolution is required. The MAGIC telescopes, equipped with the Sum-Trigger-II (cfr. Section 2.5) are capable to perform such a study. In the scope of my doctoral project, I proposed and lead a Crab pulsar monitoring project for three consecutive years. The results of the search are presented in Section 5.5. No significant variability has been found, and no correlation study was possible with the nebula, given the absence of major flares in the covered period. Upper limits were set for different types of variability, at various timescales.

1.6 Geminga Pulsar

The Geminga pulsar (PSR J0633+1746), or more often simply Geminga, is a middle-age rotation-powered pulsar. It is one of the brightest high energy gamma-ray sources in the sky, and as such it was identified in the very early gamma-ray surveys. At an estimated distance of 250 pc, Geminga is one of the closest pulsars to the Earth. It has a rotation period $P \simeq 0.237$ s, or a frequency $\nu \simeq 4.217$ Hz, and a spin-down rate $\dot{\nu} \simeq -2 \cdot 10^{-13}$ Hz². This corresponds to a characteristic age $\tau \simeq 3.4 \cdot 10^5$ a, a characteristic magnetic field $\mathfrak{B} \simeq 1.63 \cdot 10^8$ T, and a spin-down luminosity of $\dot{K} = 3.2 \cdot 10^{27}$ W. It is therefore older and less luminous than the Crab pulsar, but it is ten times closer. Its nature of pulsar was not established until several decades after the discovery, mainly due to the lack of significant radio emission: Geminga is the archetype of the class of radio-quiet pulsars.

In this section I review the historical development of the researches on Geminga, and present the state of the art of its spectral studies at different wavelengths. The highest energy pulsation ever detected from the Geminga pulsar, up to 75 GeV, is the main result of my doctoral program.

1.6.1 History and early observations

The first detection of an intense gamma-ray emission from what would have later become known as Geminga was made by the SAS-2 satellite, in a series of exposures taken between 1972 and 1973 (Fichtel et al., 1975). The emission came from the galactic longitude of $\ell = 195$ deg, close to another bright spot coincident with the Crab nebula, almost at the antipodes of the galactic center. Pulsars had been discovered few years before, and at that time it was already known that the Crab nebula hosted a bright one. The pulsed nature of the SAS-2 Crab emission, and its agreement in phase with the radio ones, clearly identified the Crab pulsar as its originating source. However, no pulsar had been detected in the radio band at $\ell = 195$ deg, and the nature of the emission remained unclear. The same observations were later finalized to produce a map of the whole region (reproduced in Figure 1.13) and the mysterious source received the temporary designation of $\gamma 195+4$ (Thompson et al., 1977). A tentative timing analysis of the emission seemed to reveal a periodicity at 59 s, but this was not confirmed by following measurements. Similar results were obtained by the newly launched COS-B satellite (Bennett et al., 1977; Hermsen et al., 1977) which gave the source the catalog entry CG 195+4. In the following years, several attempts were made to associate the gamma-ray emission with a counterpart in radio, optical and X-rays, with unsuccessful results. The situation was still essentially unchanged in 1981, when COS-B identified 2CG 195+4 as the second brightest object at energies above 100 MeV in its second gamma-ray sources catalog.

A decisive step forward was made in 1983, with the detection of a possible X-ray counterpart in the positional error box of COS-B gamma-ray observations (Bignami et al., 1983). This was also the first work in which the missing gamma-ray source was explicitly given the name *Geminga*¹⁰. The source, 1E 0630+178, was identified in exposures of the Einstein

¹⁰ The origin of the name is explained in Bignami et al. (1983). It is both a portmanteau of *Gemini* Gamma-ray

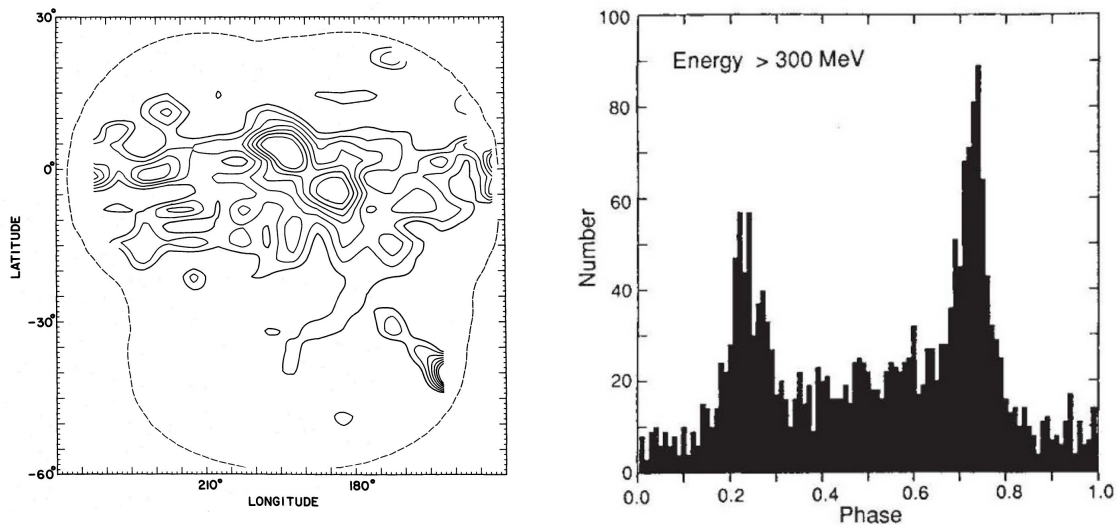


Figure 1.13: Historical results on the Geminga gamma-ray emission. **(Left)** Map of the galactic anticenter region from Thompson et al. (1977), in galactic coordinates. Geminga corresponds to the larger emission region at positive latitude, in the upper part of the plot, the close one being the Crab. **(Right)** Phaseogram of the EGRET gamma-ray data on Geminga, from Bertsch et al. (1992), confirming its nature as a radio quiet gamma-ray pulsar.

Observatory and was peculiar in that it lacked any hint of an extension and any association at lower wavelengths. The authors proposed that Geminga was a neutron star, albeit admitting that it would have been a peculiar one, in that it had no radio emission (Spoelstra and Hermsen, 1984). Few years later came the detection of an extremely faint optical counterpart (Halpern and Tytler, 1988), a bluish star with a visual magnitude $m_v \approx 25.4$ (Bignami et al., 1988). The ratio between optical, X-ray and gamma-ray emission was resembling the one of the Vela pulsar, further reinforcing the hypothesis that Geminga was a pulsar. Finally, this was confirmed with the detection of X-ray pulsations at a period of $P \approx 0.237$ s in the data of the newly launched ROSAT satellite. This first measurement of the period allowed to search for the pulsation in gamma-ray data as well. This was immediately detected by the EGRET experiment on board of the CGRO satellite (Bertsch et al., 1992), as well as in the archival COS-B (Bignami and Caraveo, 1992) and SAS-2 (Mattox et al., 1992) data. The EGRET results showed that the gamma-ray pulse profile above 300 GeV is doubly peaked (see Figure 1.13), similarly to the Crab pulsar. However, in contrast to it, the two pulses are separated by a phase difference consistent with $\delta\varphi \approx 0.5$. After almost 20 years from the first gamma-ray exposures on the region, the enigmatic Geminga was finally proved to be a pulsar. It became the archetype of the class of *radio-quiet* pulsars.

source and a pun on the frustrated searches for the origin of its emission: in the Italian dialect of Milano, “*Ghè minga!*” means “It is not there” or even “It does not exist”.

1.6.2 Multi-wavelength studies

The understanding of the nature of Geminga sparked further research in the field. In the following years, efforts concentrated on determining and modeling its spectrum, the morphology of the pulsed emission and astrometry parameters such as its distance and proper motion.

Gamma-rays

The first measurement of the gamma-ray spectrum of Geminga came soon after EGRET detected the pulsed emission. Early observations allowed to detect a power-law spectrum between energies of 70 MeV and 2 GeV, with a phase-averaged spectral index of $\Gamma \approx 1.5$ (Mayer-Hasselwander et al., 1994). A later phase-resolved spectral analysis revealed a sharp energy turnover above 2 GeV, interpreted as the exponential cutoff of curvature radiation (Fierro et al., 1998). The same analysis evidenced that the emission corresponding to the second pulse P2 was the hardest one ever measured by EGRET, and that the P1/P2 emission ratio decreased with increasing energy. This result was later confirmed by the AGILE satellite (Pellizzoni et al., 2009). With the launch of *Fermi*-LAT, these results were extended and improved. The average spectrum was measured up to energies of 30 GeV and found to be consistent with an exponentially cut-off power-law, although a better agreement could be found with a sub-exponential cut-off (Abdo et al., 2010d). Such milder energy turnover was interpreted as the result of the superposition of different exponential cut-offs at different phase intervals. Among these, the spectrum of P2 was found to be the hardest and at the same time the one with the highest cut-off energy. *Fermi*-LAT confirmed the progressive reduction of the P1/P2 ratio with increasing energy, with P1 becoming almost negligible for energies above 10 GeV (see Figure 1.14). These facts pointed to an acceleration site in the outer magnetosphere as the preferred scenario. The results were confirmed in the second *Fermi*-LAT pulsar catalog (Abdo et al., 2013), with Geminga and the Vela pulsar being the objects with the largest preference for a sub-exponential cut-off model over the exponential one. Early attempts to detect Geminga with IACTs, carried out by the VERITAS (Aliu et al., 2015) and MAGIC (Ahnen et al., 2016) Collaborations, did not yield a significant detection. The analysis of five years of *Fermi*-LAT data performed by the MAGIC Collaboration, however, showed that the P2 spectrum alone was itself best represented by a sub-exponentially cutoff power-law. The entire Chapter 6 of this thesis is devoted to the final detection of pulsed gamma-ray emission in the 15 GeV – 75 GeV range by MAGIC, the main result of my doctoral project. Not only the pure exponentially cut-off power-law model is ruled out for the P2 emission, but the sub-exponential cut-off is also disfavored when compared to a simple power-law extension, indicating that an inverse Compton component may be present. The discovery led to the well-received publication MAGIC Collaboration et al. (2020).

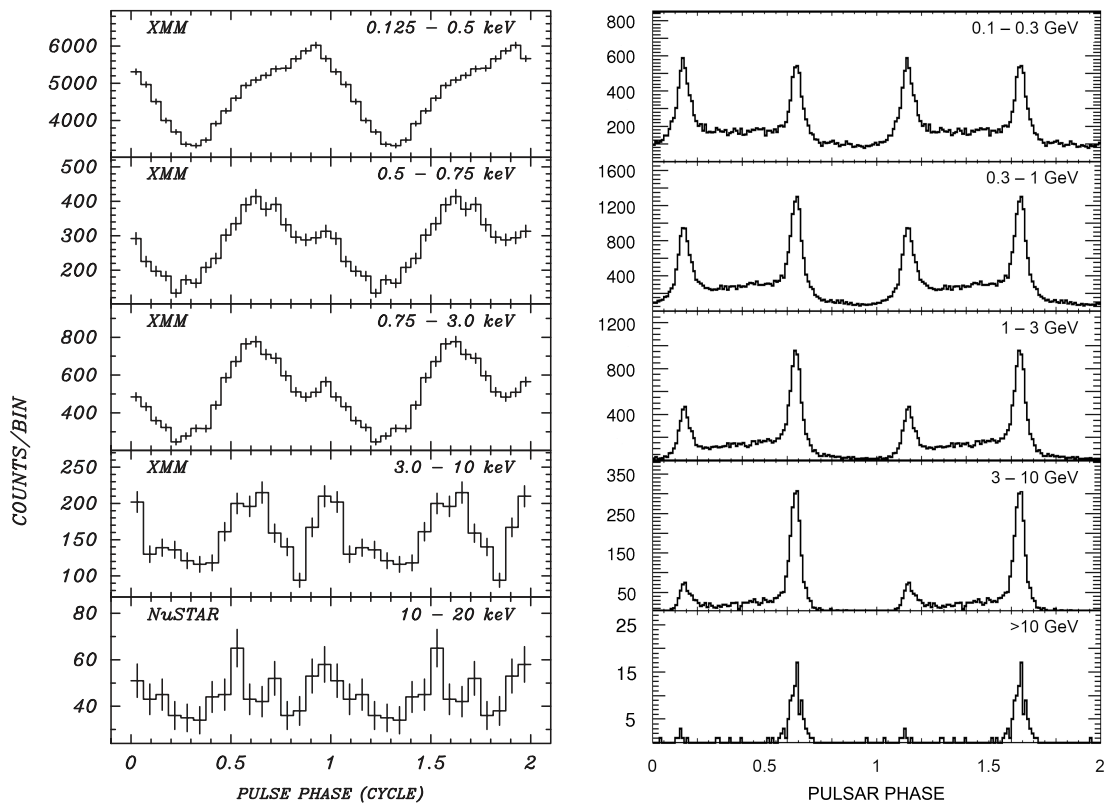


Figure 1.14: Geminga phaseograms in the X-ray (left, XMM-Newton and NuSTAR, Mori et al., 2014) and gamma-ray (right, *Fermi*-LAT, Abdo et al., 2010d) bands. The phase definition used by the two papers differs by $\delta\varphi \approx 0.55$.

X-rays

In the X-ray domain, the bulk of the phase-averaged spectrum is constituted by a superposition of a black-body component, originating from the hot surface of the star, and a non-thermal component, due to synchrotron emission (Halpern and Ruderman, 1993; Halpern and Wang, 1997). The black-body radiation has a characteristic temperature $T \simeq 5 \cdot 10^5$ K. The synchrotron emission becomes dominant above an energy $E = 0.7$ keV and produces a power-law tail with a spectral index close to $\Gamma \simeq 1.7$ (Jackson et al., 2002). The analysis of early XMM-Newton data led to the proposal of a second black-body component, with $T \simeq 2 \cdot 10^6$ K (Caraveo et al., 2004). This was linked with the possible presence of hot spots located at the polar caps of the neutron star. More recently, observations with both the XMM-Newton and NuSTAR satellites confirmed that the spectrum can not be modeled as a simple superposition of a single black-body and power-law components (Mori et al., 2014). These findings are significant for the theoretical expectations of gamma-ray emission, as several models consider X-rays as the source of the lepton pairs accelerated in the pulsar magnetosphere. The presence of the polar hot spots in the context of the outer-gap modeling of the MAGIC gamma-ray observations is briefly discussed in Section 6.6. The X-ray phaseogram of Geminga changes strongly with the energy range (see Figure 1.14, left). At energies below 0.7 keV a single broad pulse is detected, similar to a pure sinusoidal modulation. Above those energies the pulse profile becomes doubly-peaked and a phase shift develops. This is interpreted as the result of the transition from thermal to synchrotron radiation. None of these X-ray phaseograms closely resemble the gamma-ray ones, indicating that the two components are likely to stem from different emission mechanisms or different regions. The X-ray timing of Geminga has provided the only evidence for a glitch in this pulsar to date (Jackson et al., 2002). The glitch happened in October 1966 and was a minor one, as expected for a middle-aged pulsar.

Optical, Ultraviolet and Infrared

The brightness of the night sky from any observatory on Earth greatly exceeds the luminosity of Geminga, even when integrated on an angular aperture as small as 1 arcsec^2 , comparable with the point spread function of major optical telescopes. This renders ground-based optical studies of Geminga extremely challenging. Its feeble emission ($m_V \simeq 25.4$) has been used for astrometry measurements. Ground based observations delivered the first measurements of its large proper motion $\mu = 0.17 \pm 0.05 \text{ arcsec/year}$ (Bignami et al., 1993), which confirmed previous claims that Geminga is a nearby object. Two parallax measurements conducted with the Hubble Space Telescope resulted in distance estimates of $d = 157^{+59}_{-34} \text{ pc}$ (Caraveo et al., 1996) and $d = 250^{+120}_{-62} \text{ pc}$ (Faherty et al., 2007), respectively. These observations indicate that Geminga is one of the closest pulsars to the Earth. Spectral studies were performed in the optical, ultraviolet and infrared bands. It was found that the flux in the far ultraviolet region is consistent with the tail of the black-body radiation peaking at X-rays. However, the near ultraviolet, optical and infrared emission have instead a non-thermal origin, being best represented by a power-law rising for lower energies (Kargaltsev et al., 2005). The transition between the two components happens at an energy of $E \simeq 3 \text{ eV}$. The observed power-law does not connect smoothly with the one measured in hard X-rays above 0.7 keV, implying

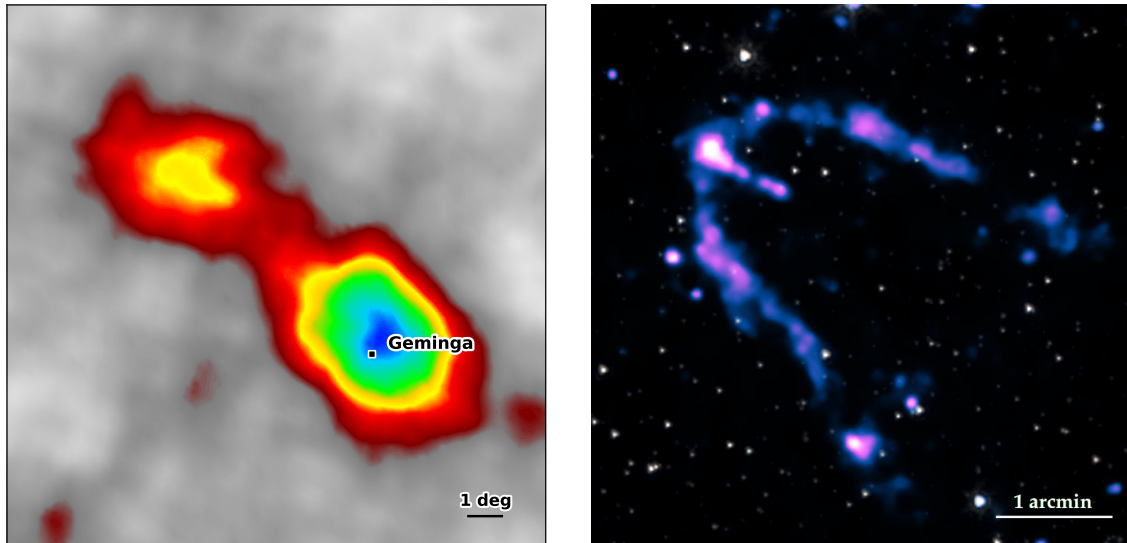


Figure 1.15: Images of the (non pulsed) extended emission of Geminga. **(Left)** TS map derived from HAWC observation with the strong emission of the TeV halos of Geminga and Monogem (adapted from Abeysekara et al., 2017b). **(Right)** Composite X-ray (Chandra) and infrared (Spitzer) picture of the Geminga pulsar wind nebula (Posselt et al., 2017). Notice the much smaller image scale. Image credit: NASA/CXC/PSU/B.Posselt (X-ray), NASA/JPL-Caltech (IR).

that the two are different components (Shibanov et al., 2006). A search for pulsed optical emission led to a 3.5σ marginal detection (Shearer et al., 1998) in the red band. Similar results were obtained in both the near and far ultraviolet ranges (Kargaltsev et al., 2005). Similarly to what is observed in the X-rays, the pulse profile broadly varies with the considered energy. The previously mentioned limitations in the optical band for ground based observations and the lack of high time resolution instruments in space telescopes prevented further studies in this field. Present-day large optical facilities, equipped with single photon counting devices could potentially contribute to this field¹¹.

1.6.3 Pulsar wind nebula

Geminga owns a pulsar wind nebula, detected in the X-ray band (Caraveo et al., 2003). Morphological studies of the nebula show two prominent tails departing from the pulsar at opposite angles, and a third shorter segment aligned with the proper motion vector of the neutron star (cfr. Figure 1.15). It has been proposed that the larger tails are produced by the bow shock of the pulsar wind in the surrounding interstellar medium, distorted by the motion of the star. On the other hand, such interpretation would predict a weaker X-ray emission between the tails, which has not been observed. Alternatively, the tails could be bent polar outflows from the neutron star. The interpretation of such curious morphology is still an open topic (Posselt et al., 2017).

¹¹ The central pixel of MAGIC (see Section 2.3.3), with a radius of 154 arcsec, yields a night sky background rate one million times larger than the optical signal of Geminga, rendering its measurement impossible.

1.6.4 TeV Halo

Geminga is associated with a vast non-pulsed gamma-ray emission. This was first detected by the MILAGRO Experiment (Abdo et al., 2007) and later decisively confirmed by HAWC results (Abeysekara et al., 2017a). Unlike pulsar wind nebulae, the emission covers a large area of several degrees, corresponding to ~ 20 pc at a distance of 250 pc (see Figure 1.15), and exhibits a hard spectrum detected up to several tens of TeV (Abeysekara et al., 2017b). This, together with the observation of a similar emission around the close-by Monogem pulsar, prompted for the definition of a new class of extended objects, the so-called *TeV halos* (Linden et al., 2017). TeV halos are understood to be produced by inverse Compton scattering on leptons originating from the pulsar, further accelerated at the termination shock of the pulsar wind, and escaping from the pulsar wind nebula (Sudoh et al., 2019). *Fermi*-LAT later revealed that the same emission in the $E < 100$ GeV band reaches an even larger extension of several tens of degrees (Di Mauro et al., 2019). The presence of such an extended inverse Compton emission sets a constraint on the diffusion coefficient of charged leptons in the interstellar medium. This is of paramount relevance for the interpretation of the flux of leptonic cosmic rays at the Earth. Specifically, nearby pulsars as Geminga have been considered the source for the cosmic positron excess at energies above 1 GeV revealed by the PAMELA (Adriani et al., 2009) and AMS (Aguilar et al., 2013) experiments. Results by HAWC and *Fermi*-LAT showed that the wind of Geminga alone is probably not sufficient to account for the whole positron excess measured at the Earth, and either a whole population of several pulsars (Manconi et al., 2020) or a single nearby undiscovered one (López-Coto et al., 2018) is required to reconstruct the fluxes. These results depend strongly on the assumptions on the lepton diffusion coefficient between Geminga and the Earth, and the topic is still actively debated (Recchia et al., 2021). It is difficult to employ current Cherenkov telescopes to reveal the emission in the 100 GeV – 1 TeV band, as the extensions of the TeV halo greatly exceeds their typical field of view.



2

THE MAGIC TELESCOPES

The MAGIC telescopes¹ are the imaging Cherenkov telescopes that were used to perform the research presented in this thesis. This chapter briefly introduces the imaging atmospheric Cherenkov telescope technique (Sections 2.1 and 2.2), and describes the basic technical implementation of MAGIC (Sections 2.3 and 2.4). Given its relevance for the pulsar studies, a large part has been devoted to the description of the novel Sum-Trigger-II system (Section 2.5), whereas my technical contributions to it are summarized in Chapter 3. Finally, Section 2.6 covers the typical observation strategy of MAGIC.

A more detailed description of the physics of extensive air showers, and their employment as probes for gamma-ray astronomy, is given, for instance, in De Angelis and Pimenta (2018). The description of the Sum-Trigger-II contained in this chapter is also in common with the publication Dazzi et al. (2021). I was a major contributor of the article, and I am a corresponding author it. The reader is referred to it for a more in-depth discussion of the technical aspects of the Sum-Trigger-II.

2.1 Extensive Air Showers

Very high energy cosmic rays impacting the Earth are absorbed by the atmosphere. Their energy is converted in a swarm of secondary particles, forming an *extensive air shower*. These large cascades of particles were first detected by B. Rossi (Rossi, 1934), and explained by P. Auger (Auger et al., 1939). The average shower properties heavily depend on the nature and energy of the primary particle, but the development of each single shower is a stochastic process. Very high energy photons experience electromagnetic interactions in the field of the air nuclei, and undergo pair production. The resulting ultra-relativistic

¹ The name MAGIC originated as an acronym for *Major Atmospheric Gamma-ray Imaging Cherenkov* telescope.

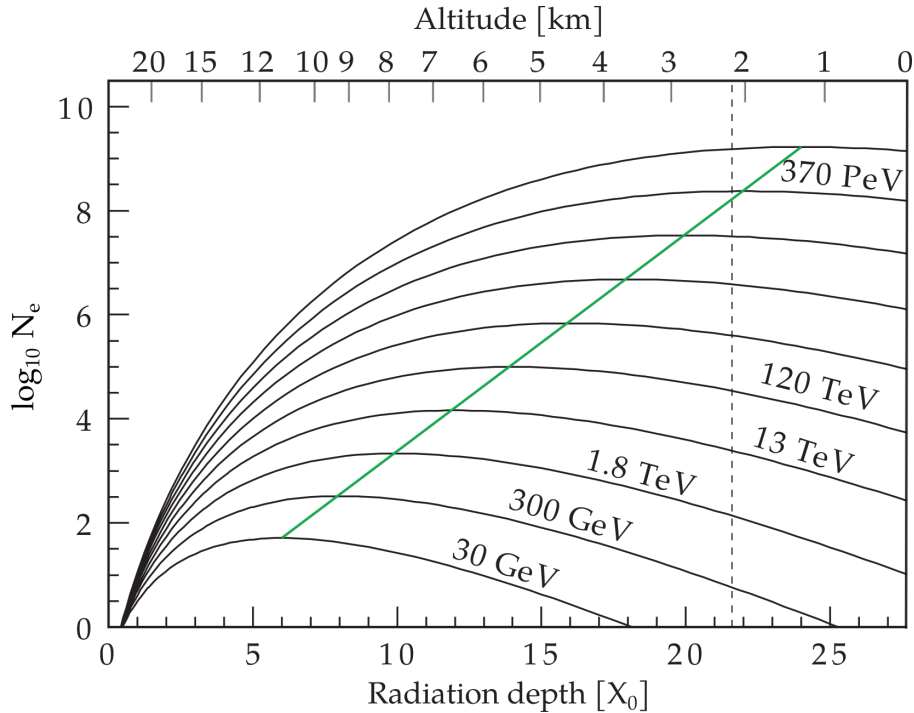


Figure 2.2: Electromagnetic shower longitudinal profiles. The number of electrons is plotted as a function of the number of traversed radiation lengths $X_0 \approx 366.2 \text{ kg/m}^2$, for different primary gamma ray energies. The top axis indicates the corresponding elevation if the gamma ray is vertical, and interacts at the average first interaction point (cfr. Figure 2.1). The green line identifies the shower maximum. Higher energy showers penetrate deeper in the atmosphere. The dashed line shows the altitude of MAGIC. Adapted from Wagner (2006).

sub-showers which appear separated from the main shower body. Charged pions decay producing muons, which travel mostly unaffected to the ground, and represent a background source for rare event particle physics experiments. These differences are key elements for the identification of the primary particle type. Cosmic-ray observatories such as AUGER⁵ and Telescope Array⁶ detect such hadronic secondary particles over vast areas on the ground, as well as the fluorescence light of ionized air, and infer the properties of the primary cosmic ray.

Figure 2.1 presents the average atmospheric profile (altitude versus air column density) at the Roque de los Muchachos observatory. In the whole range of gamma-ray energies observable with Cherenkov telescopes ($E \geq 10 \text{ GeV}$) the cross section of the electron-positron pair production is already at its saturation value. As a result, the radiation length $X_0 = 366.2 \text{ kg/m}^2$ (roughly 300 m at 1 bar and 20 °C) does not depend on the energy of the incoming particle, and the average altitude of the first interaction point $z_0 \approx 20 \text{ km}$ is also independent of it. Fluctuations of individual showers may randomly give rise to a first interaction point at lower or higher altitude. On the contrary, the following shower development is heavily determined by the primary particle energy

⁵ AUGER: <https://www.auger.org/>

⁶ Telescope Array: <http://www.telescopearray.org/>

E_0 (cfr. Figure 2.2). The total number of charged particles N_e reaches a maximum at $X_{\max} \simeq \ln(E_0/E_c) - 1/2$, which is roughly at an altitude of ~ 10 km for TeV electromagnetic showers. Such maximum number of electrons $N_{e,\max}$ is roughly proportional to E_0 . They are emitted with a characteristic opening angle $\theta_{e^\pm} = m_e c^2/E = 1/\gamma$. As the electrons are highly relativistic during the whole shower development, θ_{e^\pm} is small, and electromagnetic showers tend to be tapered. I address the reader to the original article of Rossi and Greisen (1941) for the accurate derivation of such properties. In particular, the fact that $N_{e,\max} \propto E_0$ allows a detector capable of measuring $N_{e,\max}$ to reconstruct the primary gamma-ray energy. This is a key concept of the imaging atmospheric Cherenkov telescope technique. Electromagnetic showers initiated by electrons are extremely similar to gamma-ray ones. They constitute an irreducible source of background for gamma-ray astronomy with Cherenkov telescopes, but their contribution is minor with respect to the one of hadrons (cfr. Section 4.7.2).

2.2 IACT Technique

Cherenkov radiation was discovered in 1934 by P. Cherenkov and S. Vavilov (Cherenkov, 1934) and explained few years later by I. Frank and I. Tamm (Frank and Tamm, 1937). It is caused by the coherent depolarization of the instantaneous dipoles induced by the motion of a superluminal charged particle in a material of refractive index n . Cherenkov radiation can only be produced if $c/n < v$, where v is the particle velocity. The causality requirement $v < c$ is preserved in any case. In air, at $T = 20^\circ\text{C}$ and $P = 1$ atm, the refractive index of air is $n \simeq 1.00028$. The energy threshold for Cherenkov emission is $E_{\text{thr}}^e \simeq 21$ MeV for an electron, and $E_{\text{thr}}^\mu \simeq 4.5$ GeV for a muon. Such values grow rapidly with the altitude, as the refraction index diminishes, reaching 36 MeV and 7.5 GeV at a height of 10 km, respectively. The wave-front of Cherenkov emission is conical, with the axis parallel to the charged particle direction, and an opening angle θ_c given by:

$$\cos \theta_c = \frac{1}{n\beta}. \quad (2.1)$$

In the regime of interest for extended air showers, the properties of Cherenkov radiation only weakly depend on the energy of the emitting particle. The differential number of emitted Cherenkov photons is given by:

$$\frac{d^2N}{dE_\gamma dx} = \frac{\mu\pi e^2}{h^2} \left(1 - \frac{1}{n^2\beta^2}\right) = \frac{\mu\pi e^2}{h^2} \sin^2 \theta_c, \quad (2.2)$$

where E_γ is the energy of the Cherenkov photon, μ is the magnetic permeability of the medium, and x is the length along the track of the particle. Both μ and n depend on the frequency of the Cherenkov radiation ν , but in the air the former one can be reasonably approximated with μ_0 . Cherenkov radiation is *non calorimetric*, that is, the number of Cherenkov photons produced by a particle is not proportional to its energy. The emitted radiation is subject to scattering and re-absorption in the same medium which produced it. In the atmosphere, ultraviolet wavelengths below 300 nm are strongly affected by the Rayleigh scattering. Even shorter wavelengths are absorbed by the oxygen-ozone chemical cycles and air ionization. The resulting Cherenkov light spectrum peaks at around

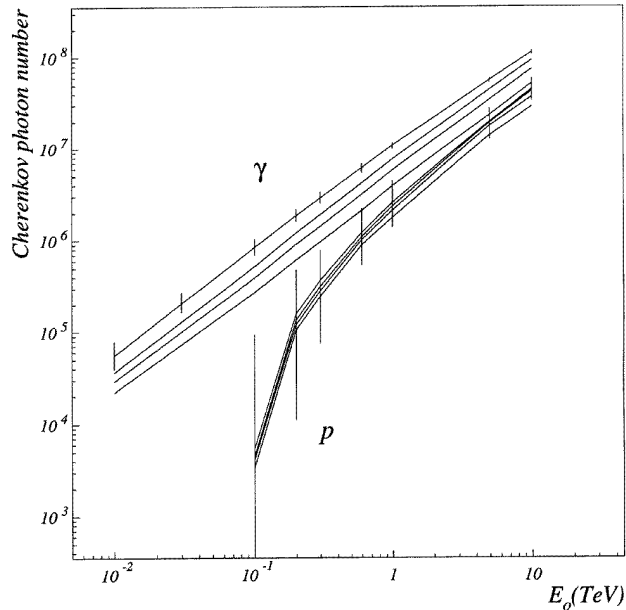


Figure 2.3: Number of Cherenkov photons for vertically incident gamma rays and protons, integrated in a radius of $R = 150$ m (entire light pool) from the shower axis. Four curves are shown for each particle species, corresponding (from top to bottom) to elevations of 4.6 km, 2.3 km, 1.3 km and the sea level. Vertical lines represent the confidence interval. The atmosphere approximately acts as a linear calorimeter for gamma rays, being the slope of their curves close to one. This is not the case for protons.

From Portocarrero and Arqueros (1998).

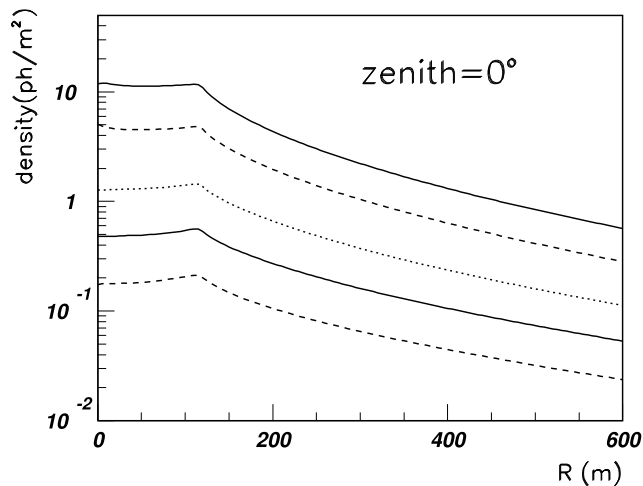


Figure 2.4: Radial Cherenkov photon density, for a vertically incident shower, at the MAGIC altitude of 2200 m above sea level. The profiles correspond (from top to bottom) to a gamma-ray energy of 100 GeV, 50 GeV, 20 GeV, 10 GeV and 5 GeV. The density is practically constant within a radius of 120 m from the shower axis (Cherenkov light pool), and falls off outside of it.

From Sobczyńska (2003).

330 nm for vertical showers, and sharply falls off for larger energies.

In an electromagnetic shower, where the critical energy is $E_c \simeq 85$ MeV, all electron-positron pairs emit Cherenkov radiation. The amount of Cherenkov photons produced is therefore proportional to the number of electrons $N_{e,\max}$ themselves, which in turn is roughly proportional to the primary particle energy (cfr. Section 2.1). Therefore, despite the non-calorimetric nature of Cherenkov radiation, the total Cherenkov light intensity from an electromagnetic atmospheric shower constitutes a measurement of the energy of the primary gamma ray (see Figure 2.3). In the plane perpendicular to the shower axis, the conical wave-fronts of each electron overlap and form a circular *light pool* with almost constant photon density (see Figure 2.4). The radius R_c of the light pool depends on the elevation of the observatory. At the MAGIC site, at 2200 m above the mean sea level, this is $R_c \simeq 120$ m for a vertical shower. The Cherenkov photons arrive at ground

as an impulse with a characteristic time spread of 3 ns. A telescope within the light pool, aimed at the source of the gamma ray, can collect the Cherenkov photons, estimate their density, and measure the energy of the primary gamma ray. In the focal plane of such telescope, the Cherenkov light forms an image of the extended air shower, pointing back to the origin of the primary particle. This is the operating principle of *Imaging Atmospheric Cherenkov Telescopes* (IACTs). The IACT technique has been pioneered by the 10 m Whipple telescope, which detected for the first time teraelectronvolt gamma-ray emission of the Crab nebula in 1989 (Weekes et al., 1989). The HEGRA system, located on the Roque de los Muchachos, extended the technique by introducing a system of multiple telescopes, instead of a single one. A stereoscopic configuration provides a net improvement in the reconstruction of the properties of the gamma ray, and of its incoming direction in particular. Present day IACT experiments include H.E.S.S.⁷, MAGIC⁸ (used for this thesis work, cfr. Section 2.3) and VERITAS⁹. The next generation Cherenkov Telescope Array CTA¹⁰ will be an observatory composed by several different-sized telescopes, with locations both in the northern hemisphere and southern hemisphere. The prototype 23 m large sized telescope (LST-1) is already in operation at the Roque de los Muchachos observatory, next to the two MAGIC Telescopes.

The large telescope surfaces of all these systems are required by the intrinsic faintness of Cherenkov light. As an example, a primary gamma ray of 100 GeV results in an average light pool photon density of 10 ph./m². The gamma-ray energy range covered by IACTs is determined by their capability to collect such dim Cherenkov light. The collection area of a Cherenkov telescope is determined by the area that it can survey, and not by the telescope surface. It is roughly of the same order of magnitude of the surface of the light pool, and has a typical value of $A_{\text{col}} \simeq 10^5 \text{ m}^2$. At the lowest end of the energy range, this figure is reduced by the low Cherenkov photon density. The typical energy threshold of major IACT systems is around $E_{\text{thr}} \simeq 100 \text{ GeV}$. The MAGIC Telescopes adopted a novel type of low-energy trigger system, the Sum-Trigger-II, to reduce such value to $E_{\text{thr}} < 30 \text{ GeV}$. This has proven to be essential for the investigation of low-energy sources, such as the pulsar studies presented in this thesis. The Sum-Trigger-II system is discussed in Section 2.5. The higher end of the energy range is limited by the low flux of gamma rays. Using very large zenith angle observations to increase the surveyed A_{col} , the present limit is at around 100 TeV (Acciari et al., 2020).

Current IACT systems have a best sensitivity spot between several hundreds of GeV and 1 TeV. The MAGIC telescopes with their standard trigger achieve this spot at $\sim 1 \text{ TeV}$. Figure 2.5 presents the differential sensitivity of the MAGIC Telescopes, computed when these are equipped with the standard trigger, and their data is processed with standard analysis procedures. A narrow spectral line at 1 TeV, with a luminosity of few percent of the Crab nebula, could be firmly detected at the level of 5 sigma in 50 h of observation time. Real spectra span several orders of magnitude in energy, and their signal is integrated over a much larger region. For a spectral shape similar to the one of the Crab nebula,

⁷ H.E.S.S.: <https://www.mpi-hd.mpg.de/hfm/HESS>, four 12 m and one 28 m telescopes in Namibia.

⁸ MAGIC: <https://magic.mpp.mpg.de>, two 17 m telescopes at the Canary Islands.

⁹ VERITAS: <https://veritas.sao.arizona.edu/>, four 12 m telescopes in Arizona.

¹⁰ CTA: <https://www.cta-observatory.org/>

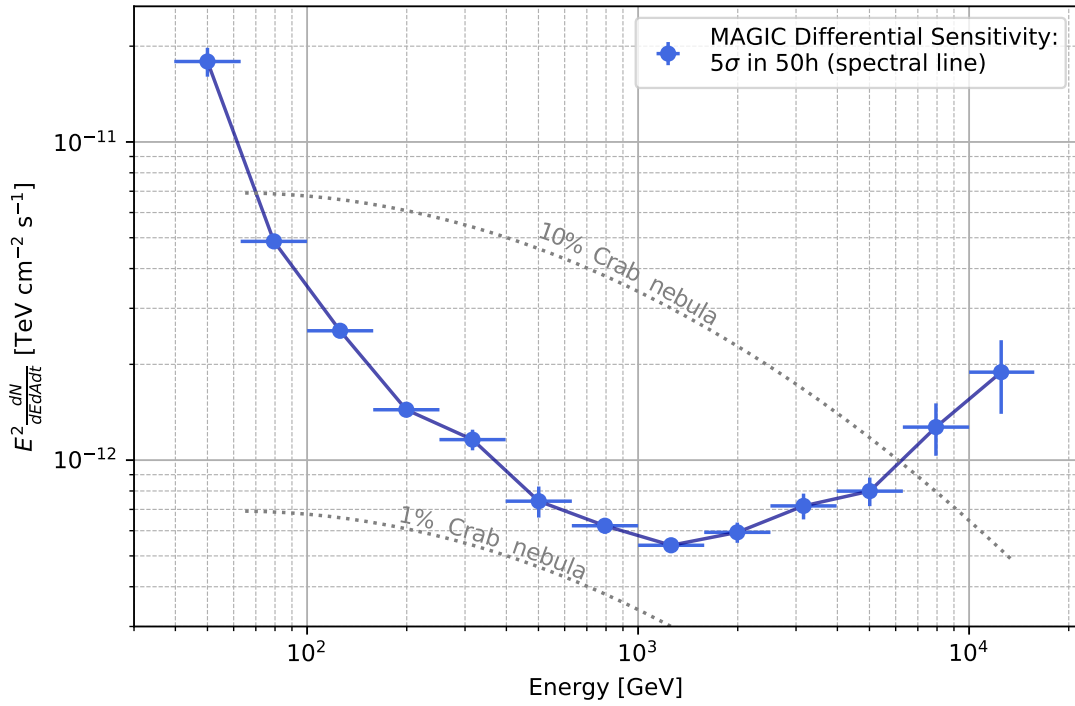


Figure 2.5: MAGIC differential sensitivity plot, with the standard trigger. The blue points and curve show how the flux threshold for a 5σ detection in 50 h of observation time changes with the energy, for a source whose spectrum is a sharp line at said energy (Dirac delta spectrum). The flux is presented as a logarithmic spectral energy distribution, and spectra corresponding to 10% and 1% of the Crab nebula are reported for comparison. The curve can be multiplied by the spectrum of a source of interest, and integrated in a certain energy range, to obtain the integral sensitivity for that particular source in said range. The sensitivity at energies below 100 GeV is improved and extended by the usage of the Sum-Trigger-II. See also: <https://magic.mpp.mpg.de/newcomers/technical-implementation/> and (Aleksić et al., 2016a).

the integral sensitivity of MAGIC is best at around 200 GeV. In 50 h of observation time, a source as weak as 0.7% of the Crab nebula can be detected with 5σ significance at energies larger than 200 GeV. The Sum-Trigger-II, presented in Section 2.5, as well as the dedicated analysis techniques discussed in Chapter 4, allow to substantially improve the sensitivity of MAGIC for low-energy events at energies below 100 GeV.



Figure 2.6: Picture of the MAGIC Telescopes at the beginning of the evening operations. MAGIC-II is in the foreground and MAGIC-I is in the background. The roof of the counting house and the small dome of the MAGIC LIDAR are visible in the lower left corner. (G. Ceribella / MPI)

2.3 MAGIC Hardware

The two MAGIC telescopes are imaging atmospheric Cherenkov telescopes (IACTs) at the observatorio del Roque de los Muchachos on the Canary island of La Palma. The observatory is located at the top of an extinct volcano, with the MAGIC telescopes at an altitude of 2200 m above sea level. The site is ranked among the best locations for optical astronomy, due to the favorable weather conditions and the low artificial light pollution. The joint operation of two telescopes allows to assess the stereoscopic geometry of extensive air showers, improving the direction reconstruction of the incoming particle. The telescopes have a diameter of 17 m and a reflecting surface of 236 m². They are separated by a distance of 83 m along the SW-NE axis. The construction of the MAGIC-I telescope was completed in 2004. It was operated in standalone mode (monoscopic observations) until 2009, when the MAGIC-II telescope was completed.

2.3.1 Mechanics

The structure of the MAGIC telescopes has been designed to be resistant and lightweight, so that the telescopes can be quickly re-pointed in case of sudden transient alerts. It consists of a mirror support structure (optical dish) hinged on an a rotating base fork. An arc holds the camera in the focal plane of the reflector. The design allows the telescope for two angular degrees of freedom, a whole rotation of the fork around the main vertical

axis, and a second rotation of the optical dish on the horizontal axis on the hinges. To this respect, the structure is not different from a standard alt-azimuthal astronomical mount.

At the bottom, a reinforced ring concrete basement bears a circular rail on its surface. The base fork matches the rails on a train of six bogies, allowing for the azimuthal rotation of the telescope. The base fork is composed of bulky rod-and-knot parts of steel. The building concept is reminiscent of some mechanical toys, and allows to build a resistant structure without welded parts. The arms of the fork end in two pins that hinge the optical dish. The latter is also built out of a frame of rod-and-knot parts, but these are made of lighter carbon fiber tubes rigidly joined by aluminum knots. A single aluminum arc raises from the rim of the dish and holds the camera in the focal plane of the reflector. The optical dish incorporates access platforms and safety lines for the maintenance of the mirrors, and weights approximately 20 Mg. It has a maximum bending of 10 cm when pointing close to the horizon. This is accounted by the pointing software, using bending models which are frequently updated. The total weight of the moving parts (including the fork understructure) is 64 Mg. Both the azimuth and elevation motions are geared by rack and pinion sets, with chains on the back of the optical dish and around the ring foundation. Two electric motors power the azimuthal motion, and a single one does so for the elevation movement. They can develop a maximum power of 11 kW. They are only used at such full power during the fast repositioning procedures for transient alerts (gamma-ray bursts). In these occasions, the telescopes can reach an angular velocity of 7 deg/s, corresponding to a bogie speed of 1 m/s. The rails are inspected for possible obstacles every evening before the beginning of the operations. Automatic safety mechanisms halt the motion and disarm the motors if any entrance gate is opened. The drive system of the MAGIC telescopes is reviewed in Bretz et al. (2009).

2.3.2 Optics

The reflecting surfaces of the MAGIC telescopes are built up of a tessellation of quartz front-coated aluminum mirrors. Each mirror has a spherical surface of 1 m², and the total reflecting surface measures 236 m². The curvature radius of the mirrors varies with the distance from the optical axis, so that the surface globally approximates a paraboloid. A parabolic shape ensures the isochrony of the reflected light. This is necessary to exploit the information carried by the timing structure of the short Cherenkov light pulses. In the MAGIC-I telescopes, an alternation of the mirror structure, known as *chess-boarding*, introduces an extra time jitter of 0.6 ns. The chess-boarding is necessary to allow the orientation of individual mirrors to be adjusted. In MAGIC-II, the design was improved and no chess-boarding is required. The reflectors are focused to a distance of 10 km, the typical one of the extensive air shower maxima for the energies at which MAGIC operates. The orientation of each mirror is adjusted several times during the observations by software-controlled actuators (Biland et al., 2008). This is required to keep the shape of the reflecting surface as close as possible to an ideal paraboloid. Adjustments happen automatically at the beginning of every observation run (~20 min). The optical performance of the telescopes is evaluated at the beginning of the night by pointing bright stars at different elevations. The starlight is focused on a movable lid with a white screen, in front of the camera surface. A dedicated CCD camera, positioned at the center of the



Figure 2.7: Close-up of some MAGIC-I mirrors at the edge of the reflector. Most of them are of an older kind, and consist of four 0.25 m^2 sub-units. Two new generation mirrors are visible at the bottom and at the top right corner. They have no subunits. (G. Ceribella / MPI)

reflector, captures a photo of the screen and the star image. Such images are used to determine the optical point spread function of the telescopes. In typical situations, this has a spread $\sigma_{\text{PSF}} \lesssim 10\text{ mm}$, corresponding to an angular size of 2 arcmin. Such optical point spread function shall not be confused with the one for the gamma-rays, which depends on the whole data analysis chain and on the energy of the incoming particle.

The mirrors are exposed to the outside weather and are subject to aging. The delicate front coating of fused quartz, selected for its excellent transmittance in the blue and near ultraviolet band, is easily damaged by any mechanical contact. As a result, the mirrors can not be cleaned. This particularly affects summer observations, during which strong winds cast large amounts of dust from the nearby Sahara desert. During those months, the reflectivity of the mirrors can be sensibly reduced. It is typically recovered after the first rain storms in early autumn. A novel mirror design is at study to overcome such issues (Will et al., 2019). Damaged mirrors are periodically replaced with newer ones. Some old mirrors in the MAGIC-I telescope are composed of four $50 \times 50\text{ cm}^2$ sub-units. They are visible in Figure 2.7.

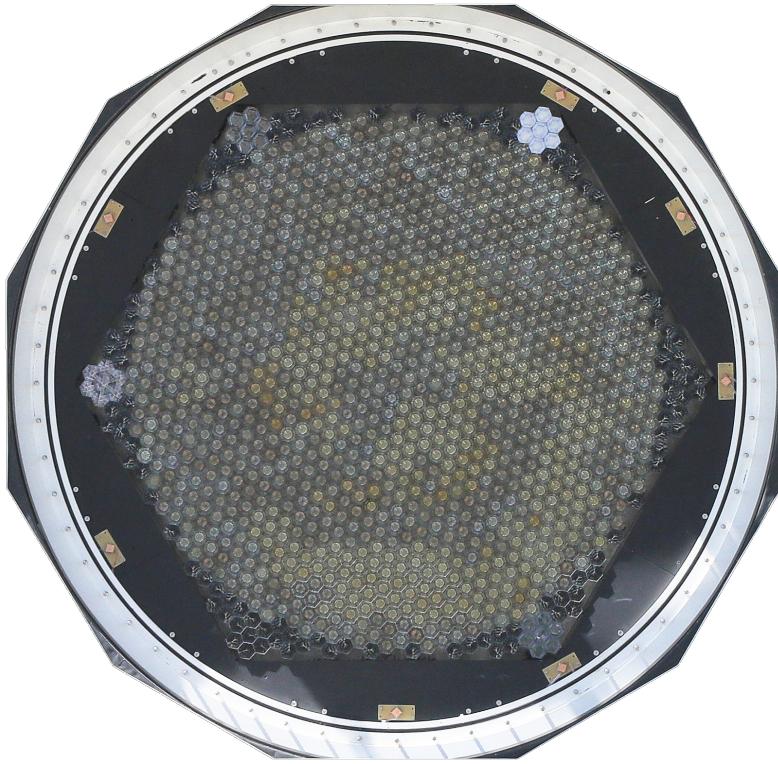


Figure 2.8: Close-up view of the MAGIC-I camera, without the sealed protective window. The Winston cones at the top of each photo-multiplier tube are visible. These are arranged in an hexagonal grid of 1039 pixels. Four experimental silicon photo-multiplier clusters are placed at the corners of the main sensor. The representation of a sample Cherenkov event detected by such camera is presented in Figure 4.3. *Courtesy of A. Hahn (A. Hahn / MPI).*

2.3.3 Camera

The camera of the MAGIC telescopes consists of 1039 photo-multiplier tubes, arranged in an hexagonal lattice, and covering a circle with a diameter of 1 m (see Figure 2.8). This gives a field of view of approximately 3.5 deg. Photo-multipliers has a spherical photocathode with a diameter of 2.54 cm. Hexagonal Winston cones on top of them allow to fill the gaps and increase the light collection. Each such sensor constitutes a pixel of the camera. A single pixel has a scale of 0.1 deg, and covers an area of 30 arcmin². The photo-multipliers employed in MAGIC have six dynodes, operate at a gain of $\sim 3 \cdot 10^4$, and have a peak quantum efficiency of 32% at $\lambda = 340$ nm (Borla Tridon et al., 2009; Nakajima et al., 2013). The gain of the whole camera is flat-fielded by adjusting the high voltage of each sensor. Hexagonal pixels are grouped together in modules of seven units, and the camera is composed by several such clusters. This modular design allows for fast maintenance operations, and can be easily extended to incorporate experimental modules using different kinds of photo-detectors (Hahn et al., 2018). A picture of the MAGIC-I camera is presented in Figure 2.9. The output of each photo-multiplier is pre-amplified immediately following the sensor. The pre-amplifier stage produces two outputs: a low-bandwidth (7 Hz) one, used to monitor the current output of each sensor, and a high-bandwidth (300 MHz) signal, which is propagated to the readout. Such amplified signal is fed to a vertical cavity surface emitting laser (VCSEL) that converts it into a light signal. These analog light signals travel via optical fibers to the MAGIC counting house, where the whole digitization and readout process happen. The optical fibers, bundled in ultraviolet resistant covers, follow the camera arc to the telescope structure and reach the ground at the central pin. The total length of each optical

fiber cable is ~ 160 m. Individual differences among them are accounted for with a calibration procedure (cfr. Section 4.1.2). The central pixels of both MAGIC cameras have been modified to enable short-timescale optical observations. This was achieved by modifying their pre-amplifier stage and rising the bandwidth of their control signals to 3 kHz. This effectively enables the MAGIC telescopes to be used as fast photometric devices for sub-second optical phenomena. The central pixels can be used to measure the optical pulsation of the Crab pulsar ($m_V \simeq 15$), reaching a 5σ detection in roughly 5 s. These optical observations of the Crab are used to test the absolute time calibration of the telescopes. The central pixels of MAGIC can be employed for a variety of optical observations, such as stellar occultations by asteroids. On the other hand, the standard high-bandwidth MAGIC signals, used together with a custom readout, can be used to perform intensity-interferometry observations (Acciari et al., 2020). Related to the MAGIC camera hardware is the *calibration box* installed at the center of the reflector, in the optical shadow of the camera itself. The calibration box produces well-characterized light pulses that uniformly illuminate the camera. These are used to calibrate the output of each photo-multiplier tube to the physical units of equivalent photo-electrons (cfr. Section 4.1.2). The light pulses are generated with a frequency-tripled solid-state laser ($\lambda = 355$ nm), and have an average full-width at half maximum of 1 ns, similar to the one of Cherenkov pulses (Aleksić et al., 2016b).

2.4 Readout

The readout system of the MAGIC telescopes is located in a small building next to them, the MAGIC counting house. This serves also as a base for the telescope operations and as a control center. There, the optical fibers from all photo-multiplier tubes of the cameras reach the electronic racks. The laser impulses are converted back to electric signals by dedicated receiver boards (Tescaro, 2012). Based on the pixel being considered, such signals are split in at most three copies. These are propagated to the sampler, to the standard digital trigger, and to the Sum-Trigger-II, respectively.

2.4.1 Sampling and Digitization

A copy of the signal of every pixel is fed to the sampling electronics. These employ general purpose PULSAR boards, developed at CERN, with ad-hoc readout mezzanines based on the domino ring sampler (DRS4) chips¹¹ (Bitossi et al., 2016). These devices can store up to 1024 samples and recover a portion of the signal upon request, with a region-of-interest based selection. They are currently operated at a sampling frequency of 1.64 GHz, corresponding to a depth of $t \simeq 625$ ns. Such frequency was chosen to allow to compensate the delay between the signals of the two telescopes, even in stereoscopic observations at high zenith angles. Whenever a trigger occurs, 50 samples (~ 30.5 ns) are read from all pixels in the cameras. These are digitized and transferred to the data acquisition system, that adds additional information (e.g. event time, trigger type, etc), and stores them in a binary format on a redundant RAID 5 archive space. These files constitute the RAW MAGIC data. The data acquisition can be configured to save only specific types of events (e.g. single-telescope trigger, stereo trigger, calibration, pedestal)

¹¹ <https://www.psi.ch/en/drs>

via an ad-hoc prescaler logic. Each event registered by the MAGIC telescopes is given a time tag that identifies the local UTC time at its occurrence. The MAGIC readout electronics includes a GPS-disciplined rubidium atomic clock for this purpose. The time tag has a resolution of 200 ns. This shall not be confused with the resolution of the relative timing among the signals of different pixels in the same event, which is three orders of magnitude smaller. The absolute time tag allows to refer the data to the approximately inertial reference frame of the barycenter of the Solar System (cfr. Section 4.6). When observing a pulsar for which a rotation model is available, this enables to attribute a pulsar phase to each detected gamma ray. This greatly enhances the capability to detect pulsar signals and to disentangle them from the cosmic-ray background (cfr. Section 4.7.3). The timing signal of the rubidium oscillator is propagated to every MAGIC readout subsystem, ensuring their synchronization.

2.4.2 Trigger

The events are saved only when particular selection conditions are met, and a trigger occurs. A subset of the pixels in each camera, clustered around the center, constitutes the trigger area (see Figure 2.9). Their signals are copied by the receiver boards and propagated to the trigger. Two independent trigger systems exist: a digital trigger aimed at general purpose observations, commonly named the *standard trigger*, and a low-energy specific device, the analog *Sum-Trigger-II*. The pulsar data that I present in this thesis have been taken with the latter one, which is described in Section 2.5. Here I provide a short description of the architecture of the standard MAGIC trigger and refer the reader to Paoletti et al. (2007) for more details. The standard MAGIC trigger is based on the contemporaneous activation of compact nearest-neighbor groups of pixels. This is based on the characteristic shape of Cherenkov light signals. The trigger logic is divided in levels, with each successive level depending on the previous ones. The *level-zero* L0 trigger is produced at the receiver boards. It is a pixel-based digital signal, produced when the analog waveform of a pixel exceeds a threshold value. Such discriminator thresholds are continuously adjusted during the observations to match for the varying observing conditions (e.g. zenith-distance, background light). They are controlled by a dedicated software that interacts with the receiver boards, and set so that the individual pixel L0 rate is roughly 900 kHz. The L0 digital signals are transferred to the *level-one* L1 trigger logic, the single-telescope (monoscopic) trigger. The L1 logic checks for the presence of compact nearest-neighbor groups of L0-triggered pixels. The geometry is configured via software, and includes the 2NN (two neighboring pixel) groups, the 3NN (three pixels in a triangle), the 4NN (four pixels arranged like a kite), and the 5NN groups (trapezium-like shape). In regular MAGIC stereoscopic observations, only the 3NN groups are used to produce the L1 trigger, which results in a L1 trigger rate close to 20 kHz. In rare occasions, monoscopic observations happen, and the 4NN geometry is employed instead with larger discriminator thresholds. The L1 triggers of the two telescopes are used to produce the *level-three* L3 stereoscopic trigger. Whenever the two L1 signals coincide within a time window of 180 ns, a stereo trigger is issued. An ordered L3 number is generated and propagated to the data-acquisition systems, enabling the MAGIC-I and MAGIC-II data to be related. In typical standard observations, such L3 trigger produces a trigger rate of 300 Hz. The MAGIC L3 trigger can be configured to

use the Sum-Trigger-II mono signals, rather than the standard L1 ones.

2.5 Sum-Trigger-II

The Sum-Trigger-II is a novel stereoscopic analog trigger for the MAGIC telescopes, that has been introduced with the specific aim of improving the performance at energies below 100 GeV. This is precisely the energy range in which the emission of pulsars is more intense (cfr. Section 1.3). The prototype for the stereoscopic Sum-Trigger-II, the Sum-Trigger (Rissi et al., 2008), was essential for the first detection of the Crab pulsar at energies above 25 GeV (Aliu et al., 2008). The development and implementation of the stereoscopic system began after the installation of the second MAGIC telescope and the update of the whole readout system (Haefner, 2011; García et al., 2014; Dazzi et al., 2015). A deep technical review of the Sum-Trigger-II is available in the recently published publication “*The Stereoscopic Analog Trigger of the MAGIC Telescopes*” (Dazzi et al., 2021). I played a central role in it and I am one of its corresponding authors. The interested readers are referred to it for a more detailed discussion of the implementation of the Sum-Trigger-II. My technical contribution to the maintenance of the Sum-Trigger-II system and its results are briefly summarized in Chapter 3.

Low-energy showers produce fewer Cherenkov photons, and their images suffer of a low signal to noise ratio. This hinders the capability of the standard digital trigger to successfully distinguish them from the background fluctuations. The Sum-Trigger-II improves the signal to noise ratio by re-binning the shower image in larger hexagonal patches, the trigger *macro-cells* (see Figure 2.9). The analog signals of the pixels in a macro-cell are summed up together, obtaining a whole macro-cell signal with a larger signal to noise ratio. Summed signals exceeding a discriminator threshold generate a trigger, and a stereo trigger is issued when the two single telescope ones are in coincidence. The analog implementation of the Sum-Trigger-II system allows for the required fast reaction time and large bandwidth.

The Sum-Trigger-II operation principle is schematized in Figure 2.10. The analog photo-multiplier tube signals are branched in the readout boards, and propagated to the Sum-Trigger-II electronics. Only a subset of the whole camera serves as the active trigger area. The timing and gain differences between the pixels are accounted for by applying a pixel-dependent signal delay and attenuation. These settings are calibrated beforehand with a dedicated procedure (cfr. Section 3.1). In a following step, the signals are clipped to a maximum amplitude, and summed up together to form the macro-cell signals. The clipping is applied to reduce the impact of the photo-multiplier tube after-pulsing. Genuine Cherenkov signals, which are time-coincident, stack together in the summation, and produce a large macro-cell signal even if they are clipped. On the other hand, after-pulses happen after real events on a random base, and their timing does not coincide in different pixels. The clipped after-pulses do not pile-up in the summation, and their impact is suppressed. Each macro-cell signal is compared with an adjustable threshold. Whenever the latter is exceeded, a single-telescope trigger is produced and propagated to the readout and L3 trigger systems. The single-pixel signal delay and attenuation, as well as the discriminator threshold of each macro-cell, are controlled

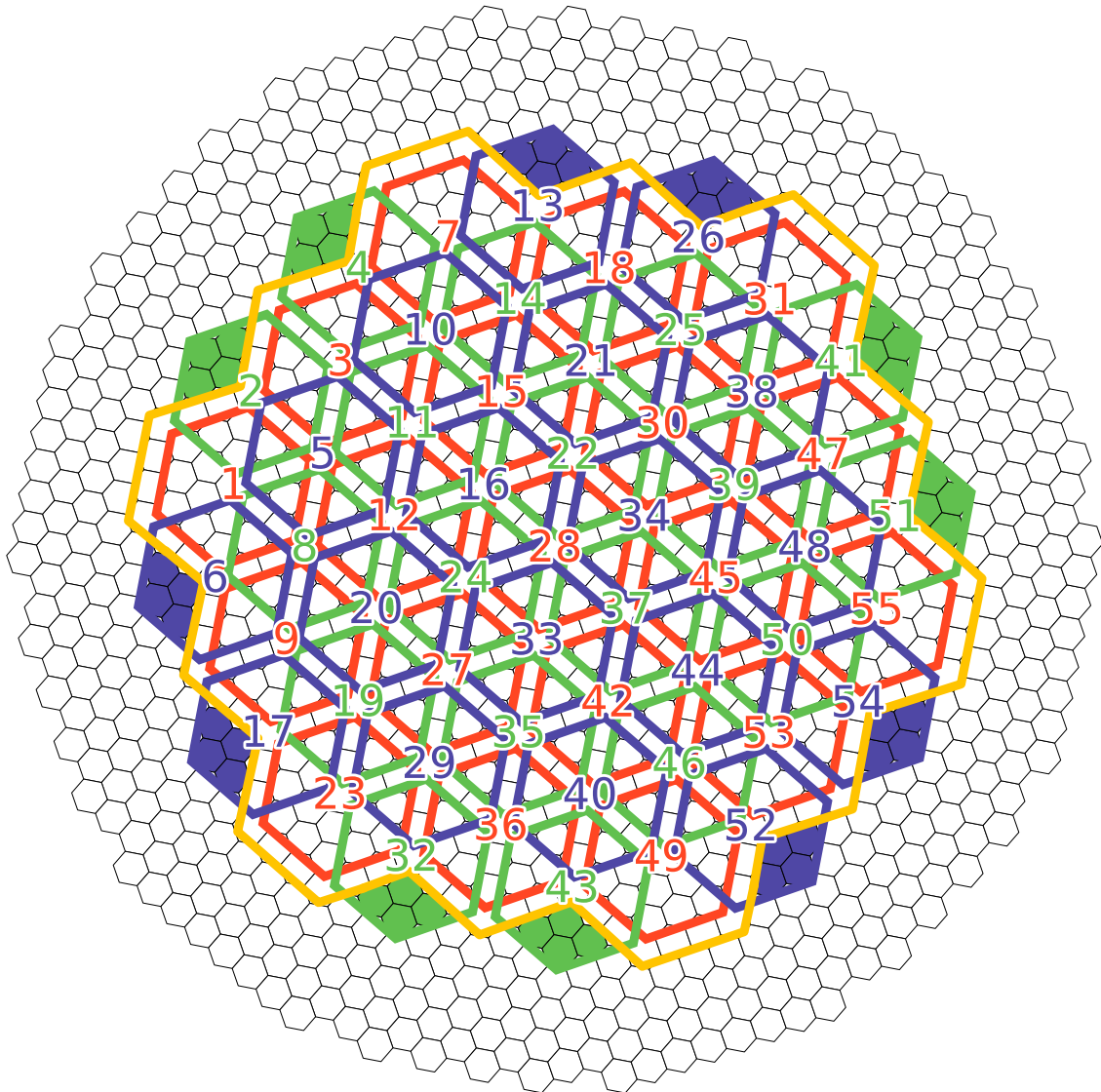


Figure 2.9: Layout of the 55 *macro-cells* of the Sum-Trigger-II. Each macro-cell is a hexagonal aggregate of 19 pixels identified by a unique number. The macro-cell dimension has been optimized for the size of a typical Cherenkov image. There are three different layers of overlapping macro-cells (colored in red, green, and blue). The overlap allows to uniformly cover the entire trigger area and achieve a uniform trigger response. The yellow line highlights the standard digital trigger area. Filled pixels do not have a trigger branch in the readout boards, and are can not part of the corresponding macro-cell. Appeared also in (Dazzi et al., 2021).

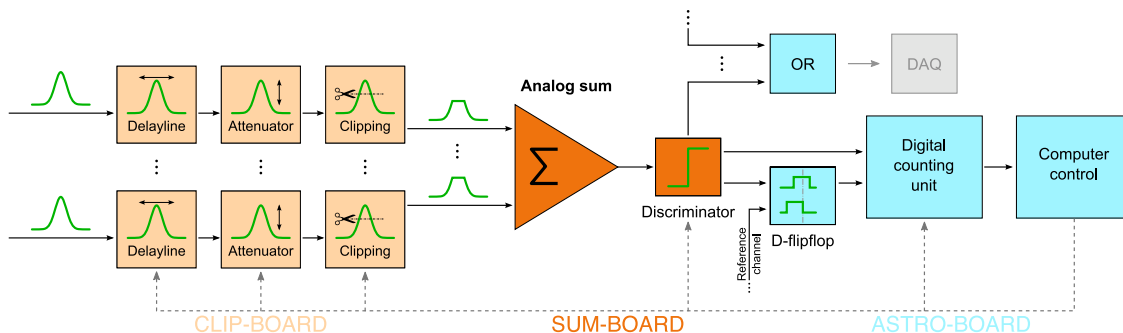


Figure 2.10: Scheme of the operating principle of the Sum-Trigger-II, from (García et al., 2014). Light-orange stages are performed on analog signals in the clip-boards. The clipped signals are transferred over the passive back-plane to the sum-boards (darker orange), where the sum and discrimination happens. The digital macrocell trigger signals are transferred back to the astro-board (light blue). This propagates them to the stereo trigger system, and controls all other stages (dashed lines).

by a dedicated control software. The macro-cell thresholds are continuously adjusted against the varying observation condition, to obtain a stable single telescope trigger rate of 30 kHz. In regular observations at low zenith distances and without moonlight this typically corresponds to a stereo trigger rate between to 500 Hz and 600 Hz.

2.5.1 Hardware

The electronics of the Sum-Trigger-II is composed by a series of printed circuit boards, connected via a large passive back-plane. The boards operate on the single pixel analog signals in cascade and execute the various stages of the trigger logic. Such electronic is housed in two dedicated racks, and equipped with an efficient cooling system. Each of the two Sum-Trigger-II units has an average power consumption of 1.8 kW. Because of this, they are switched on only if low-energy observations are scheduled, and kept off during other observations to limit the power consumption.

The clipping boards, or *clip-boards*, are the first stage of the electronics, and receive the analog signals directly from the main readout boards. A single clip-board operates simultaneously on 32 pixels, and each Sum-Trigger-II unit hosts 18 clip-boards. The signals are delayed, attenuated and clipped with dedicated modules controlled by a field-programmable gate array (FPGA). The programmable analog delay lines utilize a series of varactor diodes. This keeps the electronics simple and cost-effective, but introduces a delay-dependent attenuation of the signals. The latter complicates the calibration procedure of the pixel delay and attenuation, and requires an iterative method (cfr. Section 3.1). The signal clipping threshold was optimized against the stereoscopic trigger rate of cosmic-rays. Its value corresponds to the average amplitude of a single pixel integrated signal with 8 equivalent photo-electrons (cfr. Section 4.1.2).

The clipped single-pixel signals are transferred over the large passive back-plane to the *sum-boards*. These produce the stacked macro-cell signals by summing the single-pixel ones with the required geometry. Three layers of macro-cells with large overlap are

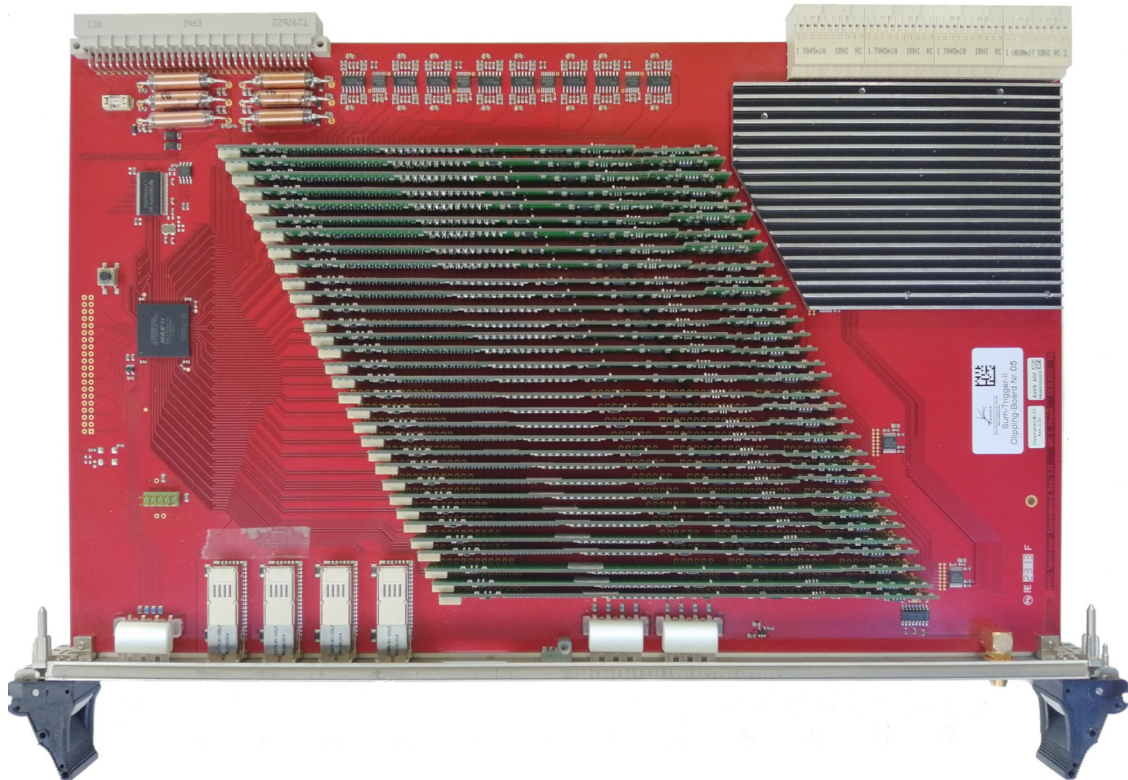


Figure 2.11: Clip-board №5 of the MAGIC-I Sum-Trigger-II unit. The board receives 32 single-pixel input signals from four multi-channel differential cables (lower left), and processes them with the delay modules visible in the center. The output signals are transferred to the sum-boards over the back-plane connection (upper right). A FPGA (left) controls the delay, attenuation and clipping settings. (G. Ceribella /MPI)

implemented, with some pixels belonging to three different macro-cells (see Figure 2.9). The overlapping layer design allows a uniform trigger response, and ensures that the efficiency is not reduced for showers falling at the border of two neighboring macro-cells. The summed signals are compared with a programmable, macro-cell-dependent, discriminator threshold. A digital signal (macro-cell trigger) is produced when the summed signals exceed the threshold. Such macro-cell thresholds depend on the observing conditions, and are continuously adjusted during the observations. The average macro-cell threshold is set to a value roughly corresponding to 20 equivalent photo-electrons.

The macro-cell trigger signals are fed back to a general control board, named *astro-board*. The the astro-board generates a single telescope Sum-Trigger-II signal from the global logical OR of all the single macro-cell ones. The astro-board communicates and controls all other boards. It hosts a small embedded system (ACME Systems Fox G20) which connects via serial peripheral interface (SPI) bus to an FPGA controller, and interfaces with the FPGAs of the other boards. The computer runs a modified version of Debian GNU/Linux for the ARM version 9 architecture. The output single-telescopes trigger signals are propagated to the standard trigger L3 logic, where the stereo coincidence is

computed. An alternative stereo trigger system, the so-called *internal L3*, is produced by the astro-boards themselves. It is used as a cross-check and a backup solution for the standard stereo trigger.

2.5.2 Software

A copy of the Sum-Trigger-II control software, CRISTAL, runs on the embedded computers of both astro-boards. The software initializes the Sum-Trigger-II, loads and controls the pixel-dependent delay and attenuation settings, and manages the macro-cell thresholds via a feedback loop. It also generates reports of the Sum-Trigger-II status (threshold settings, internal L3 value,...) and sends them to the central MAGIC control software. The software allows the user to manually interact with the Sum-Trigger-II and control it via a command-line interface. CRISTAL was developed in C by J. R. García, and is currently being maintained by myself for the MAGIC Collaboration.

2.6 Observation Strategy

The MAGIC Telescopes normally carry out observations in the so-called *wobble mode*. This is a technique that allows to measure the flux of a source of interest, and estimate the background contribution from cosmic rays, without the need of dedicated background observations (Fomin et al., 1994). The method consists in pointing the telescope at a small offset w from the source of interest, the *wobble depth*. The MAGIC standard wobble depth is $w = 0.4$ deg, or roughly 10% of the field of view. Observations are performed with such an offset for a fixed amount of time, an *observation run*, typically lasting 20 min. After such time, the wobble position is reversed, pointing with the same depth w to the mirror position with respect to the source. In this way, the source is always at a distance w from the center of the camera. The portion of the camera not occupied by it can be used to estimate the background contribution, using a variety of different methods (cfr. Section 4.7.2). Multiple pointing positions (always arranged in mirroring couples) can be employed. This drastically reduces the amount of observation time required to measure the flux of a source. The performance of MAGIC, as that of other IACT arrays, depends on the wobble depth w used for the observations, and obviously decays as w approaches the size field of view. This limits the capability of Cherenkov telescopes to study sources whose extension is comparable or larger than their field of view. However, the MAGIC performance reduction due to the use of the standard $w = 0.4$ wobble depth is negligible (Aleksić et al., 2016a). During the observations, the MAGIC weather station is used to monitor the weather conditions. Thin clouds in the upper atmosphere, and dust in the lower layers, affect the observations. A key monitoring system is the MAGIC atmospheric LIDAR, housed in a small dome in the counting house. The LIDAR probes the atmosphere at different altitudes, and provides a measurement of the transmittance as a percentage of the optimal-weather case. The standard MAGIC observations are suspended if the integrated transmission below a distance of 9 km from the telescopes (an altitude of $h \sim 11$ km) drops below $T_{<9\text{km}} = 65\%$. For the low-energy pulsar observations discussed in this thesis, a stricter cut at $T_{<9\text{km}} = 90\%$ was required. This is justified by the heavily detrimental effect that the presence of clouds have on the faint Cherenkov flashes of low-energy showers.

3

TECHNICAL RESULTS

This chapter includes information on the technical work that I carried out as part of my doctoral program. Being the Sum-Trigger-II a novel system, it frequently requires hardware interventions for regular maintenance. In particular, it is necessary to calibrate the attenuation and delay of each single pixel in the trigger area several times. This is required to achieve a uniform trigger response. The status of such calibration was monitored over a long period of time, to test its stability. In two occasions, in September 2018 and May 2019, a recalibration was required. Section 3.1 presents the Sum-Trigger-II calibration procedure. This was initially developed by J.R. García and later improved by myself. In Section 3.2 the results of the long-term monitoring of such calibration are presented. In absence of hardware changes (e.g. replacement of components), the Sum-Trigger-II calibration proved to be stable over long period of times. This allows continuous operations with the Sum-Trigger-II and long term monitoring programs, without the need of a constant tuning of the system. Finally, Section 3.3 briefly summarizes the activities of a technical shift at the Observatorio del Roque de los Muchachos, which took place in April and May 2019. I promoted and led the organization of such shift, which aimed at investigating some recurrent issues with the Sum-Trigger-II software and hardware. The shift team was composed by members of the MAGIC group at the Max-Planck-Institute for Physics: Dr. G. D'Amico, A. Detlaff, Dr. T. Schweizer (principal investigator of the Sum-Trigger-II project), Dr. D. Strom, and myself. The outcome of the shift was very successful.

Several parts of my technical work were reported in the peer-reviewed publication "*The Stereoscopic Analog Trigger of the MAGIC Telescopes*" (Dazzi et al., 2021), which I am a corresponding author of.

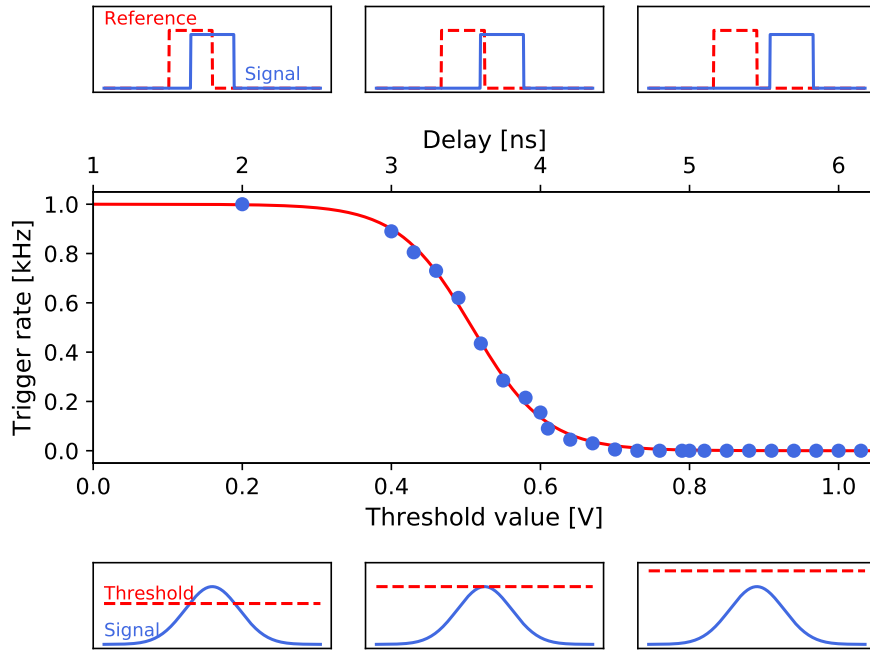


Figure 3.1: A sample rate scan for the attenuation values and the delays. In this figure, values on the x-axis can be interpreted either as voltage threshold values (bottom axis) or as delay values (top axis). Smaller panels show the relation between signals and the threshold value (for an attenuation scan) or the reference signal (for a delay scan) at various locations of the curve.

3.1 Calibration procedure

In the Sum-Trigger-II, the analog signals of the photo-multiplier tubes are stacked in larger areas (macrocells) to improve the signal to noise ratio. In order to achieve a homogeneous performance in the whole trigger area, the response of each pixel must be flat-fielded. In this way, pixels equally lit by Cherenkov light flashes produce pulses with the same average amplitude, and in the sum each pixel contributes with equal weight. The clipped photo-multiplier signals need to be calibrated in time as well, so that contemporary Cherenkov signals in neighboring pixels stack up in the summation process.

Given the interplay between delay and attenuation settings of the Sum-Trigger-II (see also Section 2.5), an iterative procedure is required in order to calibrate the signal of each of the pixels in the trigger region. This method has been developed by García et al. (2014), and later updated by myself. The procedure is based on a measurement of the trigger rates of single pixels while scanning for different attenuation or delay settings. To do so, both MAGIC cameras are uniformly illuminated by the flashes of the calibration box laser at a constant rate of 1 kHz (cfr. Section 2.3.3). The trigger rate of a certain pixel can be measured by setting a high voltage threshold on all other pixels in its macrocell, so that the rate of the whole macrocell equals the one of that sole pixel. The best delay and attenuation settings are determined at different times during the procedure. Figure 3.2

presents a flowchart of the calibration procedure. If the calibration is done from scratch, a preparatory step is required in order to have a rough calibration of the attenuation values. If instead a previous calibration already exists and needs to be improved, this step can be skipped:

- Attenuation values are initially determined by keeping all the signal delays at zero. The voltage discriminator threshold is progressively increased so that signals eventually fall below it (see Figure 3.1, bottom part). The individual trigger rate follows a sharp sigmoid function versus the threshold level, with an inflection point at its half-maximum. This corresponds to an amplitude threshold level just grazing the signal of the pixel. Such a curve is sampled by scanning for different threshold values: in such a way the amplitudes of the pulses of all pixels are estimated from the half-maxima of the sigmoids. Attenuation values are adjusted so that all pixels have the same amplitude. For the actual scan, different pixels can be investigated at the same time, provided that they do not belong to the same macrocell.

Once an initial rough estimate for the attenuation values has been found, the proper iterative calibration procedure takes place. As changing the delays affects the attenuation of the signals too, a look-up table has been produced, registering the average attenuation introduced by a certain delay (see Figure 3.3). The table is used to adjust the previously determined attenuation values during the delay scan. However, since each channel has slightly different characteristics, the attenuation determined with the table suffers some systematic effects. Because of this, after a delay scan has been made and new delays have been determined, attenuation have to be calibrated again. In other words, the final determination of the attenuation values shall always follow the one of the delays.

1. The delay calibration is performed similarly to the initial attenuation one, by observing the coincidence rate between pixels in the trigger area and the signal of a reference pixel, outside of it. The relation between the coincidence rates and the delay set for a certain pixel also resembles a sigmoid function, whose half-maximum point can be used to estimate the relative delay between that pixel and the reference one (see figure 3.1, upper part). During the scan, the look-up table is used to account for the change in the amplitude of the signals due to the related delay change. Resulting delays are loaded back to the system.
2. As the attenuation values has been affected by the newly changed delays, a further attenuation calibration is performed in a similar way to the initial one. The resulting set of delays and attenuation values does not rely anymore on the LUT for the delay-introduced attenuation. Steps 1. and 2. can be iterated in order to reach a better calibration.

In an early implementation of the method, the look-up table correction for the delay always assumed the preexistent attenuation values to have been determined for a zero delay setting. This was a bug affecting all iteration steps following the first one and hindering the correct determination of the calibration values. I solved it by introducing a new `I_DELAYSCAN` command in the CRISTAL control software, explicitly requesting the user to load previous delay settings alongside the attenuation ones. After such fix, the number of iterations required for the procedure to converge was drastically reduced.

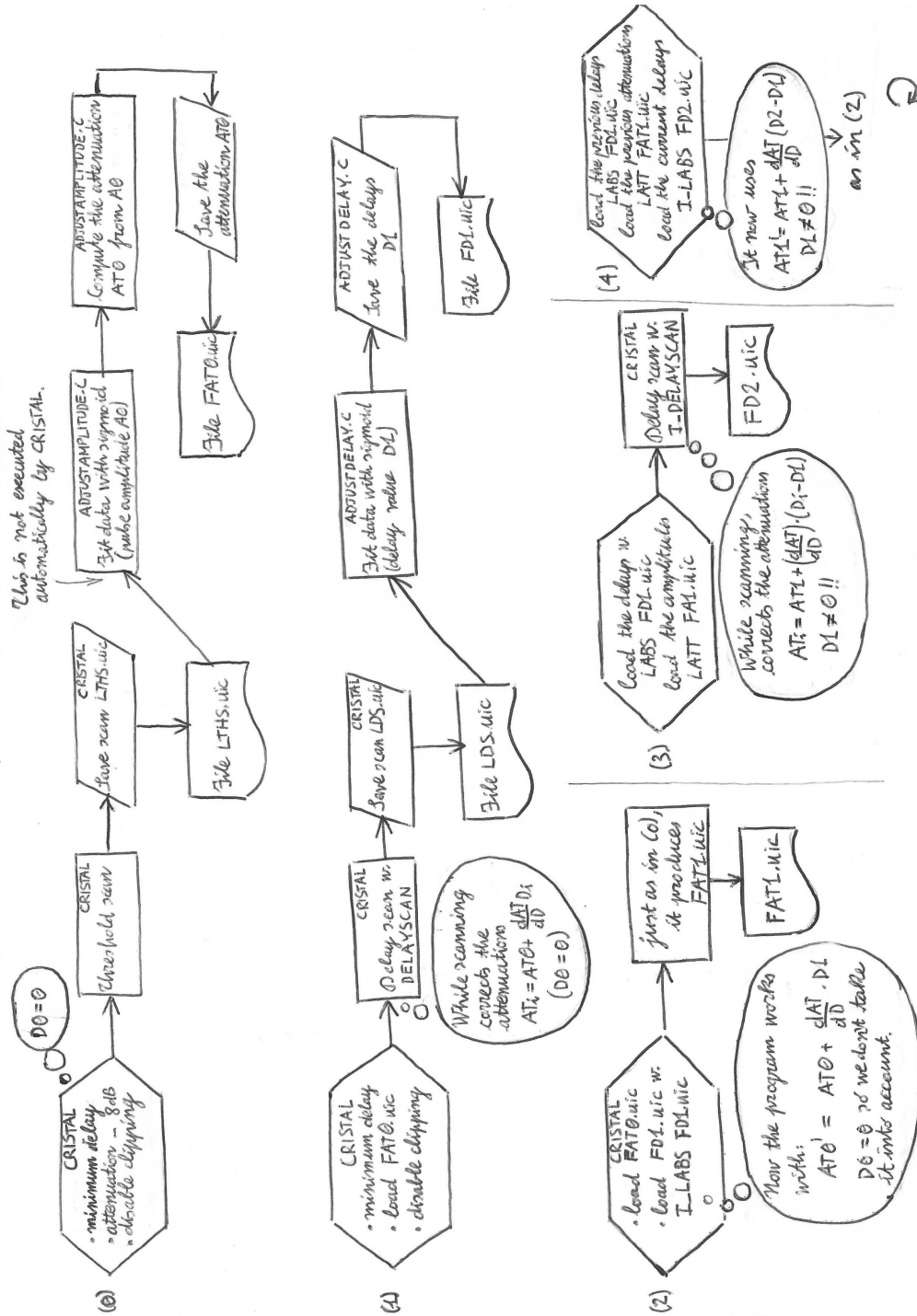


Figure 3.2: Flowchart of the Sum-Trigger-II calibration procedure, referring to CRISTAL commands used in it

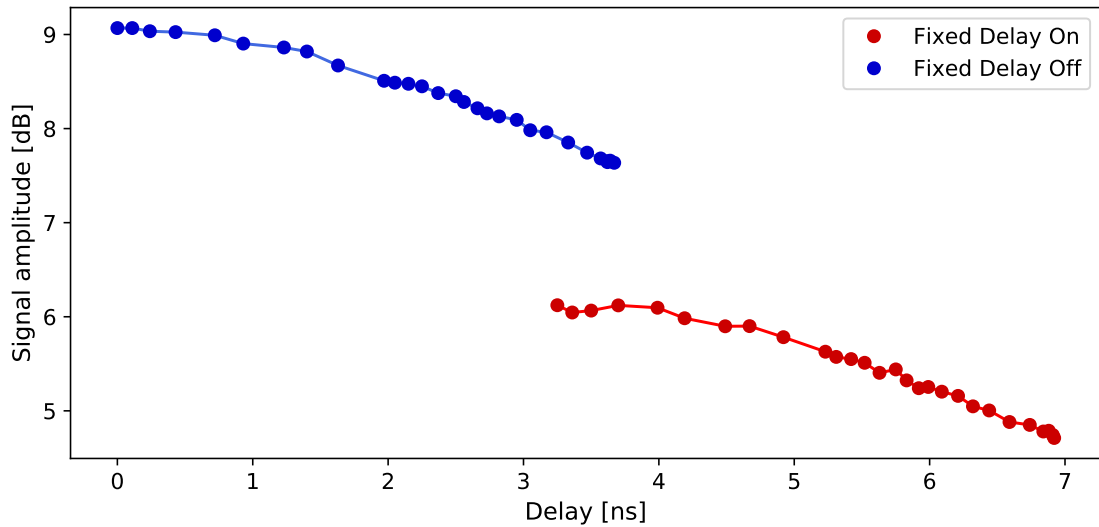


Figure 3.3: Delay-induced attenuation in the signals on the Sum-Trigger-II clip-boards. The red series of points corresponds to signals for which the additional fixed delay of ~ 3 ns has been enabled. These values are used to build a look-up table and adjust the previously determined signal attenuation values during and after a new best delay scan.

After a calibration procedure, the uniformity of the signal amplitudes can be tested with a further threshold scan. Their synchronization, on the other hand, is tested by keeping the signals fixed and performing a scan with the reference signal instead. Typically, two iterations are sufficient to provide a flat-fielding of both amplitudes and delays of all pixel at a level of few percent.

3.2 Calibration Stability

In order to monitor the the stability of the Sum-Trigger-II and ensure that its performance was stable during the period of the observations, I carried on regular tests of the calibration. These were conducted by night, during a window of dark time, and typically required approximately 20 minutes. The calibration test proceeds similarly to an actual calibration, employing scans in the amplitude and delay settings of all pixels by moving the reference signal. As an automatic procedure for the preparation of the scans is not implemented in the Sum-Trigger-II control software CRISTAL, the scans were launched manually from a remote connection, with the support of the observing shifters on site. Each scan results in the distribution of signal amplitudes and delays (see Figure 3.4). Such distributions are well described by a Gaussian law, whose dispersion σ is an indicator for the the accuracy of the calibration. In normal conditions and after a successful calibration, amplitude distributions with $\sigma \simeq 30$ mV and delays with $\sigma \simeq 100$ ps are expected. The values for several calibration tests are plotted versus time in Figure 3.5.

The delay distribution proved to be stable and within the technical requirements along the whole considered period. The spread of the amplitude distribution is also within the requirements for the whole period, however there are small variations, at the level

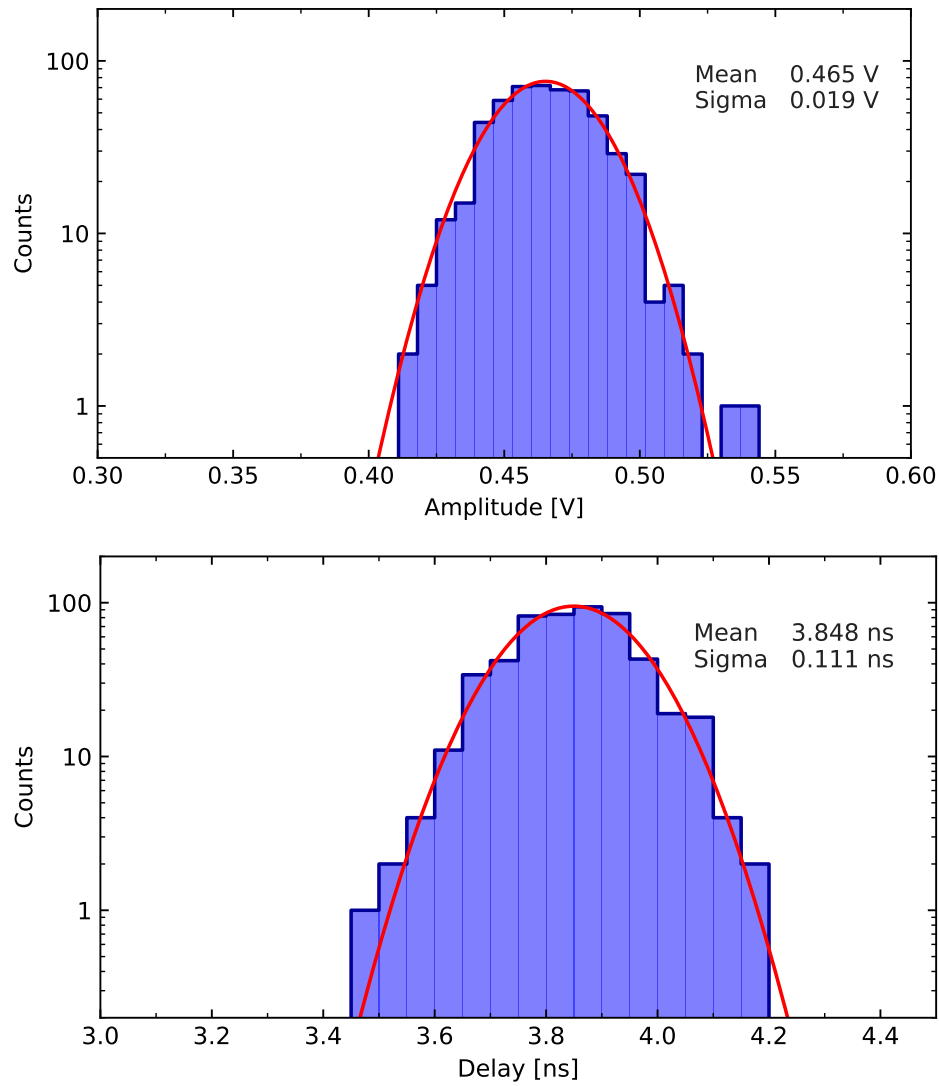


Figure 3.4: Distributions of the pixel amplitude and delay for MAGIC-II. These plots were obtained from a calibration test ran on February 20, 2020. The distribution are well approximated by normal ones (red line fit) with standard deviation $\sigma_{\text{amp}} = 19 \text{ mV}$ and $\sigma_{\text{del}} = 111 \text{ ps}$, respectively. These are well within the operation limits for the Sum-Trigger-II.

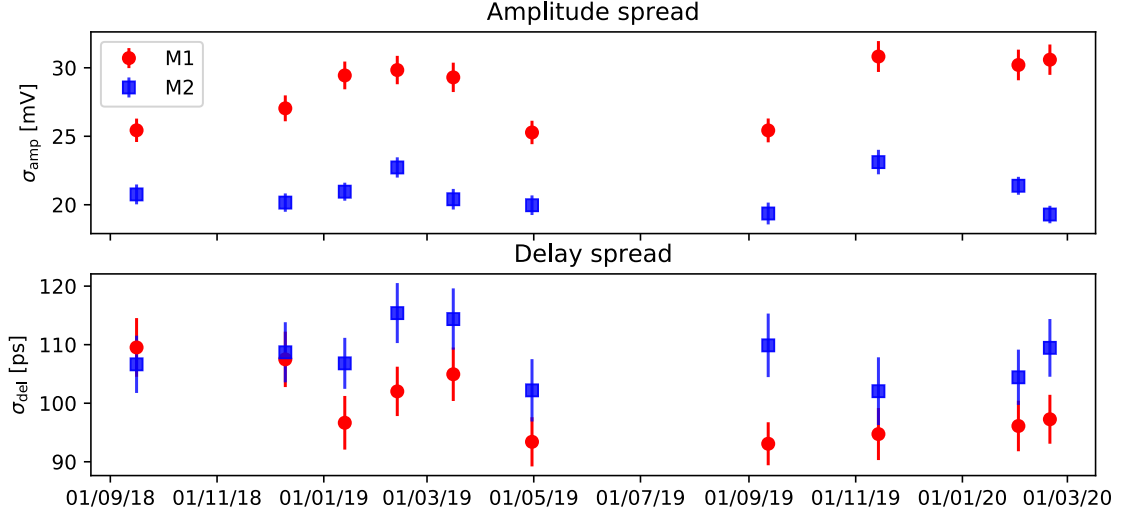


Figure 3.5: Spread of the amplitude and delay distribution in time (as standard deviation) for both the M1 and M2 Sum-Trigger-II. A re-calibration was done on the 30/04/2019, following the replacement of a defective clip-board in the M1 trigger.

of 10%, that are statistically significant. The reduced χ^2 of the amplitude spread, with respect to a constant, is 5.67 and 2.85 for M1 and M2, respectively. These figures correspond to a fluctuation probability at the level of 5.4σ and 3.0σ . This feature is attributed to varying external conditions along the long covered time interval, such as the weather, background illumination, or dust deposited on the calibration box window. The external origin of the effect is supported by the high degree of correlation between the independent MAGIC-I and MAGIC-II telescopes. Such feature is not related to a trigger instability.

The constant monitoring of the Sum-Trigger-II calibration proved that this is stable and maintains itself within the operation limits for long periods of time. However, the analysis of the delay distributions provided evidence for a defective delay module in the MAGIC-I trigger. The delays of related pixels were impossible to calibrate, and were scattered in a ± 1 ns interval with respect to the average of the other pixels. Given the mean Cherenkov pulse width of 3 ns at the summing stage, this was unlikely to severely affect the trigger efficiency. Despite this, in May 2019 a Sum-Trigger technical shift was organized, during which the faulty clip-board was replaced. The activities of such technical shift, which I coordinated, are reported in the next section. The measurement of the single pixels amplitude, together with the regular calibration output of the data analysis pipeline, allows one to determine the average proportionality factor between the equivalent photoelectron (PhE) counts (integrated deposited charge) of a signal and its amplitude at the summing stage (mV). The factors depend on the average pulse shape of the photo-multiplier tube. They were found to be 9.9 ± 1.3 mV/PhE for MAGIC-I and 11.1 ± 1.2 mV/PhE for MAGIC-II. These findings were fruitful for the aforementioned Sum-Trigger-II technical paper.

3.3 Sum-Trigger-II technical shift

In May 2019, I proposed and led an hardware intervention at the MAGIC site. The intervention had the principal aim of investigating an ongoing problem with the delay settings of some pixels in the MAGIC-I trigger. I describe in the following paragraphs the results of such technical transfer.

Internal L3 stereo coincidence

In the readout architecture of MAGIC, the two Sum-Trigger-II units communicate their single-telescope trigger signal to the common MAGIC stereo trigger mezzanine (cfr. Section 2.4.2). There, the coincidence of the two signals is used to build the third level (L3) stereo trigger, which is propagated to the readout system. In addition, the Sum-Trigger-II implements an autonomous L3 stereo trigger, using the coincidence unit of the MAGIC-II astro-board. Such “*internal*” L3 is normally not employed for the data taking, but it allows the operators of the telescopes to quickly check the stereo rate of the Sum-Trigger-II. This is a common task to assess if the weather conditions meet the requirements for the Sum-Trigger-II observations. Testing the stereo rates with the standard L3 trigger requires to setup the L3 mezzanine to use the Sum-Trigger-II signals. This causes unnecessary losses of operation time and several switches between the Sum-Trigger-II and standard trigger setups, if the observing conditions are borderline. The internal L3 solves this issue by providing an alternative and independent measurement of the Sum-Trigger-II rates. In exceptional cases, it can also be used to cross-check the validity of the standard L3 system.

The cabling of the internal L3 system makes use of the front interface of the astro-boards and frequently requires to be disassembled. This is necessary to gain access to the printed circuit boards of the clip-boards and the astro-boards. Due to the absence of a reliable reference, such procedures often resulted in errors in the rerouting of the cables. While these did not affect the data-taking, they prevented the internal L3 trigger to be produced. During the May 2019 technical shift, I found that such cabling was in an inconsistent state. It was also found that an existing reference cabling scheme contained was erroneous. I restored the correct cabling of the system, enabling the internal L3 trigger capabilities again. An updated reference scheme was produced and distributed to the Sum-Trigger-II team and the MAGIC Collaboration (see Figure 3.6). This allows the regular operators of the MAGIC Telescopes to restore the Sum-Trigger-II internal L3 system, if necessary, without the direct intervention of a member of the Sum-Trigger-II group.

Replacement of a faulty clip-board

The calibration monitoring provided evidence for a set of 32 malfunctioning pixels in the MAGIC-I trigger. The delay of their signal could not be adjusted normally, and resulted in a large spread (± 1 ns) of the corresponding delay distribution. While not critically affecting the data-taking, due to the spread being shorter than the typical Cherenkov pulse width (3 ns), a fix was required to meet the design specifications. During the hardware intervention, a faulty clip-board was found. Its status was assessed by exchanging it with another one and checking that this effectively enabled the delay

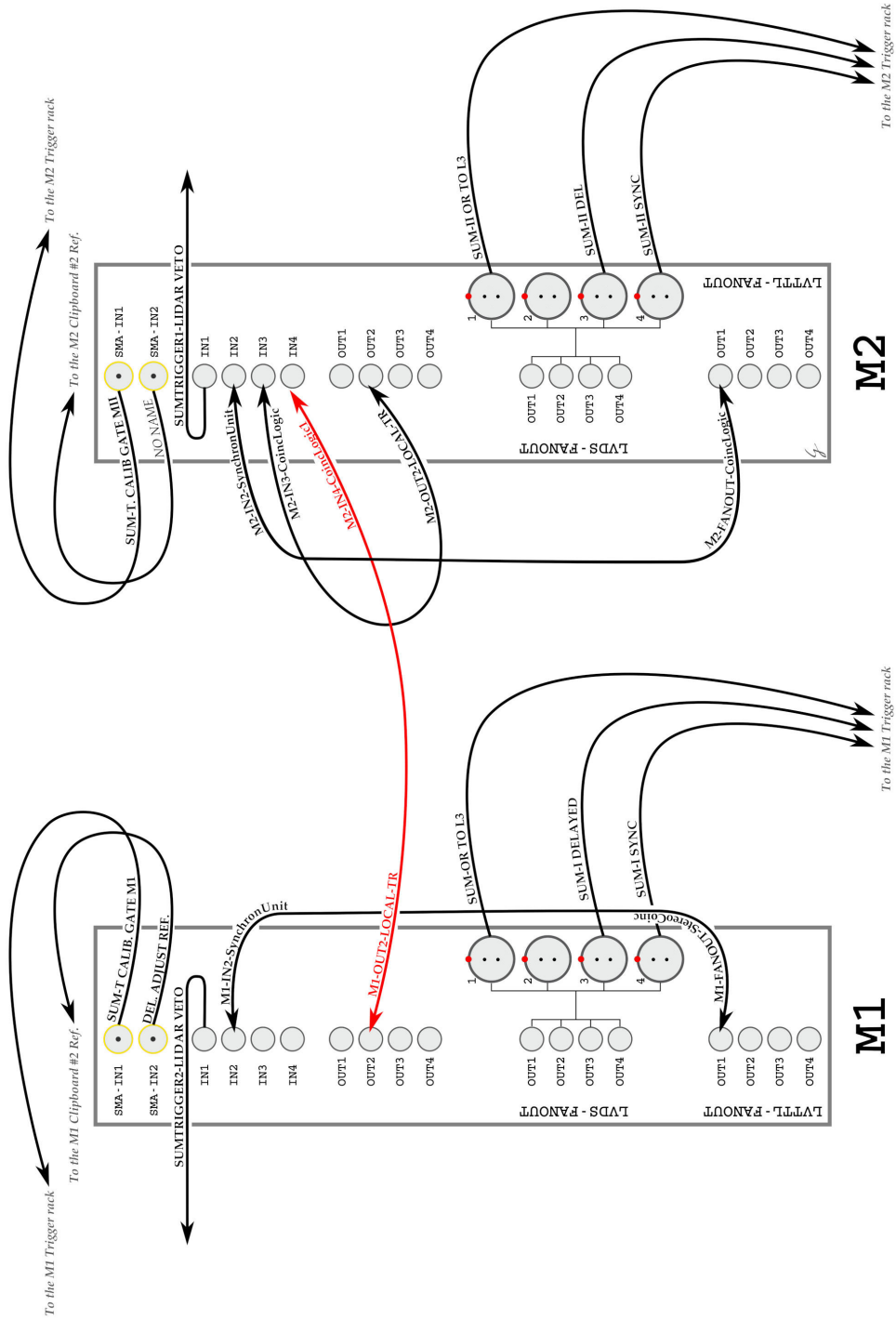


Figure 3.6: Sketch of the front cabling of the two Sum-Trigger-II astro-boards. Labels on the connections correspond to those on the real cables. The cable highlighted in red links the two triggers, for the 'internal' stereo coincidence.

lines to be normally employed. The defective clip-board was replaced and brought back to the Max-Planck-Institut electrical engineering department for further investigations.

Tests with Raspberry-PI integration

Tests were carried out to replace the obsolete Fox G20 embedded Linux board of the astro-board with a modern Raspberry PI board. It was possible to install and correctly configure the Sum-Trigger-II control software CRISTAL on such system, and to connect it with the astro-board via its SPI connections. However, it was not possible to establish an SPI communication between the Raspberry PI board and the astro-board. I found that the power supplied by the Raspberry PI board is insufficient to power the optical insulators of the astro-board. Such components secure the communication lines between the board and the embedded computer, and are powered by the latter by design. Therefore, I concluded that with the current astro-board scheme it is difficult to replace the aging Fox G20 board with a recent and widely available Raspberry PI. A redesign of the astro-board would be required to accomplish such task.

Investigation of CRISTAL and backup

During the hardware intervention, bugs affecting the control software CRISTAL were investigated. Several minor bugs were fixed, and a major bug was found, affecting the reception of commands from the MAGIC control center software SuperArehucas. The bug causes a crash of CRISTAL when several commands are issued in a short (< 1 s) period of time. The bug-fix would require an extensive rewriting of the CRISTAL code itself. Since in regular data-taking operations the MAGIC control center never issues any command to CRISTAL, a fix for the bug was given a low priority and postponed. In this occasion, backups of the whole embedded Linux system running on the astro-boards were done, to ensure the continuity of the operations in case of failures.



4

DATA ANALYSIS

In this chapter I present the methods that have been used to select, prepare and analyze the MAGIC Crab and Geminga data taken with the Sum-Trigger-II. I follow the steps from the lowest level data, the raw photomultiplier tube waveforms, to the production of scientific results such as spectra and phaseograms.

As was highlighted in Section 1.3, pulsars emit most of their radiation at energies below 100 GeV. The Sum-Trigger-II (cfr. Section 2.5) greatly improves the performance of the MAGIC Telescopes at those energies. In order to fully exploit such improvement, the data analysis techniques have to be optimized for the lowest energies as well. A large part of the methods outlined in this chapter is highly non-standard and typically not included in the MAGIC analysis chain. These include:

- **Spike removal:** a noise reduction algorithm of the raw waveforms of the photomultiplier tubes, to reduce the impact of spurious signals (Section 4.1.1).
- **MaTaJu cleaning:** a dedicated calibration and an image cleaning method, to improve the performance at the lowest energies (Section 4.2.1).
- **Bright star removal:** a special treatment of bright stars in the field of view of the telescopes, to minimize their impact on the event reconstruction (Section 4.4).
- **Pulsar phases:** assignment of a pulsar phase to each of the events (Section 4.6). In the case of Geminga, this included also the task of generating a rotational model for the pulsar from *Fermi*-LAT data (Appendix A).
- **Relaxed cuts:** attenuation of the standard criteria for event selection, to prevent the rejection of low-energy events. These are treated separately in Section 4.5.

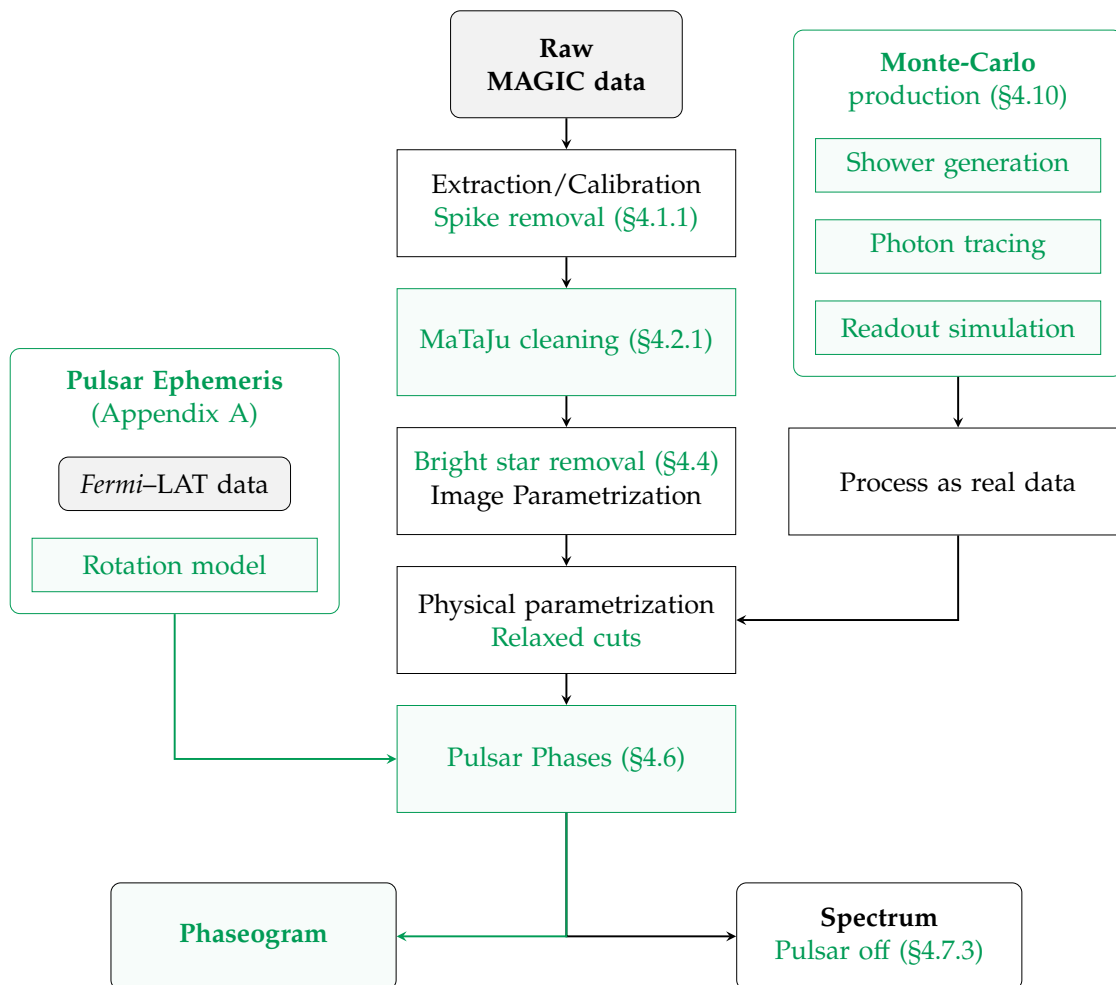


Figure 4.1: Flow-chart of the data analysis process. Tasks highlighted in green are non-standard procedures required by the low-energy pulsar data analysis.

- **Tailored Monte-Carlos:** production and employment of custom high-statistics Monte-Carlo simulations that mimic the path in the sky covered by the source being studied (Section 4.10).

A flow-chart of the analysis chain, presented in Figure 4.1, highlights the position and relation of these non-standard tasks within the analysis pipeline. The MAGIC standard analysis software MARS has been used to process the data, alongside with the TEMPO2 pulsar timing package, and custom tools which the interested reader may find in the software repository (cfr. Appendix C). This chapter provides also a general description of the standard MAGIC analysis methods. However I refer the reader to (Zanin et al., 2013) for a more specialized publication on MARS.

4.1 Raw data analysis

The signals recorded by the Photo-Multiplier Tubes (PMTs) of the MAGIC cameras are pre-amplified and transferred via optical fibers to the counting house (cfr. Section 2.4), where they are digitized by the Domino Ring Sampler v.4 (DRS4) chips of the readout boards. These analog to digital converters are set to a sampling frequency of 1.64 GHz, corresponding to a sample duration of 0.61 ns and a maximum width of 1024 samples, or 625 ns. If a trigger occurs, 50 samples (30.5 ns) are saved around the trigger time for both telescopes, and constitute the PMT waveform of that pixel for that event. These digitized waveforms and their absolute UTC time tag (cfr. Section 2.4.1) are the raw data recorded by the MAGIC telescopes. They can be integrated to obtain the total charge content and the event arrival time for each PMT, effectively constructing an image of the recorded Cherenkov light and its temporal development.

4.1.1 Signal Extraction

The first step in the data analysis chain is to obtain the total charge deposited on a PMT from its raw waveform. This is achieved by means of a *sliding window* integration algorithm. The window has a fixed size of 5 DRS4 samples, corresponding to 3 ns, the typical duration of a Cherenkov light pulse (Sitarek et al., 2013). It is used to scan the whole waveform, and selects the greatest sum of five consecutive samples above the mean signal baseline μ_{PED} (see Section 4.1.2 for the estimation of μ_{PED}). This value constitutes the raw uncalibrated signal charge C_i of pixel i , in arbitrary units of DRS4 counts. The signal arrival time for that particular PMT is analogously obtained as the charge-weighted average of the times of those five samples. Figure 4.2 presents a typical non-calibrated waveform and a signal being extracted. The sliding window algorithm is a standard procedure of the MAGIC data processing and has been used for all data taken after the upgrade of MAGIC (Aleksić et al., 2016b). In presence of noise features with an intensity comparable to that Cherenkov pulses, the signal extraction procedure is prone to a mis-identification of the signal. This issue becomes crucial for the weak signals of low-energy events. Large noise features can be produced either by the fluctuations of a strong background (as during moon observations), or as artifacts of the readout system. The first case can not be addressed during the offline analysis, and therefore low-energy aimed observations necessarily require dark background conditions (cfr. Section 6.1). Spurious readout signals can instead be compensated for in the analysis procedure. The DRS4 digitizers produce two classes of such artifacts. The first ones, *pseudopulses*, happen at predictable times, and as such their occurrence can be confidently identified. They are automatically removed from the raw waveforms, and the values of the samples affected by them are replaced with a linear interpolation of close ones. The second class is constituted by narrow (~ 1 ns) artifacts produced randomly, and known as *spikes*. Figure 4.2 presents a spike at the beginning of the waveform. A *spike removal* procedure has been developed to identify and remove such features. The procedure relies on spikes being comparatively narrower than Cherenkov signals. Each local maximum in the waveform is compared to the two neighboring samples. Based on the values of these, and accounting for the average Gaussian shape of a genuine PMT pulse, a predicted value of the central sample is calculated. The relative excess of the local maximum

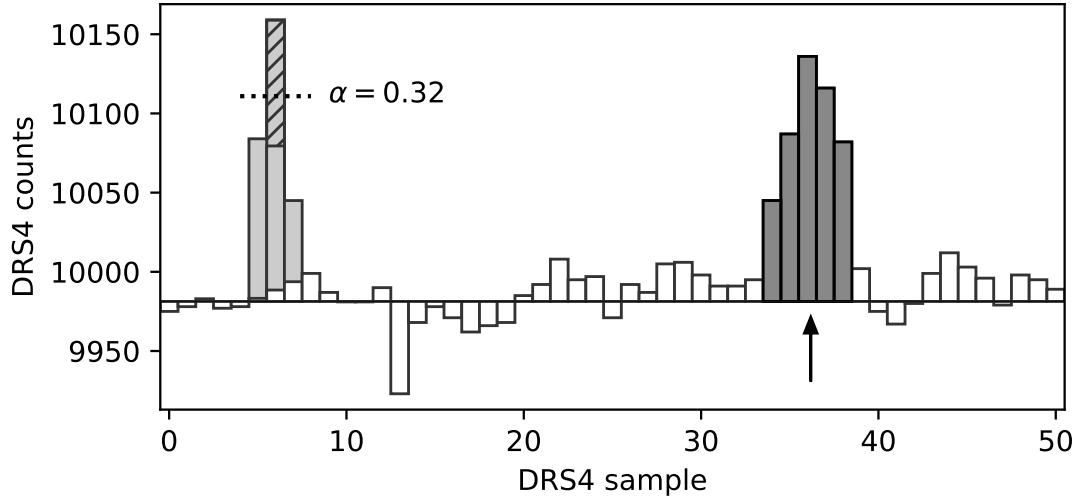


Figure 4.2: A DRS4-digitized waveform with a spike being removed (light shaded area), and a pulse being integrated (dark shaded area). **Signal extraction** The pulse integral above the pedestal level (μ_{PED} , solid baseline) defines the uncalibrated signal charge C_i . Its arrival time (arrow) is computed as the weighted average of the samples. **Spike removal** The average of the samples preceding and following the local maximum defines an expected peak value (solid gray area). The spike exceeds it (slashed area) by more than the spikeness cut $\alpha = 0.32$ (dotted line). The whole spike is clipped and samples are interpolated back from neighboring values.

over such value is taken as a measure of its *spikeness* α . Peaks exceeding a pre-defined spikeness threshold are removed from the waveform, with corresponding samples being interpolated back from the remaining ones. In this way the signal extraction is prevented from mistaking a DRS4 spike for a signal. Such single-waveform analysis significantly increases the computation time of signal extraction. As spikes very weekly affect regular MAGIC data at energies larger than 100 GeV, such spike removal procedure is not part of the standard MAGIC analysis chain. However, its employment is essential for the proper reconstruction of low energy events below 100 GeV. As such, it was used in the analysis of pulsar data presented in this thesis. A cut of $\alpha = 0.32$ in spikeness was found to be optimal to clip the DRS4 artifacts while keeping genuine signals.

4.1.2 Signal Calibration

The PMT charge and arrival times obtained by the signal extraction procedure are uncalibrated values, measured in arbitrary units of DRS4 counts and samples, respectively. A calibration procedure is required to convert these into physically meaningful units. As the peak quantum efficiency of PMTs varies in a range of $\pm 15\%$, this must necessarily be a per-pixel process. The MAGIC data analysis employs the *F-factor* calibration method (Mirzoyan, 1997). This relies on the measurement of the statistics of pure background signals, so called *pedestal events*, and of *calibration events* produced by a uniform illumination of the whole camera. The latter ones are generated by the *calibration boxes* installed at the center of the reflector of both telescopes (cfr. Section 2.3.3). These devices can flash the camera with a spatially uniform and temporally stable pulse of light. The mean

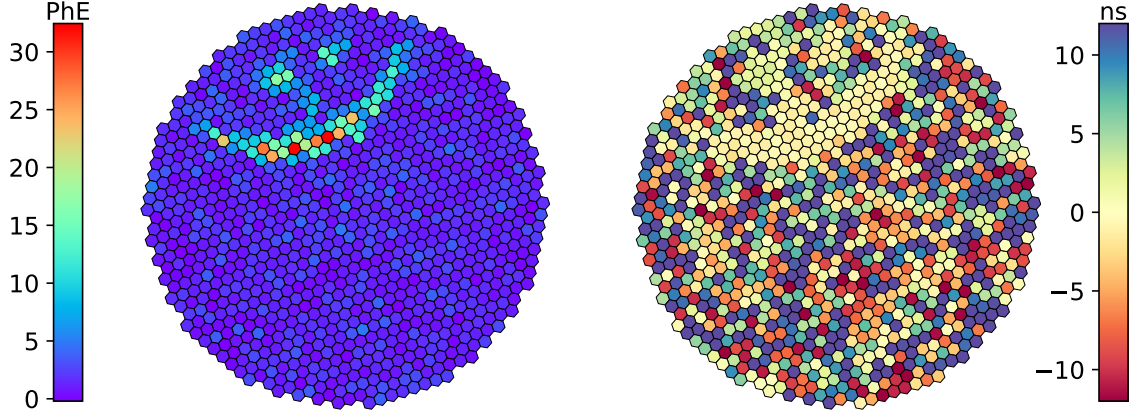


Figure 4.3: A sample event. The left panel shows charge in units of PhE, proportional to the light that hit that particular PMT. The right panel shows the arrival time distribution. This shower is of certain hadronic origin, since it presents several sub showers and a muon arc.

pedestal value μ_{PED} , its root mean square σ_{PED} , as well as the values for the calibration events μ_{CAL} and σ_{CAL} are estimated for each pixel at the beginning of the observations of each source with dedicated pedestal and calibration runs. The pixel-specific calibration constants are subsequently obtained as:

$$k_i = F^2 \frac{\mu_{\text{CAL},i}}{\sigma_{\text{CAL},i}^2 - \sigma_{\text{PED},i}^2},$$

where the index runs on different PMTs, and the F factor accounts for contribution of the multiplication process of the PMTs. The F -value for MAGIC PMTs was measured during the commissioning of the cameras, and found to be $F \simeq 1.2$. This allows to convert the arbitrary five-sample integrated DRS4 counts of the sliding window procedure into the physically meaningful photo-electron charge units $Q_i = k_i C_i$. As each pixel responds differently to the same incoming light signal, a further *flat-fielding* of the camera is required. Being the calibration pulses uniform, this is achieved by further scaling the signal of pixel i by $\langle Q_{\text{CAL}} \rangle / Q_{\text{CAL},i}$. The resulting complete calibration constants are:

$$k_i^* = \frac{F^2}{\mu_{\text{CAL},i}} \frac{1}{N} \sum_{j=0}^N \frac{\mu_{\text{CAL},j}^2}{\sigma_{\text{CAL},j}^2 - \sigma_{\text{PED},j}^2}. \quad (4.1)$$

After such flat-fielding, the signals finally have the calibrated units of *equivalent Photo-Electrons* (PhE). Such calibrated signals are often referred as the “charge” of a pixel, although they relate to the number of photons incident on the PMT and not to the charge emanated by the photocathode. This concludes the signal calibration procedure. Figure 4.3 presents the image of a calibrated event, where each pixel is colored according to its PhE counts. During the span of the observations of an object, the calibration may sensibly change from the initial one. For this reason, *interleaved* calibration and pedestal events are continuously recorded while the observations take place. The prescaler of the MAGIC trigger (cfr. Section 2.4.2) flags these events, so that they can be identified during the analysis. In regular MAGIC observations, both interleaved pedestal and calibration events are taken at a rate of 25 Hz. The calibration constants are updated every 1000

interleaved events, or once in 40 s. The same is true for the pedestal baselines μ_{PED} , which are affected by varying observing conditions such as the night sky background, the zenith distance, and the weather.

The timing of each PMT needs to be calibrated as well, so that a global isochrony of the camera is achieved. This is required to study the temporal development of Cherenkov shower images, a major channel of information for the nature of the primary particle and its incoming direction (cfr. Section 4.2). The calibration of the length of the optical fibers is straightforward and relies on the calibration events discussed before. The DRS4 digitizers require instead a dedicated calibration routine. The timing difference between different pixels is non trivial, depends on the first DRS4 capacitor to be read while recording the 50 samples for the event, and varies with time. It can amount up to 5 ns, more than the time span of a Cherenkov pulse. The interested reader may find a detailed description of the time calibration procedure in Aleksić et al. (2016b). After its calibration, the timing of the camera is flat-fielded, and different pixels are isochronous within ~ 100 ps. I stress that such accuracy is for the relative timing among different pixels in the same event. The absolute timing accuracy of MAGIC (the accuracy of its UTC time tag, as in the timing difference among different events) amounts to 200 ns.

After the extraction and calibration of the signals, a Cherenkov event can be represented as a pair of images depicting the light deposited on the camera in equivalent PhE counts and the activation time of each pixel. Figure 4.3 presents such images for a real event. Such shower images are the base for the following identification and modeling of the event. In order to save storage space, the original waveforms of the pixels are discarded from the files after this step. This results in a data reduction factor $\gtrsim 10$ between the raw and calibrated data levels, enabling a much faster processing in the following analysis steps. It is implied that a reanalysis of the heavy (~ 4 GB/min) raw data is required if the information contained in the waveforms needs to be accessed away. This was a major difficulty in the analysis of pulsar data with the special low-energy MaTaju procedure (cfr. Section 4.2.1). The disk space required for the storage of the raw Crab and Geminga observations alone (excluding related Monte-Carlo productions) exceeded 60 TB.

4.2 Image Cleaning

Image cleaning is the procedure of identifying a set of relevant pixels in the shower image and discarding the rest of the information. The resulting “cleaned” image can be parametrized with few numerical variables, the *Hillas parameters* (Hillas, 1985). These are used thereon for the analysis and reconstruction of the event (Section 4.3). Image cleaning prevents large portions of the image, presumably containing no Cherenkov signal, to dominate the determination of such Hillas Parameters. The image cleaning and parametrization tasks vastly reduce the original information of the event.

The standard MAGIC image cleaning procedure involves the detection of two classes of pixels. These are the *core* pixels, containing much of the Cherenkov light, and the *boundary* ones, on the edges of the shower image. First, compact nearest neighbor groups of two, three, and four pixels are investigated (see Figure 4.4).

Those whose summed charge exceeds a fixed threshold (~ 4 PhE), and whose signals are in time coincidence within a narrow window (~ 1 ns), are selected and proceed to the second step. The actual charge thresholds and coincidence intervals depend on the geometry of the nearest neighbor group. In this step, pixels whose signal is larger than a safety threshold of 750 PhE are clipped, to prevent possible after-pulses of the photo-multiplier tubes to affect the image. This is analogous to the procedure employed in the Sum-Trigger-II (cfr. Section 2.5), albeit on the software side. In a second step, core pixels are identified as those which bear a charge larger than 6 PhE, and have at least another neighboring core pixels. These pixels constitute the core of the shower image.

Boundary pixels are searched among those who survived the first step, have a charge larger than 3.5 PhE, and border a core pixel. The set of core and boundary pixels are retained for the image parametrization. All remaining pixels are discarded.

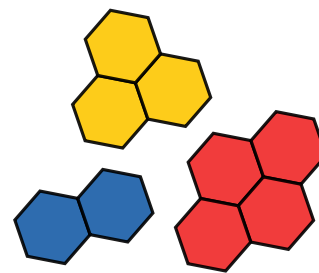


Figure 4.4: Nearest neighbor groups of order 2, 3 and 4.

The charge thresholds of the standard cleaning procedure may be altered to cope with large background noise (as in moon observations). However, its performance at energies below 100 GeV is limited by its capabilities to retain the low charge pixels of dim showers while effectively rejecting the background noise. For this reason, a dedicated low-energy image cleaning procedure was developed. The method, known as MaTaJu¹ cleaning, exploits the lower-level information available in the pixel waveforms to reconstruct more accurately the low-energy shower images. As an evident disadvantage, this requires to reprocess the large raw data files where the waveforms are stored. For this reason, the MaTaJu procedure is not enabled in the standard MAGIC pipeline, and is only employed in sources whose low-energy emission is particularly relevant. This method, and not the standard cleaning one, was used for the pulsar studies presented in this thesis.

4.2.1 The MaTaJu Cleaning

The MaTaJu cleaning is a procedure that aims to improve the reconstruction of low-energy shower images and the selection of relevant pixels, while still suppressing noise originating from the diffuse night of the sky background or the readout chain. A short description of the method is presented here, whereas interested readers are referred to Shayduk (2013) for more details.

The basic idea is to exploit the full information contained in pixel waveforms, both charge and time-wise, to better distinguish a genuine Cherenkov light signal from the noise. In order to do so, the image cleaning has to access the waveforms of the events to select the pixels with relevant information. This requires the calibration of the signals and their cleaning to be computed in a single step, as opposed to the standard MAGIC analysis. A disadvantage of this method is that the analysis chain needs to start at the raw data level, rather than with already calibrated or even partially reconstructed data, implying

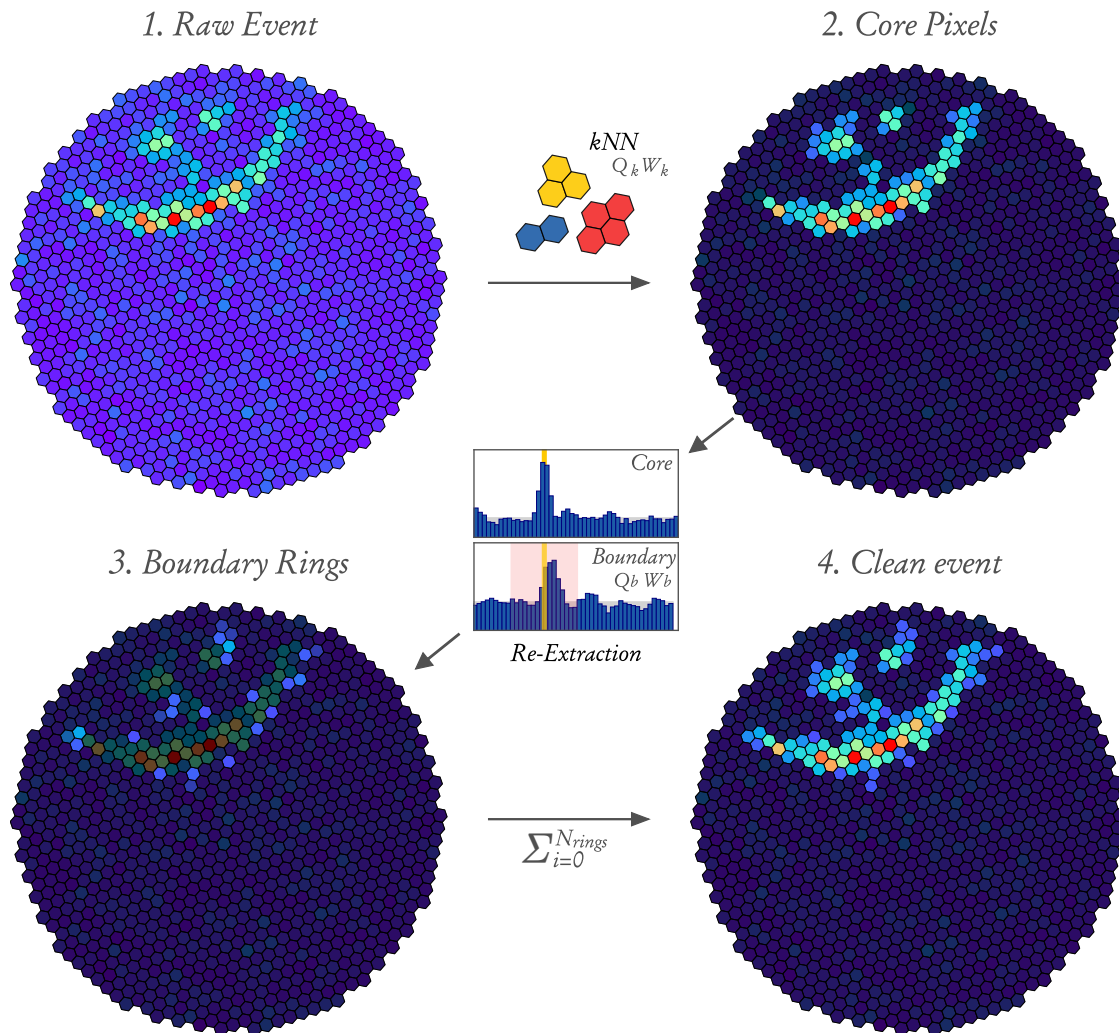
¹ The name is a contraction of the names of the original developers: Dr. Maxim Shayduk, Dr. Takayuki Saito, and Dr. Julian Sitarek.

a higher computational and data storage load. The method proceeds as follows (refer also to the scheme in Figure 4.5):

1. **Trigger Times** A first signal extraction, equivalent to the standard one described in Section 4.1.1, is performed on a small sample of events (typically 10000). The mean trigger time for the shower events is obtained by averaging the calibrated arrival times of pixels whose charge is above a large threshold of 20 PhE. The existing DRS4 time calibration allows to compare signals from different pixels and determine for each of them the sample x_{trig} which a signal is expected at.
2. **Core Extraction** Next, the charge of every pixel for each of the events is extracted with the usual sliding window method. However, as opposed to the standard procedure, the window is confined in a narrower range Δ of samples centered on the specific x_{trig} for the pixel being extracted. In such a way, the possibility that surviving spikes or unrelated signals are picked up as core pixels is largely reduced.
3. **Core Identification** Core pixels are identified as the ones which form groups of 2,3 or 4 nearest neighbors, each one with a charge exceeding a geometry-specific threshold $Q_{k\text{NN}}$ and in coincidence within a time window $W_{k\text{NN}}$ with the other ones in the group. This step is similar to the standard cleaning procedure, but no further filtering for pixels charges larger than 6 PhE is applied. It follows that the MaTaJu method does not allow isolated core pixels. This automatically suppresses contributions from after-pulses.
4. **Boundary Re-Extraction** Pixels bordering a core one but not being part of the core themselves are inspected next. Based on the timing of the signal in the neighboring core pixel, the signal in them is re-extracted in a narrower interval. If the charge is above a threshold Q_{bnd} and coincident with the core pixel signal within W_{bnd} , the pixel is marked as a boundary pixel of the first ring. In this way, the dimmer outer regions of the shower image can be reconstructed in a more reliable way, reducing the risk that a fluctuation in the waveforms is picked up the signal by the sliding window algorithm, instead of the real one.
5. **Ring Iteration** Finally, the previous step is iterated to search for following rings of boundary pixels, based on the timing of the already identified ones. The maximum number of boundary rings is usually set to $R = 3$, as the number of pixels added in iterations above the third one is negligible in all practical cases.

Optionally, the cleaning can be optimized even more by extracting all pixels twice. This double extraction uses a narrower time window (which is less prone to the mis-identification of signals) to identify core and boundary pixels, followed by a second extraction with a broader one to properly reconstruct the charge and arrival time of the signals. The double extraction was not employed in the analysis of the data presented in this thesis.

Such a procedure has 10 free parameters: the extraction range Δ , the core charge thresholds $Q_{2\text{NN}}, Q_{3\text{NN}}, Q_{4\text{NN}}$ and time coincidence windows $W_{2\text{NN}}, W_{3\text{NN}}, W_{4\text{NN}}$, the boundary ones $Q_{\text{bnd}}, W_{\text{bnd}}$ and the number of rings R . The set of parameters employed in my analysis of the Crab and Geminga pulsar observations were optimized on the fraction of

**Figure 4.5:**

Scheme of the MaTaJu cleaning procedure with data from a real hadronic event. **1.** Charge and arrival times of all the signals are extracted around the mean arrival time of Sum-Trigger-II signals, determined previously. **2.** Core pixels are detected by using compact k NN groups and related single pixel charge thresholds and time coincidence windows. **3.** Boundary pixels are re-extracted around the arrival time of the bordering core pixel, again with a charge and timing threshold. This is iterated to add more boundary rings. **4.** The final cleaned image is composed by the set of core and boundary pixels. Other pixels are disregarded in the following steps of the analysis.

The brightest pixel in the image (red, center of the muon arc) bears a charge of 32.4 PhE. The dimmest selected boundary pixel (blue) contains only 2.7 PhE. Darker pixels did not survive the image cleaning.

M1			M2		
Group	Q_k	W_k	Group	Q_k	W_k
2NN	7.3	2.31	2NN	8.4	2.31
3NN	4.3	2.81	3NN	4.6	2.81
4NN	3.3	3.14	4NN	3.6	3.14
Boundary	2.3	3.5	Boundary	2.5	3.5
Δ	12		Δ	12	
Rings	3		Rings	3	

Table 4.1: The MaTaJu cleaning parameters for both telescopes. Charge threshold parameters Q_k are in units of equivalent photo-electrons (PhE), whereas the time coincidence windows W_k and the extraction range Δ are in units of DRS4 samples (one sample equals 0.61 ns). The core k NN thresholds and coincidence windows have been fixed by requiring that the total probability to have a noise-triggered event (surviving pedestal) is at most 5%.

pedestal events (pure noise events) surviving the cleaning procedure. These were tested in the field of view of the Crab, after removing the bright star ζ Tauri (cfr. Section 4.4). The values were fixed so that the surviving ratio did not exceed $\sim 5\%$, and requiring that different NN geometries contributed equally to it. These parameters are listed in Table 4.1. Figure 4.6 presents the effect of the MaTaJu cleaning on the energy threshold of the analysis and the effective collection area (see Sections 4.8.2 and 4.9). With respect to the standard MAGIC cleaning algorithms, the MaTaJu procedure vastly improves the analysis performance at energies below 100 GeV. It reduces the analysis threshold by a factor ranging between 1.5 and 2, depending on the chosen spectral shape (cfr. Section 4.9). This makes it an essential tool for the studies of low-energy sources such as pulsars, distant active galactic nuclei, and also gamma-ray bursts, that may reach a high redshift.

Shower images that survive the cleaning stage are to be parametrized with a set of variables that collect the fundamental properties of the event, the Hillas parameters.

4.3 Image Parametrization

The assessment of event properties such as the primary particle energy and direction is done indirectly by first encoding the information contained in the cleaned image to a few key parameters, the *Hillas parameters* (Hillas, 1985). These variables describe multiple aspects of an event, such as its intensity and shape, its time development, and the stereoscopic geometry of it (see Figure 4.7). The following list contains some notable Hillas parameters. All summations are on the pixels in the cleaned shower image.

- **Size** – the total equivalent photo-electron content in the cleaned shower image, computed as the sum of the PhE counts of all of its pixels. The number of Cherenkov photons produced in a shower is proportional to the number of particles in it, which is in turn proportional to the primary particle energy (cfr. Section 2.2). However, the total number of detected photons depends also on the viewing geometry of the

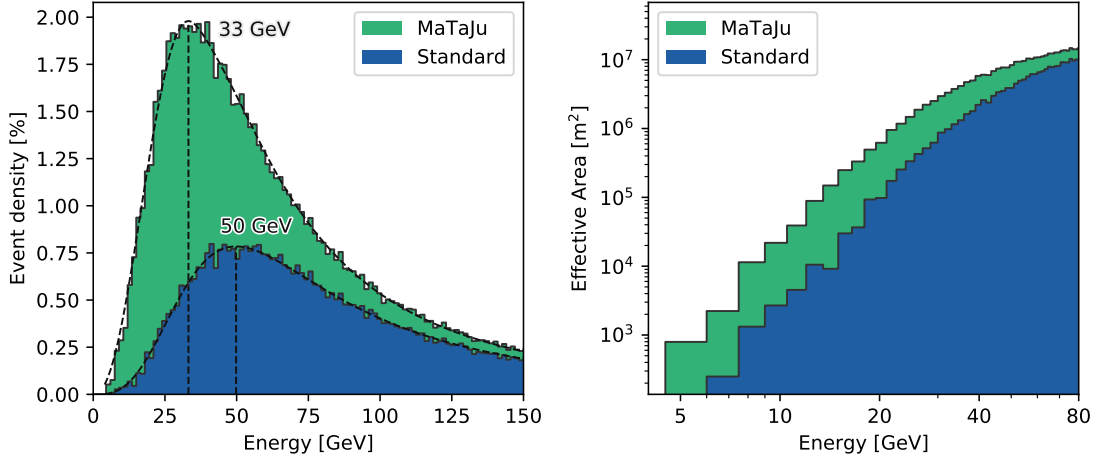


Figure 4.6: Comparison of the analysis threshold and effective area for the standard and MaTaju cleanings, computed for a gamma-ray source with a power-law spectrum and a spectral index $\Gamma = 2.6$, after the stereo reconstruction.

shower. The size of an event in one of the main parameters used to infer the event energy.

$$\text{Size} = \sum_i q_i$$

- **Position** – the position of the event in the camera is not relevant to the event shape by itself, but it is used to reconstruct its direction. The position is calculated as the barycenter of the pixel positions, weighted on their PhE content (the first moments of the charge distribution in the camera):

$$(\bar{x}, \bar{y}) = \frac{1}{\text{Size}} \sum_i (x_i, y_i) \cdot q_i$$

Related to this one is the **Dist** parameter, the distance of the shower barycenter to the position of the source being observed in the sky. This value is related to the impact parameter of the shower, calculated in the stereo reconstruction.

- **Length, Width and Delta** – the shape of the shower image can be modeled by means of the second moments of its charge distribution:

$$\begin{aligned} \sigma_x^2 &= \frac{1}{\text{Size}} \sum_i (x_i - \bar{x})^2 \cdot q_i \\ \sigma_{xy} &= \frac{1}{\text{Size}} \sum_i (x_i - \bar{x})(y_i - \bar{y}) \cdot q_i \\ \sigma_y^2 &= \frac{1}{\text{Size}} \sum_i (y_i - \bar{y})^2 \cdot q_i \end{aligned}$$

The resulting covariance matrix \mathcal{S} can be diagonalized along its eigenvectors $\mathbf{v}_0, \mathbf{v}_1$ with eigenvalues u_0, u_1 . The shower length is defined as the square-root of the larger eigenvalue, its width being the smaller one. Delta is the angle of the major eigenvector \mathbf{v}_0 with respect the camera x-axis, or the projected direction of the shower on the camera plane:

$$\text{Length} = \sqrt{u_0} \quad \text{Width} = \sqrt{u_1} \quad \text{Delta} = \arg(\mathbf{v}_0)$$

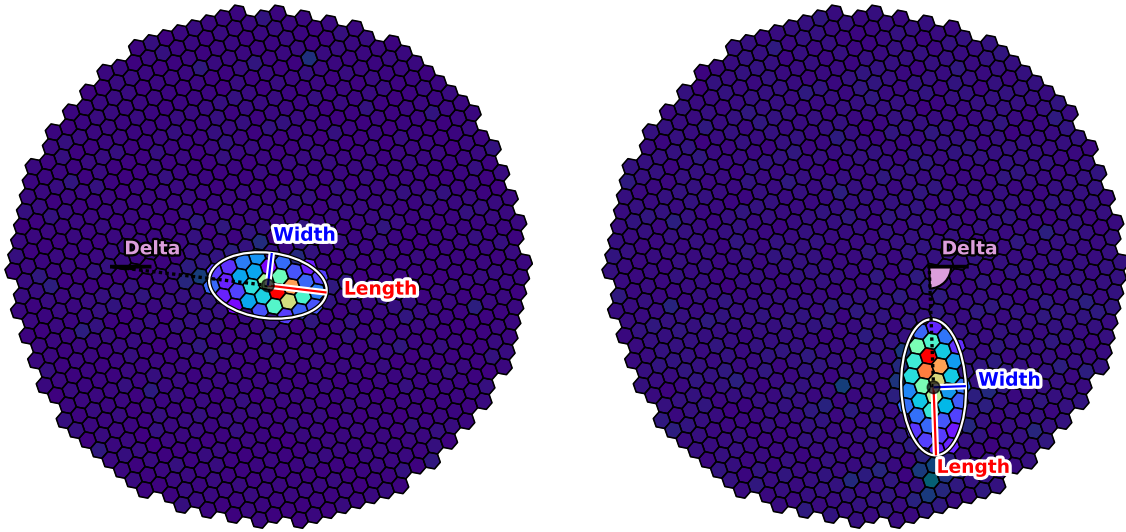


Figure 4.7: Hillas parametrization of an event in both MAGIC cameras, with some key parameters. The shape ones define an ellipse, drawn as the 99.7% (3.41σ) containment radius of a bi-dimensional Gaussian. The darker pixels outside of the ellipses did not survive the image cleaning.

If the shower image were a bi-dimensional Gaussian, its length and width would be the standard deviations along its symmetry axes. As such can be seen as the semi-major and semi-minor axes of an ellipse fitted to the shower image. Gamma-ray induced showers tend to be more tapered than cosmic-ray ones, as a result of secondary hadronic interactions and pion production in the latter. The projected shower direction delta, on the other hand, is an important parameter in the stereoscopic reconstruction of the event.

- **Time gradient** – the derivative of the pixel arrival times along the length axis of the shower. The temporal development is obtained by projecting the pixel positions onto the \mathbf{v}_0 eigenvector, and fitting the arrival times against them with a simple linear relation. The slope (measured in DRS samples per millimeter) is taken as the time gradient. This variable conveys information about the shower direction. As the velocity of the shower particles is larger than the local speed of light, those which impact close to the telescopes are seen as if they developed backwards in time, the light emitted at later times being observed before the one produced earlier. This ambiguity can be solved during the stereoscopic reconstruction of the geometry of the event.

Since shower at energies below 100 GeV are dim and small, the calculation of their Hillas parameters is easily affected by image noise, and resulting values have larger uncertainties. This becomes crucially important if a bright star lies in the field of view of the observations, as is outlined in Section 4.4

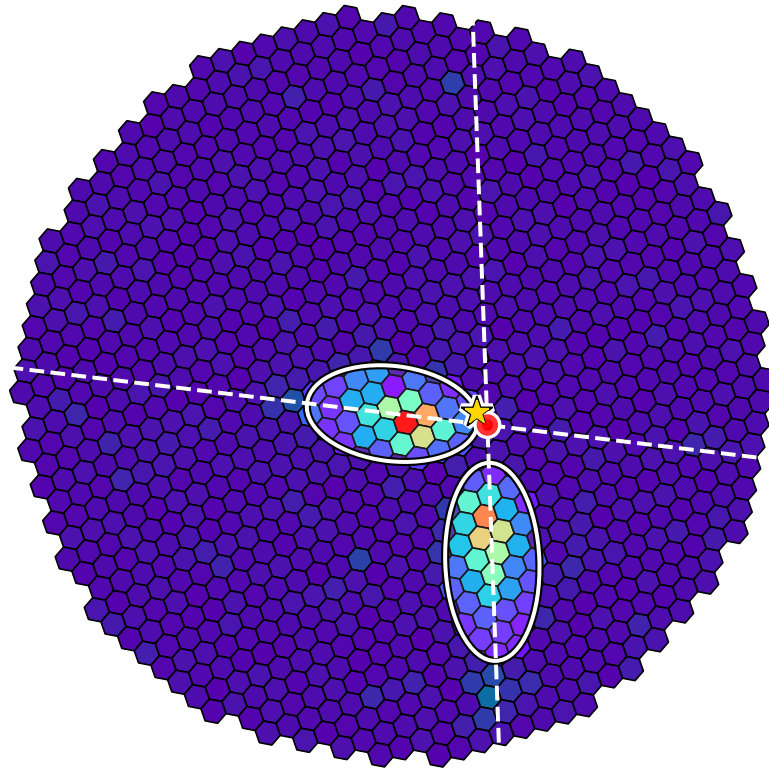


Figure 4.8: Stereo reconstruction. The Hillas parametrizations of an event in the two MAGIC cameras are used to determine the primary particle incoming direction (red dot). The star highlights the real incoming direction of this 430 GeV simulated gamma event.

4.3.1 Stereoscopic reconstruction

Based on the position and morphology of the images in the cameras of both MAGIC Telescopes, the three-dimensional geometry of the event can be reconstructed. This is of paramount importance to characterize the entire event, and the reason for the construction of the second MAGIC telescope in 2009. The shower direction vector is calculated from the projected shower axes reconstructed in the two MAGIC camera: an example is presented in Figure 4.8. With the knowledge of such a vector, several stereo parameters can be estimated:

- **Primary particle direction** – As the shower development is strongly beamed along the primary particle trajectory, its incoming direction can be estimated. For gamma-rays, such direction points back to the astrophysical source emitting them.
- **Impact parameter** – The distance between the impact point of the shower and the telescope, projected on the plane perpendicular to the incoming direction and passing by the telescope. The impact parameter conveys information on the amount of light to be expected from a shower and on its temporal development. The impact parameters for both telescopes are computed.

- **Maximum height** – the estimated altitude of the initial interaction point. This parameter is correlated to the type and energy of the incoming particle, as its cross-section with air depends on both. It is a relevant parameter for the discrimination of hadron and gamma-induced showers, required for the background suppression.
- **Theta square θ^2** – the square of the angular distance (in deg^2) from the reconstructed primary particle direction to the source being observed. If events are uniformly distributed in the field of view (as if no source is detected), θ^2 follows a uniform distribution. The θ^2 is one of the primary variables used for event selection (see Section 4.7.1.)

The stereoscopic reconstruction can be refined at a later stage in the analysis chain with dedicated machine learning techniques (cfr. Section 4.5.2). After the parametrization of the image is completed, these values are used to infer the type and momentum of the primary particle. For gamma-rays, the latter points back and carries information about the source, allowing to study its production mechanisms. The estimation of these physical quantities is treated in Section 4.5. The next Section addressed the issues in the event parametrization arising from the presence of bright stars in the field of view of the telescope.

4.4 Bright Stars

The light of stars laying in the field of view of the telescope is a source of noise for IACTs. Starlight produces a Poissonian noise, rising both the pedestal mean μ_{PED} and root mean square σ_{PED} of affected pixels. Very bright stars may even pose a risk for the integrity of the PMTs, and endangered ones are automatically ramped down by the camera control software. At the data analysis stage, the presence of starlight in an image may hinder the parametrization of the event, or make it impossible. If the image of the star is bright enough to survive the image cleaning, it may be mistaken by a secondary shower. This mimics the signal of an hadronic particle, thus causing a potential misclassification of the event. In addition, the Hillas shape parameters, being the second moments of the charge distribution, are very sensitive to pixels far from the shower core. Such an effect is intuitively more prominent for low-energy showers, as their charge distribution can be easily affected by few outlying pixels. Both the Crab and Geminga Pulsar are prospectively close to a bright ($m_V \leq 6$) star that falls within the MAGIC field of view during the observations. The Crab pulsar is affected by ζ Tauri, at a distance from it of 1.13 deg. This is a bluish B1 star with a visual magnitude $m_V = 3.03$ (Ducati, 2002a; Slettebak, 1982). In the case of Geminga, the star γ Geminorum (Alhena) is farther away from it at 1.65 deg, but it is even brighter, with $m_V = 1.92$ and spectral type A1 (Gray et al., 2003). Figures 4.9 and 4.10 present the field of view of MAGIC centered on the pulsars, with optical images of the Digitized Sky Survey. The stars ζ Tauri and Alhena are visible as large saturated dots.

As discussed in Section 2.6, MAGIC observations are conducted in *wobble mode*, with the telescopes pointing at positions close to the source and symmetric with respect of it. This allows a better control on the systematic effects due to the residual inhomogeneity of the camera. It also gives a way of estimating the background for non-pulsed signals (cfr.

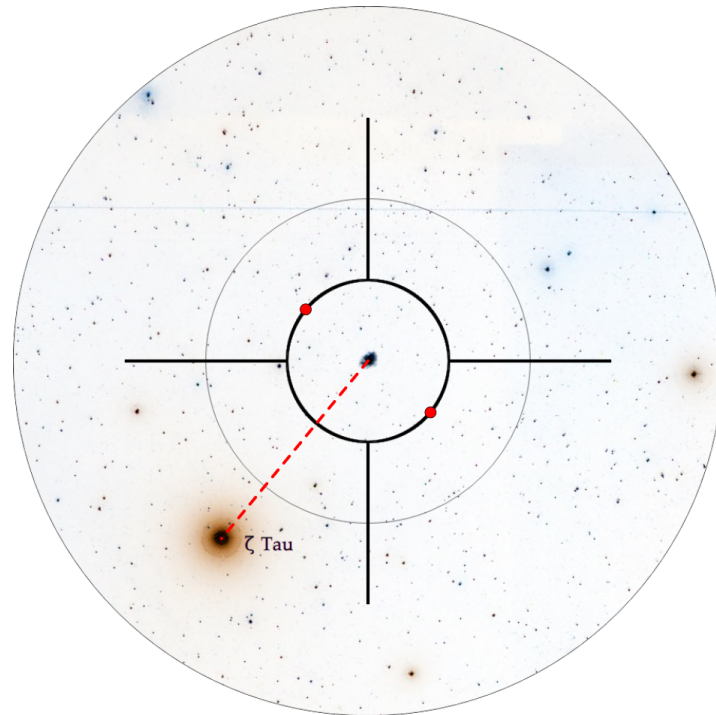


Figure 4.9: Approximate field of view of the MAGIC Telescopes around the Crab pulsar, with colors inverted. The radius of the inner target coincides with the wobble depth $w = 0.4$ deg. Its crossings correspond to the four standard MAGIC wobble positions. Red dots mark the special wobble positions used for Crab observations, symmetric with respect to the line joining Crab and ζ Tauri. The bright spot at the center is the Crab Nebula. Composition of optical images from the DSS Sky Survey (credit: STScI).

Section 4.7.2). The distance between the wobble positions and the source being observed, the *wobble depth*, is typically $w = 0.4$ deg. The employment of the wobble strategy adds further complexity to the problem posed by bright stars. In different wobble positions the star is viewed at different radial distances d from the center of the camera. In some of them it may even disappear beyond the field of view. The effect of starlight on the Hillas parametrization strongly depends on such radial distance d . This renders the impact of the star wobble-dependent, and requires a separate processing of different pointing positions of the same source. Because of this, MAGIC Crab pulsar observations use only two wobble positions, arranged in such a way that the distance of ζ Tauri from the center of the camera is the same in both of them. This simplifies greatly the following analysis and production of Monte-Carlo simulations. Geminga observations conducted in 2017 used instead the four standard MAGIC wobble positions (see Figure 4.10), with the southern and eastern wobble positions being close to the bright star Alhena and strongly affected by it. Such data required a special per-wobble analysis and the production of wobble specific Monte-Carlo simulations. To mitigate the impact of the star, the wobble scheme of following Geminga observations was changed to include a single couple, as for the Crab pulsar. In these two new wobble positions the star Alhena just barely grazes the field of view and produces no sensible effect.

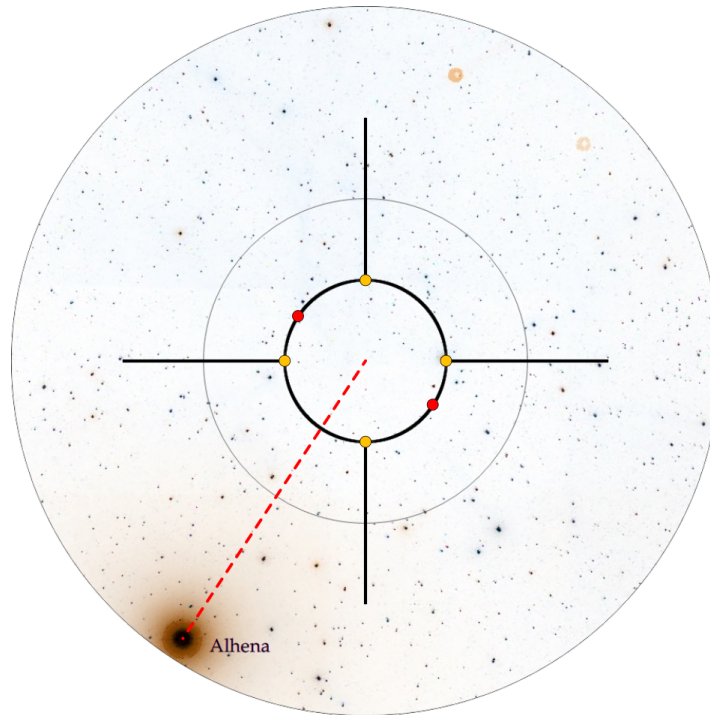


Figure 4.10: Approximate field of view of the MAGIC Telescopes around Geminga, with colors inverted. Definitions as in the previous Figure. In this case the star is farther out in the field of view, but it is brighter. Orange dots mark the initial wobble positions used for the 2017 observation campaign. Since these required a dedicated per-pointing analysis, the pointing strategy was changed for following observations (red dots) and made similar to the one of the Crab pulsar. Composition of optical images from the DSS Sky Survey (credit: STScI).

The impact of starlight can be measured in terms of the ratio of pedestal events surviving the image cleaning. As pedestals only contain background, high survival ratios point to a correspondingly large ratio of Cherenkov events being affected by the starlight. The distributions of some notable Hillas parameters in the Geminga pointing closest to Alhena is presented in Figure 4.11, where these are compared with a dark field of view. To recover such data, a circular exclusion region (a “hole”) has been defined around the star. The hole follows the star in its circular motion around the center of the camera, caused by the field rotation. Corresponding pixels are neglected during the parameter reconstruction, effectively masking the star. Figure 4.12 shows the percentage of surviving pedestals s as a function of the hole radius R , for the two pointing positions of Geminga closest to the star Alhena. Without the star removal procedure, values as high as $s = 30\%$ and $s = 10\%$ are reached, respectively. This indicates that a very large fraction of the events is likely to be affected by the starlight and possibly mis-reconstructed. No scientific measurement result can be derived from such data. Increasing the cut radius progressively decreases the fraction of surviving pedestals, until values compatible with the ones measured on a dark field are reached ($s \approx 1\%$). This happens for $R = 100$ mm and $R = 120$ mm for the eastern and southern wobble, respectively. In this way, the data taken at these pointing

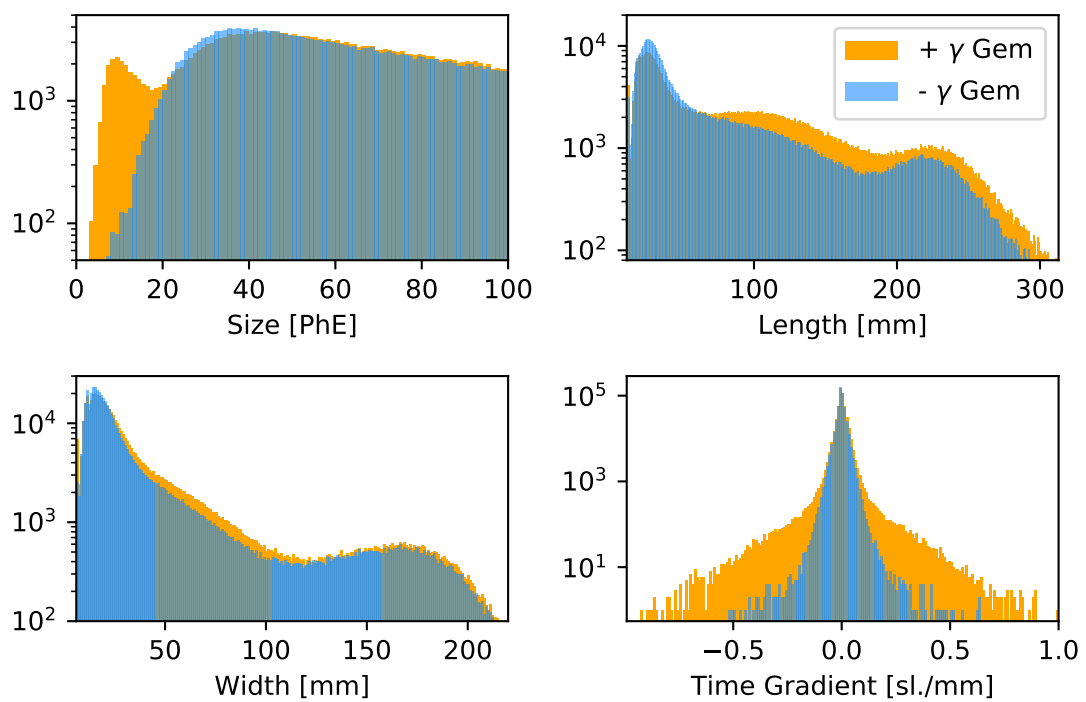


Figure 4.11: Distributions of some notable Hillas parameters affected by the starlight of Alhena (orange) and with the pixels corresponding to the star removed (blue). The star negatively affects these distributions, causing mis-reconstruction of both the shape and timing of the event.

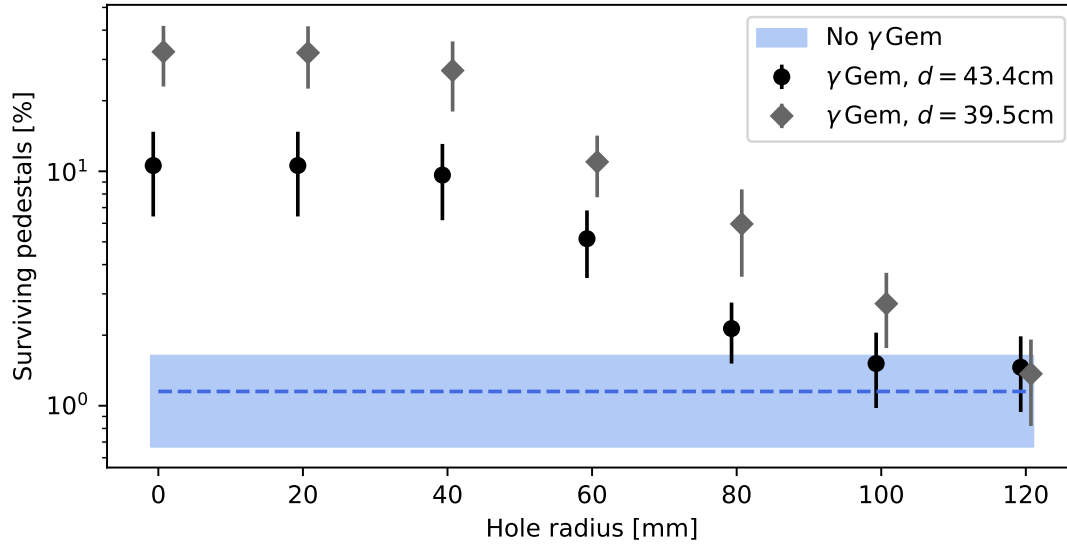


Figure 4.12: Surviving pedestals in a sample of Geminga data, as a function of the radius of the exclusion circle around the star Alhena and its distance d from the center of the camera. The blue band shows the same for a position not affected by Alhena. To recover the same performance, a 100 mm and 120 mm hole has to be cut, respectively.

positions could be partially recovered. Table 4.2 summarizes the parameters of the exclusion regions for all wobbles of the Crab and Geminga observations. Masking such a large area of the camera necessarily reduces the detection efficiency and the effective area of the telescope. The masked area accounts to 3.5% of the camera in the case of Crab. The affected Geminga wobbles lose 3.5% and 5.6% of their active area, respectively. These losses need to be properly modeled in the Monte-Carlo simulations required for the effective telescope area calculation (cfr. Section 4.10). Data with different effective areas can not be mixed together in the analysis chain until the final flux computation (see Section 4.8). In the case of Crab this does not represent a problem, as the lost area is the same in all wobbles. The Geminga analysis chain of 2017 data had instead to be split after the star removal. Data belonging to the eastern and southern wobble positions were processed separately with their own Monte-Carlo simulations. The contributions from these wobbles were added back at the end of the analysis chain, after the production of the spectrum, so that a proper estimate of the effective area could take place.

	ω [deg]	ϑ [deg]	d [mm]	R [mm]	$\Delta\Sigma$
Crab ζ Tauri	35	1.25	370	100	3.6%
	215	1.25	370	100	3.6%
	0	1.46	434	100	3.6%
	180	1.90	563	—	—
Geminga Alhena	90	1.99	591	—	—
	270	1.33	395	120	5.6%
	34	1.70	503	—	—
	214	1.70	503	—	—

Table 4.2: Values of the star exclusion circles for different pointings. All wobbles had a depth $w = 0.4$ deg. ω : bearing of the wobble position, measured clockwise from the RA axis. ϑ : angular distance between the star and the wobble center. d : corresponding distance on the camera focal plane. R : the exclusion disc radius. $\Delta\Sigma$: loss of active camera area. Four pointings are unaffected by starlight and no pixels were excluded. Wobble pairs are grouped. See also Figure 4.13 below.

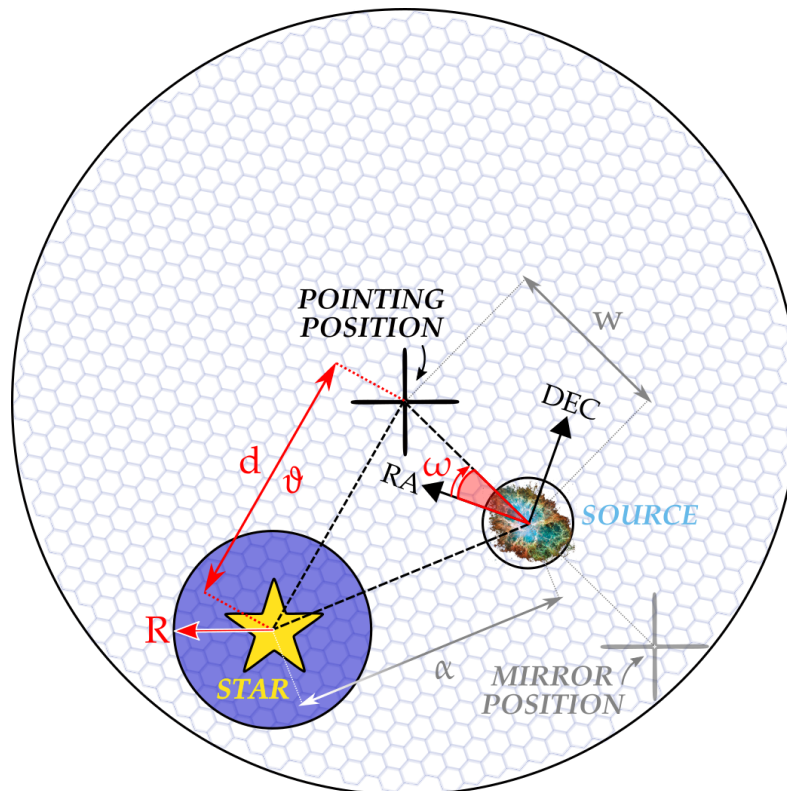


Figure 4.13: Sketch of the variables listed in Table 4.2, highlighted in red. The drawing shows also the wobble depth w , the star-source distance α and the mirror wobble position. The RA/DEC axes do not coincide, in general, with the camera axes, and rotate during the observations.

4.5 Physical Parametrization

The final step in the characterization of a Cherenkov event is the assessment of the type and momentum (energy and direction) of its primary particle. The information on the particle type allows to suppress the contribution of cosmic-ray showers, which represent a background for gamma-ray astronomy with IACTs. Measuring the energy and direction of the gamma-rays from a source allows to statistically determine its intrinsic properties (cfr. Section 4.8). Cherenkov telescopes use as an active part of the detector the Earth’s atmosphere, which is beyond the control of the experimenter. As opposed to laboratory-based particle Physics experiments, the atmosphere can not be calibrated. It follows that the reconstruction of the physical parameters must rely on extensive Monte-Carlo simulations of gamma-ray events, modeling the particle interactions and light propagation in the air, and the characteristic response of the detectors. These Monte-Carlo simulations are required to link the physical properties of an event to its observables (the Hillas parameters). In the MAGIC analysis chain, particle showers are generated with a fork of the de-facto standard CORSIKA package² (Heck et al., 1998), implementing the ray tracing of Cherenkov photons (Sobczynska, 2002). Dedicated tools are employed to simulate the focusing of photons by the mirrors of the telescope, the conversion process by the photo-multiplier tube camera, and the readout system (Moralejo, 2003; Blanch and Moralejo, 2004). The resulting Monte-Carlo “raw” events are processed with the same pipeline of real observations, obtaining a set of simulated events for which both the Hillas parameters and the physical properties are known. These serve as the base to model the relation between the image parameters and the sought physical quantities. Regular MAGIC observations rely on a standard set of pre-generated Monte-Carlo files. The highly non-standard analysis of pulsars required instead the production of special ad-hoc Monte-Carlo sets. I present the details of such numerical simulations in Section 4.10.

In the MAGIC data analysis pipeline, the correspondence between the Hillas parameters and the physical quantities is modeled by employing common machine learning procedures, such as the random forest (Breiman, 2001). I refer the reader to the relevant sections in Ishio (2020) for a detailed review on these procedures. At this stage, several programs introduce a cut condition on the *Size* (cfr. Section 4.3) of an event, requesting a minimum total charge of 50 PhE. In the scope of the analysis of standard trigger data, this prevents non interesting and poorly reconstructed events to affect the physical modeling of the source. The Sum-Trigger-II (cfr. Section 2.5) and the special MaTaJu cleaning procedure (cfr. Section 4.2.1) greatly improve the performance of the MAGIC telescopes at energies lower than 100 GeV. The 50 PhE *Size* cut is not optimized for such low energy observations, and effectively rejects most of the genuine gamma-ray signal. For this reason, the *Size* cut has been disabled in the analysis of the Crab and Geminga pulsar observations.

² <https://www.iap.kit.edu/corsika/>

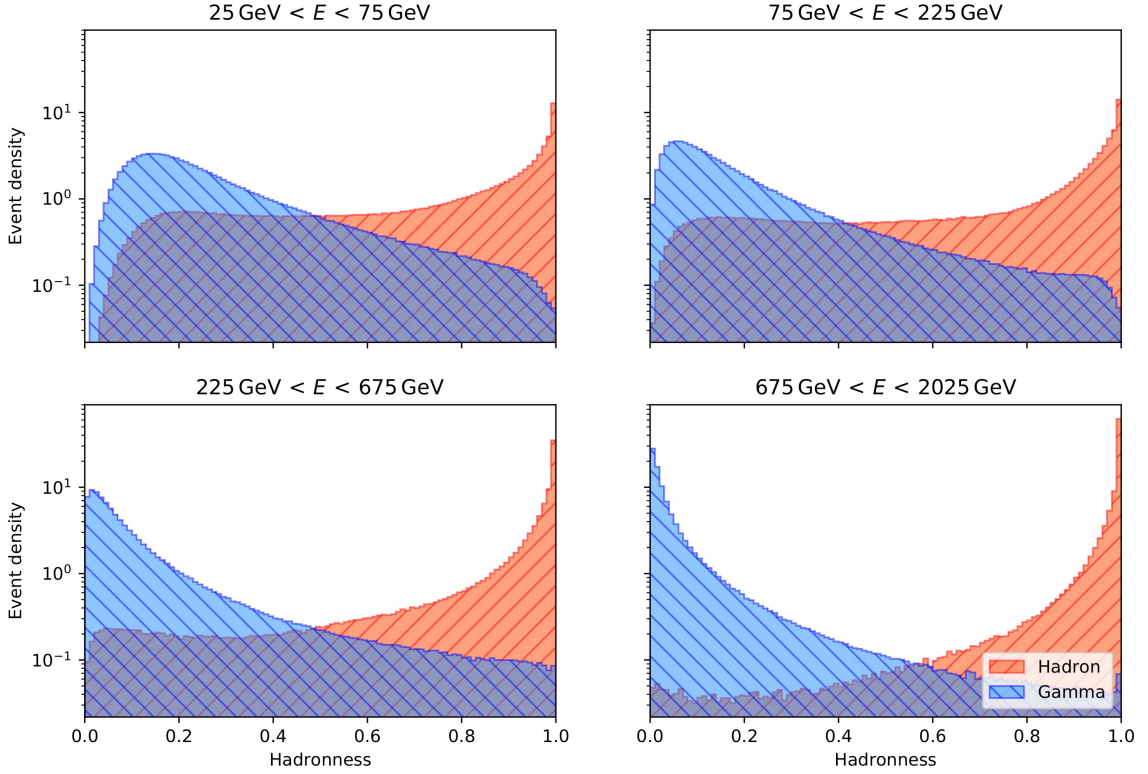


Figure 4.14: Comparison of the normalized hadronness distributions for gamma-rays (blue, simulation) and cosmic-rays (red, real events). The separation power degrades at lower energies. Gamma-rays were simulated with a spectral index $\Gamma = 1.6$, whereas the hadrons follow the cosmic-ray spectrum with $\Gamma \simeq 2.7$.

4.5.1 Gamma-Hadron separation

Cosmic-rays are the largest source of background for Cherenkov telescopes. Their flux can dominate the one of gamma-rays by several orders of magnitude, even for bright sources (Aleksić et al., 2016a). They are predominantly constituted by charged hadronic particles, with protons and ^4He nuclei being the most abundant species. The presence of nuclear interactions influences the development and the morphology of the air showers (cfr. Section 2.1). Hadronic events tend to produce wider showers, with electromagnetic sub-showers resulting from $\pi^0 \rightarrow 2\gamma$ decays. The charged pions decay predominantly in muons $\pi^\pm \rightarrow \mu^\pm + \nu_\mu$, which travel essentially unaffected through the atmosphere. The wavefront of their single Cherenkov cone produces images in the shape of arcs or rings (see Figure 4.3). These processes provide distinctive signatures for hadronic primary particles, and are key elements to identify them³. These features become progressively more vague as the energy is lowered and the Cherenkov images become smaller and dimmer. This results in a difficulty to distinguish cosmic-rays and gamma-rays at the lower energies. In the MAGIC analysis pipeline, samples of simulated gamma-ray events and real cosmic-ray ones are used to train a random forest classifier. The cosmic-ray

³ The number of muons produced in electromagnetic showers, via spallation of air nuclei, becomes significant above 10 TeV.

sample is derived from *off observations* in a part of the sky with no gamma-ray emission. The random forest is trained on a subset of the Hillas parameters (cfr. Section 4.3). Key ones are the *Length* and *Width* (shape parameters), and the *Size* and the *Impact parameter* (total Cherenkov light emitted). The *Maximum height* and *Time Gradient* (interaction cross-section) are also considered. The resulting classifier attributes to each event a value of *hadronness* h , ranging from zero to one. Such quantity provides a global estimate of how much an event resembles a gamma ($h = 0$) or cosmic-ray ($h = 1$) induced one. For the Crab and Geminga pulsar observations, dedicated gamma-ray simulations were employed to train the hadronness classifier (cfr. Section 4.10). A large hadron sample was obtained from ad-hoc observations in a region close to the pulsars and with roughly the same declination. Figure 4.14 presents the distribution of hadronness for gamma and hadronic showers, in four logarithmic energy bins. As expected, the separation power decays progressively when lowering the energy. Below 100 GeV, the distribution for gammas develops a large bias towards higher hadronness values. This is a consequence of the inherent difficulty to distinguish the two classes of events, given the small and granular images that they both produce at those energies. The hadronness is one of the major variables employed in the event selection process. An energy-dependent cut on hadronness, with a determined gamma-ray efficiency, is commonly employed to suppress the contribution from background cosmic rays (cfr. Section 4.7.1).

4.5.2 Stereo-DISP direction reconstruction

The accuracy of the direction reconstruction (cfr. Section 4.3.1) can be significantly improved by means of a machine learning approach, the *stereo-DISP* method. This is based on a procedure originally developed for single-telescope observations (Saito and Sitarek, 2009), where only a single image per event is available. Using simulated gamma-ray events, a random forest is trained to estimate the angular displacement *DISP* between the shower core position and the projected incoming direction. The latter is assumed to lay along the major axis of the shower. Figure 4.15 presents a typical situation with a 50 GeV simulated gamma-ray. The leading Hillas parameters used to determine *DISP* are the *Impact parameter*, the *Length*, and the *Time Gradient* along the main image axis. The timing information alone does not suffice to discriminate the shower propagation direction, as the observed time development of a shower may be reversed (cfr. Section 2.1). As a result, once a *DISP* value has been attributed to an event, two possible incoming directions along its image axis can still be considered. In stereoscopic observations, two images per event are available and help to solve this ambiguity. The correct incoming directions for each of the images are identified as the closest pair among the four possible couples (see Figure 4.15). The final stereo-*DISP* estimate is obtained as the average of the two mono-determined directions. Depending on the viewing geometry of the event, the stereo-*DISP* method may substantially outperform the crossing-point one. This is the case for distant impacting near parallel shower images, in which a small fluctuation on the determined shower axis can substantially shift the crossing point (see Figure 4.15). In such cases, the stereo-*DISP* method is automatically used instead of the crossing point one. In order to reject poorly reconstructed events, the standard analysis pipeline introduces an event cut on the angular distance between the two mono-*DISP* positions. Events in which these are further apart than an upper bound Δ_{\max} are regarded as badly

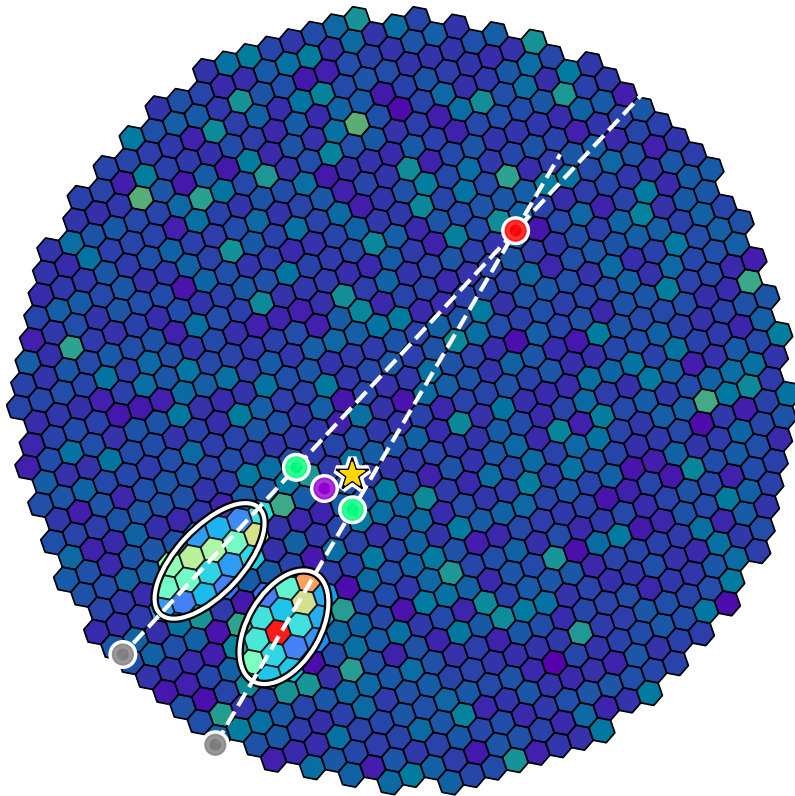


Figure 4.15: Sketch of the *DISP* method for a 50 GeV simulated gamma. A poor estimation of the shower axis in one of these nearly parallel images brings the crossing point very far from the true source position. The event is recovered by using the average direction of the mono-estimated *DISP* directions. **Golden star:** projection in the camera of the true incoming direction. **Red dot:** reconstructed direction from the crossing point of the shower axes. **Green dots:** *DISP*-determined directions for each of the two telescopes. **Purple dot:** the stereo-*DISP* determination as the average of the previous two. **Gray dots:** “ghost” positions (same *DISP*, wrong shower side) for both images. This low-energy event would have been discarded with the standard $\Delta_{\max}^2 \leq 0.05$ cut.

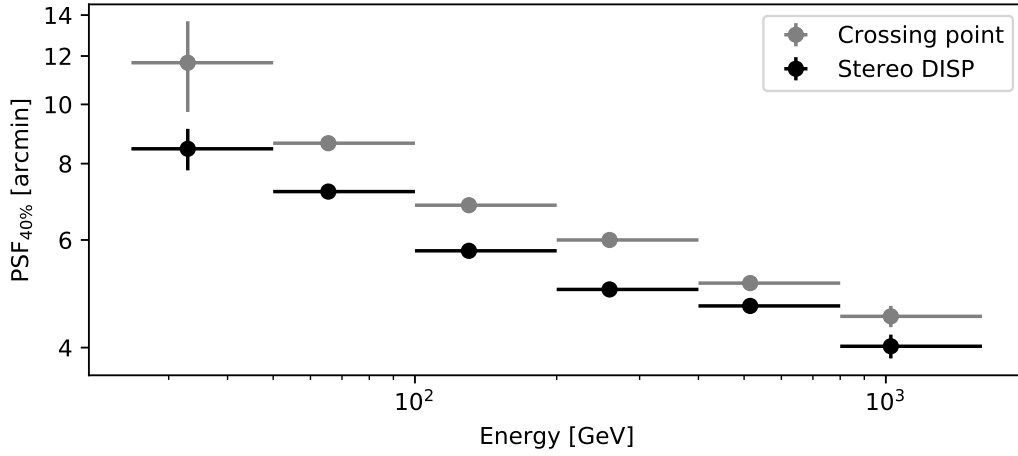


Figure 4.16: Energy evolution of the MAGIC point spread function for gamma rays, defined as the σ of a bi-dimensional Gaussian ($\sim 40\%$ containment radius). The values were determined with Crab Nebula observations. The errors bars of the two series of points are highly correlated.

reconstructed and rejected from the analysis. The standard threshold $\Delta_{\max}^2 = 0.05 \text{ deg}^2$ gives a maximum angular distance of 0.22 deg , which corresponds to two pixels in the focal plane of the camera. Such value was found to be too restrictive for the lowest energy showers, where both the *DISP* and the crossing-point determined positions may be affected by large uncertainties, due to the lack of detail in the faint shower image. The cut value was relaxed in the analysis of low-energy pulsar data, and set to $\Delta_{\max}^2 \approx 0.2 \text{ deg}^2$. This increases the allowed range of direction mismatch by a factor 2, corresponding to a maximum angular distance of 0.45 deg , or 12% of the MAGIC camera diameter. The value was optimized on low-energy Monte-Carlo gamma-ray data. Figure 4.16 presents the extension of the point spread function of MAGIC, determined with observations of the Crab Nebula, for both the line-crossing and the stereo-*DISP* method. The latter generally improves the direction reconstruction, reaching a $\sim 30\%$ figure at energies below 50 GeV . This proves to be important even for point-like sources like pulsars. A larger spread of the events prompts for the need to enlarge the signal area, increasing the integrated background. The 30% improvement of the stereo-*DISP* method effectively allows to reduce the integrated angular acceptance by 50% , suppressing background cosmic events by the same amount.

4.5.3 Energy Estimation

A measurement of the energy of the incoming gamma-rays allows to assess the spectral energy distribution of the source and its emission mechanisms. As such, its estimate is a task of primary importance. In this and the next sections, the terms *estimated* energy E_{est} and *true* energy E_{true} of an event refer to the value reconstructed by the analysis chain and to real one, respectively. These may differ substantially, as a consequence of the inherent stochastic nature of air showers (cfr. Section 2.1), the amount of light reaching the telescopes, and the fluctuations in the light detection. Events with the same true energy randomly produce showers with different Hillas parameters, which reflect in the energy

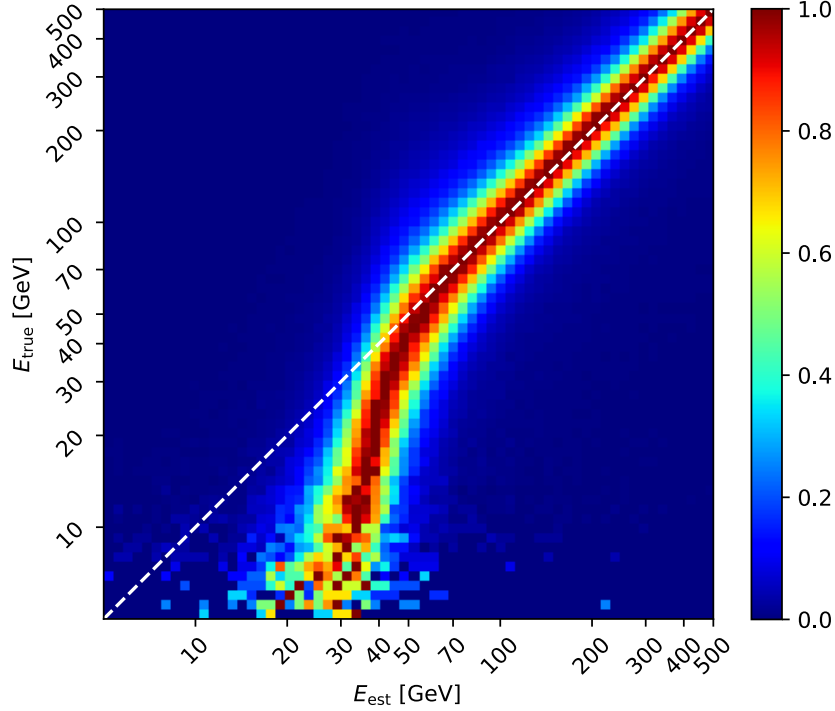


Figure 4.17: Energy *migration matrix* for the look-up table estimation method. The plot is normalized so that each horizontal slice (distribution of E_{est} for a given E_{true}) peaks at 1. The fuzziness at $E_{\text{true}} < 10$ GeV is caused by the reduction of the Monte-Carlo statistics. Events with a zenith distance $\zeta < 30$ deg were used to produce the plot.

estimate. The true energy of a single observed event is an inaccessible unknown. The energy is roughly proportional to the number of radiated Cherenkov photons. Therefore, the *Size* parameter of an event roughly represents a measurement of its energy. Cherenkov telescopes only capture a fraction of the whole Cherenkov light produced in a shower. It follows that the viewing geometry of an event also strongly affects the energy estimation. In the MAGIC analysis pipeline, two different energy estimation methods exist. The first one is based on the construction of a look-up table for the E_{true} of Monte-Carlo events. These are binned based on their *Size* and *Impact* parameters, and second order corrections are applied to the table for the telescope pointing conditions. The resulting partition of the parameter space is used to attribute an estimated energy E_{est} to the events being analyzed. The second strategy involves a random forest estimator, similarly trained on a set of simulated gamma-ray events. This novel method allows to improve the energy bias and resolution over a wide energy range (Ishio, 2020). Both methods rely on the availability of a large sample of Monte-Carlo events (cfr. Section 4.10). In the analysis of the Crab and Geminga pulsars, both strategies were employed and used to cross-check each other.

Figure 4.17 presents the relation between E_{true} and E_{est} as a bi-dimensional histogram, the *migration matrix*. This is obtained by applying the energy estimator on a second set of Monte-Carlo events, independent from the one used to train it. At the lowest energies,

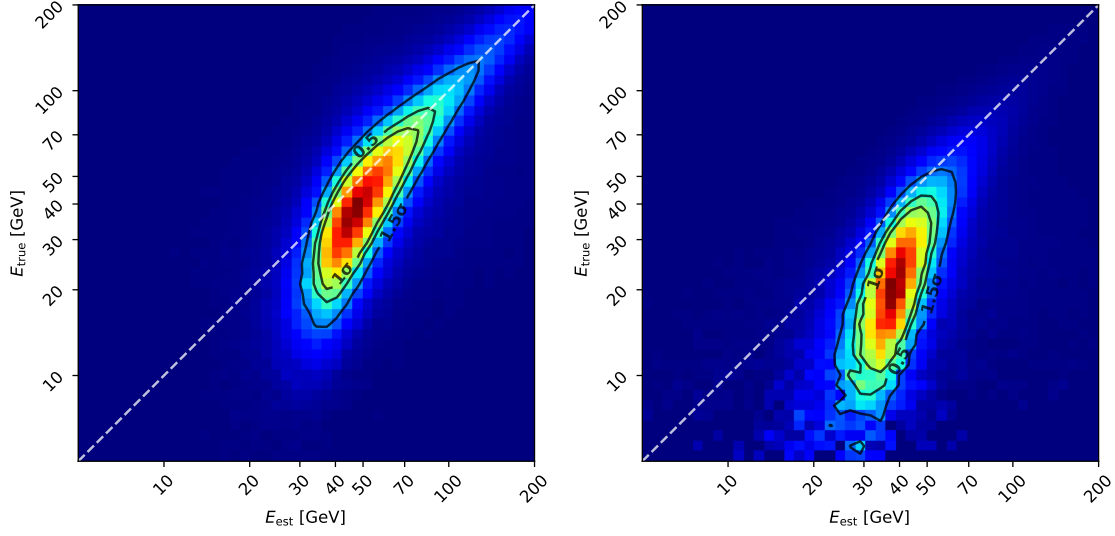


Figure 4.18: Migration of events for power-law spectra with a spectral index $\Gamma = 3.2$ (Crab pulsar, P2, left) and $\Gamma = 5.2$ (Geminga, P2, right).

the estimator develops a positive bias, and the correspondence between E_{true} and E_{est} is lost. This extensively affects events at $E_{\text{true}} \leq 50$ GeV, which are largely attributed an $E_{\text{est}} \geq 30$ GeV. This is a form of Eddington bias related to the *energy spillover*, the effect of the superposition integral between the energy resolution of the instrument and the shape of the underlying spectrum. The bias at $E_{\text{true}} \leq 50$ GeV is caused by the obvious enhancement in the detection efficiency for low energy events which are affected by an upward fluctuation of the number of Cherenkov photons. These events effectively mimic larger energy ones, biasing their energy estimation. It follows that the spectrum of soft sources below 50 GeV can not be produced by naively accumulating the number of recorded events in bins of E_{est} (cfr. Section 4.8). An accurate determination of the spectrum requires a proper analysis and correction of the spillover. The task is equivalent to the de-convolution of the instrument response function to the observed event counts. Such a technique is known as *energy unfolding* and requires an estimate of the inverse of the migration matrix (cfr. Section 4.8.3).

Figure 4.18 presents the effect of energy spillover for two power-law spectra, with spectral indices $\Gamma = 3.2$ and $\Gamma = 5.2$, respectively. These were chosen to resemble the *Fermi*-LAT spectra of the Crab and Geminga pulsars, extrapolated at energies larger than 10 GeV. For the Crab, approximately 90% of the events are mapped in the estimated energy region larger than $E_{\text{est}} = 30$ GeV. This reduces to $E_{\text{est}} = 25$ GeV for the softer Geminga. In situations in which a cut on the energy of the single events is desired, such as for the production of phaseograms (cfr. Section 1.4), these values have been taken as the minimum considered E_{est} . Integration below them enhances the background of cosmic rays and poorly reconstructed events with a minimal contribution to the signal. A full optimization of the such cut value depends on the exact spectral shape and signal to noise ratio of the source, and has not been attempted. I stress how these cuts in E_{est} do not effectively reflect the lowest true energies E_{true} of the cut data sample.

4.6 Pulsar Phases

The absolute time tag which each MAGIC event carries (Section 2.4.1) allows to select the events in terms of pulsar phase (cfr. Section 1.4). This enhances greatly the detection capability for pulsars, as a large fraction of the background events can be removed based on their timing. Since the rotational frequency changes with time as a result of energy loss, an accurate model for the rotation is needed, commonly referred to as a *pulsar ephemeris*. For the Crab pulsar, ephemerides are obtained with monitoring campaigns of several radio-telescopes in the world, and made publicly available by the Jodrell Bank Radio Observatory⁴ (Lyne et al., 1993). Unlike the Crab, Geminga is a radio-quiet pulsar and no updated public ephemeris exist. In Appendix A I present the methods that were employed to obtain an ephemeris valid for the whole span of Geminga MAGIC data, using public *Fermi*-LAT gamma-ray observations to infer the rotational model.

The ephemeris is used to model the pulsar rotation with time. However, data taken at different locations on Earth or at different times will suffer from several systematic effects, making a direct comparison among them meaningless. This happens as a result of the exceptional stability of pulsars as time references, so that time delays related to the varying geometry of the observation, but also special and general relativistic ones, become relevant. The arrival times of the events need to be corrected for these effects before generating any phaseogram. In order to do so, it is useful to refer them to the reference frame of the barycenter of the solar system. This is the best approximation for an inertial reference frame available in the immediate proximity of the Earth. By transforming the times of arrival of the photons in the solar system barycenter frame, one removes non-inertial effects that would otherwise be present in references anchored to a specific celestial body⁵. The transformation is non trivial and can be decomposed in the sum of several different timing delay components:

- **Rømer delay** — Geometrical timing effect due to the orbital motion of the Earth and its rotation. It is simply equal to the additional light travel time (in a flat space-time) needed by the pulsar photons to reach the observatory, depending on its position in the solar system. It has a characteristic magnitude of $1 \text{ AU}/c \approx 500 \text{ s}$. It is named after the fifteenth century Dutch astronomer who used a similar notion with the periods of the moons of Jupiter to produce the first measurement of the speed of light.
- **Einstein delay** — Under this name are grouped special and general relativistic effects related to the motion of the observer. These include the Doppler time dilation and the gravitational redshift due to larger solar system bodies. Their combined effect varies across the year and has an order of magnitude of 1 ms. It is worth to note that these effects strongly depend on the position of the pulsar with respect to the orbital plane of the Earth (as in stellar aberration). An imprecise measurement of the pulsar coordinates affects the Einstein delay and becomes promptly visible as an annual modulation of the phase drift of the pulsar. This is

⁴ <http://www.jb.man.ac.uk/~pulsar/crab.html>

⁵ If the pulsar is in a binary system further corrections need to be applied, and the natural choice for an inertial frame is the barycenter of the binary system.

important for pulsars without a strong radio or optical counterpart, for which the positional error is large, such as the radio quiet Geminga. In its case, the problem is further aggravated by the large proper motion, which also needs to be accounted.

- **Shapiro delay** — A general relativistic time delay observed in the coordinate time of the observer due to the non Euclidean metric of the solar system, which is better approximated by the Schwarzschild metric of the Sun. Since null geodesics that pass close to a massive object are not straight Euclidean lines, a delay in the photon arrival times develops with respect to those predicted with a Minkowskian metric. The effect was originally calculated in Shapiro (1964) and proved experimentally with radio echos from the planet Venus at superior conjunction to provide a strong independent confirmation of the theory of General Relativity (Shapiro et al., 1971). The one-way effect from an object outside the solar system can reach a magnitude of $120 \mu\text{s}$ if the object is seen close to the limb of the Sun. This is particularly relevant for radio observations of the Crab pulsar, as it lays at an ecliptic latitude $b \simeq -1.3$ deg and the Sun passes very close to it in June.

A deep discussion of these effects can be found in Backer and Hellings (1986). The computation of the various delays depends on the position of the Earth and other solar system bodies (solar system ephemerides), and on varying relations among different universal time references.

4.6.1 MAGIC TEMPO2 plugin

In order to compute ‘barycentered’ times, I employed the TEMPO2 package⁶, which is a de-facto standard for pulsar timing research. Several details on the actual implementation of the timing corrections being applied can be found in Hobbs et al. (2006) and Edwards et al. (2006). The program consists of a core C routine that computes the barycentered arrival times and the pulsar phases, and of several plugins, used to read and manipulate the data. These plugins are mostly aimed at radio observations. In order to process MAGIC data, a TEMPO2 plugin had been written, based on an similar one for *Fermi*–LAT data. Such plugin already existed, but suffered of several bugs and a poor computational performance. During the span of my doctoral project, I extensively updated and maintained the TEMPO2 plugin. This resulted in a net improvement of the reliability of the program, and a reduction of its average runtime by a factor of two. Several actions have been taken to accomplish such improvements:

- The TEMPO2 core routine allocates pulsar time of arrival objects (“observations” in the code documentation) on a C-style variable length array. Their maximum number is limited by the size of the stack of the machine, typically 8 MB on a modern 64 bit system. This is of no concern for the workflow of radio observations, as a radio times of arrival are computed from a small number of hour-scale observations. On the contrary, gamma-ray pulsation require long integration times to be detected, with observations spanning several months. This imposes to attribute a phase to each single gamma-ray event, including the background ones, and to only produce a phaseogram after each event time has been barycentered. The MAGIC TEMPO2

⁶ <https://bitbucket.org/psrsoft/tempo2>

plugin was unable to process some MAGIC data files with a large number of events. It underwent a stack overflow and was forcefully terminated without throwing an exception, and producing inconsistent results. The input/output management of the plugin was rewritten to subdivide files in several data chunks with fewer events. These are processed in parallel by TEMPO2. As the core routine sets a hard-coded limit on both the number of data chunks and the number of events in each of them, a warning is issued to the user if the fraction of stack memory to be allocated is excessive. The issue has been signaled to the TEMPO2 developers.

- The MAGIC TEMPO2 plugin uses several temporary files (TIM files) to store the times of arrival of the events to be analyzed, processes them, and finally writes the barycentered times back to the original file. When processing a large number of files in parallel, the number of such TIM files can become very large. These temporary files were named after a short random sequence of ASCII characters. With several parallel instances of the plugin launched at the same time, and the usage of a poor random number generator, there was a non negligible chance that two of them tried to create or edit the same TIM file at once. This resulted in all the events for the particular chunk of data represented by that file to be identically attributed the phase $\varphi = 0$. As typical pulsar phase regions are defined to have a pulse at $\varphi = 0$, this created a fake excess exactly where emission was expected, invalidating the measurement. I solved this serious flaw by replacing the pseudo-randomly generated ASCII pattern with a unique identifier based on the name of the input file.
- The TEMPO2 core routine requires the first time of arrival in a chunk of data to be a reference time, with respect to which all remaining phases are computed. The original implementation accomplished this by inserting such reference at the expense of the last event in the chunk, which was later recovered by replacing the second event with it and running the whole barycentering procedure again. This very inefficient algorithm effectively calculated the phases for every event twice. It was fixed, reducing the run time of the MAGIC plugin by a factor of 2.
- Bugs were found in the core TEMPO2 routine as well. In particular a new version of the header of an Earth position ephemeris (monthly updated), caused the software to load random text characters in place of numerical coefficients needed to calculate the position of the Earth in the Solar System. This caused unpredictable results, ranging from segmentation violation to seemingly normal execution, albeit with completely inconsistent results. The bug was notified to the TEMPO2 maintainers and fixed in a new version of the program.
- Several patches needed to be written to be able to compile and install the software on modern machines. Relevant comments have been added to the code to help the user understand and debug it.

The updated MAGIC TEMPO2 plugin was made available to the whole MAGIC Collaboration, together with scripts that automatize its installation.

4.7 Source Detection

The gamma-ray signal sought by Cherenkov telescopes is dominated by the background cosmic-ray events. This is true for any steady source and at every energy range. The detection of an object and its study can only proceed in a statistical sense, by measuring the *excess* of the gamma-ray events over the expected background counts. This requires the selection of an *on region*, to be used to measure the signal, and a *background region*, where the cosmic-ray contribution is estimated. Such regions may be defined in any of those event variables whose distribution is supposed to be peaked for gamma-rays, and instead uniform for the background cosmic-rays. As the latter ones are isotropic, a common choice is to select the background region from a position in the sky close to the source of interest, but without sensible gamma-ray emission. The wobble observation strategy employed by MAGIC (cfr. Section 2.6) aims at making such selection easily available without the need of dedicated off-target observations. The *significance* of a detection \mathbb{S} is characterized as the probability that a signal equal or larger than the measured one is produced by the random fluctuations of the background. It is typically reported as the number of standard deviations σ of a normal distribution that correspond to an analogous (two-sided) p-value. This is calculated with the Li and Ma (1983) formula:

$$\mathbb{S}^2 = 2N_{\text{on}} \log \left[\frac{1 + \alpha}{\alpha} \cdot \frac{N_{\text{on}}}{N_{\text{on}} + N_{\text{bkg}}} \right] + 2N_{\text{bkg}} \log \left[(1 + \alpha) \cdot \frac{N_{\text{bkg}}}{N_{\text{on}} + N_{\text{bkg}}} \right], \quad (4.2)$$

where N_{on} and N_{bkg} are the number of counts in the signal and background regions, respectively, and α is the ratio between their exposures (e.g. angular size, integration time). As in other branches of Physics, it is customary to assume a source to be detected when the significance exceeds the conventional threshold of 5σ ($p \approx 5.7 \cdot 10^{-7}$). In order to enhance the signal to noise ratio and make a detection more feasible, events can be selected based on their properties. However, to avoid a bias in doing so, the criteria of such selection must be determined on an independent data set, an applied equally both to the signal and background regions.

4.7.1 Event selection

In order to suppress the cosmic-ray background and improve the signal to noise ratio, events were selected based on their hadronness h value (cfr. Section 4.5.1). Since the distribution of h changes with energy, the cut condition was chosen in an energy-dependent way, making use of Monte-Carlo gamma-ray events, finely binned in E_{est} . The *gamma-ray efficiency* ε_γ for a cut is defined as the ratio of the number of simulated gamma-rays passing it over the initial total: $\varepsilon_\gamma = N_{<h}/N$. Cuts were optimized so that the gamma-ray efficiency was always at least 90% in every energy bin. The probability that a true gamma ray is rejected, due to its hadronness being larger than the cut value, is 10%. The same cut condition has been applied to the background events.

The Crab and Geminga pulsars are point-like sources, and their position is known from observations at other wavelengths. This allows to further improve the event selection exploiting the θ^2 value (cfr. Section 4.3.1) with respect to the predicted source position. The energy-dependent optimization of such θ^2 cut is analogous to the hadronness one,

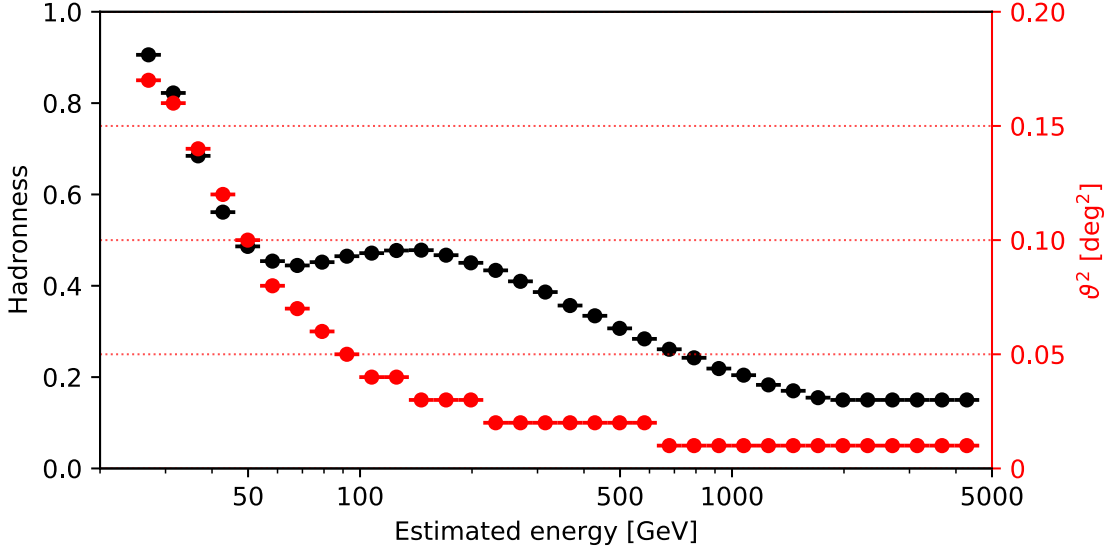


Figure 4.19: Energy dependent hadronness (black) and θ^2 (red) cuts, optimized for gamma-ray efficiencies of 90% and 75%, respectively. The loose $\theta \geq 0.3$ deg cut at energies below 50 GeV affects the feasibility of the standard background estimation methods.

and follows it. A θ^2 gamma-ray efficiency of $\varepsilon_\gamma = 75\%$ has been selected, approximately corresponding to 1.7 times the point spread function of MAGIC. The total gamma-ray efficiency of the combined energy-dependent hadronness and θ^2 cuts is $\sim 68\%$. The resulting reduction in the number of collected gamma-rays is largely over-compensated by the improvement of the signal to noise ratio. The global efficiency parameter, the effective area A_{eff} (cfr. Section 4.8.2), accounts for such reduction before the computation of the spectra.

Figure 4.19 presents the energy-dependence of the hadronness and θ^2 cuts. At the lower energies, large values are required to keep the selected gamma-ray efficiency. This is a consequence of the difficulty to properly reconstruct the particle type and incoming direction of low-energy events. In particular, the directional cut exceeds $\theta = 0.3$ deg at $E_{\text{est}} = 50$ GeV and approaches $\theta = 0.4$ deg at $E_{\text{est}} = 30$ GeV, more than 10% of the whole MAGIC camera. As $w = 0.4$ deg is the standard MAGIC wobble depth, this hinders the applicability of common background estimation methods for the lowest energy events (see the next Section 4.7.2). This does not apply to pulsar observations, in which the background region is selected in the event phase space (temporal selection), rather than in their angular distribution. Large θ^2 cut values represent instead an issue for the analysis of the nebular component of the Crab (see Section 5.4.2). For this reason, the production of spectra for the Crab nebula has followed a separate pipeline that the pulsar one. In the former one, a limit to the maximum cut at $\theta_{\text{max}}^2 = 0.09$ deg has been set. This ensures the availability of a proper background region, but further reduces the gamma-ray efficiency for the nebula at the lowest energies.

4.7.2 Standard background estimation

The availability of a proper background estimation is fundamental for an accurate determination of the gamma-ray excess. In standard MAGIC observations of non-pulsed and point-like sources, background estimation regions are defined in the two-dimensional space of the incoming particle direction. This is possible because of the isotropy of cosmic-rays. The wobble observation strategy (cfr. Section 2.6) allows to select such regions without taking dedicated background observations. Two different estimate methods are commonly employed (see Figure 4.20, top).

In the *off from wobble partner* strategy, the background is estimated in the same camera position occupied by the source, but at a delayed time. Wobble directions are always arranged in symmetric pairs with respect to the source position, so that if a wobble pointing $W1$ with bearing ω is used, an opposed position $W2$ with bearing $\omega + 180$ deg is also present. This allows to select the background for a region of $W1$ from the same region in the partner wobble $W2$. In this way, possible systematic effects resulting from efficiency inhomogeneities in the camera are reduced. However, systematics due to the non simultaneity of the background estimate are enhanced.

Conversely, a *simultaneous off* method has also being developed. In it, the background is estimated at the same time as the signal, from the position in the camera which is opposed to the source. In this method, several additional background regions can be defined to improve the background statistics. These are arranged in a ring around the pointing position. As opposed to the previous scenario, in the simultaneous off case the systematic effects due to time differences are suppressed, but possible camera efficiency inhomogeneities become more important. These largely arise due to presence of only two telescopes in the MAGIC system, so that the trigger efficiency in the camera of each of them is enhanced in the direction of the other one. To assess this issue, simultaneous off regions are accompanied by a normalization ring, extending outside of them. The exposures of each background region are scaled to the signal one before the subtraction, using the ratios of the counts in the respective normalization rings. The maximum number of simultaneous off regions is limited by the angular size of the signal region (θ^2 cut) and by the requirement for suitable sized normalization rings.

Both the wobble-partner and simultaneous methods deliver compatible results, in the limit of large observation times and good wobble direction coverage. However, residual systematic uncertainties due to the background estimation can affect the flux reconstruction up to several percent points of the background. This is one of the major contribution to the systematic uncertainties of IACT observations. For this reason, the MAGIC analysis pipeline introduces a safety criterion for the detection of a source, requiring its measured excess to be at least 5% of the estimated background. The detection significance of weak non-pulsed sources that do not fulfill such condition can not be assessed with Formula 4.2, that relies on statistical uncertainties only.

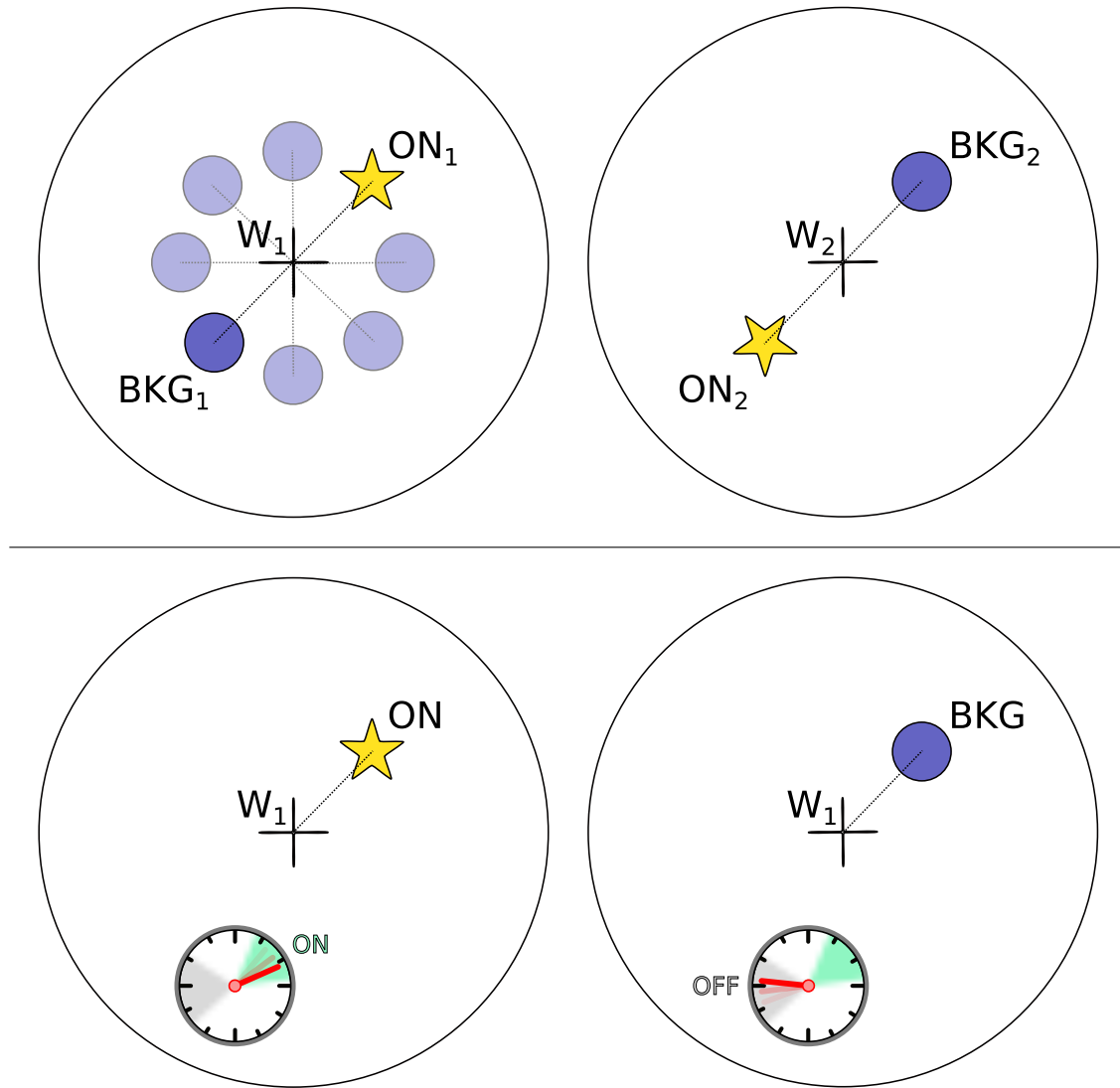


Figure 4.20: Background estimation strategies for wobble observations of a point source (star). **(Top)** Methods for non-pulsed sources. In the *wobble partner* mode, BKG₂ in wobble W_2 is taken as background for region ON₁ in wobble W_1 (and vice-versa). Signal and background share the same position in the camera, but are taken at different times. Conversely, in the *simultaneous off* mode, BKG₁ is used for ON₁, and additional background regions arranged in a ring can be used as well. The background estimate is simultaneous but from a different position in the camera. **(Bottom)** *Pulsar mode*. The background is taken from the same position as the signal, and in the very same wobble, during the off-pulse phase (represented by the clock). It is both simultaneous and from the same region in the camera, effectively removing systematics inherent to the other background estimate modes.

Geminga			Crab		
Region	Range	Size	Region	Range	Size
P1	0.056–0.161	0.105	P1	-0.017–0.026	0.043
P2	0.550–0.642	0.092	P2	0.377–0.422	0.045
OFF	0.700–0.950	0.250	OFF	0.520–0.870	0.350

Table 4.3: Signal and background regions for the Geminga pulsar, determined as described in the text.

4.7.3 Pulsar background

The previous considerations do not generally apply to pulsars, due to the additional information of the event phase (see Sections 1.4 and 4.6). This allows to define the signal and background regions in the time domain, as intervals of phase, rather than clusters of incoming directions of the events (see Figure 4.20, bottom). Since pulsar periods (< 1 s) are much shorter than the characteristic timescale for systematic variations $\gtrsim 1$ min, this method guarantees an estimate of the background which is both simultaneous and at the same position in the camera. The systematic uncertainties which affect the non-pulsed background estimation methods are effectively canceled. As a result, the largest uncertainty contribution to pulsar excesses is purely statistical, and Formula 4.2 for the detection significance may be used even without the safety criterion. Employing a phase selection of the background obviously prevents the estimate of the non-pulsed component of the source, which is present at all phases. In the case of the Crab, this allows to disentangle the pulsar component from the larger nebular one. The general applicability of the method depends on the pulse profile of the pulsar being studied, and on the effective presence of an off-pulse phase interval. Both the Crab and Geminga pulsars have low pulsed duty cycles $\eta < 0.5$ in the considered energy range and satisfy such requirement. The pulsar observations were taken in any case in wobble mode, so that they can be used to study the emission of the Crab nebula, and search for extended Geminga emission.

In the case of Geminga, to prevent a bias in the choice of the signal and background regions, these were determined on *Fermi*-LAT data in the neighboring energy band between 1 GeV and 15 GeV, and applied blindly to the MAGIC data. Figure 4.21 shows the Phaseograms obtained from ~ 11.2 a of *Fermi*-LAT data on the Geminga pulsar. Its two were fitted with an asymmetric Gaussian function, with different values of σ_L and σ_R on the left and right side:

$$f(x, \mu, \sigma_L, \sigma_R) = A_0 \exp \left\{ \begin{array}{l} -\frac{1}{2} \left(\frac{x-\mu}{\sigma_L} \right)^2, \quad x \leq \mu \\ -\frac{1}{2} \left(\frac{x-\mu}{\sigma_R} \right)^2, \quad x \geq \mu \end{array} \right\} \quad (4.3)$$

Signal regions were determined as the 95% containment interval of such distributions, corresponding to $\mu_{-2\sigma_L}^{+2\sigma_R}$. The off region was chosen to lie 5σ away from both peaks, and in the interval between P2 and P1, where no bridge emission is expected. The regions determined in this way are reported in Table 4.3. It is evident from the diagrams of Figure

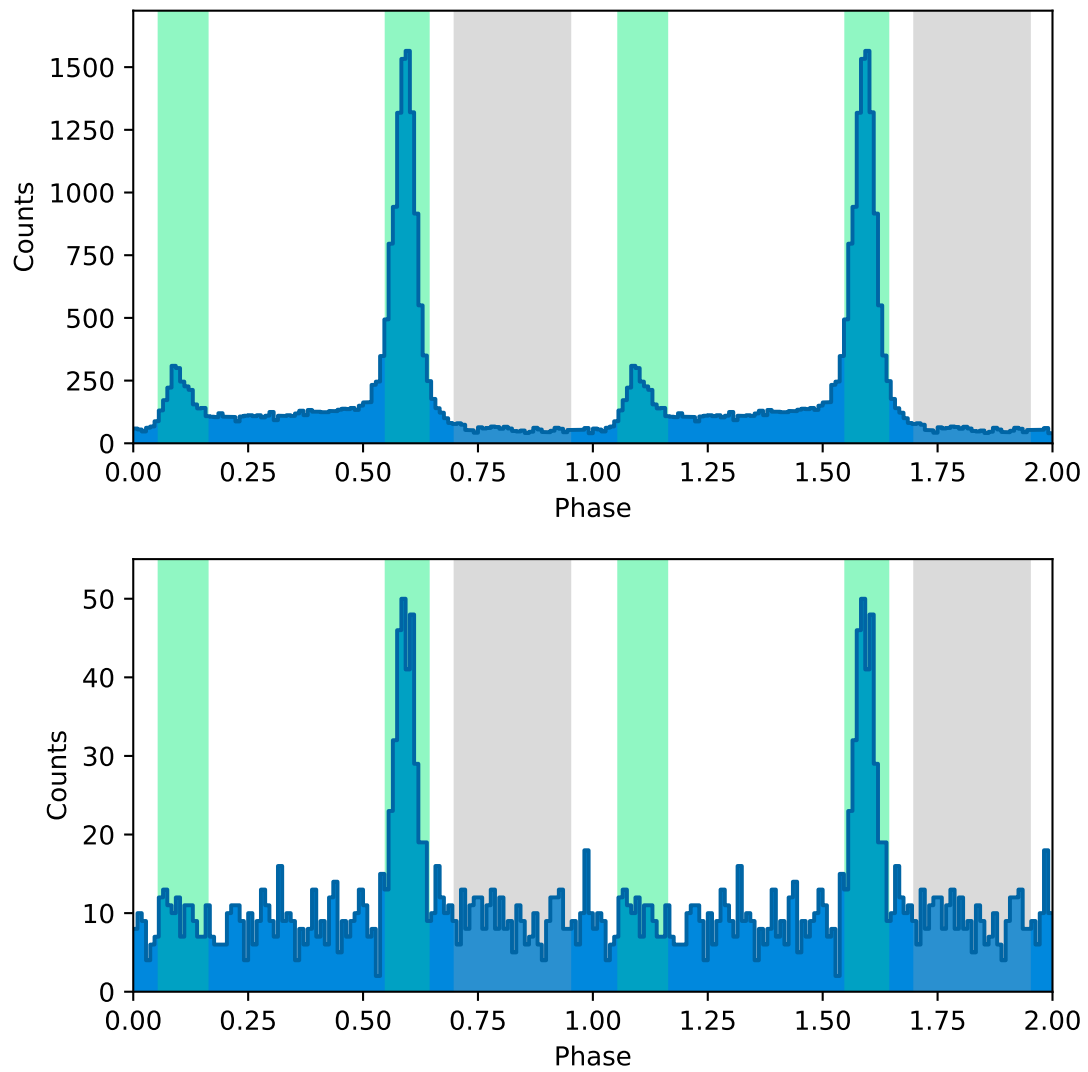


Figure 4.21: Phaseograms of *Fermi*-LAT Geminga data, integrating an observation period of approximately 11.2 years, for energies above 5 GeV (top) and 15 GeV (bottom). These were used to determine the on and off regions (in green and gray shaded color, respectively) for the P1 and P2 pulses (cfr. Table 4.3).

4.21 that the P1 pulse of Geminga is practically absent at energies above 15 GeV. A similar decreasing trend, with the P1/P2 ratio progressively reducing as energy increases, has been observed in the Crab pulsar as well (cfr. Section 5.3). For this reason, the MAGIC observations of the pulsed emission of Geminga, presented in Chapter 6, concentrated on the P2 pulse. The count number and statistics for P1 are reported for completeness, but have not been considered in the calculation of the detection significance. For the Crab pulsar, the same regions used in previous MAGIC publications have been chosen Ahnen et al. (2016). This allows a direct comparison with previously published results.

4.8 Spectra

By measuring the differential flux $\mathcal{F}(E)$ of a source, or equivalently its spectral energy distribution (SED), it is possible to infer information on the gamma-ray emission mechanisms (cfr. Section 1.3). As the emission spans a vast range of energies, it is more useful to define the differential flux and spectral energy distributions in logarithmic energy intervals:

$$\begin{aligned} \text{Diff. Flux} &= \frac{dN}{d \log(E) dA dt} = E \mathcal{F}(E) \\ \text{SED} &= \frac{EdN}{d \log(E) dA dt} = E^2 \mathcal{F}(E) \end{aligned}$$

Their determination requires the estimation of the number of gamma-rays N detected in a certain logarithmic energy range per unit time t and unit area A . Since pulsars are point-like sources, the dependence solid angle of incoming directions Ω is omitted. The number of detected gamma-rays is measured as the excess over the background level (cfr. Section 4.7) in logarithmic bins of estimated energy E_{est} (cfr. Section 4.5.3). This provides an estimate of $dN/d \log(E)$. To obtain the differential flux, the *effective time* t_{eff} of the observations and the *effective area* A_{eff} must be calculated.

4.8.1 Effective Time

The MAGIC readout chain (cfr. Section 2.4) introduces a small dead time per triggered event, $t_d \simeq 26 \mu\text{s}$. With a typical Sum-Trigger-II stereoscopic trigger rate of 600 Hz, this corresponds to an average loss of 1.5% of the duty cycle. The effective observation time t_{eff} is calculated by means of a fit of the distribution of the time interval between two following triggers. For $t_d = 0$, and assuming a constant trigger rate λ , this would follow an exponential law. In presence of $t_d \neq 0$, such distribution rigidly shifts to larger times, allowing the value of $t_d \neq 0$ to be fit as a parameter. Such elapsed time between a trigger and the previous one is registered as an independent information for each event. This is because at this point in the analysis process several events have already been discarded (for instance, all those that did not survive the image cleaning). This renders the direct comparison between the arrival times of two successive events useless. Once t_d is known, the effective observation time is obtained from the observed one with $t_{\text{eff}} = t_{\text{osb}}/(1 + \lambda t_d)$. Since the trigger rate λ may also vary during the observation, effective times are computed for slices of 20 s, and summed up at the end. The reader is referred to Wittek (2002) for a review on the implementation of the method in the MAGIC spectrum estimation program *flute*.

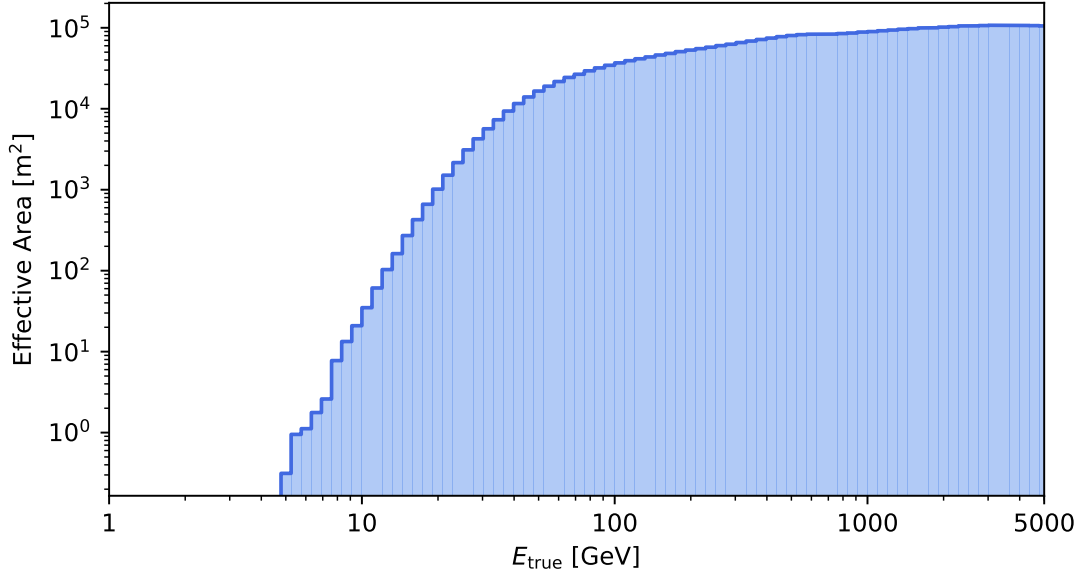


Figure 4.22: Effective area A_{eff} as a function of the true event energy E_{true} , after the whole analysis chain. A rapid turnover is present at energies below 100 GeV.

4.8.2 Effective Area

The *effective area* A_{eff} represents the total collection area of the MAGIC system for gamma-rays, corrected for the efficiency of the analysis pipeline. It is different from the physical area of the telescope mirrors ($A_{\text{mir}} \approx 240 \text{ m}^2$). This is because Cherenkov light can trigger an event even if the primary particle does not directly impact on the reflector. Both the maximum impact parameter producing a detectable event and the collection efficiency ε_{col} as a function of it depend on the energy of the gamma-ray, and on the pointing position of the telescopes. The collection area A_{col} is the integral of such efficiency for all possible impact parameters I :

$$A_{\text{col}}(E, \zeta, \dots) = \int_0^{2\pi} d\vartheta \int_0^{+\infty} \varepsilon_{\text{col}}(I, \vartheta, E, \zeta, \dots) I dI, \quad (4.4)$$

where the polar coordinates (I, ϑ) map the plane perpendicular to the incoming direction and passing by the telescopes, and the collection efficiency ε_{col} depends on the energy E , zenith distance ζ , and possibly on other observation parameters⁷. Such quantity is estimated employing a large set of gamma-ray Monte-Carlo simulations, with a uniform bi-dimensional distribution of impact parameters (cfr. Section 4.10). The maximum impact parameter I_{max} of such simulation must be chosen so that the residual tail of ε_{col} beyond it is negligible. For the MAGIC altitude of 2200 m above sea level, a value of $I_{\text{max}} = 370 \text{ m}$ meets such requirement. The collection area A_{col} is then obtained as the ratio of events that triggered MAGIC over the total simulated ones, multiplied by πI_{max}^2 .

⁷ In case of observations of extended sources, the effective angular acceptance of the telescopes shall be modeled as well, and a further dependence on Ω is required.

In low zenith distance observations, it has a typical value of $A_{\text{col}} \simeq 10^5 \text{ m}^2$ for energies larger than 100 GeV, and falls rapidly when lower energies are considered. In order to determine the flux, it is also necessary to assess the contribution of the efficiency of the analysis pipeline (e.g. image cleaning and parametrization). To this respect, it is not relevant to distinguish the collection efficiency ε_{col} from the total post-analysis efficiency ε . The effective collection area A_{eff} of the whole analysis chain is obtained by replacing ε_{col} with ε in Formula 4.4. It acts as a global efficiency parameter, including also the contribution of the analysis chain. It can be estimated from the fraction of Monte-Carlo events that survive the whole analysis pipeline, when processed exactly as the data (including the event selection cuts, cfr. Section 4.7.1):

$$A_{\text{eff}}(E, \zeta, \dots) = \frac{N_{\text{sur}}(E, \zeta, \dots)}{N(E, \zeta, \dots)} \cdot \pi J_{\text{max}}^2. \quad (4.5)$$

In the MAGIC analysis chain, A_{eff} is computed in fine logarithmic bins of E_{true} and zenith distance ζ . The estimate of A_{eff} is a critical passage for the generation of the spectrum. An under- or overestimate of the effective area promptly translates in an up- and down-scaling of the computed fluxes, respectively. Energies at the extremes of the MAGIC sensitivity window are potentially more affected by such systematic effects, as the low number of recorded events N_{sur} introduces a large fluctuation in Formula 4.5. For this reason, for the pulsar analyses, it was necessary to employ much larger Monte-Carlo sets than with regular MAGIC observations (see Section 4.10). The uncertainty on the effective area estimation is propagated to the final flux values.

4.8.3 Unfolding

The difference between the estimated energy E_{est} of the events and their true energy E_{true} needs to be properly accounted upon the generation of the spectra (cfr. Section 4.5.3). This can be done with two complementary approaches, *forward folding* and *unfolding*.

Forward folding

In the forward folding approach, a pre-defined intrinsic functional form is assumed to describe the spectrum. This can be written as $\mathcal{F}(E) = a(E, \vartheta)$, where ϑ is a vector of the model parameters. As a typical example, a power-law relation $\mathcal{F}(E) = f_0(E/E_0)^{-\Gamma}$ can be assumed, with the pre-factor f_0 and the spectral index Γ being its parameters. The spectral shape is multiplied by the energy-dependent effective area A_{eff} and the effective time t_{eff} , and further convolved with the migration matrix (cfr. Section 4.5.3) to obtain a model of the counts in bins of estimated energy E_{est} . This is the so-called *folding* procedure. The folded model is fit to the real data, typically with a maximum Likelihood approach, obtaining a set of correlated best-fit parameters ϑ_{ML} . Likelihood ratio tests can be employed to test if a model is better at representing the spectrum than another one, provided that these are nested. This method is widely employed in the analysis chain of several gamma-ray instruments, such as *Fermi*-LAT. If the spectral shape of the data is already known, it is the most natural way to obtain an estimate for its parameters. On the other hand, it depends on such assumed spectrum, and does not deliver a set of spectral points as an output.

Reverse unfolding

The unfolding approach is opposite to the forward folding one. The procedure takes the observed counts in bins of E_{est} as an input, and tries to unfold the contribution of the migration matrix, accounting for the energy dispersion. The resulting event counts, in bins of E_{true} , can be divided by A_{eff} and t_{eff} to obtain a series of correlated unfolded spectral points. The task is analogous to a deconvolution problem and shares its typical issues. The migration matrix is, in general, non-invertible, or it may not even be square. Small fluctuations of the off-diagonal terms may result in large variations of the unfolded spectral points. The task configures itself as a classical linear inverse problem. It requires regularization procedures such as those widely employed in applied mathematics for the treatment of ill-posed problems. In the MAGIC analysis pipeline, common regularization procedures are available, such as the one of Bertero (1989), Schmelling (1994), and Tikhonov (1963). It is customary to run several of these, in order to cross-check the correctness of the reconstructed spectrum. Depending on the counts in several E_{est} bins, each unfolded spectral point is correlated with the other ones. Their statistical uncertainties are usually reported as a standard 1σ error bar. However, a whole correlation matrix \mathcal{S} is required to properly fit a spectral model to them. Such correlation matrix is also provided as an output by the unfolding program. Further details on the implementation of the reverse unfolding procedure are available in Aliu and Wittek (2006). Interested readers may find a mathematical review of the unfolding process in Wittek (2006).

Because of their complementarity, in the final spectra presented in Sections 6.4 and 5.4 both strategies were employed. Reverse unfolding with the Tikhonov regularization was used to obtain the spectral points and their correlation matrix. This was further used for the joint spectral fits with *Fermi*–LAT data (cfr. Section 6.5). The forward folding approach was instead employed to determine the parameters of the fitted spectral models. These were simple power-law relations for Geminga and the Crab pulsar components, and a log parabola for the Crab Nebula.

4.8.4 Lightcurves

Possible variabilities in the flux of a source can be assessed by producing a *lightcurve* for it. This is a time dependent measurement of the integral flux in a given energy range. Variabilities in the very high energy band are often measured for active galactic nuclei and gamma-ray binaries. In the high-energy band, at energies between 100 MeV and 1 GeV, flares have been detected from the Crab nebula by AGILE and *Fermi*–LAT (cfr. Section 1.5.4). As part of my doctoral project, I produced a search for a possible variability in the very-high energy emission of the Crab pulsar, to be connected with the nebular flares (cfr. Section 5.5). These Crab pulsar lightcurves are distinct from the phaseograms (cfr. Section 5.3), which are also sometimes referred to as “lightcurves”.

The production of a single integral flux measurement, a point of the lightcurve, follows the same procedure described for spectra. A large estimated energy range is selected, and the excess counts in it are converted to an integral flux measurement (number of events per unit area, per unit time) dividing it by the effective time t_{eff} and effective area A_{eff} , and

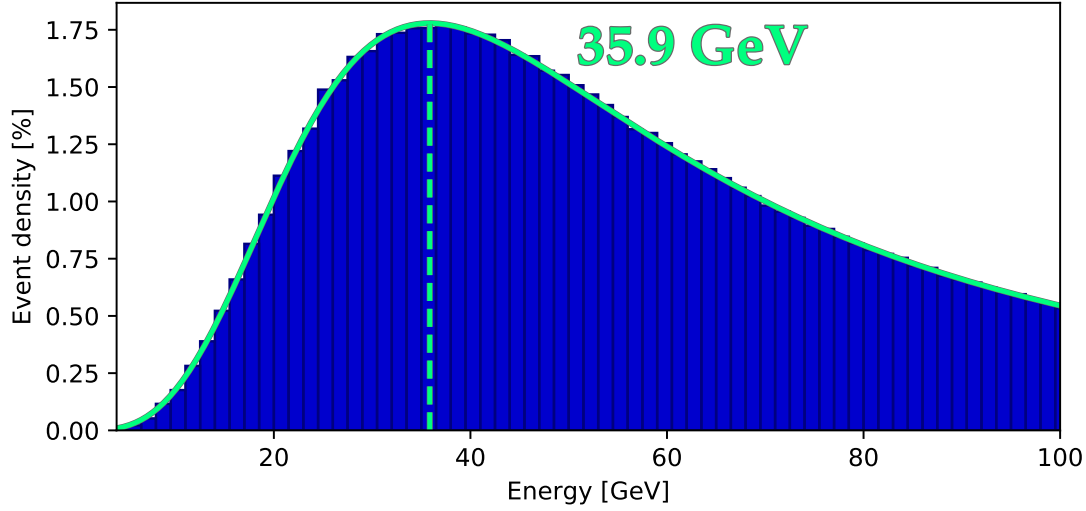


Figure 4.23: Normalized true energy distribution for Monte-Carlo events analyzed with the pipeline presented in this chapter, for a power-law spectrum with spectral index $\Gamma = 2.6$. An energy threshold of $E_{\text{thr}} = 36$ GeV is achieved for this spectral shape.

applying a correction for the event spillover. I introduced a modification in the standard MAGIC flux estimation program, `flute`, to allow lightcurves to be computed for pulsars as well. A common quantity employed to measure the variability of a lightcurve is its *normalized excess variance*:

$$\sigma_{NXS}^2 = \frac{\sigma^2 - \langle \sigma_{\mathcal{F},i}^2 \rangle}{\langle \mathcal{F} \rangle^2}, \quad (4.6)$$

where σ^2 is the variance of the lightcurve, $\langle \sigma_{\mathcal{F},i}^2 \rangle$ is the average squared error of each point in it, and $\langle \mathcal{F} \rangle$ is the mean flux value. The excess variance measures the relative dispersion of the data with respect to a constant, accounting for the additional contribution of the statistical uncertainties of each measurements. In literature, its square root, $F_{\text{var}} = \sigma_{NXS}$, the *fractional variation*, is often employed to characterize how variable a lightcurve is. In situations in which the statistical uncertainties $\langle \sigma_{\mathcal{F},i}^2 \rangle$ dominate the measurement, as for the Crab pulsar, the excess variance may be negative. Because of this, in Section 5.5 I used σ_{NXS}^2 and not F_{var} as a test statistic for variability.

4.9 Analysis threshold

In the scope of the validation of an analysis, it is useful to investigate how its efficiency at different energies affects the excess counts from a particular source. This can be assessed by multiplying the effective area A_{eff} of the analysis (cfr. Section 4.8.2) with the intrinsic spectrum of the object $\mathcal{F}(E)$. The resulting curve represents a model for the differential event rate $dN/(dE dt)$ from that source. Depending on the spectral shape, the peak energy of such distribution shifts. Such peak is commonly referred to as the *energy threshold* of the analysis for that particular source. Below the threshold, the distribution steeply falls off. This rendering flux measurements below the threshold prone to large

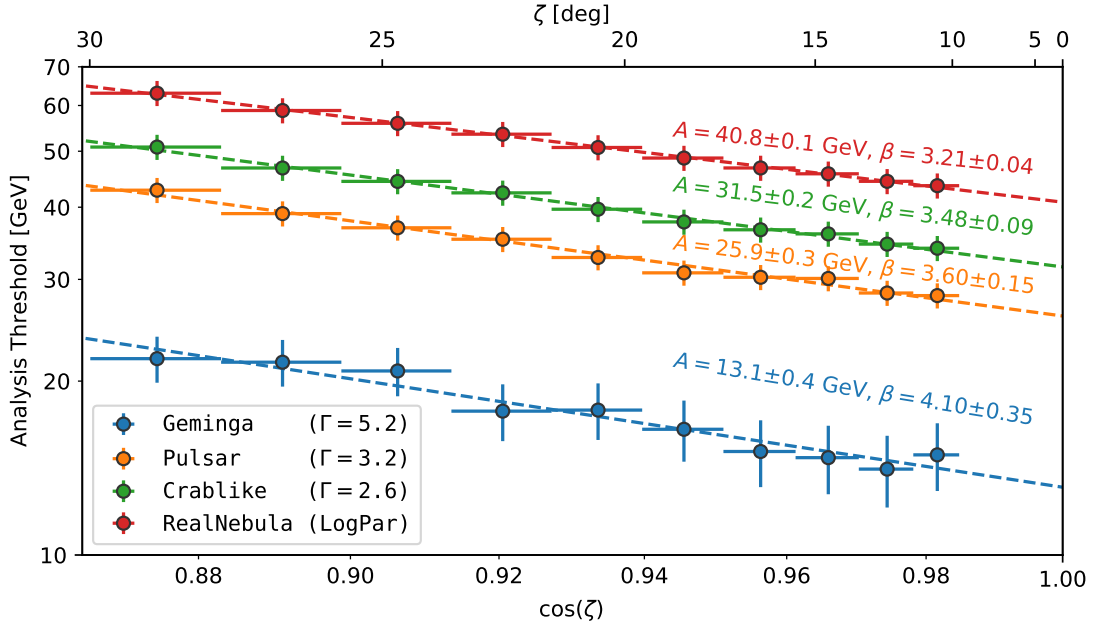


Figure 4.24: Energy threshold variation with the zenith distance ζ of the observations, for several possible spectral sources. The threshold increases with ζ due to the atmospheric absorption. The variation has been modeled as a power-law relation $E_{\text{THR}} = A \cos(\zeta)^{-\beta}$ (dashed lines).

systematic uncertainties. The value of the analysis threshold can be estimated by plotting a histogram of the true energies E_{true} of Monte-Carlo events processed as the real data. Different spectral shapes can be simulated, by re-weighting each event with an energy dependent weight function $w(E)$, defined as:

$$w(E) = \mathcal{F}(E)/\mathcal{F}_{\text{MC}}(E),$$

where \mathcal{F}_{MC} is the simulated spectrum of the Monte-Carlo events, typically a power-law relation. Figure 4.23 presents such a histogram for a power-law spectrum with a spectral index $\Gamma = 2.6$, the average slope of the Crab nebula. For this spectral shape, an energy threshold $E_{\text{thr}} \approx 36$ GeV is found. The energy threshold depends on the observing conditions as well. The atmospheric absorption at larger zenith distances ζ raises the energy threshold, for all spectral shapes. Figure 4.24 illustrates the dependency of the energy threshold on ζ for a set of spectral shapes. Power-law spectra corresponding to the P2 emission of Geminga and the Crab pulsar are represented, as well as the average power-law spectrum of the Crab nebula, and a more realistic model using a log parabola. The dependency on ζ is stronger for softer sources, and needs to be taken into account in observation proposals. Both the Crab and Geminga pulsars culminate at a very low ζ at the MAGIC site, $\zeta_{\text{min}}^{\text{C}} = 6.5$ deg, and $\zeta_{\text{min}}^{\text{G}} = 10.5$ deg, respectively. The observations were restricted in the $\zeta < 25$ deg zone, to exploit the lowest possible energy threshold (cfr. Sections 6.1 and 5.1).

	Code	ζ [deg]	E [GeV]	ρ Ev.	N ^o Events	Aim
Geminga	8	10 – 30	5 – 500	2^{12}	$4.01 \cdot 10^6$	RF
	9	10 – 30	5 – 500	$7 \cdot 2^{12}$	$2.78 \cdot 10^8$	
	10	10 – 30	500 – 5000	1652	$1.61 \cdot 10^6$	
	11	10 – 30	5 – 500	2^{16}	$6.41 \cdot 10^7$	A_{eff}
	13	10 – 30	500 – 5000	3305	$3.23 \cdot 10^6$	
	12	10 – 30	5 – 500	2^{16}	$6.41 \cdot 10^7$	A_{eff}
14	10 – 30	500 – 5000	3305	$3.23 \cdot 10^6$		
	16	10 – 30	1 – 20	10^5	$9.78 \cdot 10^7$	Test
Crab	15	5 – 10	5 – 500	2^{16}	$4.17 \cdot 10^7$	A_{eff}
	17	5 – 30	5 – 500	2^{14}	$1.83 \cdot 10^7$	RF

Table 4.4: List of the Monte-Carlo simulations produced for the pulsar data analysis. The table reports the defining production code, the zenith distance ζ and energy E ranges, the event density ρ per production bin ($0.5 \times 0.5 \text{ deg}^2$), the total number of produced events and the primary aim. *RF*: the simulation was used to train the random forest and look-up tables; A_{eff} : the simulation was used to estimate the effective area. The extremely low-energy test sample 16 was not employed for the analysis. Rows grouped together indicate Monte-Carlo files which produce a smooth power-law spectrum when used together. The spectral index for all simulation was fixed at $\Gamma = 1.6$.

4.10 Tailored Monte-Carlo simulations

Several steps of the analysis chain require the usage of Monte-Carlo simulations of gamma-rays showers. Standard MAGIC analyses commonly rely on generic sets of such simulations, which are adapted from case to case to the particular analysis chain being used. The exceptional nature of the low-energy Sum-Trigger analysis required instead ad-hoc simulation. I produced them employing the large computing cluster of the Max-Planck-Institute computing and data facility⁸, in Garching, and the LST-1 IT Cluster on La Palma. It is beyond the scope of this thesis to discuss the implementation of the numerical simulations. The reader is addressed to Sobczynska (2002), Moralejo (2003) and Blanch and Moralejo (2004) for a review on them. Besides the obvious replacement of the standard trigger with the Sum-Trigger-II, several other aspects were tuned to provide reliable estimates at the lowest energies. They are summarized in the next paragraphs. The parameters for each of the Monte-Carlo productions are given in Table 4.4.

⁸ MPCDF: <https://www.mpcdf.mpg.de/>

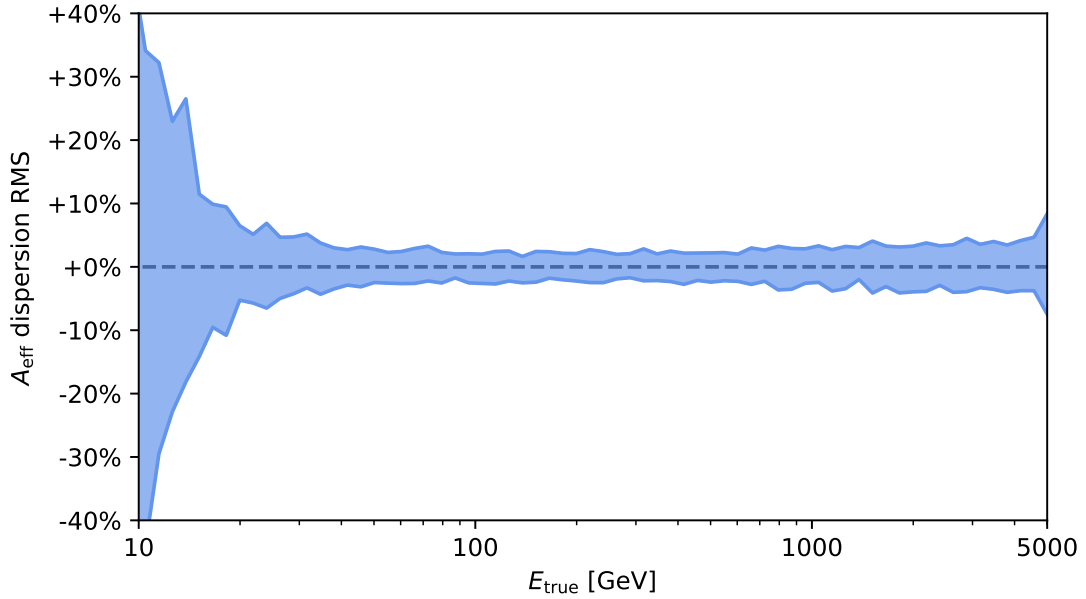


Figure 4.25: Relative dispersion of the effective area caused by a low-statistic Monte-Carlo ($2.5 \cdot 10^6$ events, the standard size in MAGIC). The colored band represents the 1σ region for the fluctuations around the average. Obtained by bootstrapping samples from a larger Monte-Carlo set ($1.35 \cdot 10^8$ events, production codes 11+12+13+14 in Table 4.4).

Enhanced statistics

A large number of events is required to accurately model the low effective area A_{eff} at energies $E_{\text{true}} < 50$ GeV, and to overcome the detrimental effect of the statistical uncertainties. Figure 4.25 presents the effect on the usage of a low-statistics Monte-Carlo simulation on the estimate of the effective area. It was produced with the *bootstrapping* technique: several independent samples with reduced statistics ($2.5 \cdot 10^6$ events) were drawn from the larger set of the full Monte-Carlo production ($1.35 \cdot 10^8$ events). Such samples were used to calculate the dispersion caused by the low statistics on the effective area estimate. This is displayed in the plot as a 1σ confidence band for the relative fluctuations. At $E_{\text{true}} = 15$ GeV, the threshold for the Geminga pulsar analysis, a low-statistic simulation can induce a $\pm 15\%$ fluctuation in the value effective area. The enhanced statistics allows to suppress such fluctuations. An inaccurate value of the effective area promptly translates into a miscalculation of the source fluxes. In Figure 4.26 a similar effect is displayed for the migration matrix of the analysis. Employing a low-statistic Monte-Carlo affects the capability to sufficiently reconstruct the lowest energy events. The lack of proper statistics causes small fluctuations to dominate the matrix at $E_{\text{true}} < 20$ GeV, effectively rendering any unfolding or forward folding procedure meaningless. This is further worsened by the poor performance of the energy estimators, when these trained with an insufficient number of low-energy events. The usage of a vast set of Monte-Carlo files has a bad impact on the computational performance of the analysis. Nevertheless, it proved to be essential for the reconstruction of the pulsar spectra.

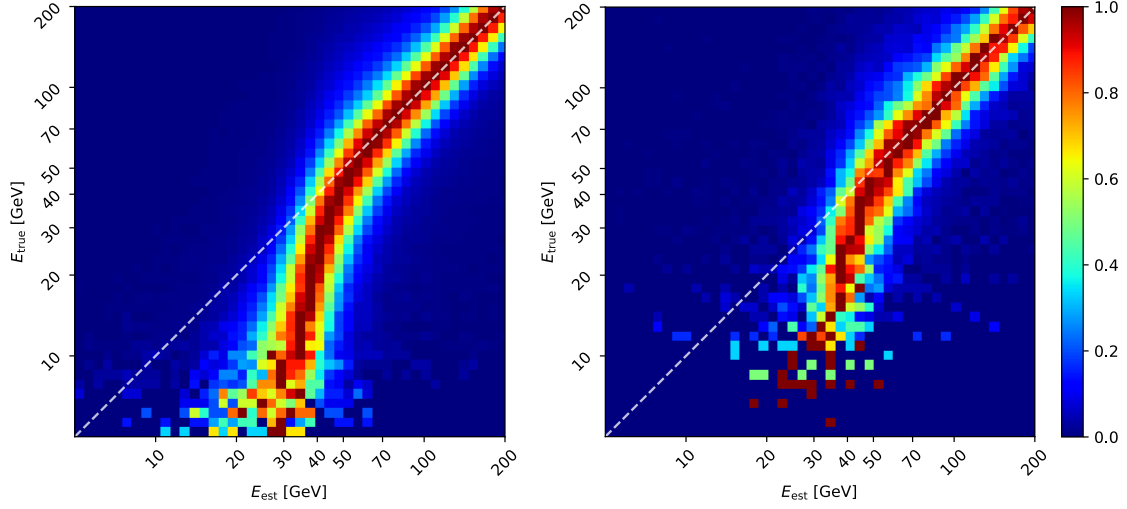


Figure 4.26: Comparison between migration matrices obtained with a large (left, $1.35 \cdot 10^8$ events) Monte-Carlo set, and a standard-sized one (right, $2.5 \cdot 10^6$ events).

Source path in the sky

The special simulations were *tailored* for Geminga and the Crab pulsar. This means that the simulated telescope pointing was chosen to match the apparent motion of the source in the night sky, when viewed from La Palma. As most observations were taken at zenith distances below 15 deg, the density of simulated events was increased in that region. This was done by dividing the observable sky in bins of $0.5 \times 0.5 \text{ deg}^2$ in the space of zenith distance ζ and azimuth α . Such binning ensures that the density of events scales as $\csc \zeta$. The bins intercepted by the path of the object were selected, and so were all their direct neighbors. Bins bordering at least two of such first order neighbors were also considered. The resulting selection (see Figure 4.27) consists of a stripe centered on the path in the sky of the source, with an average transverse width of 1.7 deg. This corresponds roughly to half of the field of view of the MAGIC cameras. Upon calculating the fluxes, the relative amount of simulated events in a certain ζ bin was re-weighted to match exactly the ζ distribution of the data.

Bright stars

In Section 4.4, I presented the issues arising from the presence of bright stars in the field of view. Circular exclusion zones were cut in the MAGIC camera around the stars to limit their effects. Such blind regions affect the effective area of the observations. This has been reproduced in the Monte-Carlo simulations to obtain a reliable model of A_{eff} . In the real data, the position of the exclusion hole varies with the observation time. This is because the MAGIC telescopes track celestial objects with alt-azimuthal motions, causing a field rotation during the observations. Objects in the field of view appear to follow circular arcs in the camera, centered on the pointing position. The apparent angular velocity of such field rotation depends on the pointing coordinates. For objects passing close to the zenith, it is maximum at the culmination. In the simulation, such behavior has been simplified, and the position of the star was fixed. The radius of the exclusion circle R and

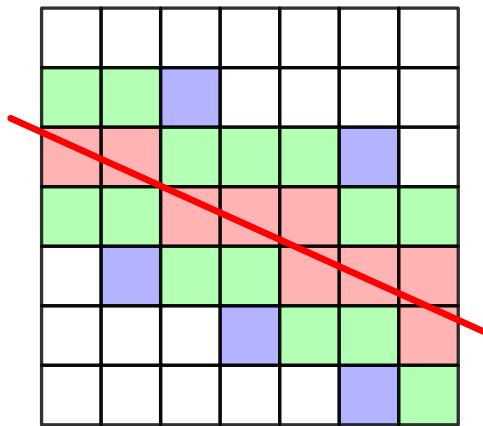


Figure 4.27: Scheme for the selection of the bins to be simulated for the source-tailored Monte-Carlo. The zenith distance - azimuth space is divided in small bins with a side of 0.5 deg. The apparent source track in the sky (red line) intercepts a subset of these bins (red shaded), which are considered for the simulation. Their first neighbors (green shaded) are also added to the selection. The further addition of diagonal first neighbors (blue shaded) ensures a more uniform coverage. The stripe is centered on the path of the source with an average width of 1.7 deg.

its radial distance d from the pointing position (cfr. Figure 4.13) were set as in the real observations. The exact position of the simulated hole was chosen so that the number of pixels masked by it was closest to the average number of pixels masked in the real data. The latter also varies during the observations, due to the field rotation. As three different exclusion zone configurations were used for Geminga, and one for the Crab pulsar, a total of four different branches of Monte-Carlo simulations were produced. Each of them mimics the data of a particular wobble position, and was used for the analysis of the data taken with it. The exclusion zones were not replicated in the Monte-Carlo simulations used to train the physical parameter classifiers (cfr. Section 4.5). This is because their inclusion could only marginally improve the performance for the events grazing the exclusion circle and leaking into it. As the number of such events is comparatively low, and they have a large probability to be rejected by the image cleaning, such marginal improvement was judged superfluous.



5

CRAB PULSAR

The Crab Nebula is considered the standard candle of very high energy astrophysics, and as such is the most studied object at these energies. The pulsar located at its center that powers the nebula is instead a more elusive object. It was detected for the first time at energies larger than 25 GeV in 2008 with mono observations of MAGIC and the prototype of the Sum-Trigger system, the Sum-Trigger-I (Aliu et al., 2008). Since then, measurements were refined multiple times by the MAGIC and VERITAS collaborations: see for instance Aleksić et al. (2014) and Aliu et al. (2015). Its pulsed emission was found to extend up to energies above 1 TeV (Ansoldi et al., 2016), which requires an Inverse Compton mechanism close to the light cylinder or just outside it to be explained.

Compared to the previous studies, the sound statistical basis harvested by the stereoscopic Sum-Trigger-II at energies above 25 GeV enables to study the long-term stability of the pulsed emission. This topic is of interest because a variability of the pulsar could be connected with the existence of flares of the nebula in the 100 MeV – 1 GeV range (cfr. Section 1.5.4). Such flares have been observed multiple times by the *Fermi*-LAT and AGILE¹ experiments (Tavani et al., 2011b; Abdo et al., 2011; Striani et al., 2013b) but their origin is still not well understood. A list of flares for which an ATEL² was issued either by the *Fermi*-LAT or AGILE collaborations was given in Table 1.1.

In this chapter, I present the results of the analysis of Crab pulsar data taken by the MAGIC telescopes with Sum-Trigger-II between 2018 and 2020. Section 5.1 gives some basic information about the observations. Section 5.2 presents a brief summary of the analysis techniques, which are treated more in detail in Chapter 4. The analysis is

¹ AGILE: <http://agile.rm.iasf.cnr.it/>

² Astronomer's Telegram: <http://www.astronomerstelegam.org/>

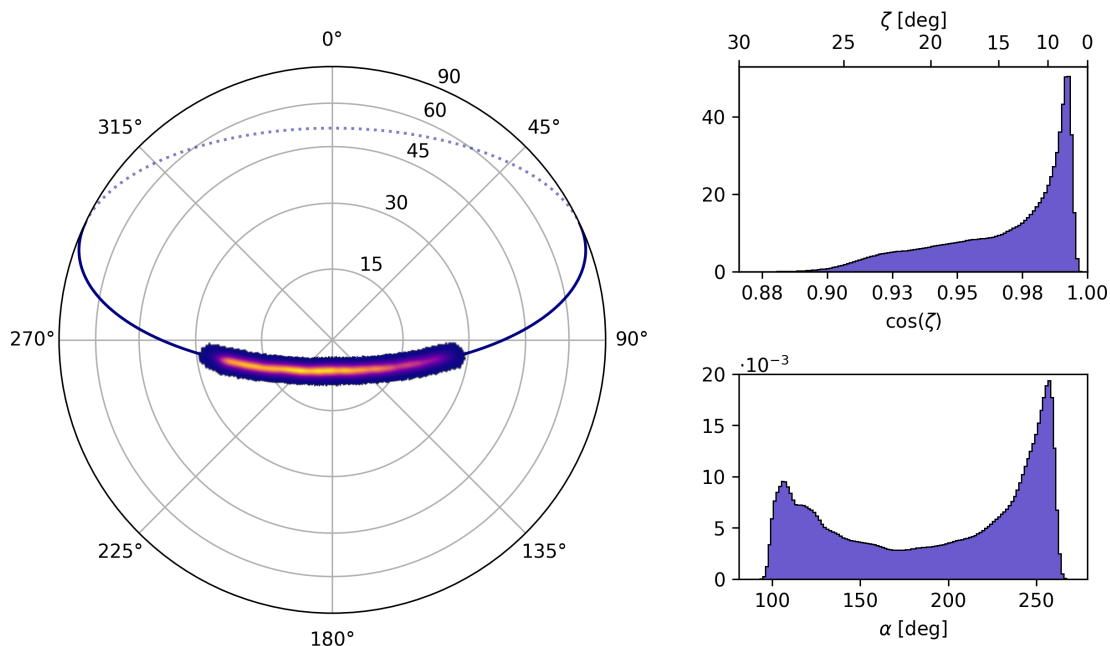


Figure 5.1: Density of the reconstructed directions of the events in the MAGIC Crab observations, in orthographic projection, with the Zenith distance (ZD) and Azimuth (AZ) distributions.

analogous to the one employed for the Geminga Pulsar (Section 6.2). Sections 5.3 and 5.4 present the phaseograms and the spectra of both the P1 and P2 components of the pulsed emission. The MAGIC spectra below 50 GeV are compared with space-borne measurements of *Fermi*-LAT and agree with them. The morphology of the pulses in phase and their change with varying energy are also investigated. The ratio of the emission of P1 over P2 is found to decrease with increasing energy, and so does the pulse width of each of the two components. In Section 5.5 the results on the long-term variability search of the pulsed component are presented. The emission is found to be stable in the range between 30 GeV and 200 GeV within the statistical uncertainties at timescales ranging from days to months. No major flare of the nebula occurred during the period of the observations, nor in the 5 months window given by the travel time of the relativistic wind from the pulsar to its termination shock in the nebula. Therefore, within the sensitivity limitations, these observations do not allow one to inquire a connection of the flares with the varying activity of the pulsar. The observations are used to validate the performance of the Sum-Trigger-II system and the feasibility of a further variability study with it.

5.1 Observations Overview

A total of 69.5 h of good-quality data were collected between September 2018 and February 2020 on the Crab pulsar and nebula. The fundamental parameters of the observations are given in Table 5.1, whereas the distribution of detected events in the sky is plotted in Figure 5.1. Because of the energy threshold variation with zenith distance ζ seen in

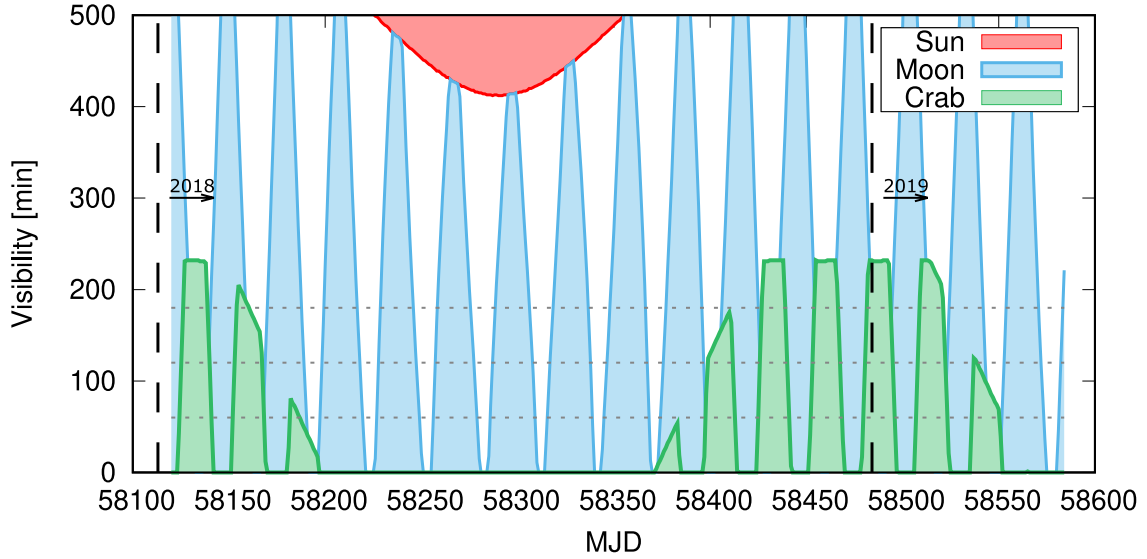


Figure 5.2: Nightly observability window of the Crab pulsar below $\zeta = 25$ deg for the year 2018 (green bands). Blue and red areas correspond to times during which the Moon and the Sun are above the horizon.

Section 4.9, observations were essentially limited to $\zeta < 25$ deg. The selection criteria were identical to the ones applied for the Geminga pulsar. When available, LIDAR measurements were used as a criterion to judge the quality of the data: observations with a transmission of light from an altitude of 9 km above ground level lower than 0.9 were discarded. Stereo trigger rates were required to be above 500 Hz for the whole observation, implying a minimum rate of Cherenkov events of roughly 320 Hz.

All observations were performed in wobble mode with just two wobble positions. These were chosen to be at the same distance from the bright star ζ Tauri (Tianguan), which has a visual magnitude of $m_V = 3.03$ (Ducati, 2002b). As a result, data of both pointing positions can be analyzed together, without the need of using separate Monte-Carlo samples. The parameters of the wobble positions are summarized in Table 4.2. The wobble observation mode allows to study the emission of the nebula too.

I requested that the observations were performed on a regular schedule. This was done with the intent to allow the monitoring of the pulsed emission at regular time intervals. Figure 5.2 shows the nightly observability intervals for the Crab pulsar; during full moon periods observations can not be performed. A simple observation scheme which enables the exploration of different variability time scales can be constructed by scheduling observations in three consecutive nights at the beginning and at the end of each window. In order to collect enough statistics to detect the pulsed emission, a minimum of 2 h of observations (3σ detection significance) per night is sufficient. Despite the efforts made to follow such schedule, varying weather conditions, and constraints by other projects and by targets of opportunity often reduced the nightly time available for the Crab observations. The impact of these effects is discussed in Section 5.5.2.

Date	MJD	T_{eff} [h]	$\langle L3 \rangle$ [Hz]	$\langle \cos \zeta \rangle$
2018/09/19	58380	0.65	530.48	0.92
2018/10/11	58402	1.29	573.43	0.97
2018/10/12	58403	1.94	573.89	0.97
2018/10/13	58404	1.94	555.94	0.97
2018/10/15	58406	1.29	555.53	0.99
2018/11/05	58427	1.94	581.14	0.98
2018/11/06	58428	1.61	574.52	0.98
2018/11/07	58429	2.18	556.55	0.98
2018/11/16	58438	1.81	575.12	0.97
2018/12/02	58454	2.48	602.39	0.98
2018/12/04	58456	0.97	604.09	0.99
2018/12/14	58466	3.23	570.08	0.97
2018/12/16	58468	1.29	593.23	0.96
2018/12/29	58481	1.42	588.28	0.99
2019/01/01	58484	2.58	604.69	0.98
2019/01/10	58493	2.26	604.87	0.98
2019/01/12	58495	1.62	603.76	0.97
2019/01/13	58496	0.59	600.89	0.94
2019/01/28	58511	2.89	623.93	0.97
2019/01/29	58512	2.90	628.95	0.97
2019/02/04	58518	2.44	620.99	0.97
Date	MJD	T_{eff} [h]	$\langle L3 \rangle$ [Hz]	$\langle \cos \zeta \rangle$
2019/02/05	58519	0.77	594.90	0.98
2019/02/24	58538	0.24	583.46	0.99
2019/02/25	58539	1.94	600.19	0.96
2019/02/26	58540	1.45	594.05	0.98
2019/02/27	58541	0.96	593.51	0.98
2019/11/23	58810	3.23	587.38	0.97
2019/11/24	58811	2.58	583.77	0.98
2019/11/25	58812	1.27	583.81	0.96
2019/11/26	58813	2.91	580.68	0.97
2019/11/28	58815	1.29	585.71	0.97
2019/11/30	58817	1.16	572.30	0.97
2019/12/01	58818	2.91	563.86	0.97
2019/12/04	58821	2.35	589.17	0.98
2019/12/22	58839	0.26	588.43	0.91
2019/12/29	58846	0.32	564.65	0.91
2020/01/15	58863	1.29	582.66	0.95
2020/01/21	58869	0.65	600.27	0.93
2020/01/27	58875	0.48	603.28	0.94
2020/02/19	58898	2.17	544.20	0.98
2020/02/20	58899	1.94	547.93	0.98

Table 5.1: Summary of the Crab pulsar and nebula observations. Dates are in the year/month/day format. The MJD for such date is given too, together with the effective observation time, the average stereo trigger rate, the mean zenith distance during the observations.

5.2 Data Analysis

The data analysis pipeline employed for the Crab data is the same that was used for the Geminga pulsar, and discussed in depth in Chapter 4. The raw MAGIC data were calibrated and cleaned with the low-energy aimed “MaTaJu” procedure (cfr. Section 4.2.1). The cleaning threshold (presented in Table 4.1) were optimized versus the surviving pedestal rate on Crab data itself, after the removal of the bright star ζ Tauri. The typical analysis cuts on the *Size* of the shower (photoelectron content, see Section 4.3) and the maximum deviation between the reconstructed arrival directions in each of the telescopes Δ_{\max}^2 (cfr. Section 4.5.2) were relaxed, as this showed to sensibly lower the analysis threshold on Monte-Carlo data. A cut in *Size* = 20 photo-electrons and $\Delta_{\max}^2 = 0.2 \text{ deg}^2$ was applied.

Pixels in a radius of $d = 100 \text{ mm}$ (0.34 deg) from the position of the star ζ Tauri in the camera were excluded from the analysis to avoid contamination by starlight. As the wobble positions are symmetrical with respect to the star, the distance of the exclusion zone from the center of the camera is the same for both pointings, and these were analyzed together with the same Monte-Carlo simulations.

The phase information was added using the absolute time tag given by the MAGIC clock system (with a resolution of 200 ns) and the TEMPO2 software for the barycentric corrections. The rotational model for the young and glitchy Crab pulsar was obtained from the publicly available monthly radio ephemerides of the Jodrell Bank Observatory³ (Lyne et al., 1993). These ephemerides account up to the second derivative of the pulsar rotational frequency $\dot{\nu}$ and generally have a validity of one month, with shorter time intervals close to pulsar glitches. Each MAGIC observation was analyzed with the monthly ephemeris valid on the night the data was taken. *Signal regions* corresponding to P1 and P2, as well as a *background region* between P2 and P1 were selected using the same definitions of previous MAGIC papers, to allow a direct comparison among them. These regions are given in Table 4.3. The selection of the background sample in phase allows to remove the steady contribution of the Crab nebula, which is dominant over the pulsar in the whole considered energy range. A spectral analysis of the nebula itself was done to validate the analysis chain. For this purpose, the background level was obtained with the *simultaneous background* technique, presented in Section 4.7.2.

Both the spectra of the pulsar and the nebula were produced with energy dependent θ^2 and hadronness cuts, analogous to the ones given in Section 4.7.1 and presented in Figure 4.19 therein. An unfolding procedure using the Tikhonov regularization (Tikhonov, 1963), as well as a forward folding approach with a power-law (pulsed components) and a log-parabola (nebular emission) was applied to account for the MAGIC energy resolution and bias. Results between the different methods agree within the statistical errors. Spectral points at lower energies were derived from 12 years of *Fermi*–LAT public data. The analysis of *Fermi*–LAT data followed the a pipeline similar to the one presented in Section 6.2.1. In order to disentangle the pulsed P1 and P2 emission from the steady nebular one, the spectrum of the nebula was determined by fitting first the *OFF phase*

³ Jodrell Bank Crab Pulsar Monthly Ephemeris: <http://www.jb.man.ac.uk/~pulsar/crab.html>

region alone. The spectral parameters determined in this way⁴ were fixed during the following fits for the pulsed components of P1 and P2.

In order to produce the lightcurve of the pulsed components versus time, a small modification was introduced in the MAGIC standard analysis tool MARS. This was required to enable the computation of fluxes versus time in the presence of the phase-selected background estimation. Lightcurves were produced separately for the two pulsed components and for the sum of the two. Three different time scales have been probed, aiming at nightly, fortnightly and monthly range of variability. The boundaries between monthly time bins were chosen to reflect the periods during which MAGIC observations were impossible due to the strong background resulting from the full moon. The fortnightly binning was determined simply by dividing in two equal parts the monthly bins.

5.3 Phaseograms

The phaseogram of the MAGIC Crab data in the estimated energy range 30 GeV – 200 GeV is presented in Figure 5.3, with statistical data in the accompanying table. Both impulses are detected with high statistical significance, 11.0σ and 13.5σ for P1 and P2, respectively, with the total being 16.4σ . Since the detection significance \mathcal{S} is limited by the large background, its square is expected to scale linearly with the observation time:

$$\mathcal{S} = s\sqrt{t}, \quad (5.1)$$

the resulting *quality factor* s for the pulsed component of the Crab emission with MAGIC is $s = 2.0 \pm 0.1 \sigma/\sqrt{h}$. This figure is equivalent to a detection at the level of 4σ in $t = 4$ h of observation, or 5σ in $t = 6.5$ h. This enables MAGIC, equipped with the Sum-Trigger-II, to search for a possible variability of the pulsed emission, by repeatedly measuring the Crab pulsar over a time span of several nights. The results of such study are presented in Section 5.5.

5.3.1 Phaseogram morphology

The span in phase of the P1 and P2 components and their relative height change with energy. I produced a simple pulse template consisting of three cyclic Gaussian functions, modeling P1, P2 and the bridge emission between them, respectively. The cyclic Gaussian function is given by:

$$\mathcal{G}(\varphi, A, \mu, \sigma) = A \sum_{k=-\infty}^{+\infty} \exp \left[-\frac{1}{2} \left(\frac{\varphi + k - \mu}{\sigma} \right)^2 \right]. \quad (5.2)$$

Such function was chosen because it is simple and well behaved (no discontinuities) on cyclic data sets as phaseograms. The resulting model has nine free parameters: the mean

⁴ The nebular spectrum was modeled through two standard components representing the synchrotron emission at energies $\lesssim 1$ GeV (power-law) and the inverse Compton one above 1 GeV (log-parabola), respectively.

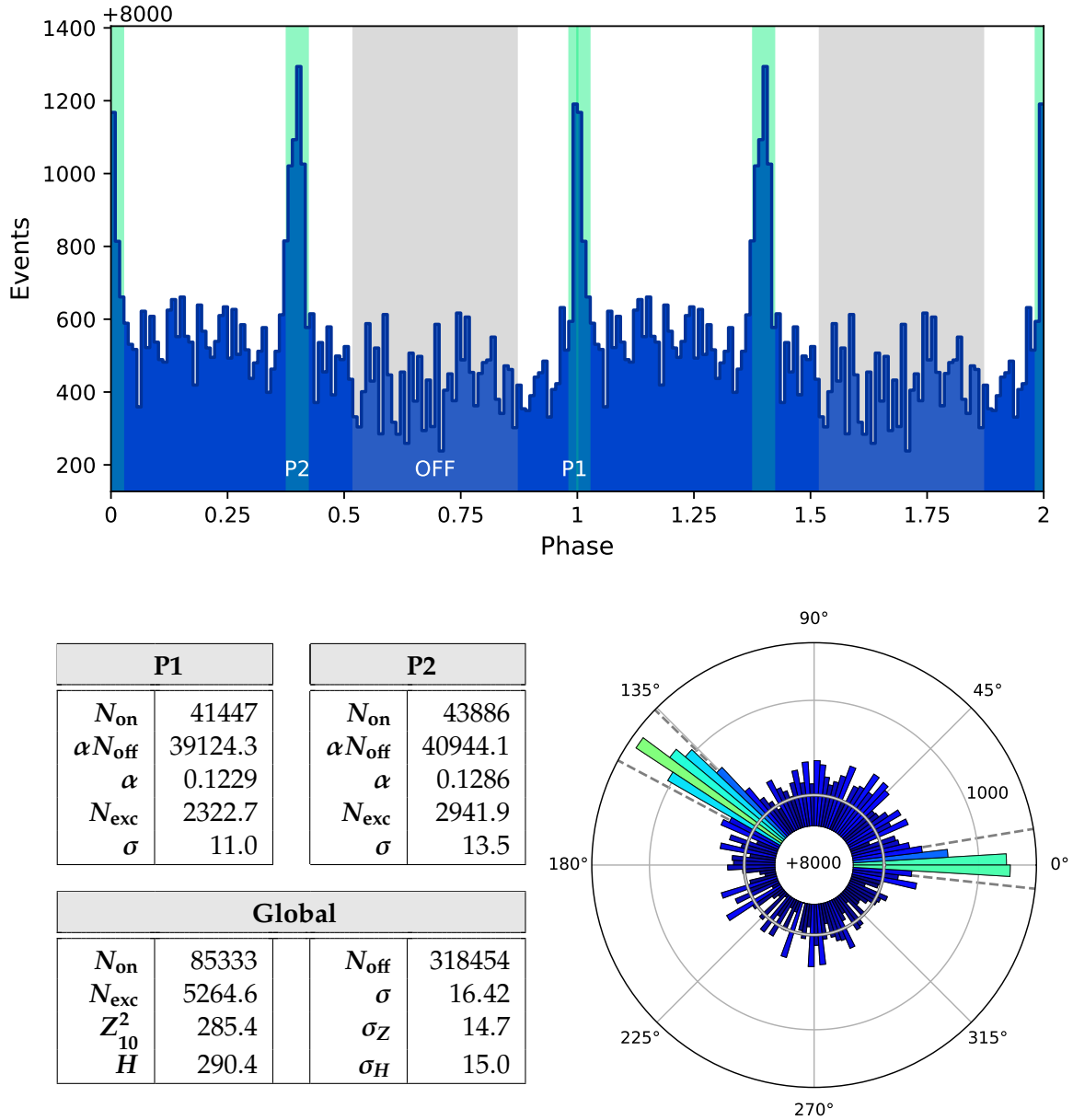


Figure 5.3: Top: phaseogram of the MAGIC Crab data, in the $30 \text{ GeV} < E_{\text{est}} < 200 \text{ GeV}$ energy range. The signal regions, determined a-priori, are highlighted in green, while the gray shaded area corresponds to the background estimation region. Two cycles of the pulsar are shown on the phase axis. Labels on the y-axis refer to the count of events minus 8000. **Bottom left:** Statistical data relative to the phaseogram, with event counts in each phase region, corresponding background counts, excess events and significances. Global variables such as the values and significances for the H and Z^2 tests are also presented. **Bottom right:** Cyclic projection of the same phaseogram, presenting the directional clustering of events corresponding to P1 (at $\varphi = 0^\circ$) and P2 (close to $\varphi = 135^\circ$). The background level is given by the gray circle and colors are proportional to the number of excess events in each bin. Phase regions for P1 and P2 are outlined by dashed gray lines.

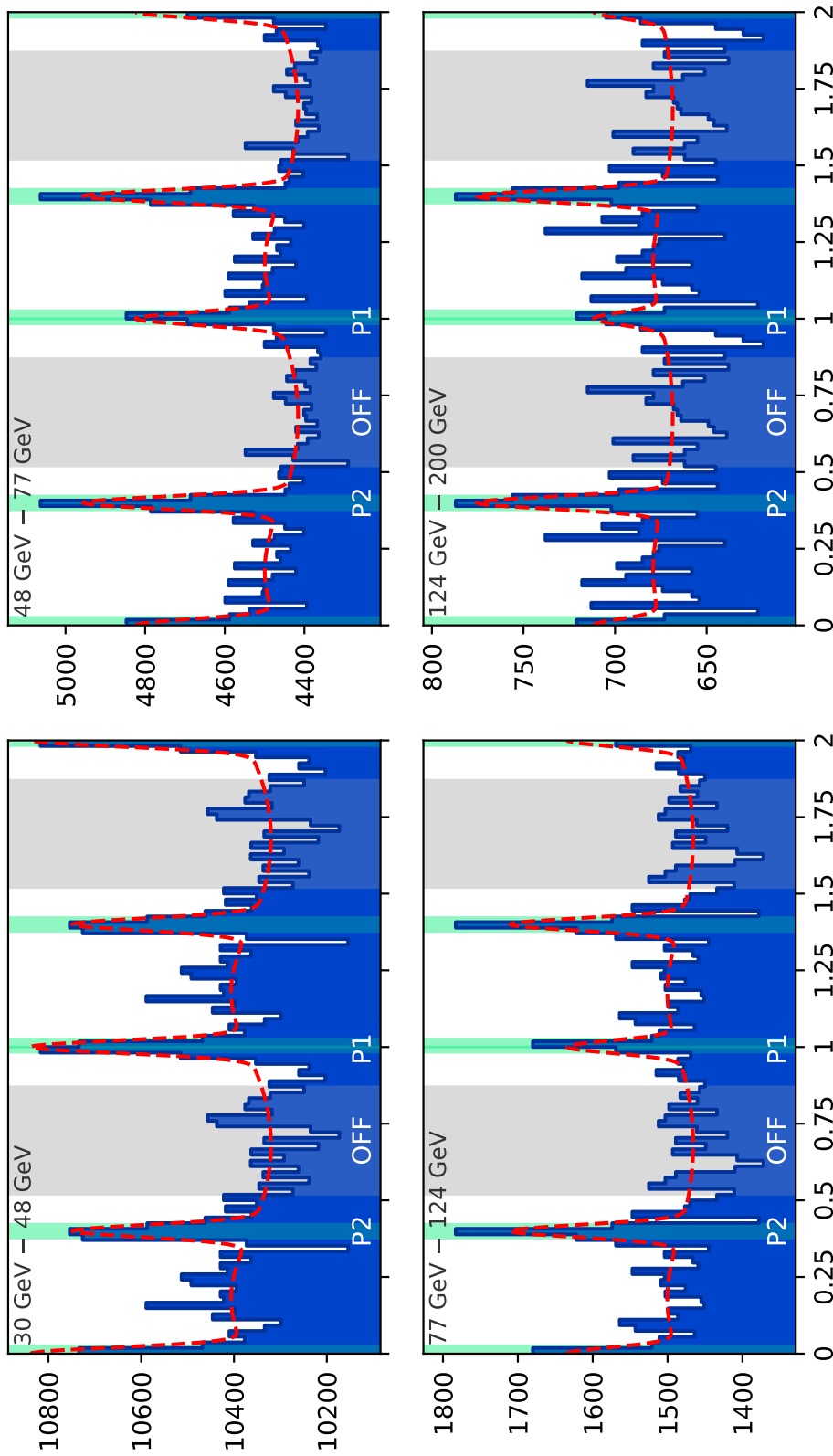


Figure 5.4: Phaseograms of the MAGIC Crab pulsar data in neighboring estimated energy bands, used to fit for the variation of the relative height of P1 and P2. Red dashed lines are the best fit curves, defined as in Formula 5.3. For the fits of the pulse width, a finer binning with $N_{\text{bin}} = 200$ has been used. This is to avoid the bin size to systematically affect the measurement of the pulse width (Nyquist theorem).

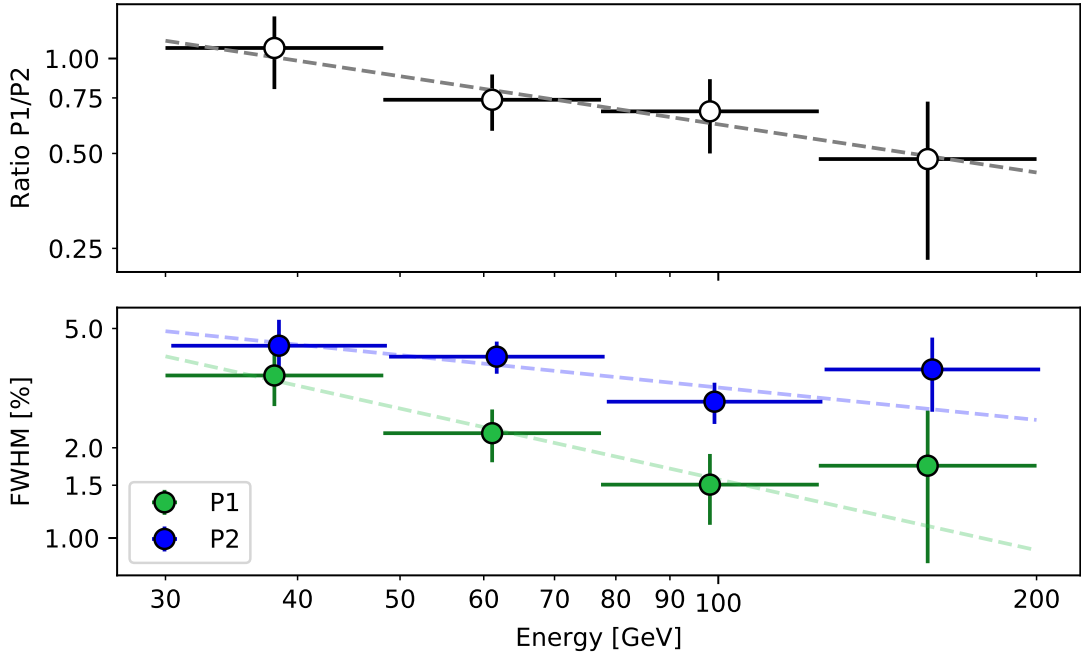


Figure 5.5: Relative P1/P2 height ratio (upper plot) and pulse widths (lower plot) as a function of estimated energy. In the lower graph, P2 points were offset by a small amount in energy to make them more visible. Dashed lines represent fitted trends with a power-law function.

position μ and height A (in counts per phaseogram bin) of the three components, and their span in phase, measured as the σ of the cyclic Gaussian:

$$\mathcal{T}(\varphi, \dots) = \mathcal{G}(\varphi, A_1, \mu_1, \sigma_1) + \mathcal{G}(\varphi, A_2, \mu_2, \sigma_2) + \mathcal{G}(\varphi, A_b, \mu_b, \sigma_b), \quad (5.3)$$

where the indices stand for P1, P2 and bridge, respectively. Four phaseograms were derived in the estimated energy interval between 30 GeV and 200 GeV, with a logarithmic spacing. The average number of background counts, as calculated from their off phase region between P2 and P1, was subtracted from each of the phaseograms. Initial values of A , μ and σ not far from the the expected ones were imposed for the fits, which were performed following the least square approach. The phaseograms with their fitted functions are presented in Figure 5.4. All fits converged to reasonable minima, with χ^2 over the number of degrees of freedom being $\simeq 1$. Figure 5.5 presents the ratio of the pulse heights and the phase range of the P1 and P2 components. The latter was expressed as the full width at half maximum of the fitted Gaussian functions. A fine binning of $N_{\text{bins}} = 200$ bins was used for the pulse width fits, which corresponds to a smallest detectable width $w \geq 2/N_{\text{bins}} = 1\%$. In the fits for the P1/P2 ratio, a coarser binning with $N_{\text{bins}} = 54$ was used instead, in order to suppress the fluctuations from the background.

In agreement with previous findings (Aleksić et al., 2012, 2014), these results suggest that both the P1/P2 ratio and the pulse width decrease with increasing energy. The data were fit with power-law functions, obtaining a spectral index of $\Gamma_R = 0.5 \pm 0.3$ for the

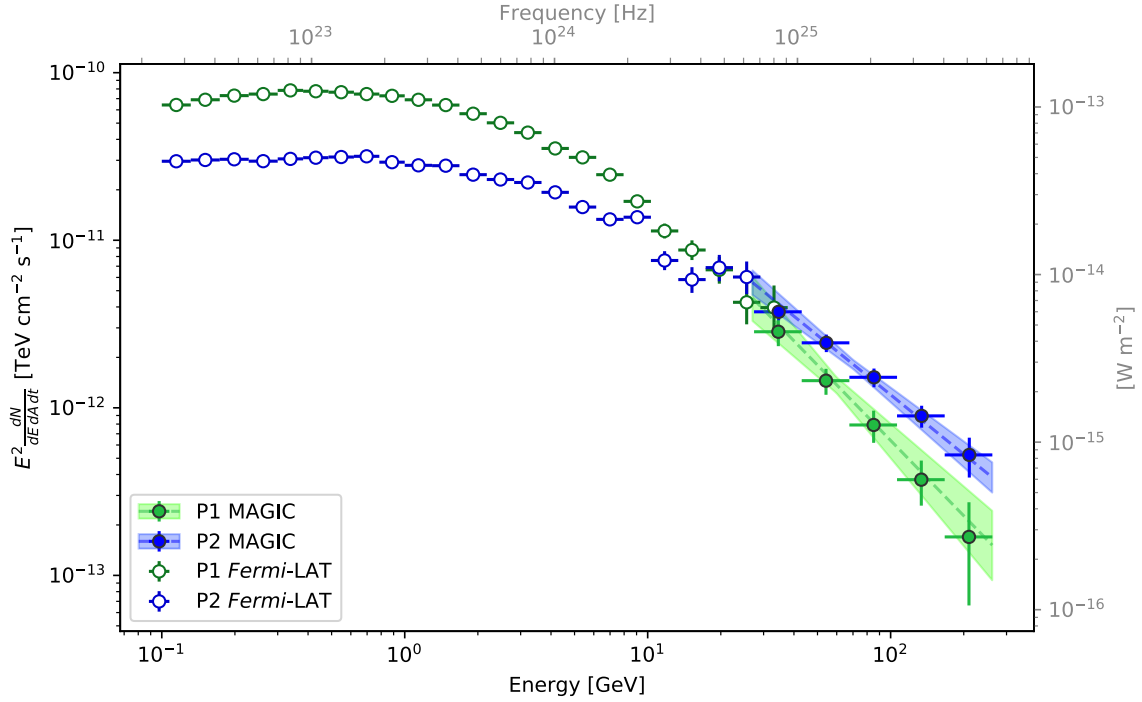


Figure 5.6: Spectra of the P1 (green) and P2 (blue) components of the Crab pulsar emission. Open circles: *Fermi*–LAT measurements. Full circles: MAGIC measurements, Tikhonov unfolding. Dashed lines and shaded areas: forward folding results and 1σ confidence band of the MAGIC measurements. The MAGIC and *Fermi*–LAT measurements overlap in the region between 20 GeV and 30 GeV and provide similar estimates.

P1/P2 ratio, and spectral indices $\Gamma_{W1} = 0.8 \pm 0.3$ and $\Gamma_{W2} = 0.4 \pm 0.2$ for the P1 and P2 widths, respectively. These facts bear a significance for the theoretical modeling of the emission mechanisms of the Crab pulsar and the viewer geometry. In particular, in an earlier striped wind model (Aharonian et al., 2012), in order to reproduce the observed P1/P2 ratio, an anisotropy of the wind needs to be assumed. However, this assumption leads at the same time to the prediction of an increase of pulse width with energy. The new measurements by MAGIC confirm the previous observations and set therefore a constraint for the validity of the wind model for the Crab Pulsar. The collection and analysis of additional data is expected to improve further the measurement accuracy, which is limited by statistics.

5.4 Pulsed Spectra

The spectra of the P1 and P2 components of the Crab pulsar emission are plotted in Figure 5.6, together with the spectra measured by the *Fermi*–LAT in the neighboring energy range. Each of the MAGIC spectra is well described by a single power-law function which joins smoothly with the *Fermi*–LAT measurements at a lower energy. The observations confirm the previous results of a harder P2 emission (Ansoldi et al., 2016). The spectral index of P1 and P2 are found to be $\Gamma_1 = 3.45 \pm 0.25$ and $\Gamma_2 = 3.18 \pm 0.11$, respectively. The spectral parameters (obtained with a forward folding procedure) are given in Ta-

$\mathcal{F}(E) = f_0(E/E_0)^{-\Gamma}$				
Pulse	E_0	f_0	Γ	χ^2/NDF
P1	59.86	$(3.83 \pm 0.42) \cdot 10^{-10}$	3.49 ± 0.25	4.6/3
P2	70.33	$(3.66 \pm 0.23) \cdot 10^{-10}$	3.18 ± 0.11	4.0/5

Table 5.2: Spectral parameters for the MAGIC observations of P1 and P2, derived with a forward-folding procedure. Energy values are in GeV, flux values are in $\text{TeV}^{-1}\text{cm}^{-2}\text{s}^{-1}$. The base energies E_0 have been chosen to match the decorrelation energies of the spectral parameters.

Spectral points					Correlation matrix					
N ^o	E_{low}	E_{mid}	E_{up}	SED	N ^o	1	2	3	4	5
1	27.4	34.6	43.1	2.85 ± 0.53	1	1				
2	43.1	54.4	67.6	1.46 ± 0.26	2	0.02	1			
3	67.6	85.4	106.0	0.79 ± 0.18	3	-0.41	0.15	1		
4	106.2	134.2	166.9	0.35 ± 0.11	4	-0.28	0.19	0.32	1	
5	166.9	210.8	262.3	0.16 ± 0.08	5	-0.11	-0.17	-0.11	0.40	1

Table 5.3: Spectral points for the MAGIC observations of P1, derived with an unfolding procedure. Energy values are given in GeV, SED values are in $10^{-12} \text{TeV cm}^{-2} \text{s}^{-1}$

Spectral points					Correlation matrix					
N ^o	E_{low}	E_{mid}	E_{up}	SED	N ^o	1	2	3	4	5
1	27.4	34.6	43.1	3.74 ± 0.41	1	1				
2	43.1	54.4	67.6	2.44 ± 0.29	2	-0.07	1			
3	67.6	85.4	106.0	1.52 ± 0.19	3	-0.45	0.11	1		
4	106.2	134.2	166.9	0.89 ± 0.13	4	-0.31	0.21	0.22	1	
5	166.9	210.8	262.3	0.52 ± 0.14	5	-0.11	-0.15	-0.21	0.23	1

Table 5.4: Spectral points for the MAGIC observations of P2, derived with an unfolding procedure. Energy values are given in GeV, SED values are in $10^{-12} \text{TeV cm}^{-2} \text{s}^{-1}$

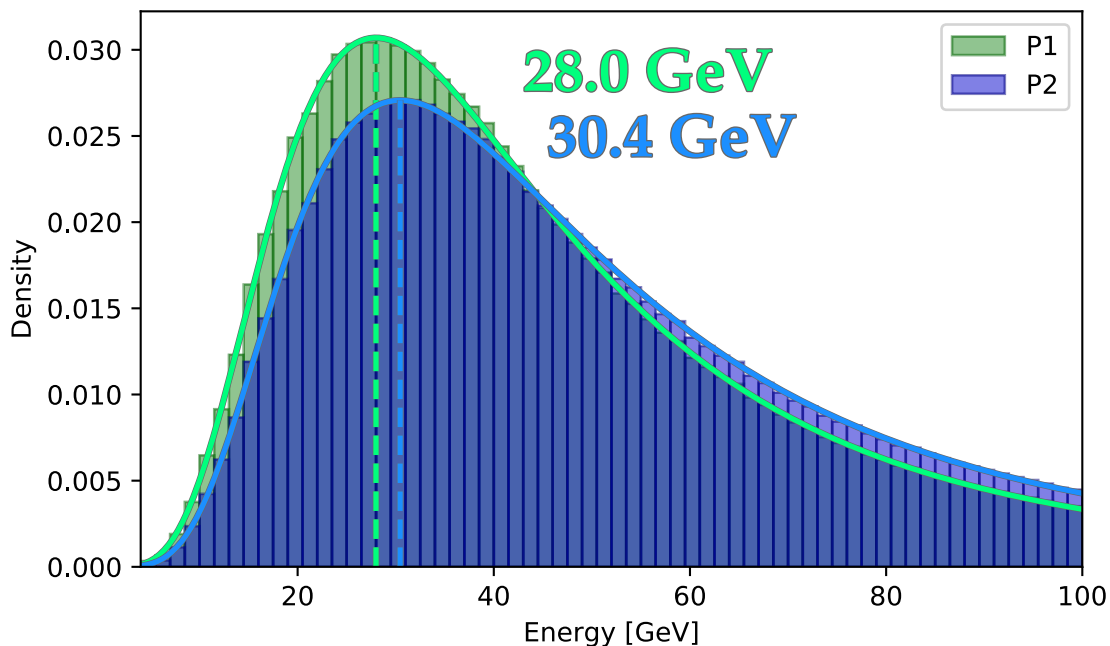


Figure 5.7: Analysis thresholds for P1 (green) and P2 (blue), computed with Monte-Carlo simulations. Spectral indices $\Gamma_1 = 3.5$ and $\Gamma_2 = 3.2$ were assumed for P1 and P2, respectively.

ble 5.2, whereas the list of spectral points and their correlation matrix (derived with an unfolding) are given in Tables 5.3 and 5.4, respectively. The MAGIC measurements have a limited overlap with those of *Fermi*-LAT at energies greater than 25 GeV. Compared to the Geminga measurements presented in Section 6.4, the Crab pulsar ones have a higher energy threshold, due to the harder spectrum. Nevertheless, they agree with both the extrapolation of the *Fermi*-LAT spectrum and previous MAGIC measurements (Aleksić et al., 2012) in a similar energy range.

A spectral feature similar to a dip is observed in the *Fermi*-LAT spectrum of P2 at energies between 10 GeV and 25 GeV. Such feature was present in several earlier analyses of *Fermi*-LAT Crab pulsar data (Ansoldi et al., 2016; Yeung, 2020), some of which used different P2 phase definitions, but has never been studied in detail. The MAGIC P2 spectrum provides an independent evidence that the spectral energy distribution at energies close to $E = 25$ GeV is compatible with $SED = 5 \cdot 10^{-12} \text{ TeV cm}^{-2} \text{ s}^{-1}$, thus reinforcing the significance of *Fermi*-LAT measurements at the same energy. A systematic origin of the effect can be excluded, based on the fact that the P1 spectrum does not exhibit a similar flattening. The quantification of the significance and theoretical implications of such a “cliff” are beyond the scope of this thesis. Since this feature seems to be fully genuine, further research on it will be interesting.

5.4.1 Analysis Threshold

The analysis thresholds for both P1 and P2, computed in the same way as described in Section 6.4.1, are presented in Figure 5.7. As discussed in the previous section, the

spectrum of both components is harder than the one of Geminga (cfr. Section 6.4). This results in a higher energy threshold for the Crab pulsar. Assuming spectral indices $\Gamma_1 = 3.5$ and $\Gamma_2 = 3.2$ for the two pulses, energy thresholds of $E_{\text{thr},1} = 28.0 \text{ GeV}$ and $E_{\text{thr},2} = 30.4 \text{ GeV}$ are found.

5.4.2 Nebula Spectrum

MAGIC observations can be used to measure the spectrum of the Crab nebula as well. The same data-set used for the pulsar studies has provided a spectrum of the nebular emission, shown in Figure 5.8 together with the associated *Fermi*-LAT emission. The “Off from Wobble partner” mode (cfr. Section 4.7) has been used to determine the cosmic ray background. Energy dependent θ^2 and hadronness cuts similar to the ones employed for the pulsar were used to limit its contribution. Both an unfolding procedure and a forward folding one were used take into account the energy resolution and obtain spectral points and a spectral fit with a log parabola, respectively. The measured spectrum agrees well with previous measurements by MAGIC (Albert et al., 2008; Aleksić et al., 2015, 2016a). The pulsed emission is dominant at energies $E \approx 1 \text{ GeV}$. Incidentally, this is the same range where the harder inverse Compton component of the nebular emission becomes dominant over the softer synchrotron one. The synchrotron emission of the Crab Nebula was observed to be variable (Abdo et al., 2011) at time scales of a few weeks. As the source of the electrons that produce the gamma-ray emission of the nebula is the pulsar, it is meaningful to ask whether a similar variability is observed at the highest energies reached by the pulsed gamma-ray emission. A search for such variability is presented in the next section.

5.5 Long-Term Lightcurve

The sound quality factor of $s = 2.0 \sigma / \sqrt{n}$ (cfr. Section 5.3) allows one to rapidly detect the very high energy emission of the Crab pulsar. I studied such component over a long-term period in search for possible variability. The Crab pulsar is observable by MAGIC at $\zeta < 25 \text{ deg}$ for a maximum of 3.6 h per night, but weather and scheduling constraints can sensibly reduce this time. To limit the statistical uncertainties for longer time scales, observations were re-binned on a fortnightly (14 days) and monthly base. A month period was taken as the time interval between two full moons: this seems a natural choice as strong moonlight renders pulsar observations impossible and these were necessarily interrupted during full moon period.

No variability was detected during the time span of the observations at any time-scale. The following Figures 5.10, 5.11 and 5.12 present the light curves of the pulsed emission of P1, P2 and their sum for different time bins. An energy range of 30 GeV to 200 GeV was used to calculate the fluxes. The lower extreme was fixed by the analysis threshold and the upper one was imposed to limit the amount of irreducible gamma-ray background from the nebula. In particular, 200 GeV is the value for which the significance of the pulsed signal reaches saturation (see Figure 5.9): the chosen energy range maximizes therefore the sensitivity for a variability search. Often the observations could not be performed following the scheme outlined in Section 5.1, due to weather constraints. To

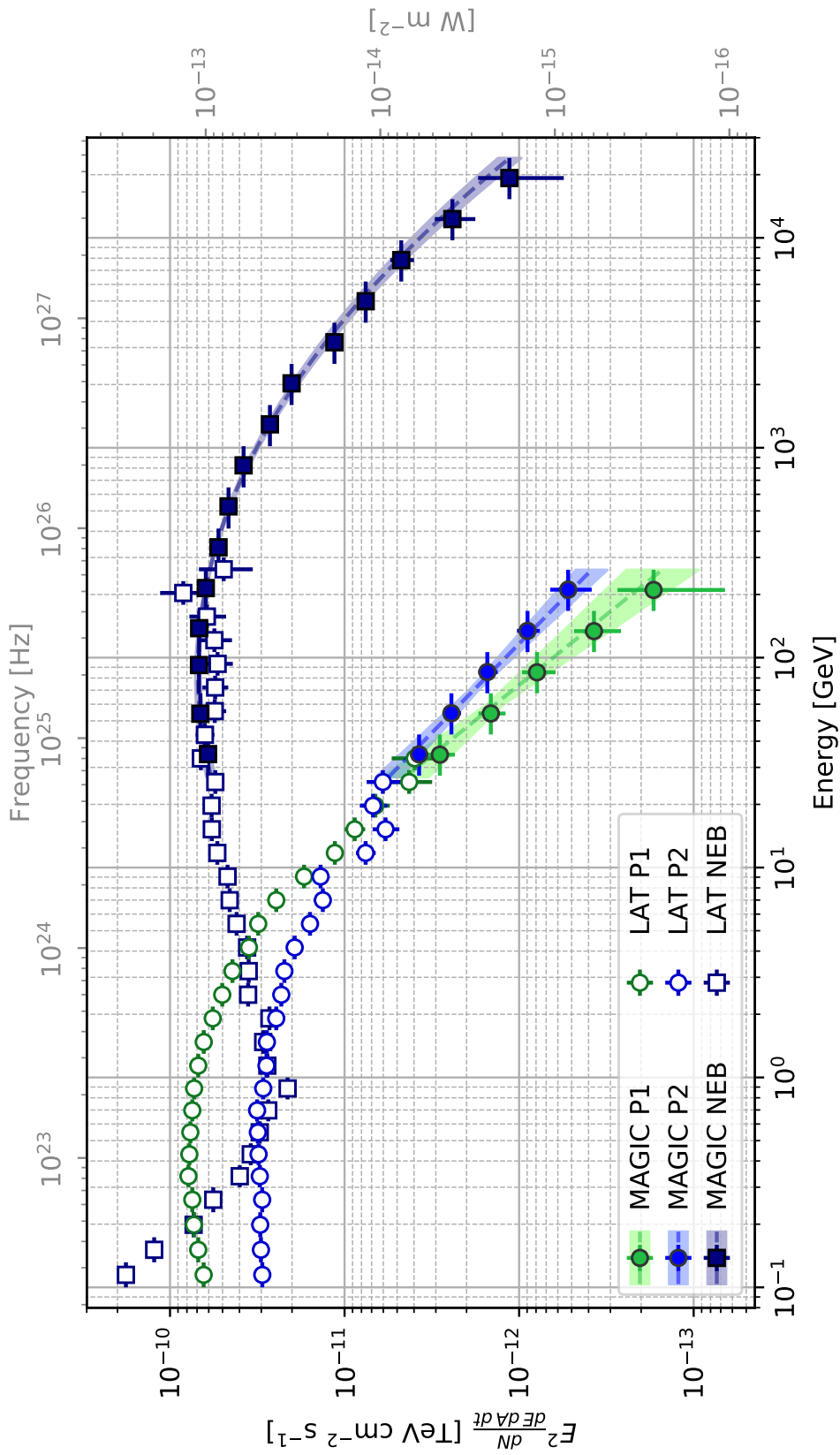


Figure 5.8: MAGIC and *Fermi*-LAT spectra of the Crab pulsar and nebula. The MAGIC spectral points were obtained with an unfolding procedure (cfr. Section 4.8.3), using the Tikhonov regularization method. Power-law functions (pulsar) and a log parabola (nebula) were used as assumed spectra. Confidence bands depict the result of a forward-folding approach with the same spectral shapes.

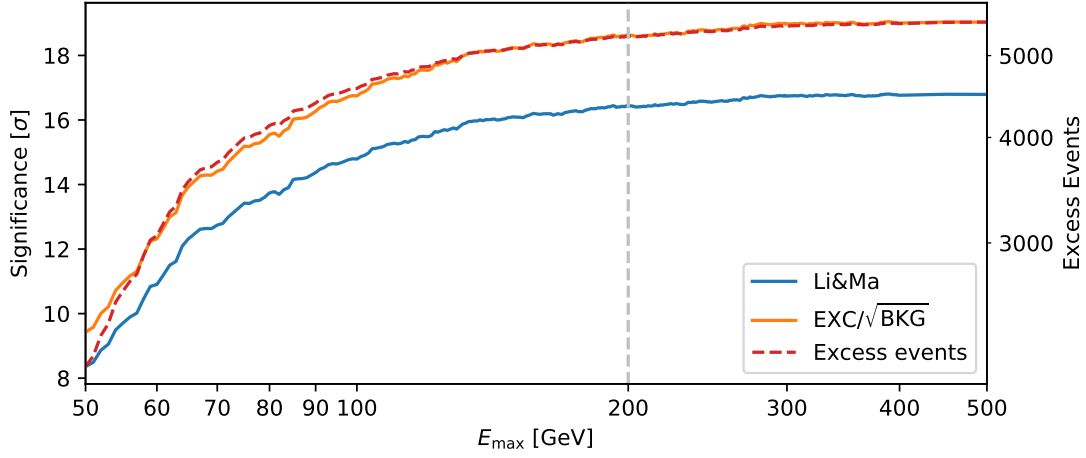


Figure 5.9: Cumulative scan in the significance of the Crab pulsar emission in the range $30 \text{ GeV} < E_{\text{est}} < E_{\text{max}}$, as a function of E_{max} . The significance is given both with a crude approximation (number of excess events over the square root of background), and with the statistically correct Li&Ma 17 formula. The number of excess events (P1+P2) is given by the dashed red line (right y-axis). For $E_{\text{est}} > 200 \text{ GeV}$ both the significance and the number of excess events saturate.

reduce the impact of highly fluctuating low statistic measurements on the lightcurve analysis, a minimum observation time per flux point was required. This was set to one half of the time originally asked per flux point, and corresponds to 1 h, 3 h and 6 h for the nightly, fortnightly and monthly lightcurves, respectively.

Each of the data sets was tested for variability with a simple χ^2 test (goodness-of-fit with respect to the average flux) and the *excess variance* σ_{NXS}^2 method (Section 4.8.4). None of the lightcurves significantly supports a time variation of the fluxes. As an example, the χ^2 values over the number of degrees of freedom for the total pulsar emission are $\chi_N^2/NDF = 24.6/30$, $\chi_F^2/NDF = 6.7/10$ and $\chi_M^2/NDF = 3.8/5$ for the nightly, fortnightly and monthly binning, respectively. These figures are consistent well within 1σ with a steady emission. Similar results are obtained for the P1 and P2 components separately. All of them are listed in Table 5.5.

The excess variance σ_{NXS}^2 results similarly suggest a constant flux. The values for all data sets and binning schemes are close to zero and compatible with it. Most values are negative: this is to be expected in case of statistical uncertainties on single measurements larger than the actual flux variations, and bears no deep physical significance.

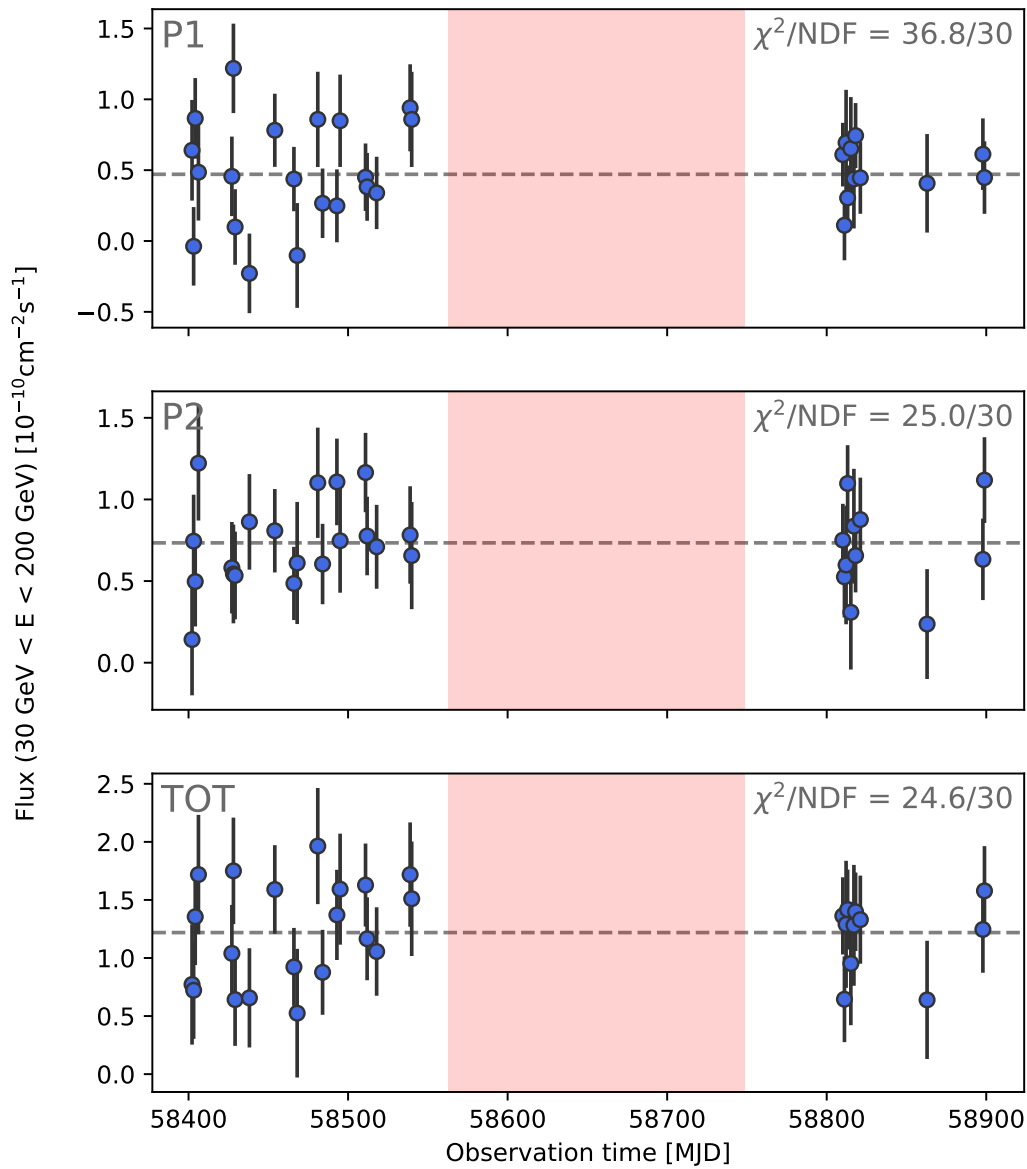


Figure 5.10: Nightly flux in the 30 GeV to 200 GeV energy range of the P1 (top panel) and P2 (middle panel) emission, as well as the total sum of the two (bottom panel), plotted against time in MJD. No significant deviation from a constant can be seen (χ^2 test) for any of the components. The red shaded area corresponds to the summer period during which the Crab pulsar is not observable from La Palma (from March to September).

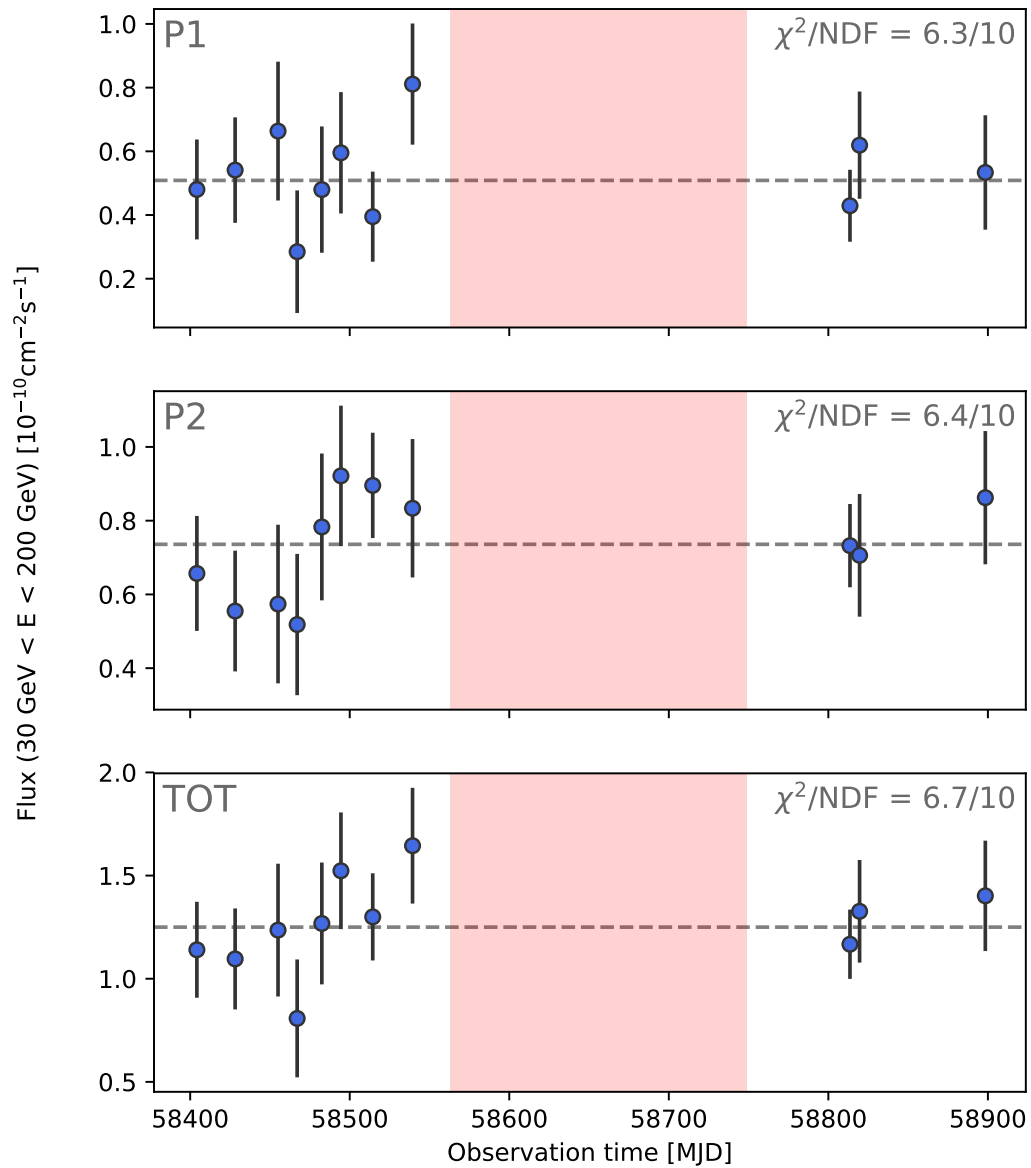


Figure 5.11: Fortnightly flux in the 30 GeV to 200 GeV energy range. No significant variability is found. See also Figure 5.10.

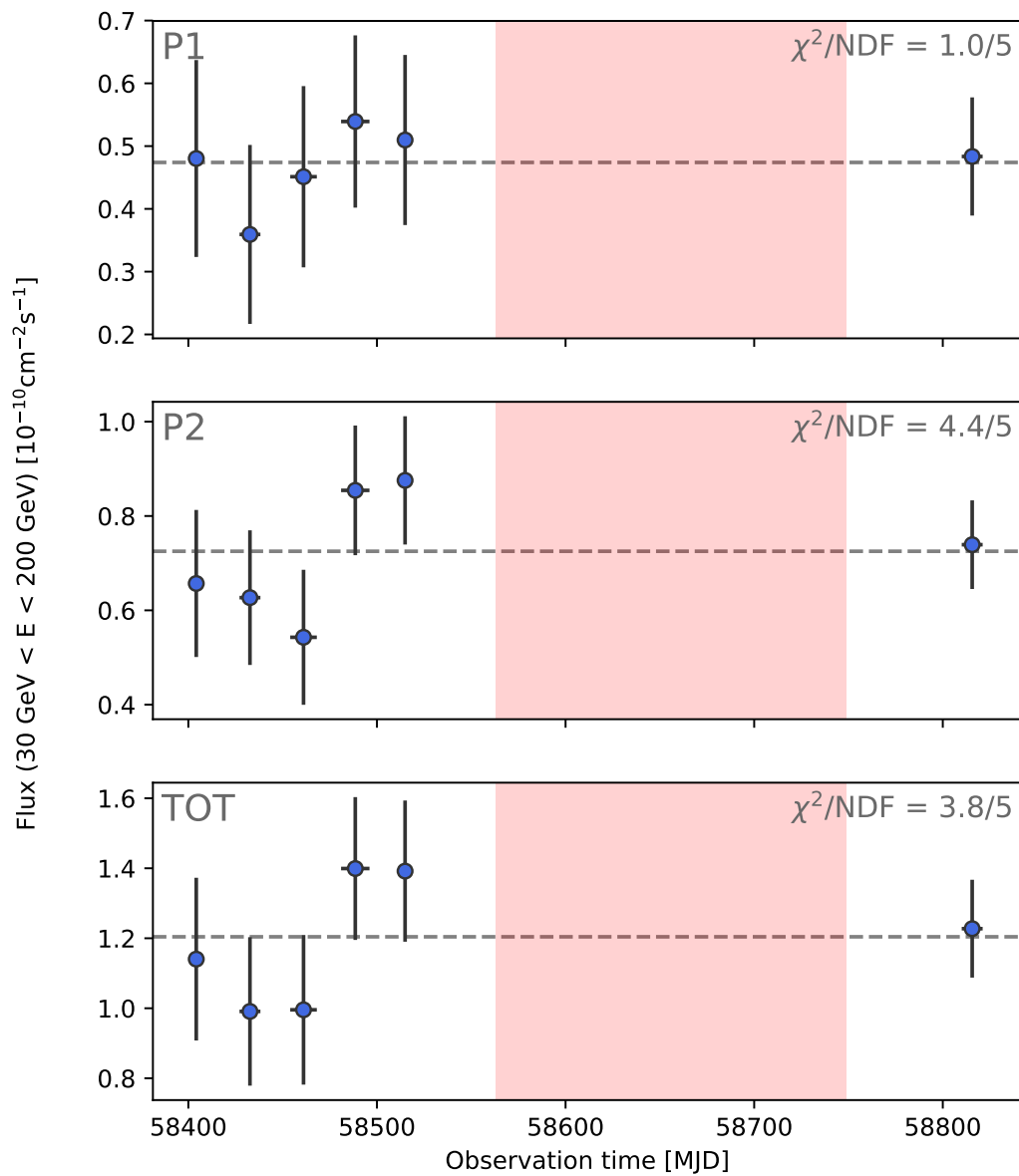


Figure 5.12: Monthly flux in the 30 GeV to 200 GeV energy range. No significant variability is found. See also Figure 5.10.

	Nightly		Fortnightly		Monthly	
	χ^2/NDF	σ_{NXS}^2	χ^2/NDF	σ_{NXS}^2	χ^2/NDF	σ_{NXS}^2
P1	36.8/30	0.10 ± 0.10	6.3/10	-0.04 ± 0.05	1.0/5	-0.07 ± 0.05
P2	25.0/30	-0.02 ± 0.04	6.4/10	-0.02 ± 0.02	4.4/5	-0.02 ± 0.02
TOT	24.6/30	-0.02 ± 0.03	6.7/10	-0.01 ± 0.02	3.8/5	-0.01 ± 0.02

Table 5.5: Variability tests on the data sets of Figures 5.10, 5.11, 5.12. For each lightcurve, the value of the χ^2 with respect to the average (goodness-of-fit test) and the excess variance σ_{NXS}^2 are reported. The errors on σ_{NXS}^2 are calculated according to (Vaughan et al., 2003).

5.5.1 Sum-Trigger-II performance stability

The absence of variability has implications both for the stability of the performance of the Sum-Trigger-II system and on the capability of the system to detect a real variability. The observed lightcurves can not be explained assuming that a real variability of the pulsar has been exactly canceled by an opposite variability of the detection efficiency, since the two are independent processes. As statistical fluctuations are sufficient to explain the observed excess variance ($\sigma_{\text{NXS}}^2 \simeq 0$), systematic effects due to fluctuations of the detector efficiency must be small compared to the statistical uncertainties. This is of major technical importance for a novel system such as the Sum-Trigger-II. An empirical limit on the fluctuations of the energy scale of MAGIC ϵ during the time span of the observations can be derived from the observed light curves. To do so, I assumed that the entire observed excess variance is solely due to a mis-reconstruction of the energy, and calculated an *equivalent energy scale factor* ϵ_{RMS} corresponding to it. Since the spectra of P1 and P2 are power-laws, this can be estimated as:

$$\epsilon_{\text{RMS}}^{\Gamma-1} = s_{\text{RMS}} \quad (5.4)$$

with Γ the spectral index of the power-law and the *equivalent flux scale parameter* s_{RMS} given by:

$$s_{\text{RMS}} = \frac{\langle F \rangle \pm \sigma_F}{\langle F \rangle}, \quad (5.5)$$

where $\langle F \rangle$ is the average integral flux and σ_F^2 is the variance associated with the lightcurve. The index Γ was set to be 3.5 and 3.2 for P1 and P2, respectively, following the results of Section 5.4. Table 5.6 shows the values of ϵ_{RMS} for both P1 and P2 at different time scales. To compile it, I chose the largest value between the two possible ones resulting from the choice of the sign in Formula 5.5. The largest values, of the order of 10%, are found for the nightly lightcurve: this is expected, as it is the one with the largest measurement uncertainties per flux point. Correspondingly, the value decreases for fortnightly and monthly lightcurves as the statistics of the single flux measurements increases.

These findings give confidence that the MAGIC Telescopes equipped with the Sum-Trigger-II have a stable performance over time. Compared to the quoted standard MAGIC flux scale systematic of $\pm 15\%$ (Aleksić et al., 2016a), results seem to suggest a better performance of MAGIC with the Sum-Trigger-II. However, this can be explained with a selection effect due to the very stringent data quality cuts required for the pulsar observations to be taken in the first place.

	Nightly	Fortnightly	Monthly
P1	$(11.2 \pm 1.5)\%$	$(4.5 \pm 0.8)\%$	$(1.6 \pm 0.3)\%$
P2	$(9.0 \pm 1.2)\%$	$(4.4 \pm 0.8)\%$	$(3.3 \pm 0.8)\%$

Table 5.6: Empirical limits on the systematic energy scale factor ϵ_{RMS} variation due to the MAGIC and Sum-Trigger-II performance fluctuations. This is derived by assuming that the whole observed variance in the very high energy flux is produced entirely by a mis-reconstruction of the energy. As the statistical uncertainties are already sufficient to fully explain the observed variance, these values shall be interpreted as upper limits.

5.5.2 Variability Upper Limits

To evaluate whether variability of the Crab pulsar can be detected with the proposed strategy in future observations, I produced a toy Monte-Carlo simulation of pulsar lightcurves. Lightcurves were simulated assuming a pulsar event and background rates similar to those measured in the real observations presented in the previous sections. In order to enhance the statistics, only the total emission of P1 and P2 was considered. The number of simulated data points per lightcurve was chosen to be similar to the observed ones, and a minimum observation time per measurement was required, as in the analysis of real data. The observation time per flux measurement was randomly sampled from a Gaussian distribution fitted to the parameters of real observations. These parameters are summarized in Table 5.7. ON and OFF counts were simulated separately assuming a Poisson distribution with the measured rates as parameters. Similarly to the real analysis, excess events were estimated as $N_{EXC} = N_{ON} - \alpha N_{OFF}$ and $\sigma_{EXC}^2 = N_{ON} + \alpha^2 N_{OFF}$, and divided by the simulated observed time t_s to obtain an excess event rate. A value of the effective area A_{eff_s} for each flux measurement was simulated too, sampling from its distribution as found in real data. The final simulated flux point was given by the event rate over the simulated effective area:

$$\left(\frac{dN}{dA dt} \right)_{sim} = \frac{N_{EXC}}{t_s A_{eff_s}}. \quad (5.6)$$

The uncertainty of the effective area was propagated to the flux uncertainty.

A sample of $N = 10^7$ lightcurves was simulated for each time scale (nightly, fortnightly, monthly). The distributions of the excess variance σ_{NXS}^2 in case of a stable pulsar emission are given in Figure 5.13. These have their peak close to $\sigma_{NXS}^2 \simeq 0$, which is consistent with the measured values (Table 5.5, third row). Their standard deviation, on the other hand, is $\sigma_N \simeq 0.05$, $\sigma_F \simeq 0.03$ and $\sigma_M \simeq 0.02$: this is in turn compatible with the error estimates of Table 5.5, which were derived by Vaughan et al. (2003) following a similar method. Monte-Carlo simulations can be used to derive a limit on the expected scale of the variability, given the observed lightcurve. To do so, a variability model needs to be chosen. I investigated three models: a sudden variation of the flux of the pulsar, otherwise constant, affecting only one flux point of the lightcurve (spike variability) or half of them (step variability), and a continuous flux variation following a red noise with a power spectrum $P(\omega) \propto \omega^{-2}$ (stochastic variability). The index of the power-spectrum of the red noise was chosen to resemble similar cases already observed in astrophysical

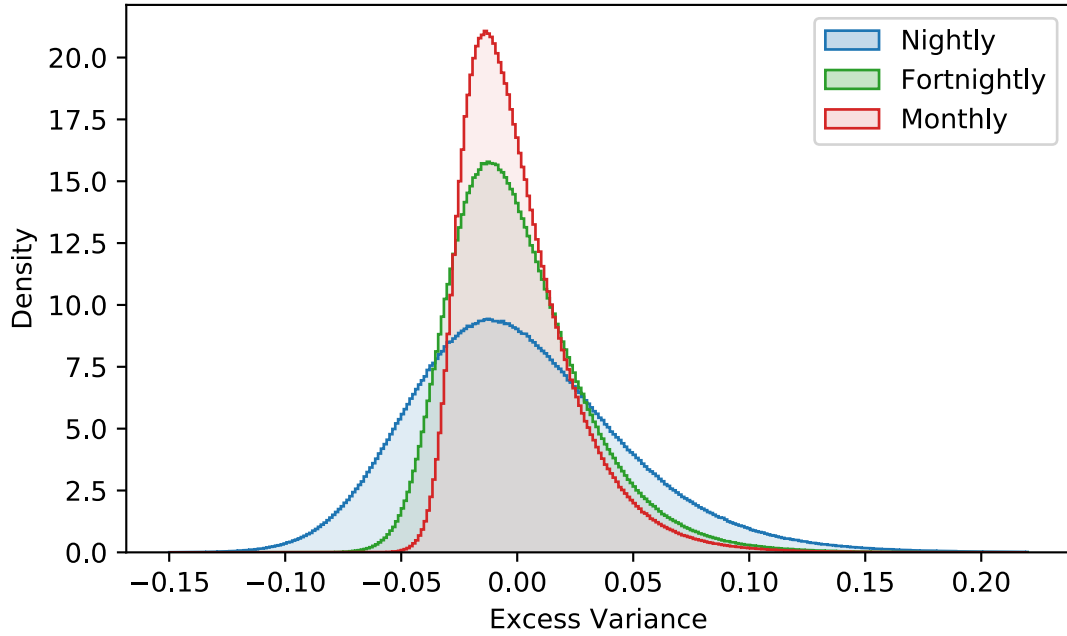


Figure 5.13: Excess variance distributions from Monte-Carlo simulations of $N = 10^7$ lightcurves with realistic pulsar fluxes and observation time distributions. Stable pulsar emission ($\Delta = 0$) was assumed.

	N/LC	$t_{\text{eff}} = \mathcal{N}(\mu, \sigma)$	t_{min}	t_{max}
Nightly	31	$\mu = 1.8 \text{ h}, \sigma = 1.2 \text{ h}$	1 h	3.2 h
Fortnightly	11	$\mu = 4.7 \text{ h}, \sigma = 1.8 \text{ h}$	3 h	13 h
Monthly	6	$\mu = 8.25 \text{ h}, \sigma = 1.0 \text{ h}$	6 h	–

Table 5.7: Parameters for the lightcurve simulations. Number of flux points per lightcurve, mean μ and standard deviation σ of the effective time distribution per flux point, minimum and maximum time cuts. All simulations were for the total P1+P2 emission.

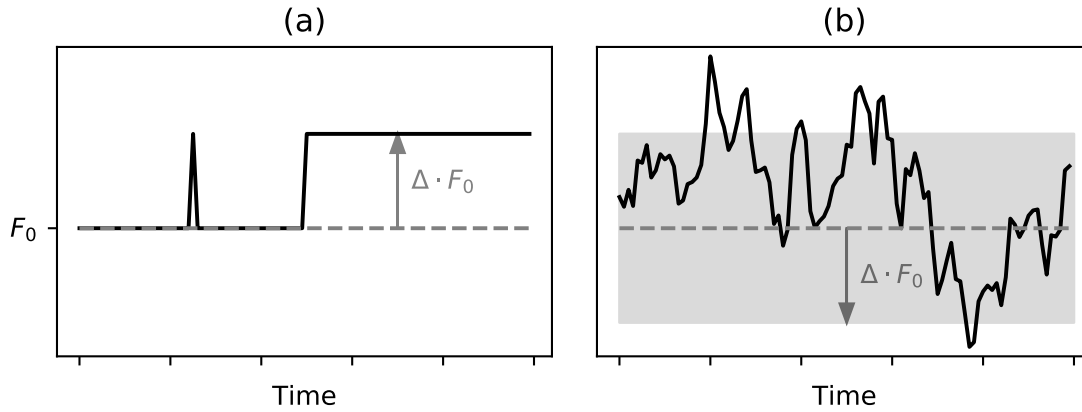


Figure 5.14: Models considered for the variability Monte-Carlo study. **(a):** the spike (left part) and step (right) model, with the flux increasing by a factor Δ . **(b):** a Brownian noise stochastic process with scale Δ .

sources. The models probed are sketched in Figure 5.14. In the spike and step models, the pulsar flux increases by a factor Δ . Correspondingly, in the stochastic model, at each point of the lightcurve, the pulsar flux is $F(t) = F_0[1 + \Delta \cdot \mathcal{R}(t)]$, with $\mathcal{R}(t)$ being a zero-centered red-noise component with unitary variance. Additionally, the obvious constrain that the intrinsic flux of the pulsar must be positive for each of the measurements was set.

Similarly to what was done for the constant flux in Figure 5.13, distributions of the excess variance were derived from Monte-Carlo simulated lightcurves for different values of the variability scale factor Δ . A subset of these distributions is plotted in Figure 5.15 for the stochastic model. As expected, larger values of Δ yield on average larger excess variances. Distributions obtained in this way represent the probability densities of observing an excess variance s^2 given the value δ of their scale parameter: $P(s^2 | \Delta = \delta)$. The Bayes rule can be used to derive a probability distribution for the scale factor Δ given the observation of an certain excess variance \hat{s}^2 . Assuming no prior knowledge on Δ , so that all possible values are equally probable, the sought probability is determined by:

$$P(\Delta | s^2 = \hat{s}^2) = \frac{P(\hat{s}^2 | \Delta)}{\sum_{\delta} P(\hat{s}^2 | \Delta = \delta)}, \quad (5.7)$$

where the sum runs on all possible values of Δ . In practice, a step size of $d = 0.05$ in δ was used with an upper bound D on the sum, chosen so that the remaining terms for $\delta > D$ are negligible at the observed excess variance \hat{s}^2 . Figure 5.16 presents the probability density functions determined in this way, calculated for the three possible variability models and the values of the excess variance for the total emission found on real data (listed in Table 5.5) and the three different time binning strategies. As expected, the mean of the distributions peaks close to $\Delta = 0$, indicating the absence of pulsed variability as the most likely hypothesis. Upper limits were derived for each of the cases.

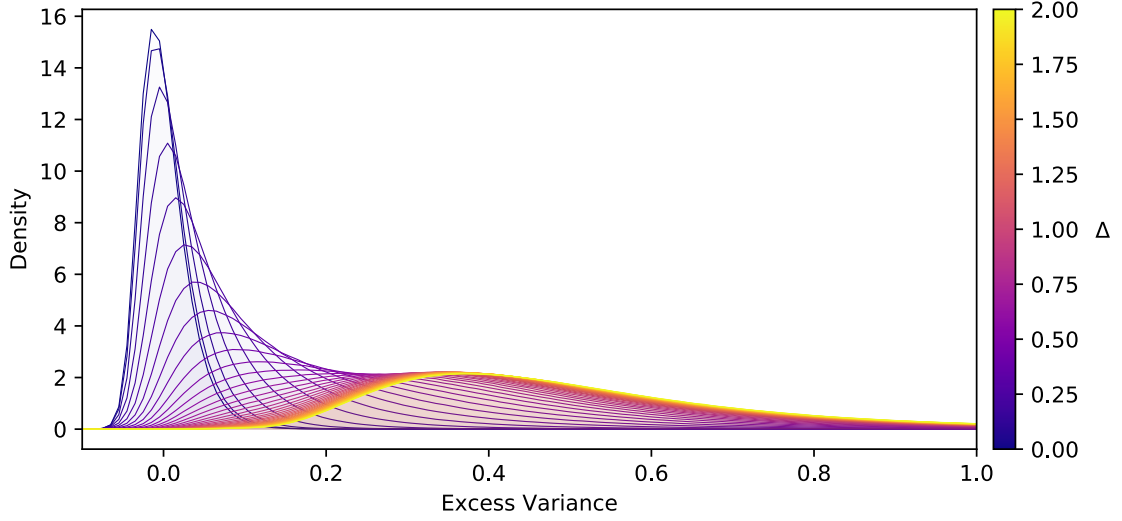


Figure 5.15: Excess variance σ_{NXS}^2 distributions for toy Monte-Carlo simulations of fortnightly lightcurves. A constant pulsar flux, with the addition of a red noise is assumed: $F(t) = F_0(1 + \Delta\mathcal{R}(t))$. The curve for $\Delta = 0$ is equivalent to the one in Figure 5.13.

The less constrained case is the spike variability. Given the observed excess variances, a 95% upper limit on Δ was set for the nightly, fortnightly and monthly time-scales. These are $UL_N = 179\%$, $UL_F = 94\%$ and $UL_M = 74\%$, respectively. This means that an increase of the flux of the pulsar by a factor of 2 can be excluded on the timescale of 14 days, and an increase of a factor 1.75 is similarly excluded on timescales of a month. Given the large uncertainty that affects the nightly measurements, the limit at such timescale is less constraining. For the step-like and red noise stochastic variability models, upper limits are less dependent on the binning strategy and fall in the range 50% to 68%. This is expected, as such kinds of variability are invariant for a dilation of the time scale.

In conclusion, no variability of the pulsed emission was detected in the MAGIC observations of the Crab Pulsar. The upper limits derived on the pulsar variability are affected by the statistical uncertainties of the measurements, their number and sparseness. It is expected that such limits will improve with the collection of more data. However, in the scope of searching of a possible pulsar variability, it is critical that measurement are taken on a regular basis. As no major flare of the Crab nebula happened during the MAGIC observations⁵, it is not possible to draw a conclusion on the possible link between these phenomena and the flux of the Crab pulsar.

⁵ A minor flare was detected in May 2019 (Cheung, 2019), within five months from the end of the first MAGIC observation campaign. Five months is the expected light travel time between the pulsar and the termination shock of its wind. The flare was a minor one and was detected only by *Fermi*-LAT. Since the MAGIC light curve for the period preceding the 2019 flare is fully consistent with constant emission, I did not attempt to perform a time correlation analysis with the *Fermi*-LAT data.

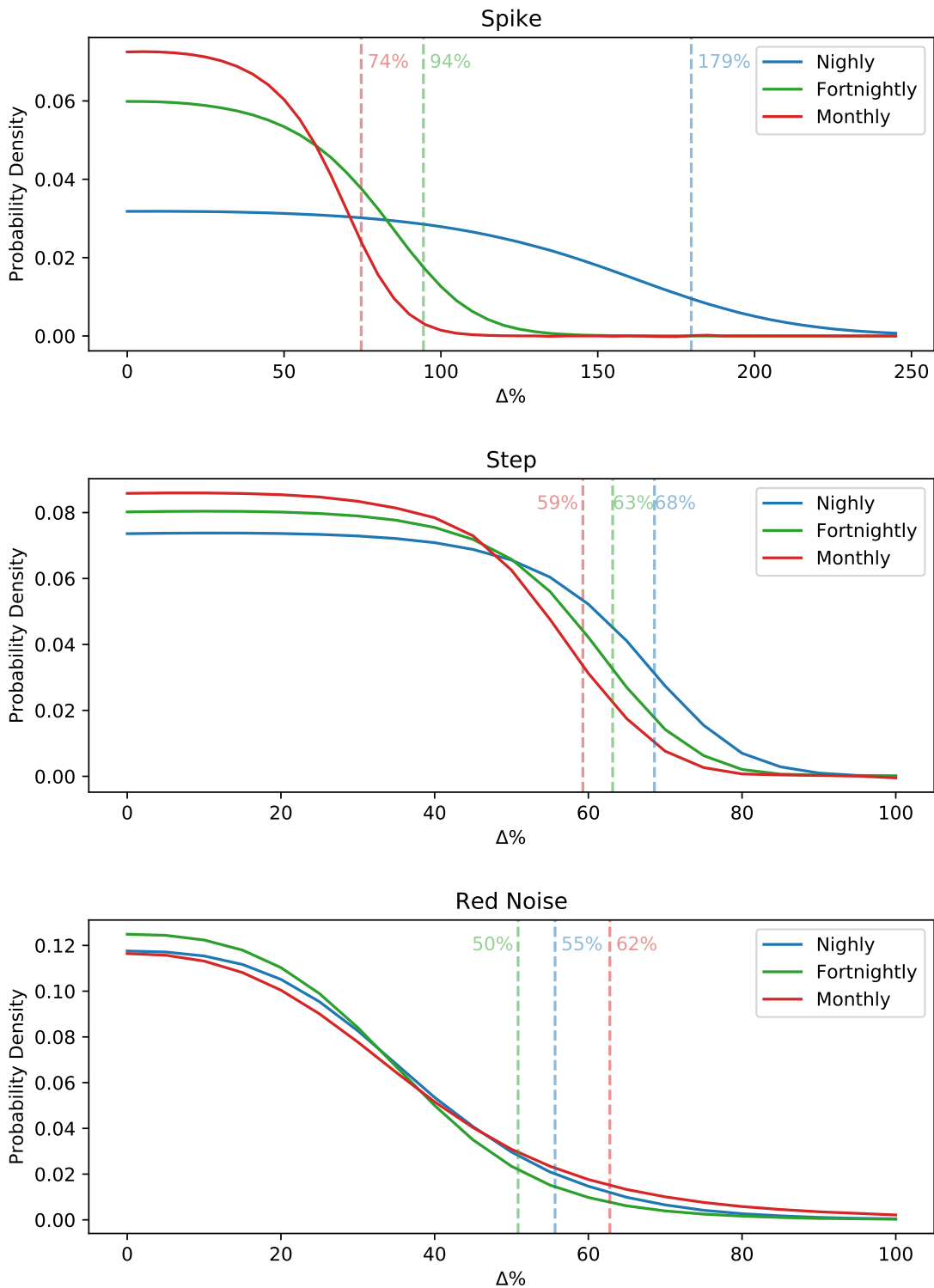


Figure 5.16: Probability density functions of the flux increase Δ given the observed excess variance, for different timescales. Shaded dashed lines correspond to the 2σ confidence intervals (95% upper limits).

5.6 Summary

MAGIC collected approximately 70 h of good quality data on the Crab pulsar during the 2017-2020 period. The novel Sum-Trigger-II system improves the performance of the telescopes at energies below 100 GeV and allows one to collect data with a sound statistical basis in a short time. The phaseograms of the pulsed emission present a significant signal both in the P1 and P2 phase regions, with P1 being the dominant one at energies below 50 GeV and P2 being more intense above 50 GeV. The cumulative significance for the two pulses, in the estimated energy range $30 \text{ GeV} < E_{\text{est}} < 200 \text{ GeV}$, was found to be $S_1 \simeq 11.0 \sigma$ and $S_2 \simeq 13.5 \sigma$, respectively, with the total one being $S_{\text{TOT}} \simeq 16.4 \sigma$. This gives a detection quality factor $s = 2.0 \sigma/\sqrt{h}$, a remarkable figure that allows MAGIC to perform long-term variability studies of the pulsar.

The data analysis was specifically aimed at energies below 100 GeV (see Chapter 4). This allowed me to achieve an energy threshold of $E_{\text{thr}} \lesssim 30 \text{ GeV}$ and to produce spectra of both pulses in the energy range 27 GeV – 260 GeV. Both pulsed emissions are modeled well by a power-law, which is softer for P1 ($\Gamma_1 = 3.5 \pm 0.2$) than for P2 ($\Gamma_2 = 3.2 \pm 0.1$). This is consistent with previous findings and agrees well with the *Fermi*-LAT measurements, which overlap with the MAGIC ones below 40 GeV. In the spectrum of P2, *Fermi*-LAT measurements show an interesting structure, with a small “cliff” at 10 GeV followed by a rather flat spectrum up to 30 GeV. This spectral feature has been observed in multiple independent works making use of the *Fermi*-LAT data, but has never been studied in detail before. MAGIC measurements reinforce the significance of such feature, as they give an independent confirmation of the fluxes of P2 at 30 GeV measured by *Fermi*-LAT. Further research on this topic is recommended to study in depth the significance of such spectral feature.

The unique capability of MAGIC to significantly detect the Crab pulsar in a short ($t < 5 \text{ h}$) observation time has been exploited to produce the first assessment of the variability of the pulsed emission at the very high energies. Lightcurves spanning a period of time of 16 months were produced on a nightly, fortnightly and monthly base. No significant variability has been detected and upper limits to its value have been derived for different models of variability. Unfortunately, no major flare of the Crab nebula occurred during the time of the observations, or in the five months time window after them, corresponding to the travel time of the relativistic pulsar wind from the pulsar to its termination shock. Therefore, it is impossible to constrain the hypothesis of a pulsar origin for the flares observed in the nebula. Conversely, the stability of the pulsar emission has been used to validate the performance and stability of the Sum-Trigger-II system, which can now be considered a mature component of the MAGIC Telescopes. This latter fact opens the possibility for a future usage of the Sum-Trigger-II in other contexts that require good performance at the low energies, different for the pulsar research, such as the detection of distant blazars, and the search for the very high energy emission of gamma-ray bursts.

6

GEMINGA PULSAR

In this Chapter the main scientific results of my work on the Geminga pulsar are presented. MAGIC observations led to the discovery of its pulsed gamma-ray emission at the very high energies. This makes Geminga the third gamma-ray pulsar revealed by ground-based instruments (the other two being Crab and Vela) and the first “middle-age” one known to emit at those energies. Such detection has been made possible by the enhancement in the sensitivity of the MAGIC Telescopes in the 10 GeV – 100 GeV range, due to the Sum-Trigger-II system. The enrichment of the meager family of very high energy pulsars with new members is a promising way to better understand and characterize the common properties of these objects and their evolution.

Sections 6.1 and 6.2 give a brief overview of the observations that were performed and the analysis methods, explained more in detail in Chapter 4. In Section 6.3 the reader will find a summary of the phase measurements that led to the detection, with a significance of 6.3σ . The very high energy radiation is significantly detected only from the second pulse of Geminga (P2, see Section 1.3).

In addition to this, the pulsed spectrum was measured for the first time at energies larger than 50 GeV, the highest ever detected from the Geminga pulsar, as reported in Section 6.4. The MAGIC measurements are described well by a steeply falling power-law, which follows the general trend observed in *Fermi*-LAT data. Section 6.5 presents a combined analysis of the observations of both instruments. The standard model with a sub-exponential cutoff is disfavored by the measurements, which hint instead that the spectrum continues as a power-law to higher energies. This implies that the production mechanism of the VHE emission is substantially different from the ones previously considered for this source. The MAGIC observations prompt a review of the current theoretical framework for the gamma-ray emission of Geminga, as I discuss in Section

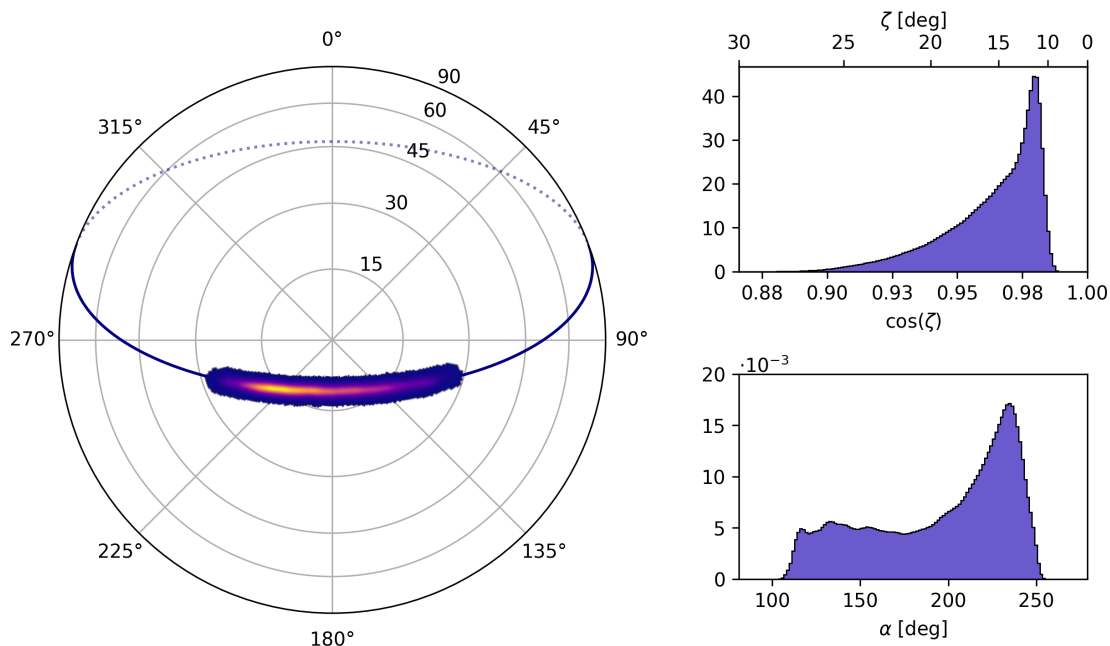


Figure 6.1: Left side: density of the reconstructed directions of the events in the MAGIC Geminga observations, in orthographic projection. North is up and East is right. The path on the sky of Geminga is shown as a solid dark-blue line. Right side: zenith distance ζ and azimuth α distributions of the events (normalized). Observations were performed mainly in late Autumn and Winter: because of this, the density distribution is shifted westwards.

6.6.

This work led to the scientific publication “*Detection of the Geminga pulsar with MAGIC hints possible power-law tail emission beyond 15 GeV*”, in *Astronomy & Astrophysics Letters* (MAGIC Collaboration et al., 2020). I played a central role in the data analysis, group organization and writing of the article, which was recognized as a highlight letter of the journal for the year 2020. With respect to the analysis presented in the publication, the one described in this thesis took advantage of an updated ephemeris, generated with the methods described in Appendix A, which enabled the use of a broader data-set for the *Fermi*–LAT analysis. The results reported here are similar to those of the above-mentioned publication, and constitute the main scientific outcomes of my doctoral project.

6.1 Observations overview

The MAGIC observations of Geminga are summarized in Table 6.1 and plotted schematically in Figure 6.1. Strict quality requirements were imposed during the observation and in the analysis process to reduce systematic uncertainties. The stereo trigger rate, which is dependent on the zenith distance and the weather conditions, was requested to be above 500 Hz for the whole length of the observations. Considering the typical accidental trigger rate for the Sum-Trigger-II of 180 Hz, this means that a threshold of 320 Hz of events was imposed on the observations. The MAGIC LIDAR (cfr. Section 2.6)

was used when possible to measure the transparency of the atmosphere. The minimum allowed transparency was $T_{9\text{km}} = 90\%$ from an altitude of 9 km above the ground level. Unfortunately, in the early part of the data-taking, reflected light from the laser beam of the LIDAR was interfering with the data-taking, and the LIDAR had to be switched off. For these data, only the stereo rates have been used as a selection criterion. The observations were performed in the zenith distance range from $\zeta_{\text{min}} = 11$ deg (culmination of Geminga in La Palma) to $\zeta_{\text{max}} = 25$ deg. The airmass in this range varies between 1.02 and 1.10, respectively. The effect of atmospheric absorption due to this small variation has been taken into account in the Monte-Carlo simulations. The total time collected in this way (corrected for the small dead time of the readout system) was $T = 80$ h.

Observations were taken in wobble mode (cfr. Section 2.6), with the wobble offset being $w = 0.4$ deg. This was done to enable possible further studies of the non-pulsed Geminga extended halo, which is not part of this work. Data taken in 2017 used the standard four wobble positions, disposed in a cross oriented as the right ascension and declination axes. The wobble bearings were therefore $\omega = 0^\circ, 180^\circ, 90^\circ, 270^\circ$. This was later recognized to be non optimal because of the presence of the bright star Alhena (γ Gem, with visual magnitude $m_V = 2$) close to two of such pointings. The configuration was changed for the following observation campaign to just two wobble positions, equidistant from the bright star: $\omega = 34^\circ, 214^\circ$. In this way the effects can be modeled in the same way in both pointings, and separate Monte-Carlo productions are no longer needed.

6.2 Data Analysis

The analysis of the data followed the workflow presented in Chapter 4. The raw files recorded by the MAGIC readout systems were calibrated and cleaned using a custom pipeline based on the MARS executables. The special MaTaJu Cleaning (Section 4.2.1) was applied, with cleaning thresholds optimized on the close-by field of the Crab Pulsar. This is reasonable, considering that both objects lie on the Galactic plane, are close to each other, and have bright stars of similar magnitude in the field of view. The following analysis steps were carried out using the standard analysis workflow, presented in Chapter 4. Given the exceptional low-energy of the data being analyzed, some of the selection cuts from the standard analysis have been relaxed. In particular the cut on the *Size* parameter (Section 4.3) was lowered to a value of 20 photo-electrons (compared to the standard one of 50 photo-electrons), and the maximum allowed deviation between the single-telescope reconstructed directions *DispDiff2* was raised to 0.2 deg^2 (compared to the standard of 0.05 deg^2). These relaxed cuts provide a larger effective area of the telescope at energies below 50 GeV at the expense of accepting a larger background (see Section 4.7.1). For the training of the random forest estimators, custom Monte-Carlo productions, closely following the apparent path in the sky covered by Geminga, were employed (cfr. Section 4.10). A similar simulation, with much larger statistics, was used to estimate the effective area of the telescopes. The resulting pipeline was tested and validated with quasi-contemporaneous data on the Crab Nebula and Pulsar, whose analysis is presented in Chapter 5.

The pulsar ephemeris used for the phaseogram was derived from *Fermi*-LAT data cov-

Date	MJD	T_{eff} [h]	$\langle L3 \rangle$ [Hz]	$\langle \cos \zeta \rangle$	Date	MJD	T_{eff} [h]	$\langle L3 \rangle$ [Hz]	$\langle \cos \zeta \rangle$
2017/01/23	57776	2.98	580.35	0.96	2018/12/16	58468	0.90	597.88	0.94
2017/01/24	57777	1.94	581.84	0.96	2018/12/17	58469	1.29	582.25	0.95
2017/01/25	57778	1.45	571.13	0.96	2018/12/31	58483	0.32	566.08	0.97
2017/01/26	57779	1.54	569.17	0.97	2019/01/03	58486	1.42	572.09	0.97
2017/01/27	57780	2.58	577.75	0.97	2019/01/09	58492	0.65	574.43	0.97
2017/01/28	57781	2.03	566.62	0.97	2019/01/12	58495	0.65	600.83	0.94
2017/01/29	57782	2.58	572.69	0.96	2019/01/14	58497	0.71	582.60	0.94
2017/01/30	57783	1.94	560.78	0.97	2019/01/27	58510	0.53	616.68	0.96
2017/01/31	57784	2.30	556.02	0.97	2019/01/31	58514	2.58	605.50	0.97
2017/02/01	57785	1.62	560.93	0.97	2019/02/01	58515	2.25	609.12	0.97
2017/02/16	57800	1.21	571.07	0.96	2019/02/03	58517	0.60	618.52	0.96
2017/02/19	57803	1.28	570.76	0.97	2019/02/04	58518	0.64	619.26	0.96
2017/02/20	57804	0.96	576.76	0.97	2019/02/05	58519	0.64	581.87	0.96
2017/02/26	57810	1.32	548.44	0.97	2019/02/06	58520	1.87	603.57	0.97
2017/02/27	57811	1.94	553.85	0.97	2019/02/07	58521	1.46	609.60	0.97
2017/02/28	57812	0.65	565.04	0.97	2019/02/08	58522	2.26	608.03	0.97
2018/11/08	58430	1.61	577.85	0.97	2019/02/09	58523	1.17	607.75	0.97
2018/11/09	58431	1.13	567.10	0.96	2019/02/10	58524	0.65	609.50	0.96
2018/11/10	58432	2.26	570.11	0.97	2019/02/24	58538	0.48	597.62	0.96
2018/11/11	58433	3.12	550.74	0.96	2019/02/27	58541	0.96	595.13	0.96
2018/11/14	58436	1.19	569.42	0.96	2019/02/28	58542	1.99	574.92	0.97
2018/12/04	58456	0.97	599.67	0.98	2019/03/01	58543	0.89	595.74	0.96
2018/12/10	58462	2.02	545.08	0.97	2019/03/02	58544	1.84	596.24	0.97
2018/12/11	58463	1.20	537.85	0.95	2019/03/03	58545	1.73	587.63	0.97
2018/12/12	58464	3.08	563.87	0.96	2019/03/04	58546	1.24	588.96	0.98
2018/12/13	58465	1.62	573.98	0.97	2019/03/05	58547	1.62	583.63	0.97
2018/12/14	58466	0.77	562.82	0.94	2019/03/06	58548	0.97	575.15	0.97

Table 6.1: Summary of the Geminga observations. Dates are in the year/month/day format. The MJD for such date is given too, together with the effective observation time, the average stereo trigger rate and the mean zenith distance during the observations.

ering a time span of $4381 \text{ d} \approx 12 \text{ a}$, using the methods presented in Appendix A. The ephemeris was tested on *Fermi*–LAT data and proved to be precise at the level of 0.1% (phase RMS, see Section A.4) for the whole period of validity between MJD 54683 (5. August 2008) and MJD 59062 (1. August 2020). Different wobbles of the observations have been analyzed separately to account for the presence of the bright star Alhena in the different field of views (cfr. Section 4.4). Energy-dependent θ^2 and hadronness cuts were applied to the data, with optimal cut values being determined from gamma-ray Monte-Carlo simulations, as described in Section 4.7.1. The MAGIC spectral points presented in this chapter were obtained with an unfolding procedure (cfr. Section 4.8.3) using the Tikhonov regularization method (Tikhonov, 1963). Other regularization methods provided compatible results. A regularization-independent forward folding of the spectrum with a power-law function was also applied. This provided the spectral parameters and the statistical confidence intervals listed in the tables.

6.2.1 *Fermi*–LAT Analysis

The *Fermi*–LAT spectral points used in this work were derived using 12 a of publicly available data in the energy range 100 MeV – 300 GeV and the Fermipy¹ (Wood et al., 2017) package for the binned likelihood analysis. The same data set was used to derive the pulsar ephemeris (Appendix A). A square field of view with a side of 27 deg centered on Geminga was adopted, and all sources of the 4FGL *Fermi*–LAT catalog (Abdollahi et al., 2020) within 30 deg were considered in the model. The data were processed with the P8R3_SOURCE_V2 instrument response functions (both front and back conversion events), and divided in separate components according to their Point Spread Function (PSF) class and energy. For data in the energy range 100 MeV – 300 MeV, only the better classes (PSF2 and PSF3, equivalent to a 50% containment radius) were considered. This cut was raised to a 75% containment radius (PSF classes 1 – 3) for data in the energy range 300 MeV – 1 GeV. Data above 1 GeV, for which the *Fermi*–LAT resolution is considerably better, was not cut in PSF at all. Finally, data were cut in the P2 phase region (0.550–0.642) and exposure was corrected for such a phase selection. A first coarse fit to all sources in the model was performed, in order to ensure that their starting values were close to the sought minima. Subsequently, model sources with predicted counts lower than unity were locked to their catalog values. The emission of Geminga was fit with a power-law with a sub-exponential cutoff model (function “PLSuperExpCutoff2”) and a point like spatial model. The normalization parameters of sources within 7 deg from Geminga were left free to be fit, as well as the spectral parameters of the ones closer than 5 deg. The galactic and isotropic gamma-ray diffuse emissions were also left free. In a second step, all sources were fixed to their values and Geminga was fitted once more letting also its exponential index β free (see Formula 6.4). The fits converged and no significant residual is found in the field of view. The count maps and TS significance map after the fit are presented in Figure 6.2. The spectral energy distribution was produced by fitting the measured emission separately on each of the intervals given by the energy binning, assuming a power-law with a spectral index of $\Gamma = 2$. This is equivalent to a flat line in log-log space.

¹ <https://fermipy.readthedocs.io/en/latest/>

6.3 Phaseogram

The phases of the MAGIC Geminga observations are shown in Figure 6.3. For this phaseogram, I used an estimated energy range between 25 GeV and 100 GeV. An excess of $N_{\text{exc}} = 2489.2$ events is identified in the region corresponding to the $P2$ pulse. This excess corresponds to a detection at the significance level of 6.3σ . The associated p-value is $p = 2.4 \cdot 10^{-10}$, equivalent to an odd ratio of 1 over 4 billion. On the other hand, no significant emission was found from the $P1$ pulse, as predicted in Section 4.6. Energy cuts were adopted to suppress the background signal by cosmic rays. Events with an estimated energy $E_{\text{est}} < 25$ GeV are extremely noisy and unlikely to have a meaningful primary particle reconstruction (see Section 4.5.3). On the other hand, the performance of the Sum-Trigger-II system above 100 GeV is roughly equivalent to the one of the standard MAGIC trigger. Previous MAGIC Geminga studies with the standard trigger and similar observation time did not result in a detection of pulsed signal (Ahnen et al., 2016). For this reason, the pulsation search was limited to $E_{\text{est}} \leq 100$ GeV. It is worth to stress that an *estimated energy* range of 25 GeV – 100 GeV does not correspond to a true gamma-ray energy in the same range, because of the relatively poor energy resolution that the imaging Cherenkov telescopes technique has at the lowest energies (see Section 4.5.3). To further reduce the background, upon producing the phaseogram, events were selected with energy-dependent θ^2 and hadronness cuts. The cut values were determined from Monte-Carlo simulated gamma-rays, with a false-positive ratio (gamma-ray events discarded by the cuts) set to a conservative maximum of 25% and 10% for θ^2 and hadronness, respectively. A plot of the cuts is given in Figure 4.19. Despite these event selections, a large remaining background is found, with $N_{\text{off}} \simeq 1.12 \cdot 10^5$ events produced by low-energy cosmic rays surviving the cuts. The signal to noise ratio amounts to $N_{\text{exc}}/N_{\text{off}} \simeq 2.2\%$. Given that the background selection is carried out in phase rather than time or position, systematic effects on it are rendered negligible and a low signal to noise ratio does not constitute a problem (see Section 4.7). The global deviation of the phase series from a uniform angular distribution was also tested. This is an alternative approach to search for the presence of a pulsed signal, free from any assumption on the signal and background regions, and commonly employed in blind pulsar searches. The Z_{10}^2 and H statistical tests (Buccheri et al., 1983; de Jager and Büsching, 2010) were used. With respect to the consolidated χ^2 test statistics for histograms, these statistical tests take advantage of the directional nature of the data under study. The interested reader may find a simple introduction to them in Appendix A. Both tests result in a rejection of the hypothesis of uniformly distributed data (signal generated by a fluctuation), at the level of 5.2σ and 4.8σ significance, respectively.

The MAGIC detection of pulsed gamma-rays from Geminga establishes it as the third known very high energy gamma-ray pulsar, and the first “middle-aged” one, which is observable at very high energies. Figure 6.4 gives its position in a $P - \dot{P}$ diagram (cfr. Section 1.4). These pulsars belong to the same class of non-recycled rotational powered pulsars. Among these, Geminga, at a characteristic age of $\tau \simeq 3.4 \cdot 10^5$ a, is the oldest one. The enlargement of this limited family of objects is crucial for the understanding of their properties and evolution. In light of the MAGIC Geminga detection, new candidates very high energy pulsars may be searched among the ones with $\tau \lesssim 10^5$ a and $B \gtrsim 10^8$ T.

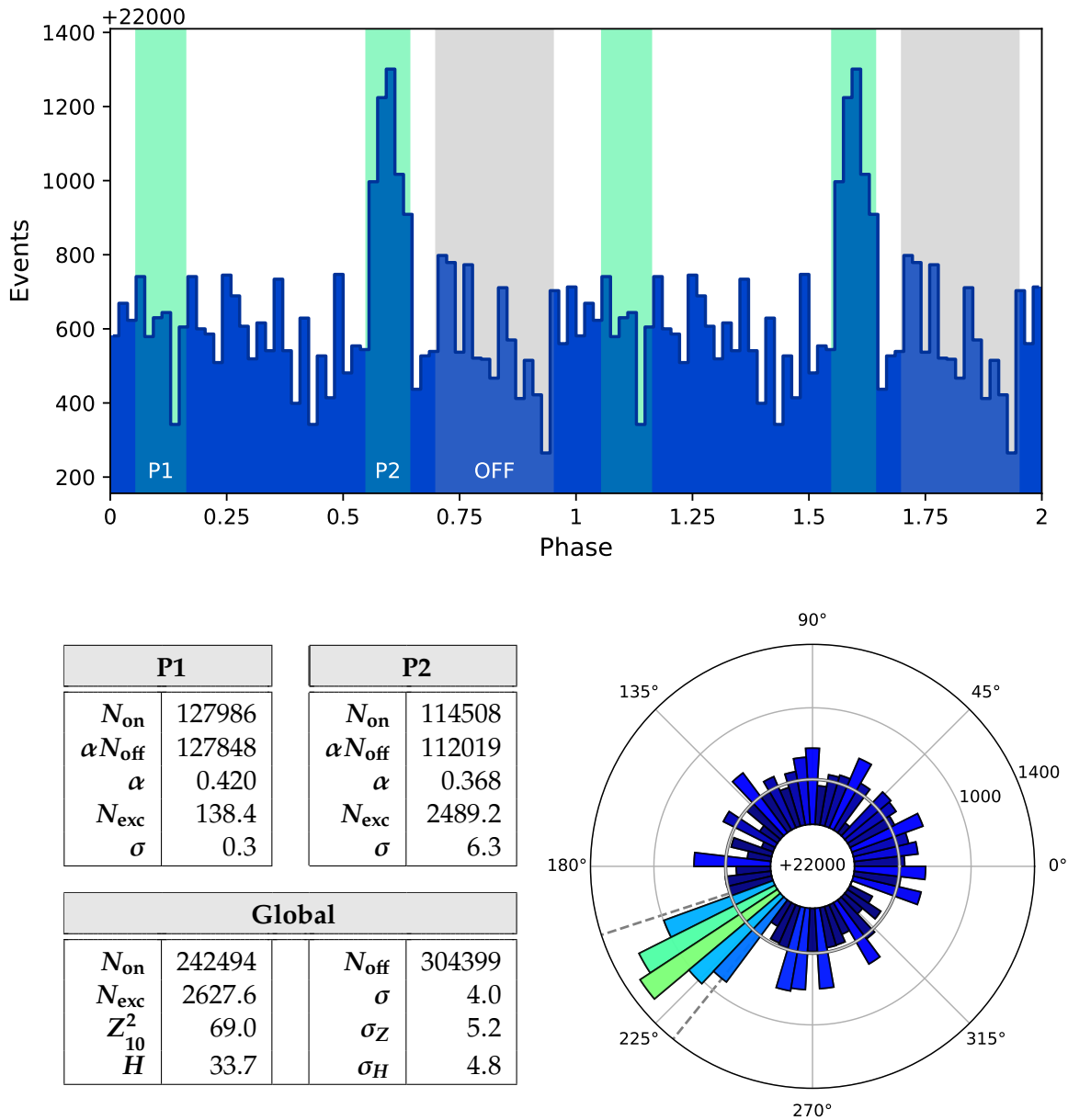


Figure 6.3: **Top:** phaseogram of the MAGIC Geminga data. The signal regions, determined a-priori from *Fermi*-LAT data, are highlighted in green, while the gray shaded area corresponds to the background estimation region. Two cycles of the pulsar are shown on the phase axis. Labels on the y-axis refer to the count of events minus 22000. **Bottom left:** Statistical data relative to the phaseogram, with event counts in each phase region, corresponding background counts, excess events and significances. Global variables such as the values and significances for the H and Z^2 tests are also presented. **Bottom right:** Cyclic projection of the same phaseogram, presenting the directional clustering of events corresponding to the P2 region (between the dashed gray lines). The background level is given by the gray circle. Colors are proportional to the number of excess events in each bin.

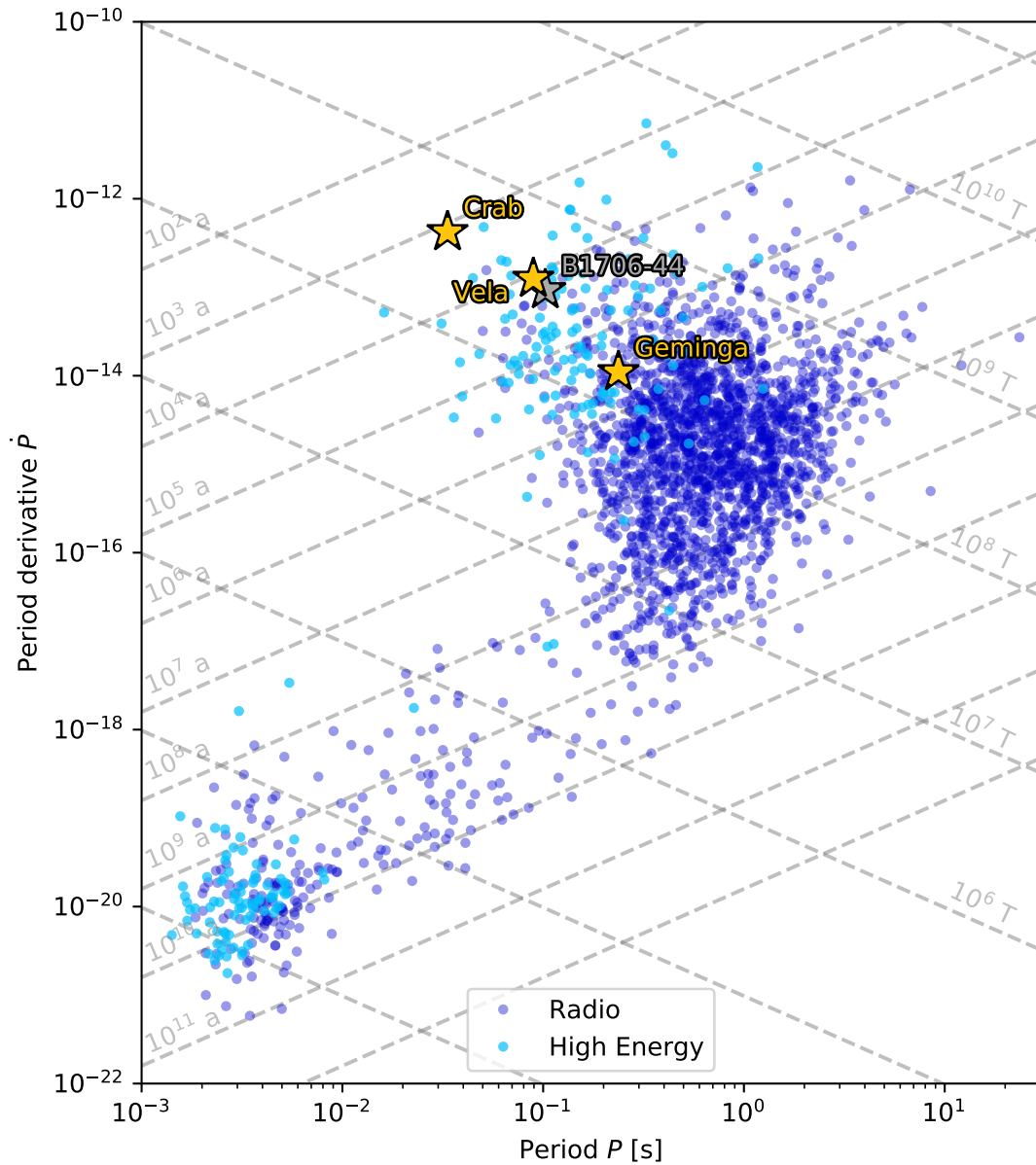


Figure 6.4: $P - \dot{P}$ diagram with known VHE pulsars. Among these, Geminga, in the central part of the plot, is the oldest one and the one with the weaker characteristic magnetic field. The plot includes also PSR B1706-44, preliminary reported by the H.E.S.S. collaboration in (Spir-Jacob et al., 2019). Data from the ATNF pulsar Catalogue: <https://www.atnf.csiro.au/research/pulsar/psrcat/>. In this context “High Energy” pulsars are those with detectable emission above radio wavelengths.

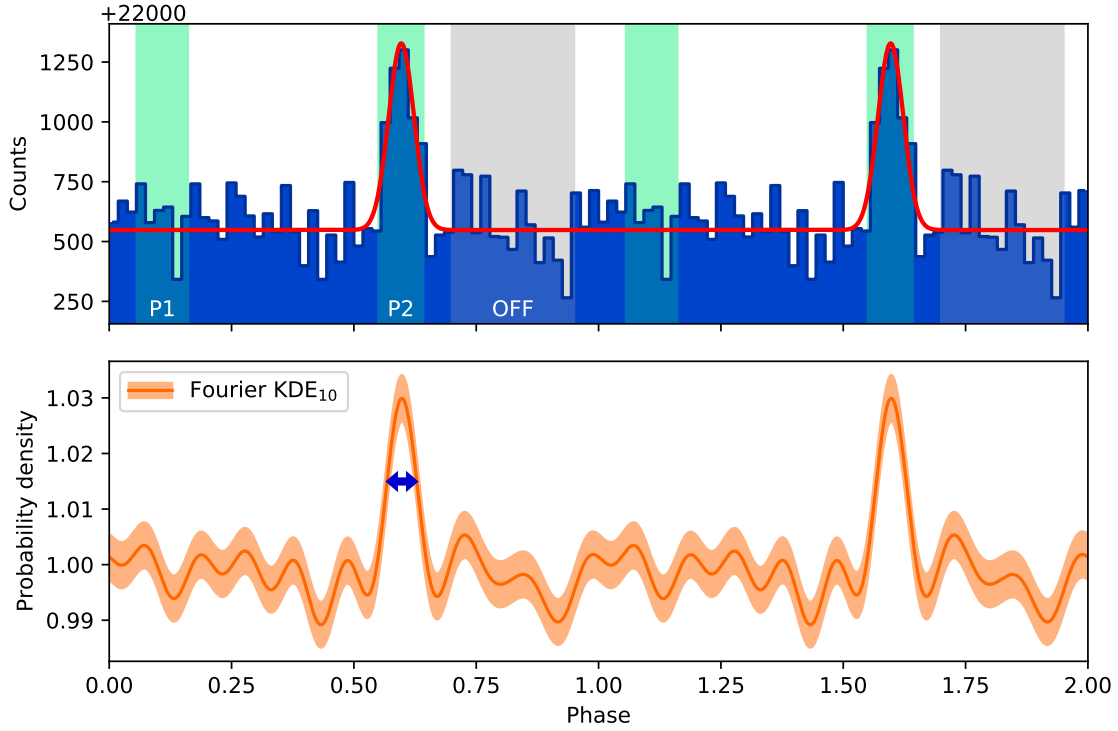


Figure 6.5: **Top:** MAGIC Geminga phaseogram of Figure 6.3 with the fitted cyclic Gaussian function. **Bottom:** probability density function for the phase, estimated with a Fourier kernel with $n = 10$ harmonics, with a 68% error band.

6.3.1 Phaseogram Analysis

The limited statistics of Figure 6.3 renders an energy-dependent morphology study of the phaseogram challenging. Instead, a fit of the P2 pulse in the whole $25 \text{ GeV} \leq E_{\text{est}} \leq 100 \text{ GeV}$ estimated energy range has been done with a cyclic Gaussian function. This is defined by:

$$\mathcal{G}(\varphi, A, \mu, \sigma) = A \sum_{k=-\infty}^{+\infty} \exp \left[-\frac{1}{2} \left(\frac{\varphi + k - \mu}{\sigma} \right)^2 \right]. \quad (6.1)$$

The background level of $N_{\text{bkg}} = 22548$ events per bin, as estimated from the off phase region, was subtracted from the phaseogram before the fit. The least-square fit converges at a reasonable minimum ($\chi^2/\text{NDF} = 0.68$) and leads to an estimate of the P2 pulse position $\mu_{\text{P2}} = 0.597 \pm 0.005$, with a spread $\sigma_{\text{P2}} = (2.6 \pm 0.5) \cdot 10^{-2}$, as in Figure 6.5. This figure is similar to the one found for *Fermi*-LAT data above 15 GeV. An alternative estimate of the pulse spread was obtained with a kernel density estimator method. To assess the probability density function of the phases of the MAGIC Geminga data, I employed a *Fourier kernel* $K(y) = \text{sinc}(y)/\pi$ (de Jager et al., 1986), which is associated to the Z_n^2 test statistics (cfr. Section A.3). The pulse spread was determined as the full width at half maximum of the largest peak in the distribution, and converted to a standard deviation assuming a Gaussian shape. The result of such binning-independent method, $\sigma'_{\text{P2}} = (2.6 \pm 0.2) \cdot 10^{-2}$, confirm the estimate obtained with the cyclic Gaussian fit.

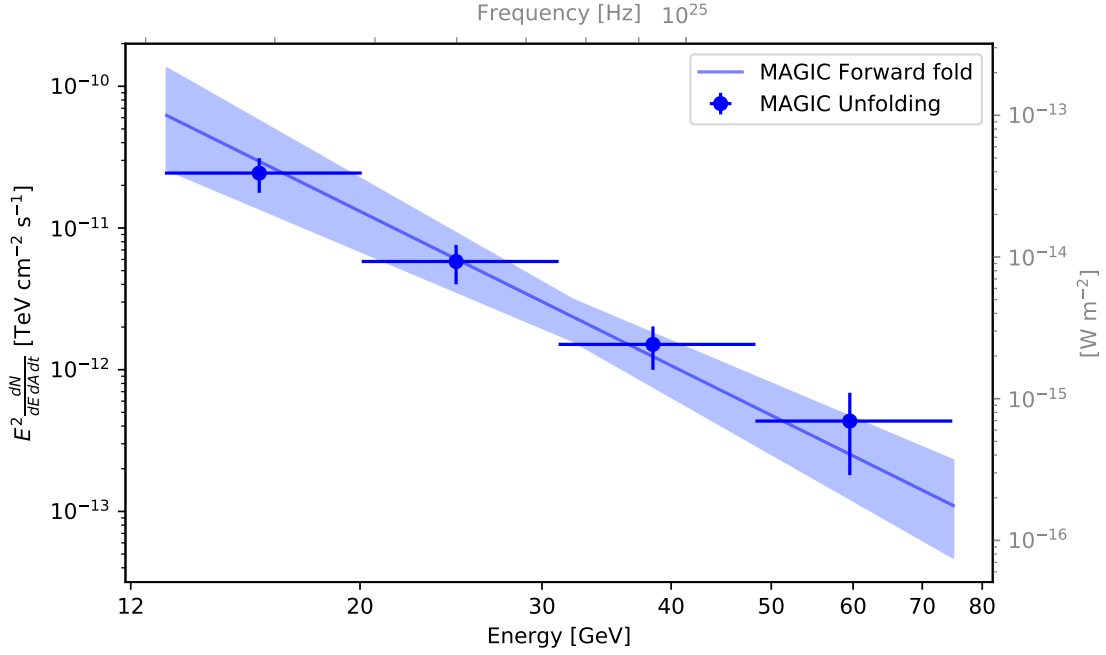


Figure 6.6: MAGIC spectrum of Geminga. Spectral points were produced with an unfolding procedure (Tikhonov regularization). The power-law parameters (solid line) were obtained instead with the forward folding method. Its error band gives the 1σ confidence interval. The power-law parameters are listed in Table 6.2, while the values of the spectral points are given in Table 6.3.

6.4 Pulsed Spectrum

The spectrum of the P2 pulse, as measured by MAGIC, is presented in Figure 6.6. It was reconstructed both with a forward folding approach and with a unfolding method, using the Tikhonov regularization strategy (cfr. Section 4.8.3). While the first method delivers an estimate of the optimal parameters for the fitted model, the second results in a series of (correlated) spectral points, corrected for the MAGIC Telescopes energy migration matrix. These points can be fit with a functional form, provided that their correlation is taken into account. A simple power-law relation has been used as a model:

$$\mathcal{F}(E) = f_0(E/E_0)^{-\Gamma}, \quad (6.2)$$

where E_0 is a fixed normalization energy, f_0 measures the differential flux at E_0 , and Γ is the spectral index of the power-law. The parameters found by the forward folding are listed in Table 6.2, whereas details about the spectral points of Figure 6.6 are given in Table 6.3. The forward folding approach reconstructs a very soft spectral index of $\Gamma = 5.62 \pm 0.54$, among the steepest spectra ever measured by Imaging Atmospheric Cherenkov Telescopes. The quoted uncertainties are statistical only: systematic uncertainties are described in the following paragraph (6.4.1). The presence of a similar power-law component in the spectrum of the Crab pulsar (Aliu et al. (2008) and Section 5.4), which is explained by Inverse-Compton scattering, suggests a similar mechanism for the emission, albeit the spectrum of Geminga is much steeper. Details on the physical

$\mathcal{F}(E) = f_0(E/E_0)^{-\Gamma}$			
E_0	f_0	Γ	χ^2/NDF
32.15	$(2.3 \pm 0.7) \cdot 10^{-9}$	5.62 ± 0.54	15.0/15

Table 6.2: Power-law parameters obtained from the forward folding procedure. The fixed normalization energy $E_0 = 35.15$ GeV is the decorrelation energy of the spectral points. The flux parameter f_0 is given in units of $\text{TeV}^{-1}\text{cm}^{-2}\text{s}^{-1}$.

Spectral points					Correlation matrix				
N ^o	E_{low}	E_{mid}	E_{up}	SED	N ^o	1	2	3	4
1	12.9	16.0	20.1	24.4 ± 6.7	1	1			
2	20.1	24.8	31.1	5.80 ± 1.79	2	0.03	1		
3	31.1	38.4	48.3	1.51 ± 0.51	3	-0.58	0.14	1	
4	48.3	59.5	74.8	0.43 ± 0.25	4	-0.47	-0.44	0.25	1

Table 6.3: Left: MAGIC Geminga spectral points obtained with the unfolding procedure. Energy is given in units of GeV, and SED values are in $10^{-12} \text{TeVcm}^{-2}\text{s}^{-1}$. Right: the correlation matrix among the flux values. The correlation arises as an effect of the unfolding procedure.

significance of the Geminga power-law component, and a comparison with the properties of the Crab, are given in the following paragraphs.

6.4.1 Systematic Effects

In Section 4.9, I reported that a value of the analysis energy threshold E_{thr} can be computed using Monte-Carlo simulations. This is defined as the peak of the distribution of the true energy of the simulated events, which have been processed exactly in the same way as real data, and survived the entire analysis chain. Such a value is indicative of the minimum energy that can be trustfully reconstructed by the analysis. Below the energy threshold, small fluctuations in the estimated energy can produce large variations in the effective area and yield large systematic uncertainties in the measured fluxes. The energy threshold for the MAGIC analysis of Geminga was computed by processing a large set of Monte-Carlo simulation with the same analysis pipeline used for the data. A power-law spectrum with $\Gamma = 5$ was used. The true energy distribution of the events surviving the entire analysis chain is given in Figure 6.7, and a threshold value of $E_{\text{thr}} \approx 15$ GeV is found. This is the lowest energy threshold ever achieved by an Imaging Atmospheric Cherenkov Telescope system. Compared with the MAGIC standard analysis energy threshold of 50 GeV reported in (Ahnen et al., 2016), such improvement is justified by the technical innovations represented by the Sum-Trigger-II and MaTaJu cleaning (cfr. Sections 2.5 and 4.2.1). The threshold value of 15 GeV supports the reliability of the MAGIC measurements of Figure 6.6.

To confirm the low energy threshold found with Monte-Carlo simulations, its value was assessed with an alternative approach, using a set of constrained forward folding (ref. Section 4.8.3) fits of a power-law spectrum on real data. The minimum true energy that

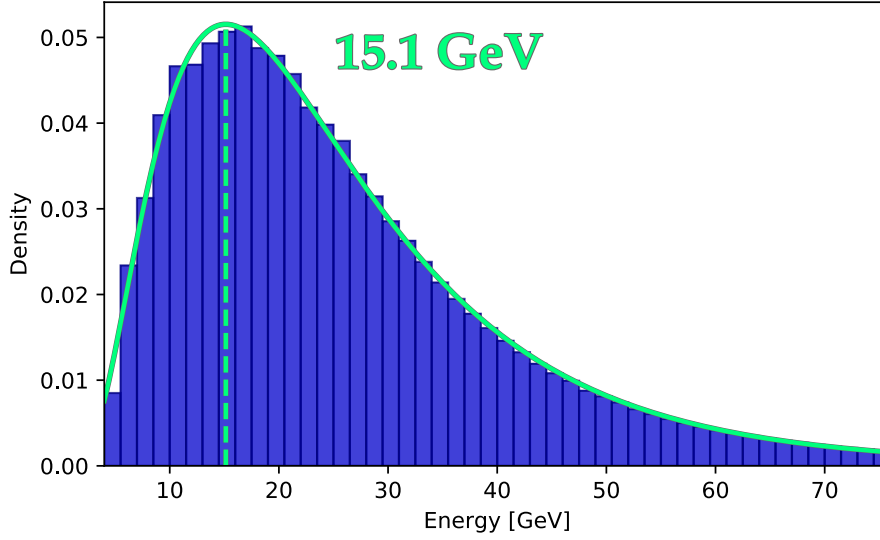


Figure 6.7: Energy threshold for the MAGIC Monte-Carlo data, assuming a power-law spectrum with a spectral index $\Gamma = 5$, similar to the Geminga one. The histogram plots the density of Monte-Carlo events surviving the entire pipeline of data analysis, with the same settings used for real data. The energy threshold value is defined as the peak of the distribution, and found to be $E_{\text{thr}} = 15.1$ GeV.

could be reconstructed by the forward folding was artificially limited to be larger than a cut value E_{min} . Such procedure is analogous to a removal of entries with $E_{\text{true}} \leq E_{\text{min}}$ from the migration matrix. The power-law fit χ^2 and its associated p-value are plotted as a function of E_{min} in Figure 6.8. For $E_{\text{min}} \leq 10$ GeV, no significant change is observed with respect to an unconstrained forward folding. As the E_{min} value is further increased, the quality of the power-law fit determined by the χ^2 goodness-of-fit test worsens. This is a consequence of real events with $E < E_{\text{min}}$ being forced by the constraint to be accounted at a larger energy, distorting the resulting spectrum. The lowest energy for which this is observed is $E_{\text{min}} \approx 15$ GeV, corresponding to the lowest energy events which are significantly detected. This is in good agreement with the value of E_{thr} found in the previous paragraph.

These arguments provide confidence that the MAGIC measurements of the Geminga spectrum are not affected by abrupt changes under the effect of systematic uncertainties. The possible entity of such effects was estimated by repeating the forward fold fits of the spectrum and introducing an artificial bias in the model of the telescope efficiency. This was achieved by multiplying the true energy of the Monte-Carlo simulations used to estimate the effective area with an *energy scale factor* ϵ . The resulting model is affected by a miscalculation of the effective area, simulating an under or overestimate of the telescope light throughput per shower. A similar effect could be caused by varying weather conditions or fluctuations in the telescope performance. Table 6.4 lists the effects on power-law fits of the Geminga spectrum, for ϵ in a $\pm 15\%$ range. A mild energy mismatch ϵ results in a large variation of the estimated fluxes. This is a consequence of the steepness of the Geminga spectrum. Energy scale factors of 5% and 15% produce an average variation in the base flux f_0 of $\sim 22\%$ and $\sim 80\%$, respectively. On the contrary, in a broad interval

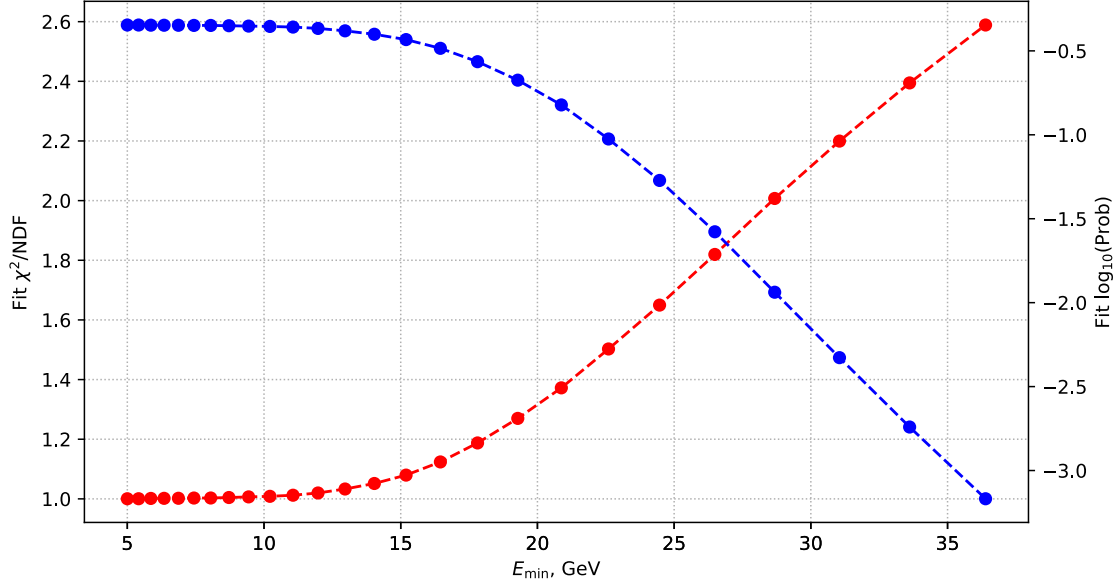


Figure 6.8: Validation of the lowest energy spectral points in the gamma-ray spectrum of Geminga. Forcing the forward folding reconstruction of a power-law spectrum to energies above a threshold E_{\min} causes a degradation of the fit quality. The increase in the χ^2 (red dots, left axis) and decrease in p-value (blue dots, right axis), become visible for $E_{\min} \geq 10$ GeV.

ϵ	f_0	Γ	s_{f_0}	s_{Γ}
0.85	1.1 ± 0.4	5.64 ± 0.55	0.47	1.005
0.90	1.4 ± 0.5	5.63 ± 0.55	0.61	1.003
0.95	1.8 ± 0.6	5.62 ± 0.54	0.78	1.001
1.00	2.3 ± 0.7	5.62 ± 0.54	1	1
1.05	2.8 ± 0.8	5.56 ± 0.53	1.21	0.991
1.10	3.4 ± 0.9	5.51 ± 0.53	1.48	0.981
1.15	4.1 ± 1.0	5.46 ± 0.52	1.78	0.972

Table 6.4: Base fluxes f_0 in $10^{-9} \text{TeV}^{-1} \text{cm}^{-2} \text{s}^{-1}$ at $E_0 = 32.15 \text{GeV}$ and spectral index Γ with the energy of Monte-Carlo events artificially scaled by ϵ . The corresponding scale factors of the spectral parameters are given by s_{f_0} and s_{Γ} .

of ϵ , the spectral index Γ varies on the order of 1%. This is one order of magnitude lower than its statistical error, which constitutes the dominant source of uncertainty for its measurement. These results suggest that a systematic miscalculation of the effective area can be modeled as a rigid shift of the power-law spectrum of Geminga, without inducing a sensible deformation in it.

Based on these findings, a scale parameter ς on the values of MAGIC spectral energy distributions, to be treated as a nuisance parameter, was introduced in all joint fits of MAGIC and *Fermi*-LAT Geminga data. For a power-law spectrum, the scale factor ς is related to the energy scale factor ϵ by:

$$\varsigma = \epsilon^{\Gamma-1}, \quad (6.3)$$

with Γ being the spectral index. The overlap between MAGIC and *Fermi*-LAT measurements at energies below 30 GeV introduces a stringent constraint to the range of such scale parameter ς . The maximum likelihood value of ς for each fit is provided in the summary Table 6.9 and Appendix B. For a simple power-law model, including the overlapping *Fermi*-LAT and MAGIC measurements, a flux scale $\varsigma = 1.07 \pm 0.15$ is found (see Table 6.6). Assuming a spectral index of $\Gamma = 5$, this corresponds to an energy scale mismatch between MAGIC and *Fermi*-LAT of $\epsilon = 1.02 \pm 0.03$. This is a remarkably good result, and confirms that MAGIC are a very powerful and reliable instrument to study the emission of pulsars in the energy range below 100 GeV.

6.5 Joint MAGIC and *Fermi*–LAT Spectrum

In order to study the emission of P2 in a broader energy range, the MAGIC spectral points were fitted together with the Geminga spectral measurements of *Fermi*–LAT. Figure 6.9 gives the global spectrum obtained by stacking the MAGIC results of Figure 6.6 with *Fermi*–LAT spectral points above 100 MeV. The two data sets overlap and deliver compatible estimates of the flux in the 10 GeV to 40 GeV range. In this interval, due to its large effective area, MAGIC provides flux measurements with a similar uncertainty in only 80 h of observation, compared to the 12 years integration time of *Fermi*–LAT.

The joint spectral points were fitted with a power-law with an exponential cutoff function (referred in the following text as “free exponential cutoff”) of the kind:

$$\mathcal{F}(E) = f_0 (E/E_0)^{-\Gamma} \cdot \exp \left[-(E/E_{\text{cut}})^{\beta} \right] \quad (6.4)$$

The parameters f_0 and Γ have the same meaning as in Equation 6.2. The parameter E_{cut} is the *Cutoff Energy* and β is the *Cutoff Index*, indicating the steepness of the cutoff. The case with a purely exponential cutoff is given by $\beta = 1$ (described in the following as “pure exponential cutoff”). Such spectral shape is predicted to be result of a synchro-curvature emission mechanism (Aliu et al., 2008). Cases with $\beta > 1$ describe a super-exponential cutoff, in which the flux falls off with increasing energy faster than an exponential. Similar spectral shapes are predicted by the Polar-Cap emission model, due to single photon pair production in the intense pulsar magnetic field (Baring, 2004). The opposite happens for $\beta < 1$, which gives rise to a sub-exponential cutoff. This case is the most widely considered for *Fermi*–LAT pulsars with high energy emission (Abdo et al., 2013) and is usually interpreted as a superposition of independent pure exponential cutoff components (Abdo et al., 2010a) from different emission regions.

The joint *Fermi*–LAT and MAGIC data for P2 were fitted with a maximum likelihood approach. The likelihood distributions for the parameters of a pure and free exponential cutoff power-law were sampled by means of a Markov-Chain Monte-Carlo algorithm using the EMCEE Python package². The results are presented in Figure 6.9, in which curves corresponding to the maximum likelihood parameters are drawn. These parameters are reported in Table 6.5 with uncertainties corresponding to the standard deviation of their distribution (1σ confidence interval). The full parameter distributions and their

² <https://emcee.readthedocs.io/>

Function	f_0	Γ	E_{cut}	β	$-2 \log \mathcal{L}$
<i>Pure cutoff</i>	0.357 ± 0.002	1.089 ± 0.003	2.88 ± 0.02	1 (fixed)	362.4
<i>Free cutoff</i>	0.534 ± 0.019	0.915 ± 0.014	1.48 ± 0.08	0.742 ± 0.013	42.5

Table 6.5: Parameter values of the joint MAGIC and *Fermi*–LAT fits with an exponentially cutoff power-law. The base flux f_0 is given in units of $10^{-3} \text{ TeV}^{-1} \text{ cm}^{-2} \text{ s}^{-1}$ at the pivot energy of $E_0 = 1 \text{ GeV}$. The cutoff energy E_{cut} is in units of GeV. The maximum likelihood ratio test statistic TS equals to $-2 \log \mathcal{L}$. The parameter values are given as the median of their likelihood distribution, with uncertainties given by the 16% and 84% quantiles (analogous to one standard deviation). The Pure exponential cutoff model can be rejected based on its TS value.

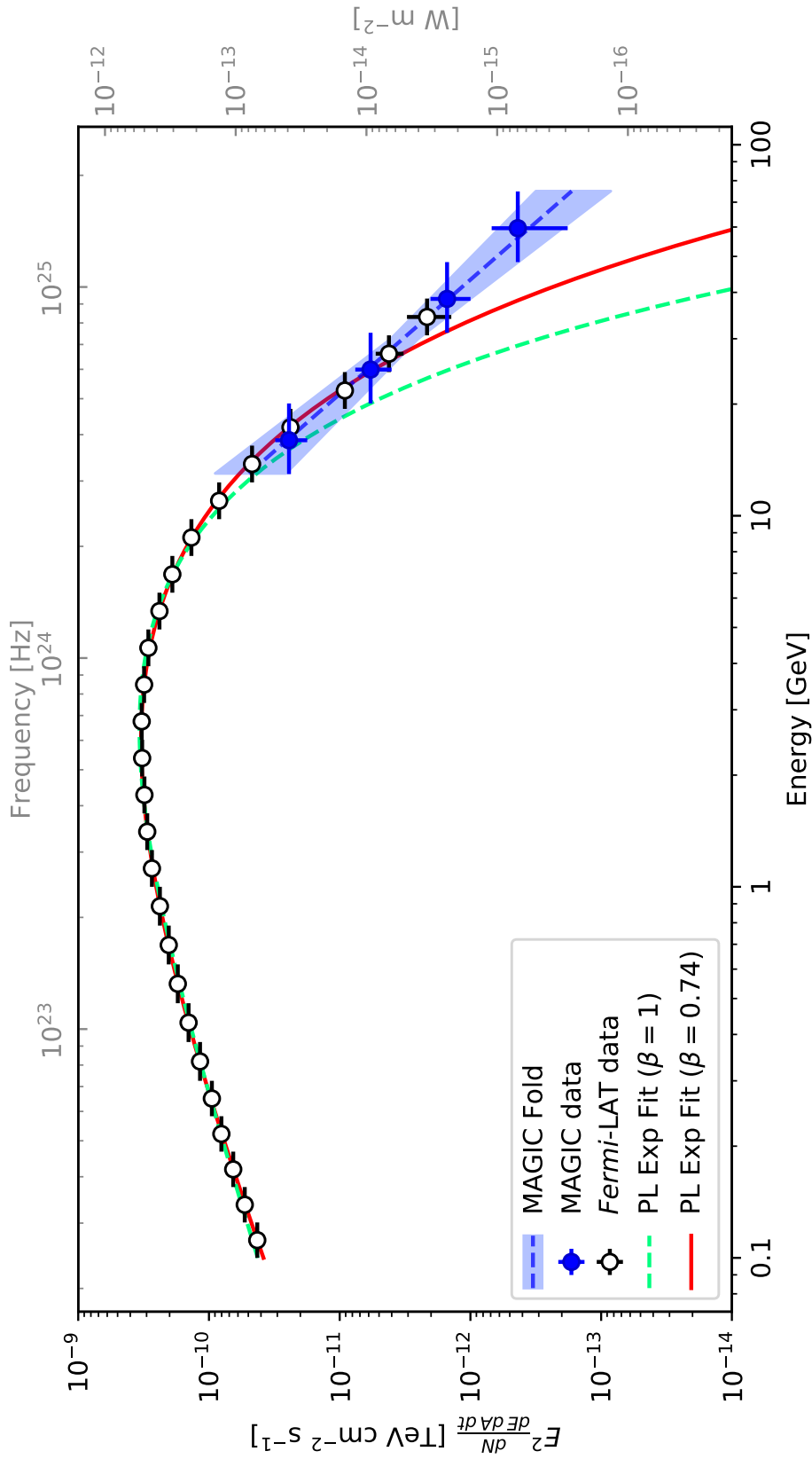


Figure 6.9: Geminga spectrum with joint *Fermi*-LAT and MAGIC data for P2. The two data sets agree well in the overlapping region. The spectral fits were carried out with a power-law function with an exponential (dashed green) and sub-exponential (solid red) cutoff. These spectral parameters are reported in Table 6.5.

correlations are provided in Appendix B. Since the unfolding procedure carried on the MAGIC spectra produces a set of correlated spectral points (cfr. Table 6.3), the fits were performed using a likelihood function which takes the correlation matrix of MAGIC points into account. The *Fermi*-LAT spectral points were instead assumed to be uncorrelated³.

In the free exponential cutoff fit, the best value for the cutoff index is found at $\beta = 0.742 \pm 0.013$, significantly below unity. As the pure and free exponential models are nested, a likelihood ratio test can be used to compare them, yielding a test statistics $-2\Delta \log \mathcal{L} = 320$ in favor of the free cutoff model, corresponding to a significance of $\sim 18 \sigma$. I therefore conclude that the pure exponential cutoff does not represent the joint *Fermi*-LAT and MAGIC data on the P2 emission of Geminga. This is in agreement with what was found in (Ahnen et al., 2016), where *Fermi*-LAT data spanning five years of operation were used. In previous works, a similar analysis of the phase-averaged spectra of multiple pulsars led to the proposal that such a sub-exponential cutoff results from the superposition of several pure exponential cutoff components, originating in different regions of the pulsar magnetosphere (Abdo et al., 2010a, 2013). The fact that a similar spectrum is found in the non-averaged P2 phase region constraints this hypothesis. In addition, the highest energy MAGIC and *Fermi*-LAT points seem to deviate from the best fit free cutoff model. These considerations prompted a study to quantify how significant the disagreement with the free cutoff model is and if the data suggests instead a continuation of the spectrum with a power-law tail at the highest energies. Such a power-law emission has already been observed in the spectrum of the Crab pulsar (Ansoldi et al., 2016), where it is explained by the inverse Compton emission mechanism.

6.5.1 Tests for a Power-Law component

Two tests were made on the joint MAGIC and *Fermi*-LAT points to constrain the presence of a power-law like tail at the highest energies. In the first test, overlapping MAGIC and *Fermi*-LAT Geminga data were fitted with a power-law and a log-parabola function in order to determine if they favor a model with curvature (deviation from a power-law) at the highest energies of the spectrum. The log-parabola function, given by:

$$\mathcal{F}(E) = f_0 (E/E_0)^{-\Gamma + b \log(E/E_0)} \quad (6.5)$$

was chosen because it is among the simplest models which possesses curvature and includes the power-law as sub-case. Fits with both functions are given in Figure 6.10 and their resulting parameters are listed in Table 6.6. The most likely log-parabola model has a spectral index of $\Gamma = 5.42 \pm 0.64$ and curvature index $b = 0.01 \pm 0.65$, compatible with 0. The power-law model delivers a spectral index of $\Gamma = 5.41 \pm 0.18$, essentially identical to the previous one. This is further evidenced by the maximum Likelihood values for both fits being equal. The spectral index is consistent with the one derived

³ The *Fermi*-LAT spectral points are obtained with a maximum likelihood fit with power-law segments. Each segment is defined *independently* on the energy binning intervals, and corresponds to one spectral point. The correlation among them could arise only from the small energy resolution of the *Fermi*-LAT telescope, which is of the order of 10% in the considered energy range: https://www.slac.stanford.edu/exp/glast/groups/canda/lat_Performance.htm. See also Section 6.2.

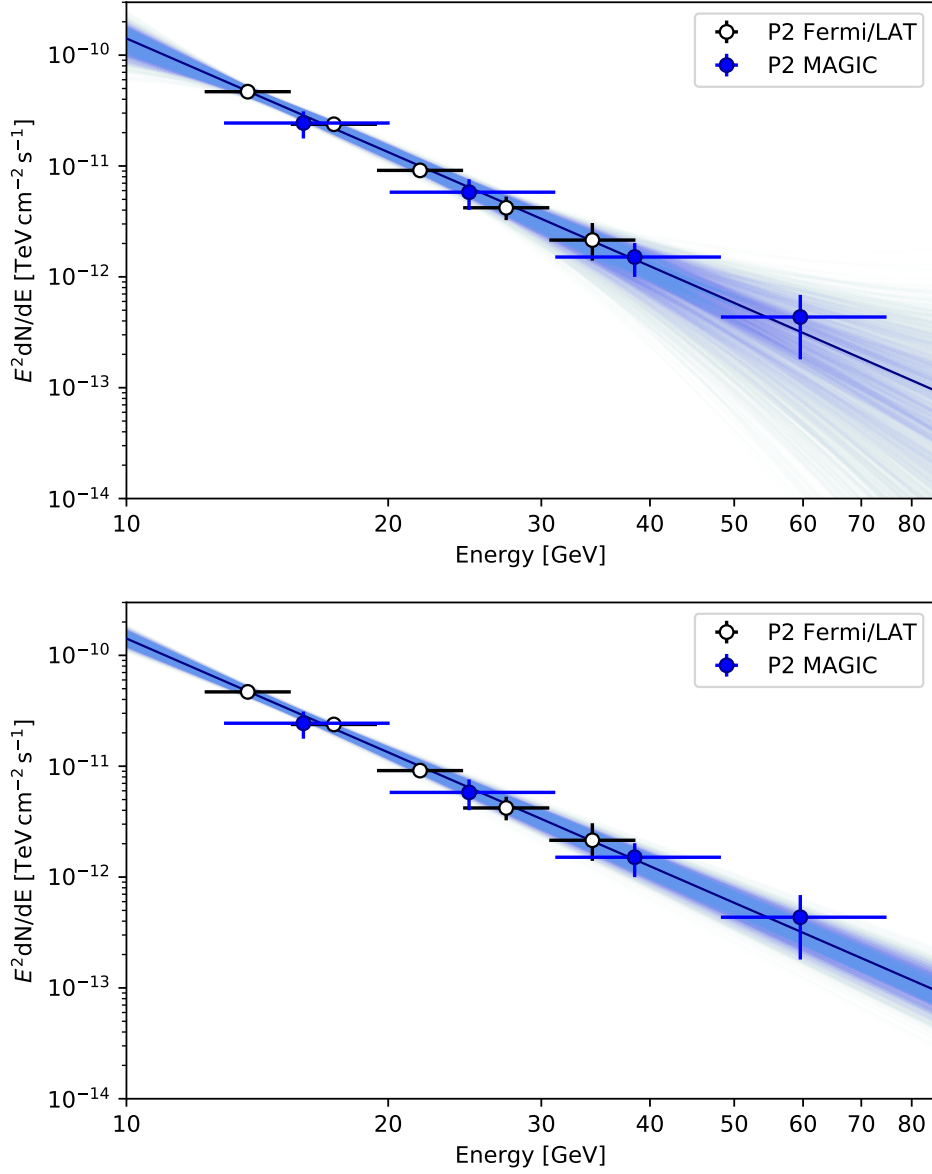


Figure 6.10: Maximum likelihood fits for the log parabola described by Formula 6.5 (**top**) and the power-law from Formula 6.2 (**bottom**). The black solid line indicates the maximum likelihood solution, whereas light blue lines are random samples from the parameters distribution.

Function	f_0	Γ	b	$-2 \log \mathcal{L}$
<i>LP</i>	$(0.255 \pm 0.046) \cdot 10^{-8}$	5.42 ± 0.64	0.01 ± 0.65	2.14
<i>PL</i>	$(0.256 \pm 0.035) \cdot 10^{-8}$	5.41 ± 0.18	0 (fixed)	2.14

Table 6.6: Parameter values of the log-parabola and power-law fits of MAGIC and *Fermi*-LAT spectral data above 10 GeV. The base flux f_0 is in units of TeV⁻¹cm⁻²s⁻¹ at $E_0 = 32.15$ GeV.

by the forward folding of MAGIC data alone, $\Gamma = 5.62 \pm 0.54$. I conclude that the data are not described significantly better by the log parabola than by the simpler power-law. Therefore, the combined MAGIC and *Fermi*-LAT data above do not seem to significantly support a model with curvature any better than a simple power-law.

A second test employed a fit of the *Fermi*-LAT and MAGIC points in the whole energy range between 100 MeV and 100 GeV. Since a unified theoretical description of the pulsar emission in a broad energy range is still lacking (see later Section 6.6), I employed a model which results from the composition of a free exponentially cutoff power-law with a power-law like tail in the overlapping energy range of *Fermi*-LAT and MAGIC:

$$\mathcal{F}(E) = \begin{cases} f_0 (E/E_0)^{-\Gamma} \exp[-(E/E_{\text{cut}})^\beta] & (E \leq E_M) \\ f_M (E/E_M)^{-\Gamma_1} & (E > E_M) \end{cases}, \quad (6.6)$$

where f_M is the flux at the lowest energy of the overlapping MAGIC and *Fermi*-LAT spectra, $E_M \simeq 12.3$ GeV. It has to be stressed that the model is not nested with a simple power-law with a free exponential cutoff and a significance test based on the likelihood ratio is not possible. A qualitative comparison based on the Bayesian Information Criterion (BIC) has been done instead. This is defined as:

$$\text{BIC} = p \log(N) - 2 \log \mathcal{L}, \quad (6.7)$$

where p is the number of parameters in the model, N is the number of data points and $\log \mathcal{L}$ is the maximum likelihood. A BIC test acts as a penalized likelihood ratio test, with the penalization term $p \log(N)$ being larger for models with more parameters. A BIC difference of $\Delta\text{BIC} = 5.8$ is found between the free exponential cutoff model and the one with a power-law tail. This can be interpreted as a positive evidence in favor of the latter one. The parameters found in the maximum likelihood fit for both models are given in Table 6.7. It shall be noted that models deliver fully compatible estimates of the parameters. This is due to the number of *Fermi*-LAT data points below E_M being larger than the ones above E_M , which suffer a larger statistical uncertainty. A graph of the two solutions is presented in Figure 6.11. The reader may find the resulting distributions of the parameters in Appendix B.

The tests carried on joint *Fermi*-LAT and MAGIC data show that the statistical significance is not sufficient to exclude the free exponential cutoff model, however they give an indication that the spectrum of Geminga at energies immediately above 10 GeV may not follow a sub-exponential cutoff and decay as a power-law instead. This trend could be naturally explained if Inverse Compton Scattering of e^\pm in the pulsar magnetosphere

Function	f_0	Γ	E_{cut}	β	Γ_1	BIC
<i>Composite</i>	0.54 ± 0.02	0.914 ± 0.016	1.48 ± 0.09	0.740 ± 0.012	5.4 ± 0.2	53.7
<i>Free cutoff</i>	0.53 ± 0.02	0.915 ± 0.014	1.48 ± 0.08	0.742 ± 0.013		59.5

Table 6.7: Maximum likelihood parameter values for the composite model of Equation 6.6. The base fluxes f_0 is in units of $10^{-3}\text{TeV}^{-1}\text{cm}^{-2}\text{s}^{-1}$ at the energy of $E_0 = 1$ GeV. The cutoff energy E_{cut} are in units of GeV.

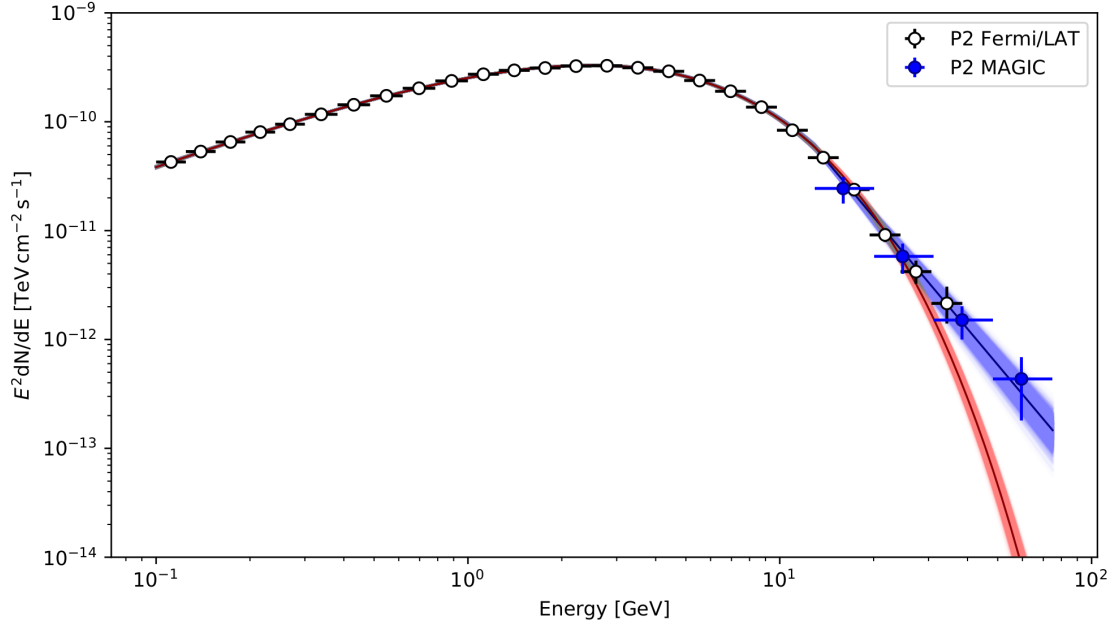


Figure 6.11: Maximum likelihood fits for the composite model with a power-law tail of Formula 6.6 (blue), in comparison with the free cutoff power-law model (red). Confidence intervals were constructed by randomly sampling the parameter distribution.

is the responsible mechanism for the production of the observed gamma-rays. The next section discusses such possibility in the context of some current pulsar emission models. This possibility has currently been confirmed only for the Crab pulsar, with the observation of its TeV pulsed component (Ansoldi et al., 2016).

6.6 Outer Gap modeling⁴

The MAGIC observation of Geminga at the very high energies questions the models considered for its emission. The hint of a power-law behavior of the spectrum above 30 GeV, seemingly without a cutoff, points to an inverse Compton emission mechanism. Such possibility has been studied in the framework of the stationary Outer Gap model Hirotani (2006, 2013). This is one of the classical models for high-energy and very-high energy pulsar emission and has been briefly discussed in Section 1.3.

Figure 6.12 presents a selection of the simulated spectra of the gamma-ray emission of Geminga. A distance of $d \simeq 250 \text{ pc} = 815.4 \text{ ly}$ (Faherty et al., 2007) was assumed for Geminga, and spectra were produced in a range of the three physical parameters that affect their shape: the magnetic inclination angle α and the viewing angle ζ with respect to the rotational axis, and the strength of the magnetic moment with respect to the dipole solution μ/μ_d . I stress that the curves were not fit to the data. The best agreement is found for a set of parameters not far from $\mu/\mu_d \simeq 1.4$, $\alpha \simeq 30 \text{ deg}$ and $\zeta \simeq 95 \text{ deg}$, represented by the blue curve in Figure 6.12. The model interprets the observed spectrum as the superposition of two emission components. The first component should be given by

⁴ The work presented in this section has been done in collaboration with Dr. K. Hirotani.

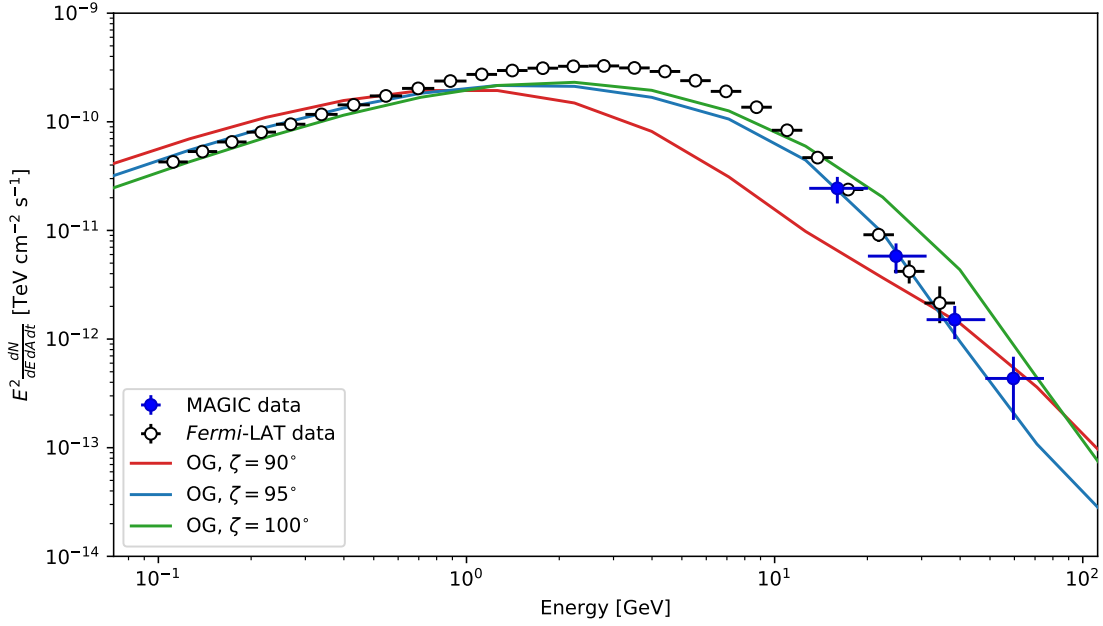


Figure 6.12: Set of theoretical predictions for the Geminga P2 emission, simulated according to the Outer Gap model. Curves shown are for a magnetic inclination $\alpha = 30^\circ$, a magnetic moment $\mu = 1.4\mu_d$ and three different viewing angles ζ . Simulations were produced by Dr. K. Hirotani. Curves are not fit to the data.

synchrotron-curvature radiation produced by electrons e^- streaming along the field lined towards the light cylinder of the magnetosphere (see Section 1.3). These outward going electrons produce the fluxes observed by the *Fermi*-LAT fluxes below 15 GeV. Above 15 GeV a second component becomes relevant, resulting from the positrons e^+ streaming towards the pulsar. The head-on interaction of the latter with the seed X-ray field photons from the black body emission of the pulsar give rise to an inverse-Compton process. The very high energy gamma-ray flux with a steep power-law spectrum observed by MAGIC is explained as a result of this process. The inverse Compton component is predicted to become dominant over the synchrotron-curvature one at the energy of 40 GeV, and to extend further at energies above 100 GeV.

However, none of the theoretical curves reproduces the shape of the observed *Fermi*-LAT spectrum, which is systematically underestimated at its peak of emission around 3 GeV. This indicates an intrinsic inadequacy of the outer gap model to describe the spectrum of Geminga and prompts for caution in the interpretation of the results. In order to better constrain the emission properties of the magnetosphere of Geminga, new theoretical solutions shall be developed. In these field, Particle In Cell extensive simulations such as the ones presented in (Kalapotharakos et al., 2018; Brambilla et al., 2018) for the equatorial current sheet emission model seem a promising way to proceed. A similar study for the outer gap electrodynamics would be beneficial for the field of very high energy gamma-ray pulsars.

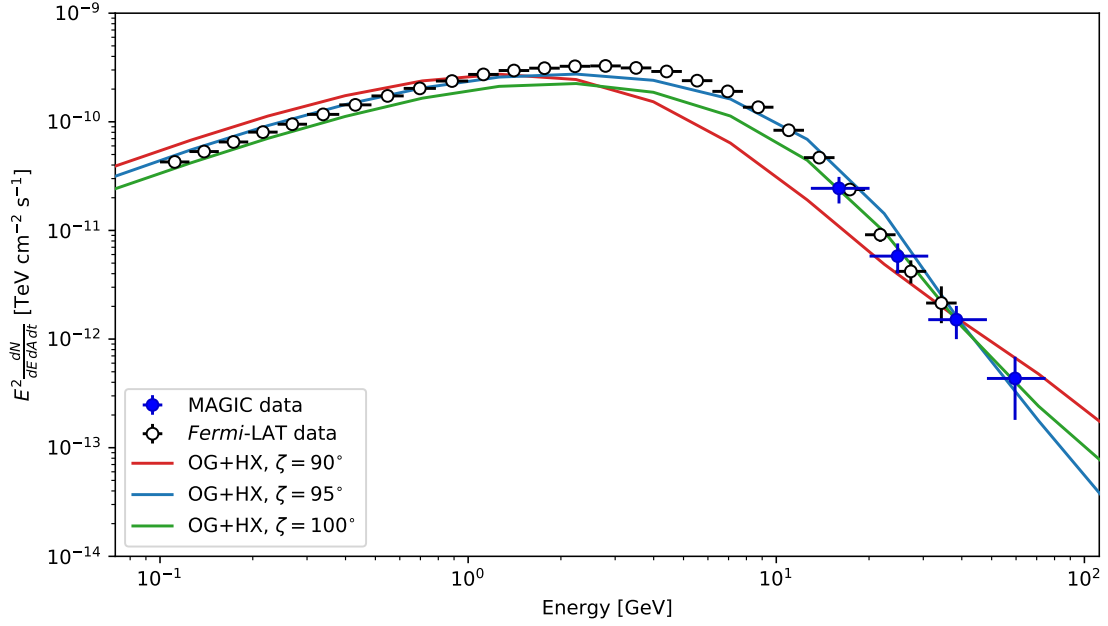


Figure 6.13: The same curves of Figure 6.12, after including the additional harder X-ray component discussed in (Caraveo et al., 2004) in the seed X-ray spectrum. Simulations produced by Dr. K. Hirotani. Curves are not fit to the data.

6.6.1 High temperature X-ray component

In the simulated spectra of Figure 6.12, a seed X-ray radiation field from the neutron star was assumed. Following (Halpern and Wang, 1997), the X-ray spectrum was assumed to be modeled by a single component black body emission with a temperature of $T = (5.6 \pm 0.6) \cdot 10^5$ K. The seed radiation field has implications in the electrodynamics of the outer gap and in the yield of the inverse Compton process invoked to explain the possible power-law extension of the Geminga spectrum. A set of alternative simulations, assuming instead the results discussed in (Caraveo et al., 2004) was also produced. The authors derive therein a better fit to the XMM-Newton X-ray spectrum of Geminga using a two-component black body model. The first component corresponds to an emission with a temperature of $T_1 = (5.1 \pm 0.1) \cdot 10^5$ K from the whole surface of the neutron star. The second one is associated with a hotspot, identified with the heated magnetic polar cap, at $T_2 = (2.1 \pm 0.2) \cdot 10^6$ K. Figure 6.13 presents the outer gap simulated spectra for the same parameters of Figure 6.12, but with the addition of such hotspot component in the underlying X-ray spectrum. Its effects are non negligible and cause a mild reduction of the fluxes in the *Fermi*-LAT energy range, accompanied by an increase in the MAGIC ones. The overall agreement of the theoretical expectations with the observed data seem to increase by including such a hotspot of harder X-ray component. However, it is not possible at the present stage to assess whether the very high energy emission observed by MAGIC is associated with the presence of such a hard X-ray component. Further studies, including a revised simulation code for the outer gap non-stationary emission process and new X-ray data on Geminga are needed to shed light on this possibility.

6.7 Summary

The analysis of the MAGIC Geminga data acquired with Sum-Trigger-II led to its first significant detection at energies above few tens of GeV. This makes Geminga the third known pulsar in the very high energies, and the first one among middle aged pulsars. The significance of the detection is a solid 6.3σ . I produced the spectrum for the pulsed emission corresponding to the P2 phase region. This novel spectrum is well modeled by a power law with a very soft spectral index of $\Gamma = 5.6 \pm 0.5$, and extends from 15 GeV to 75 GeV. The spectrum overlaps in its lower energy range with *Fermi*-LAT measurements, and is compatible with them. In agreement with previous findings, an emission model given by a power law with a pure ($\beta = 1$) exponential cutoff is ruled out by the observations. In addition, the new MAGIC measurements suggest that the sub-exponential cutoff model ($\beta < 1$) is also in disagreement with the data, and that the spectrum extends as a power law towards higher energies. Such a possibility points to an inverse Compton gamma-ray production mechanism in the magnetosphere of Geminga. This hypothesis has been explored with likelihood ratio tests on the joint *Fermi*-LAT and MAGIC datasets. The overlapping MAGIC and *Fermi*-LAT data do not present a significant deviation from a power law, the spectral index for a joint MAGIC and *Fermi*-LAT fit resulting in $\Gamma = 5.4 \pm 0.2$. The whole spectrum in the 100 MeV to 75 GeV seems to prefer a model with a secondary power-law tail at the highest energies. In these fits, the systematic uncertainties on the MAGIC measurements were taken into account.

Overall, the MAGIC findings suggest that the emission of Geminga at energies above 15 GeV is more complex than what was previously thought. Inverse-Compton scattering could be a viable explanation for the production of a power-law tail. The standard outer gap model for very high energy pulsar emission can accommodate such scenario if the particles involved in the inverse Compton emission are the ones accelerated towards the neutron star, so that a “head-on” interaction with X-ray photons is possible. In such case, it requires the Geminga viewing angle from the Earth to be almost perpendicular to the pulsar rotation axis, and predicts an extension of the power-law spectrum towards energies above 100 GeV. However, simulations are in disagreement with the measured spectrum at energies of a few GeV. This implies that the outer gap model needs to be revised to be able to explain the observed gamma-ray emission of Geminga, or that alternative emission scenarios should be considered.

These results show that Geminga is an interesting source in the research field of young and middle aged gamma-ray pulsars. At the same time, they indicate Geminga as a good candidate for the observation with the next generation of imaging atmospheric Cherenkov telescopes. These include the LST telescopes, presently under construction in the scope of the CTA Observatory. The results presented here yielded the scientific publication “*Detection of the Geminga pulsar with MAGIC hints possible power-law tail emission beyond 15 GeV*”, in *Astronomy & Astrophysics* (MAGIC Collaboration et al., 2020). I played a central role in the production of this important result, and I am one of the corresponding authors of the relevant publication, which was chosen as a highlight letter of the year 2020 by the journal editor.

	Crab	Geminga	Vela*	B1706-44*
Catalog name	J0534+2200	J0633+1746	J0835-4510	J1709-4429
Age [a]	967	$3.4 \cdot 10^5$	$1.1 \cdot 10^4$	$1.8 \cdot 10^4$
Distance [kpc]	2.00	0.25	0.28	2.6
Radio?	Yes	No	Yes	Yes
Period [ms]	33.4	237.1	89.3	102.5
Period derivative	$4.2 \cdot 10^{-13}$	$1.1 \cdot 10^{-14}$	$1.2 \cdot 10^{-13}$	$9.3 \cdot 10^{-14}$
Luminosity [W]	$4.5 \cdot 10^{31}$	$3 \cdot 10^{27}$	$7 \cdot 10^{29}$	$3 \cdot 10^{29}$
Polar B [T]	$3.8 \cdot 10^8$	$1.6 \cdot 10^8$	$3.4 \cdot 10^8$	$3.1 \cdot 10^8$
Light-cylinder B [T]	9.55	0.12	4.45	2.70
Gamma efficiency	0.14%	97%	1.3%	25%
Energy range [GeV]	27 – 1500	15 – 75	< 20 – 110	10 – 65
Spectral index	~3.2	~5.4	~4.1	~3.8

Table 6.8: Pulsar comparison table, for the four known very-high-energy gamma-ray pulsars (including also the preliminary reported PSR B1706-44). Astrometry and timing-derived parameters are derived from the ATNF pulsar catalog (Manchester et al., 2005, <http://www.atnf.csiro.au/research/pulsar/psrcat>). The gamma-ray efficiencies were obtained from the *Fermi*-LAT second pulsar catalog (Abdo et al., 2013). In the case of Crab, the reported age is the real time passed from 1054 CE, rather than the spin-down estimate $\tau = P/2\dot{P}$. The spectral index reported for Crab is the one of P2, its hardest component. The spectral index reported for Geminga is the one resulting from the joint *Fermi*-LAT and MAGIC fit of this work.

* The Vela pulsar, in the southern hemisphere, has been detected by the H.E.S.S. Collaboration (Abdalla et al., 2018). Preliminary results on TeV emission have been reported as well, but no spectral information is available to date. H.E.S.S. also presented preliminary results on PSR B1706-44 (Spir-Jacob et al., 2019), with a marginal detection at the level of 4.5σ significance. If confirmed, PSR B1706-44 will be the fourth gamma-ray pulsar detected from ground with Cherenkov telescopes.

In conclusion, Table 6.8 lists the currently known very high energy gamma-ray pulsars, including Geminga, and the recently announced (and still preliminary) PSR B1706-44. These pulsars are all young to middle-age rotation powered pulsars, with periods below 1 s, and age less than one million years. Geminga is the oldest, and the only radio-quiet pulsar in the list. With a spin-down luminosity of the order of 10 solar luminosities, it is also the weakest, but at a distance of ~ 250 pc, it is the closest one to the Earth, and it bears the largest gamma-ray conversion efficiency among all of them. The opposite is true for the Crab pulsar, which is by far the one with the largest spin-down luminosity, but sits at the far-away distance of ~ 2 kpc, and has a low conversion efficiency. The Vela and PSR B1706-44 pulsars have physical properties that lay between those of Crab and Geminga. Consistently, the spectral indices of their very high energy emission are also similar, and fall between those of Crab and Geminga. It is tempting to attribute these differences to the different evolutionary stage reached by the four sources. However, for a solid investigation, it is necessary to enrich the population by searching for new very high energy pulsars. MAGIC and the up-coming CTA LST telescopes are strategic instruments to perform this challenging task, where the instrument sensitivity at energies below 50 GeV will play a crucial role.



Data	E_{range}	Function	E_0	f_0	Γ	E_{cut}	β	b	Γ_1	s	$-2 \log \mathcal{L}$	BIC
M	12.3 – 75	PL (FF)	32.15	$(2.3 \pm 0.7) \cdot 10^{-9}$	5.62 ± 0.54						0.054	2.83
M	12.3 – 75	PL	32.15	$(2.6 \pm 0.5) \cdot 10^{-9}$	5.12 ± 0.64							
M+F	12.3 – 75	PL	32.15	$(2.56 \pm 0.35) \cdot 10^{-9}$	5.41 ± 0.18			0		1.05 ± 0.15	2.1411	8.73
M+F	12.3 – 75	LP	32.15	$(2.55 \pm 0.46) \cdot 10^{-9}$	5.42 ± 0.64			0.01 ± 0.65		1.05 ± 0.18	2.1409	10.92
M+F	0.1 – 75	PLEC1	1	$(3.57 \pm 0.02) \cdot 10^{-4}$	1.089 ± 0.003	2.88 ± 0.02	1			0.46 ± 0.06	362.4	376.0
M+F	0.1 – 75	PLEC	1	$(5.34 \pm 0.19) \cdot 10^{-4}$	0.915 ± 0.014	1.48 ± 0.08	0.742 ± 0.013			0.87 ± 0.11	42.5	59.5
M+F	0.1 – 75	COMP	1	$(5.35 \pm 0.22) \cdot 10^{-4}$	0.914 ± 0.016	12.3			5.4 ± 0.2	1.05 ± 0.15	33.32	53.7

Table 6.9: Summary of the fits performed on MAGIC and *Fermi*-LAT data, with the maximum likelihood parameters and their standard deviation. The “Data” columns identifies the dataset: M - MAGIC; F - *Fermi*-LAT. The E_{range} and E_0 ones give the energy range and the base energy in GeV, respectively. The functions used to fit the data are identified by: PL - Power-law; LP - Log-parabola; PLEC1 - Pure exponential cutoff power-law; PLEC - Free exponential cutoff power-law; COMP - Composite model of Section 6.5.1. The first row gives the values of the forward-fold of MAGIC data. The value of the base flux f_0 is expressed in $\text{TeV}^{-1} \text{cm}^{-2} \text{s}^{-1}$. The spectral index Γ is the one at the base energy E_0 . E_{cut} and β give the cutoff energy (in GeV) and index for the models with a cutoff. The column b presents the curvature parameter for log-parabolic fits. Γ_1 is the second spectral index in the composite model. s is the most likely spectral energy distribution scale factor between MAGIC and *Fermi*-LAT data for that particular model. Finally, the last two columns report the TS according to the classical likelihood ratio test and the BIC. Models for which a likelihood is significant are grouped together. See Appendix B for the plots of the full parameter distributions.

7

CONCLUSIONS

During my doctoral work, I have developed and applied methods to enhance the sensitivity of the telescopes below 100 GeV, and performed unprecedented studies on two pulsars, the Crab (PSR J0534+2200) and Geminga (PSR J0633+1746). I was involved in the commissioning of a stereoscopic trigger of new concept, the Sum-Trigger-II, and in the validation of novel low-energy analysis techniques. My activities resulted in the discovery of pulsed emission of the Geminga pulsar in the energy range between 15 GeV and 75 GeV. Geminga became the third pulsar to be detected with imaging atmospheric Cherenkov telescopes. I was the main actor of this detection, and corresponding author for the MAGIC Collaboration for the publication “*Detection of the Geminga pulsar with MAGIC hints at a power-law tail emission beyond 15 GeV*” MAGIC Collaboration et al. (2020). The publication was selected as a *highlight letter* of the journal *Astronomy and Astrophysics* for the year 2020. I also led the efforts to study the emission of the previously detected Crab pulsar, and to evaluate, for the first time, its possible temporal variability above 20 GeV on timescales of days, weeks, and months. The methods employed for the study of pulsars naturally extend to other kind of low-energy sources, such as high-redshift active galactic nuclei, and gamma-ray bursts. In this sense, my work demonstrates that the MAGIC Telescopes can be proficiently used to study the gamma-ray sky at energies between 10 GeV and 100 GeV.

It is yet unclear what processes allow some peculiar pulsars to exceed the curvature radiation cutoff, and observations in the 10 GeV to 100 GeV range are crucial to distinguish among different models. The Sum-Trigger-II allows to reduce the MAGIC energy threshold by a factor of two, improving the sensitivity in such energy band. I was involved in the commissioning and maintenance of this novel hardware component, whose technical aspects are discussed in “*The Stereoscopic Analog Trigger of the MAGIC Telescopes*”

(Dazzi et al., 2021). In order to fully exploit the lowered energy threshold, the observation required a specialized data analysis. I built, optimized, and validated a pipeline to perform such analysis. The tools were made available to the whole MAGIC Collaboration, and two Sum-Trigger-II analysis schools, where I was one of the main tutors, were organized to spread the knowledge among the collaboration members.

My efforts were concentrated on two objects, the well known gamma-ray pulsars Crab and Geminga. Observations on the Crab pulsar aimed to search for a possible variability of the flux at the very high energies. As reported in Chapter 5, no significant flux variability was found in the MAGIC Sum-Trigger Crab observations, and upper limits for it were derived. The absence of variability could not be put in relation with the nebula flares, as no major flare happened during the time span of the observations (2018-2019). Conversely, these observations have been used to characterize and to prove the stability of the novel Sum-Trigger-II system. The spectra of the Crab pulsar and nebula were measured down to 27 GeV, and found to agree with the *Fermi*-LAT measurements at similar energies, without the need to introduce scaling factors. This remarkable result demonstrates that MAGIC is a powerful instrument to probe the gamma-ray sky in the 10 GeV to 100 GeV energy range, where satellite missions suffer from low photon statistics. A dedicated publication with the results of the MAGIC observation campaigns on the Crab pulsar and nebula is currently in preparation.

The discovery of the very high energy pulsed emission of Geminga, presented in Chapter 6, is the major result of my doctoral project. Previously, only the Crab and Vela pulsars had been detected with ground-based Cherenkov telescopes. Searches for very high energy emission of Geminga with standard hardware and analysis techniques by VERITAS (Aliu et al., 2015) and MAGIC (Ahnen et al., 2016) resulted in non-detections. The novel MAGIC result is a direct consequence of the advancements in the low-energy analysis techniques, and the development of the stereoscopic Sum-Trigger-II. The detection, down to 15 GeV, sets a record for the lowest energy measurement achieved with a Cherenkov telescope. The excellent overlap found with *Fermi*-LAT measurements up to 40 GeV proves that, despite its strong dependence on Monte-Carlo simulations, the imaging atmospheric Cherenkov telescopes technique is a mature and accurate method to study the gamma-ray sky below 100 GeV. Pulsed gamma-rays are detected by MAGIC with a sound significance of 6.3σ . The spectrum of the very high energy emission is well described by a power law extending up to 75 GeV, without any indication for an energy cutoff. The spectral index of $\Gamma = 5.6 \pm 0.5$ is one of the steepest ever measured by Cherenkov telescopes, and a careful validation procedure was employed to assess the systematic uncertainties associated with it. In order to address the significance of such a power-law behavior, I analyzed 12 years of *Fermi*-LAT data as well, and carried out joint *Fermi*-LAT and MAGIC spectral fits. The simple power law with an exponential cutoff scenario, indicative of curvature emission, is ruled out by the observations. A sub-exponential cutoff trend is also disfavored over a model with a power law like tail. Finally, likelihood ratio tests in the overlapping *Fermi*-LAT and MAGIC region show no preference for the more general model with a curved spectrum over the simple, straight power-law case. These facts are interpreted as an indication of an inverse Compton component in the very high energy spectrum of Geminga, similar to the one detected in the

Crab pulsar. The presence of such an inverse Compton component is very significant for the modeling of pulsar magnetospheres, as Geminga is a much older and less powerful pulsar than Crab. This hypothesis was put at test, comparing the data with predictions of the classical outer magnetospheric gap model (Hirotani, 2008). Numerical simulations of the latter one confirm that an inverse Compton component with properties similar to the observed ones can indeed be produced in the magnetosphere of Geminga. However, at the same time, the model fails short to consistently reproduce the GeV emission measured by *Fermi*-LAT, and its properties are heavily dependent on the details of the seed X-ray spectrum. This is an evidence that the stationary outer gap model, for long considered as a standard for high energy pulsar emission, requires a review. Alternatively, novel classes of gamma-ray pulsar emission models, such as the equatorial current sheet, the striped wind, or the magneto-centrifugal acceleration, should also be considered. It is also possible that several of these acceleration mechanisms are acting simultaneously in the pulsar magnetosphere.

In order to fully understand the physics of gamma-ray pulsars, it is crucial to detect more of them, and to build a larger sample of this mysterious family. My doctoral work proves that this search is indeed possible. The MAGIC telescopes equipped with the Sum-Trigger-II, as well as the up-coming LST telescopes of the CTA Observatory, can and should perform a systematic search for other similar objects. I recommend that special attention is given in the future to the research of very high energy gamma-ray pulsars.





PULSAR EPHEMERIDES

The number of gamma-rays which can be detected during a single pulsar period is extremely small. In order to detect the signal of a pulsar a model of its rotation is needed. In this way, gamma-rays originating from the same region can be grouped together and the average impulse profile can be studied.

As a result of the energy loss, the pulsar spins down with time (cfr. Section 1.2): its rotational frequency at a generic time t can be represented with the Taylor expansion:

$$\nu(t) = \nu_0 + \dot{\nu}_0(t - t_0) + \frac{\ddot{\nu}_0}{2}(t - t_0)^2 + \frac{\dddot{\nu}_0}{6}(t - t_0)^3 + \dots \quad (\text{A.1})$$

The pulsar phase Φ is defined as the number of turns it has completed since a reference time time t_0 :

$$\Phi(t) = \int_{t_0}^t \nu(\tau) d\tau = \quad (\text{A.2})$$

$$= \Phi_0 + \nu_0(t - t_0) + \frac{\dot{\nu}_0}{2}(t - t_0)^2 + \frac{\ddot{\nu}_0}{6}(t - t_0)^3 + \dots \quad (\text{A.3})$$

The fractional part of Φ is the same for events coming from the same emission region, and it shall be indicated by φ . A histogram of the observed events binned on φ is named a *phaseogram*. The phaseogram conveys physical information on the number of the emission regions and their size and shape, as well as on the viewing geometry. A polynomial expansion for phase like the one given by Formula A.3 holds at any time far from pulsar glitches (cfr. Section 1.4.1). During a glitch, the order of the expansion needed to model the sudden jumps in phase and frequency becomes prohibitively large. A model for the

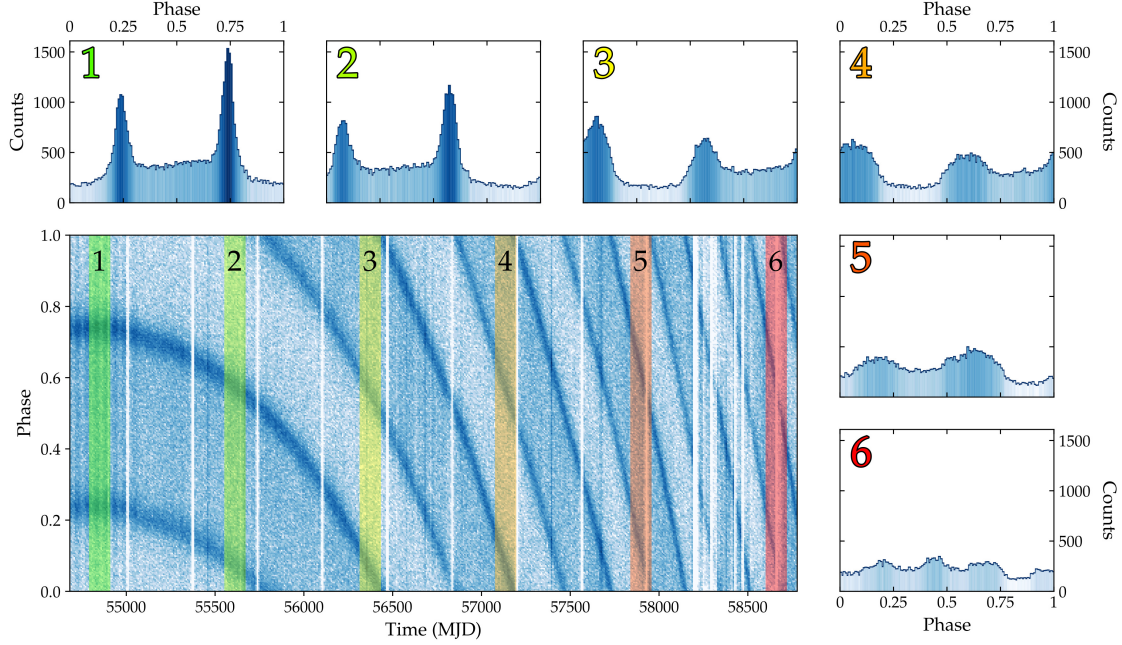


Figure A.1: Effects of phase drift due to a non-refined ephemeris on *Fermi*-LAT data of the Geminga pulsar. The larger panel shows the *phase trace*, a two-dimensional scatter plot of the events in time and phase. The density of dots is proportional to the logarithm of the event density. Both impulses of Geminga are visible as traces of bolder color. If the ephemeris were correct on the whole period, traces would be straight horizontal lines. Six *phaseograms* are showed, corresponding to the colored and numbered bands. The first phaseogram presents the intrinsic pulse profile. In the second one, a phase drift has developed and the impulses are shifted. In the following ones, the drift changes during the stacking period, resulting in a “smearing” of the pulse shape. The last diagrams show a completely degraded signal.

pulsar rotation is a set of estimates of the parameters $(\nu_0, \dot{\nu}_0, \ddot{\nu}_0, \dots)$ at a reference time t_0 and is commonly referred to as a *pulsar ephemeris* at epoch t_0 . The inaccuracy of an ephemeris grows with increasing time from the initial parameter estimation. This is as a result of measurement errors and the limited order of the Taylor expansion. A *phase drift* ψ slowly develops, producing an apparent shift of the measured pulsar profile with respect to the expected one. The phase drift eventually changes sensibly even during the time interval required to collect enough events to produce a phaseogram. This produces a smoothing of the pulse profile. Such situation is presented in Figure A.1 with real data collected by *Fermi*-LAT on Geminga.

By noting the estimated phase with $\bar{\Phi}$, the phase drift ψ can be written as:

$$\psi(t) = \Phi(t) - \bar{\Phi}(t) = \varphi(t) - \bar{\varphi}(t) \quad (\text{A.4})$$

$$= \delta(t - t_0) + \frac{\dot{\delta}}{2}(t - t_0)^2 + \dots + \frac{1}{(N + 1)!} \left[\frac{d^N \nu}{dt^N} \right]_{t_0} (t - t_0)^{N+1} + \dots, \quad (\text{A.5})$$

with the polynomial coefficients $\delta, \dot{\delta}, \dots$ being the measurement errors committed in the estimate of $\bar{\varphi}$ on the frequency and frequency derivatives up to the order N of the

ephemeris. Higher order terms, originally ignored in the model, follow in the expansion. As long as the phase drift is small compared to the size of a bin in the phaseogram, the only effect is a cyclical shift by ψ . By measuring how the phaseogram shifts with time, it is possible to reconstruct the measurement errors δ and possibly the trailing orders of the ephemeris, and correct for them.

In the following sections I present the methods that have been developed to model the pulse profile, derive its shift and obtain an ephemeris valid for the whole time span of the MAGIC Geminga data. The ephemeris was produced by using 12 years of *Fermi*-LAT data.

A.1 Ephemeris extension

If an ephemeris is given but it is not valid for the whole time span of the data, such as the one in Figure A.1, its validity range can be extended by measuring the progressive shift of the pulse shape. The whole time range is divided in finer time bins (folding intervals), which are used to produce phaseograms. The duration of each time interval is a *folding period* T_F at time t_i . In order to estimate the phase drift among different phaseograms, a fit with an analytical pulse template $p(\varphi)$ may be used. However, constructing such a template is not straightforward, as the pulse profile is not a simple curve and changes with the energy. Moreover, if the phase drift varies significantly during the folding period, the pulse shape is distorted and the quality of the fit degrades. Instead, I employed a cross-correlation alignment method that relies only on a good reference phaseogram. The latter can be produced during the period of validity of the ephemeris which is going to be updated. The method follows these steps:

1. Select a time range in which the ephemeris that needs to be updated is valid. Both gamma-ray and radio ephemerides usually specify their validity range as a parameter, so that such interval can be taken. A reference phaseogram R_φ is produced from events in this folding interval, and its cyclic discrete Fourier series (DFS) is computed: $\mathcal{R}_k = \mathcal{F}[R_\varphi]$.
2. The remaining time range is divided in several folding intervals. Their duration T_F has to be chosen in such a way that the corresponding phaseograms have enough statistics to determine the pulse profile. However, the time span is limited by the accuracy of the original ephemeris. A set of $P_{\varphi,i}$ phaseograms is produced, accompanied by their discrete Fourier series $\mathcal{P}_{k,i}$.
3. The discrete cross-correlation function $X_{\varphi,i}$ of each of the $P_{\varphi,i}$ with the reference one is computed as:

$$X_{\varphi,i} = \mathcal{F}^{-1} [\mathcal{R}_k^* \cdot \mathcal{P}_{k,i}], \quad (\text{A.6})$$

with $(\cdot)^*$ denoting the complex conjugate. It is easy to prove that if R_φ and $P_{\varphi,i}$ differ only by a cyclical shift ψ_i , then $X_{\varphi,i}$ has a maximum at $-\psi_i$. The shape of $X_{\varphi,i}$ depends on the pulse profile of the phaseogram, however its maximum can usually be approximated in a reasonable phase interval by a Gaussian or a Lorentzian function. The $X_{\varphi,i}$ values are strongly correlated, as each of them depends on the whole R_φ and $P_{\varphi,i}$. As opposed to a simple fit of the impulse peak position in

$P_{\varphi,i}$, the value determined from $X_{\varphi,i}$ benefits from the information contained in the whole phaseogram $P_{\varphi,i}$, rather than a small sub-interval of it.

4. The *phase drift* measurements (t_i, ψ_i) are fitted with a polynomial function to obtain the $\psi(t)$ behavior. The original ephemeris is corrected by adding $\psi(t)$ to its Taylor expansion, producing an updated ephemeris. The whole procedure can be iterated, until following ψ_i determinations are not significant with respect to the statistical uncertainties.

In order to have a correct estimate of the statistical uncertainties resulting from the procedure, their propagation through the cross-correlation operator has to be calculated. Following the implementation of the DFS in the Numpy Python package¹,

$$\mathcal{X}_k = \sum_{n=0}^{N-1} f_n \exp\left(-2\pi i \frac{nk}{N}\right) \quad k = 0, \dots, N-1, \quad (\text{A.7})$$

it can be proved that the covariance matrix of the values of the discrete cross-correlation of two histograms A_m and B_n with N bins and with bin uncertainties a_m and b_n , is:

$$\mathcal{S}_{m,m} = \sum_{r=0}^{N-1} a_r^2 b_{r-m}^2, \quad (\text{A.8})$$

and, for the cross-elements with $m \neq n$:

$$\mathcal{S}_{m,n} = \sum_{r=0}^{N-1} a_r^2 B_{r-m} B_{r-n} + b_r^2 A_{r+m} A_{r+n} \quad (\text{A.9})$$

If counts follow a Poisson distribution and their number is sufficiently high so that the central limit theorem applies, the above relations reduce to:

$$\mathcal{S}_{m,m} = \sum_{r=0}^{N-1} A_r B_{r-m} \quad (\text{A.10})$$

$$\mathcal{S}_{m,n} = \sum_{r=0}^{N-1} A_r B_{r-m} B_{r-n} + B_r A_{r+m} A_{r+n} \quad (\text{A.11})$$

With respect to the pulse template fitting, the proposed method has the advantage of being less sensitive to the degradation of the phaseogram at times far from the ephemeris validity range. Once the phase drift $\psi(t)$ is roughly known, the smoothing during the folding period T_F can be accounted for by replacing formula A.6 with:

$$X_{\varphi,i} = \mathcal{F}^{-1} [(\mathcal{R}_k \cdot \mathcal{Q}_k)^* \cdot \mathcal{P}_{k,i}], \quad (\text{A.12})$$

with \mathcal{Q}_k being the DFS of the square function Q_φ with width $L = \psi(t_i + T_F/2) - \psi(t_i - T_F/2)$:

$$Q_\varphi = \begin{cases} 1 & -L/2 \leq \varphi \leq L/2 \\ 0 & \text{elsewhere} \end{cases} \quad (\text{A.13})$$

$$\mathcal{Q}_k = \frac{1}{N} \frac{\sin(\pi L k)}{\sin(\pi \frac{k}{N})} \quad (\text{A.14})$$

¹ <https://docs.scipy.org/doc/numpy/reference/routines.fft.html>

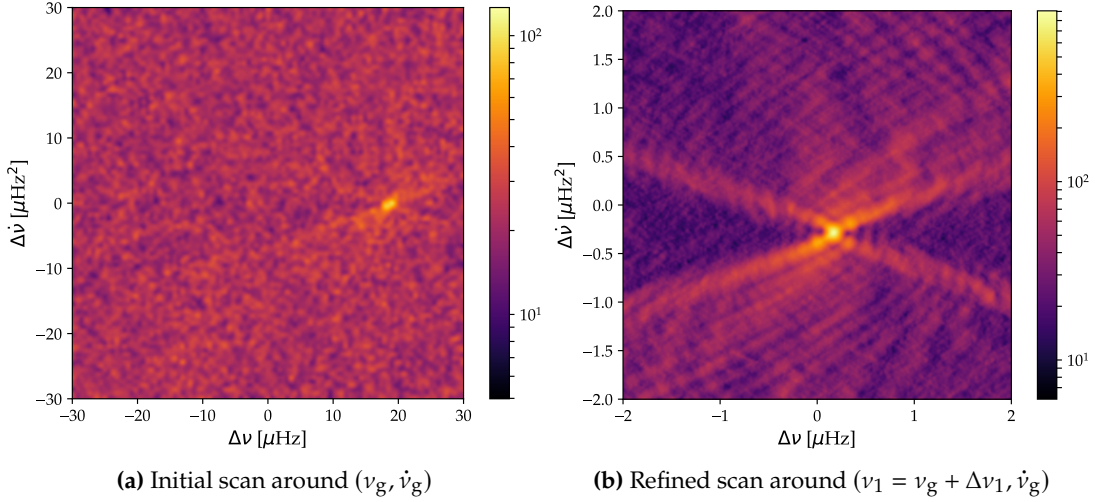


Figure A.2: Two dimensional scans of the Z_{10}^2 test statistics in the $(\nu, \dot{\nu})$ space after a major glitch of PSR J2229+6114, the Boomerang pulsar. **(a)** First scan around ν_g and $\dot{\nu}_g$, the initial estimates on the frequency and frequency derivative, as from the pre-glitch ephemeris. A cluster of high Z_{10}^2 values appears close to $\Delta\nu = 20 \mu\text{Hz}$. **(b)** Refined scan around $\nu_1 = \nu_g + 18.5 \mu\text{Hz}$, with a narrower range and a finer binning, identifying the post-glitch parameters.

When extending an ephemeris for a period of several years, timing noise from the pulsar itself (see Section 1.4.2) may become a major limiting factor. Intrinsic phase noise induces a low frequency red noise component. This produces quasi-periodical oscillations in the phase trace plot, with a characteristic timescale of several months. If timing noise is not a subject of study, a segmented ephemeris (see later Section A.4) is a convenient way to account for the intrinsic phase noise.

The implementation of the previous methods was achieved with a Python/Numpy code for the calculation of the cross-correlations functions $X_{\phi,i}$ and their correlated errors, and a ROOT² macro for the polynomial fitting of the phase drifts. These programs are available upon request.

A.2 Post-glitch recovery

During a pulsar glitch, the Taylor expansion in Formula A.3 ceases to be valid. Glitches are characterized by a sudden increase in ν and $\dot{\nu}$ followed by an exponential decay process, after which the polynomial behavior is recovered. Both the impulsive change in frequency and the decay process would require a Taylor expansion with a large number of orders to be modeled. It is therefore customary to break the pre-glitch ephemeris at the time of the glitch t_g and to start a new one afterwards. In order to do so, one needs to estimate the impulsive change in frequency $\Delta\nu$ and frequency derivative $\Delta\dot{\nu}$ at t_g : these shall be added to the pre-glitch variables ν_g and $\dot{\nu}_g$ to obtain an initial post-glitch ephemeris. The latter can be later refined with the methods presented in the previous section. By folding post-glitch events with an inaccurate ephemeris, a pulse profile

² <http://root.cern.ch/>

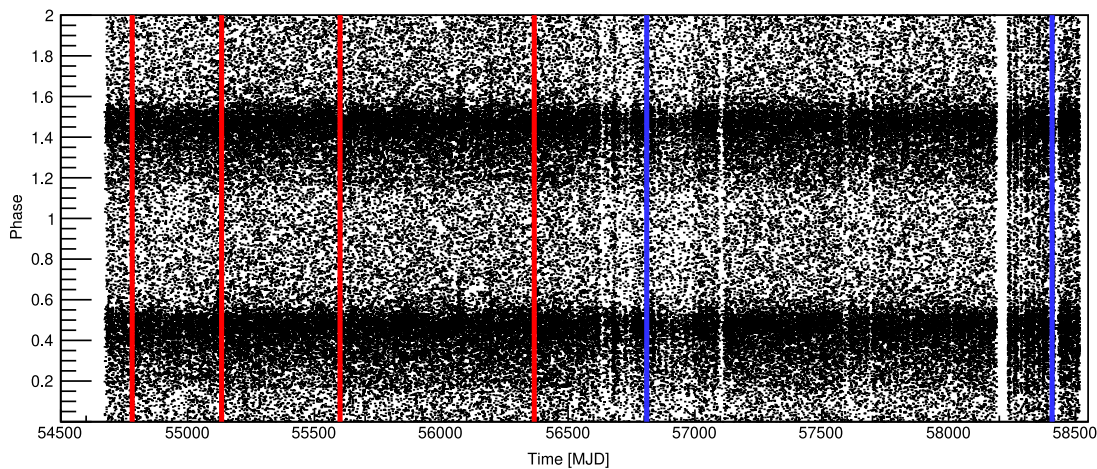


Figure A.3: Phase stack for the Boomerang pulsar (PSR J2229+6114), using the timing solution derived with the methods presented in this section. Vertical lines correspond to glitches. The blue ones were not listed in previous publications at the time of the ephemeris production and have been detected with a $\nu\dot{\nu}$ scan. Since then, they were independently published in Güercinoğlu et al. (2020).

smearing takes place. If the ephemeris is not valid anymore, any detail of the profile is flattened out to a constant. The agreement of the phaseogram with a constant can be taken as a measurement of the inaccuracy of the ephemeris. This can be done with the common χ^2 goodness-of-fit test, or with specialized tests for cyclic data, such as the Z_n^2 and H tests (cfr. Section A.3). The post glitch frequency and frequency derivative can be obtained with a scan in the $\nu\dot{\nu}$ space. Each $(\nu, \dot{\nu})$ couple is used to fold data shortly after a glitch and parameters which maximize the test statistic value (least compatible with a constant) are selected. Examples of such bi-dimensional scans are shown in Figure A.2 Since typical pulsar $\dot{\nu}$ are in the range $10^{-10} - 10^{-13} \text{ Hz}^2$, the time that an ephemeris neglecting $\dot{\nu}$ takes to develop an unitary phase drift, and hence to become invalid, is of the order of few days. Folding periods required to produce a phaseogram are generally larger, hence bi-dimensional scan in $(\nu, \dot{\nu})$ is needed. Once the approximate values of $\Delta\nu$ and $\Delta\dot{\nu}$ are known, a more refined scan can be made, or an initial guess of the ephemeris after the glitch as the one with $\nu_1 = \nu_g + \Delta\nu$ and $\dot{\nu}_1 = \dot{\nu}_g + \Delta\dot{\nu}$ can be used to measure the phase drift after the glitch and proceed with the methods of the previous section. The Geminga pulsar has a stable timing: only a minor glitch has been detected in 1996 (Jackson et al., 2002). During the time span of *Fermi*-LAT and MAGIC data no such event has been detected. The glitch scan were instead used to produce an ephemeris for the Boomerang pulsar (PSR J2229+6114). This was part of a support activity for an observation campaign on that pulsar and its associated Nebula conducted by MAGIC in the 2018-2020 period. The timing solution evidenced the presence of several glitches. It is given in Figure A.3. Scans were run employing a simple C++ code, which is also available to the interested reader.

A.3 Cyclic data statistical tests

Statistical tests for the evaluation of a directional preference in a set of cyclic data are widely employed in pulsar analysis. The most common ones are the Z_n^2 test (multimodal Rayleigh test) and the H test, which is based on the former one. With respect to the standard χ^2 test, these take advantage of the periodical nature of the data, and allow a more powerful search for weak signals. Given a set of cyclic measurements $(\varphi_1, \dots, \varphi_N)$, the Z_n^2 value is given by:

$$Z_n^2 = \frac{2}{N} \sum_{k=1}^n \left(\sum_{j=1}^N \cos 2\pi k \varphi_j \right)^2 + \left(\sum_{j=1}^N \sin 2\pi k \varphi_j \right)^2 \quad (\text{A.15})$$

The Z_n^2 is proportional to the total power carried by the signal up to its n -th Fourier harmonic. It follows asymptotically a χ^2 distribution with $2n$ degrees of freedom (Bucher et al., 1983). As a consequence, p -values against the null-hypothesis (no directional clustering of the events) can be promptly computed. The Z_n^2 and χ^2 tests are related in the context of *kernel density estimators* (de Jager et al., 1986). These are generic methods to estimate a probability density function that a set of experimental measurements is generated from. It can be proved that the χ^2 test with respect to the mean density of the measurements is associated with the *histogram density estimator*. The latter gives an estimate of the density function simply as the normalized histogram of the measurements. The number of bins in the histogram acts as a smoothing parameter. Analogously, the Z_n^2 variable is the test associated with the *Fourier density estimator*. This constructs a density function from the discrete Fourier transform of the measurements, applying a low-pass filter at the n -th harmonic of their fundamental period. This justifies why the Z_n^2 test is a natural choice for a cyclic data set such as pulsar phases. Among its advantages over the χ^2 test, the Z_n^2 one removes the dependence on the number of bins used to histogram the data. However, the choice on n is arbitrary. This fact induced de Jager et al. (1989) to propose a criterion aimed at setting an optimum number of maximum harmonics n for the Z_n^2 test in an unbiased way. Given a set of measurements and the values of the Z_n^2 variable for $1 \leq n \leq 20$, an H value can be defined:

$$H = \max_{n \leq 20} (Z_n^2 - 4n) + 4 \quad (\text{A.16})$$

The value of n that maximizes H is the optimum number of harmonics of the Z_n^2 test for the given data set. By choosing n with this criterion, one avoids biases in the judgment of the significance of the test. These could easily arise if several values of n are tried in succession on the same data set, and the highest significance is selected. Alternatively, the H value itself can be used as a test variable, completely removing the dependency on n . This goes under the name of H -test (de Jager and Büsching, 2010). The p -value of obtaining an H larger than h in the null hypothesis (absence of any pulsed signal) follows an exponential distribution with $p(H \geq h) \simeq \exp(-0.4h)$. The H -test proved to be reliable against a vast set of possible pulse profiles. Both the H and the Z_n^2 test statistics are commonly used by blind periodicity searches with the *Fermi*-LAT satellite to detect new gamma-ray pulsars.

A.4 Segmented ephemerides

An ephemeris spanning a large period of time necessarily needs to account for the intrinsic timing noise of the pulsar (cfr. Section 1.4.2). To do so, since timing noise is typically quasi-periodical, a large order is required in the Taylor expansion A.3. However, this renders the ephemeris unstable against small deviations of its parameters. This causes a vicious circle in which large ephemeris orders are required to model long time spans of data, but the updated ephemeris obtained from them immediately diverges as newer data is added. Dedicated procedures exist to solve this problem. The simplest method is to add a set of sinusoids, representing the timing noise, atop the Taylor expansion for phase (Hobbs et al., 2004). This procedure is known as the FITWAVES algorithm in its TEMPO2 implementation. A more advanced procedure employs a spectral decomposition of the phase drift, to correctly disentangle the intrinsic timing noise from systematic effects (Coles et al., 2011). It is named the Cholesky decomposition method. However, a simpler approach can be adopted in applications in which the timing noise is not the direct object of research. These include the ones covered in this thesis. A long time interval of data can be divided into shorter time segments, and a set of ephemerides \mathcal{E}_i with a constant low order N can be produced for each segment. The duration T of a segment has to be chosen in such a way that deviations produced by the orders $n > N$ not included in the model can be neglected. Supposing that the leading neglected order $N + 1$ is the largest contributor, and with the wish to obtain a phase accuracy ε , T can be estimated as:

$$T = \left[\frac{(n+1)!}{v^{(n)}} \varepsilon \right]^{\frac{1}{n+1}} \quad (\text{A.17})$$

The ephemerides \mathcal{E}_i can be joined together in a *segmented ephemeris* adding a continuity requirement for phase, frequency, and its first $N - 2$ derivatives at the extremes of the segments, effectively replacing the Taylor expansion of phase with a *spline interpolation* of order N . This approach proved to work extremely well for the modeling of gamma-ray pulsars such as Geminga. Figure A.4 presents the cubic spline ephemeris used for it in Chapter 6, covering twelve years of data with a minimal root mean square phase drift of 1‰, corresponding to 200 μs . The usage of a segmented ephemeris also allows to naturally incorporate glitches in the expansion, thus reducing the number of ephemeris files needed to process large data sets.

To implement these methods, I wrote a Python class `Ephemeris` for the manipulation of the `.par` ephemeris files of TEMPO2. Its methods allow to easily accomplish common operations such as: reading and saving `.par` files; adding a constant phase shift to the whole ephemeris; changing the defining epoch t_0 without altering the ephemeris; obtaining the (fractional) phase, the frequencies and frequency derivatives at a certain time instant; manipulating the time-based definitions of φ_0 of TEMPO2 without affecting the solution; converting a FITWAVES ephemeris into an equivalent segmented one; . The production of the segmented ephemeris uses such tools and the standard interpolation methods of the `scipy` package. The code, as well as the larger methods of the `Phaseogram` class for the production of phaseograms from MAGIC and *Fermi*-LAT data, is available upon request. The TEMPO2 software itself supports segmented ephemeris through the usage of its “glitch” parameters. These allow to introduce an instantaneous jump in

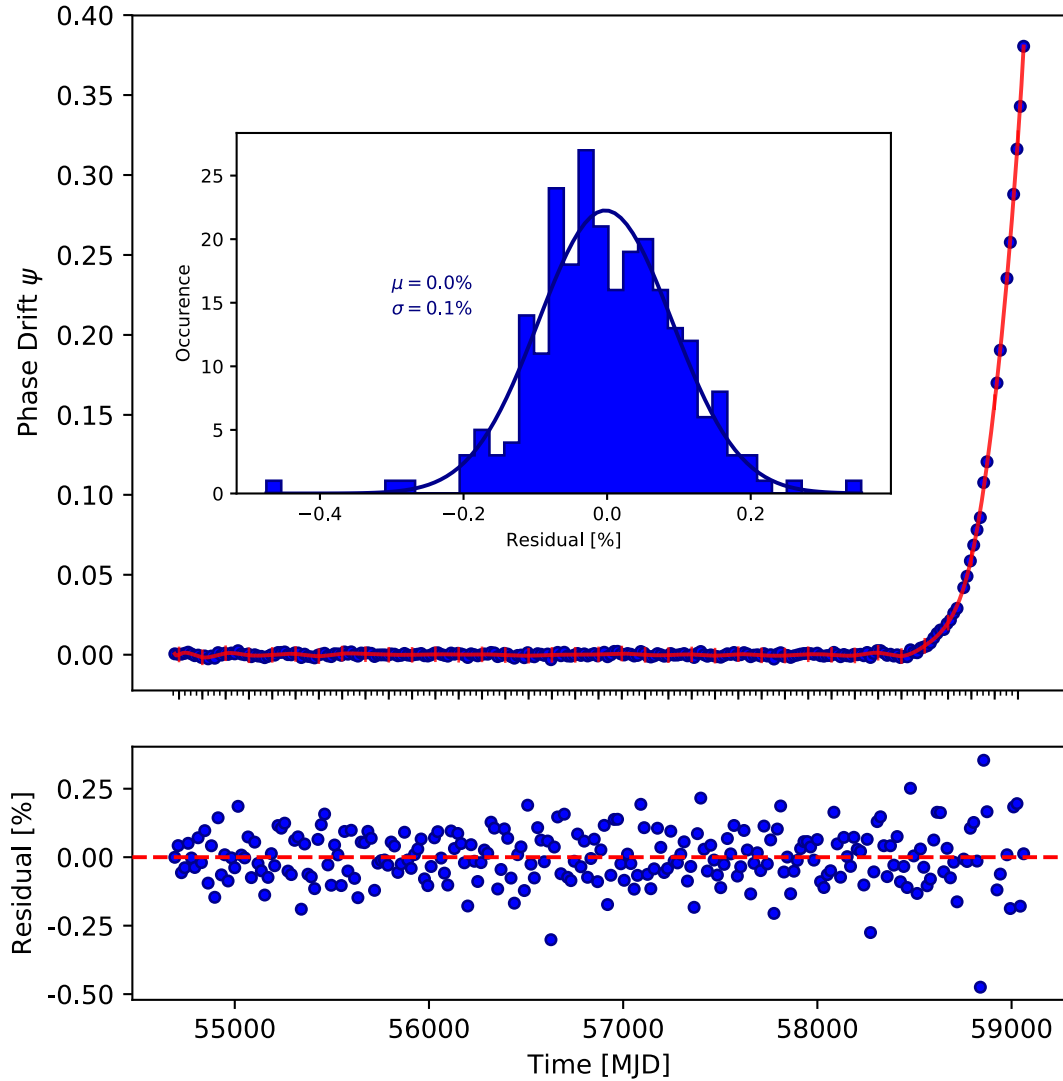


Figure A.4: Segmented ephemeris for the Geminga pulsar, spanning twelve years of *Fermi*-LAT data. The top panel presents the phase drift of a previous ephemeris obtained with conventional methods (blue dots), and the new segmented ephemeris (red line). The larger ticks on the time axis represent the extremes of the segments used to derive a cubic solution. Each of these is subdivided into even narrower intervals (smaller ticks), each one with a different $\nu, \dot{\nu}, \ddot{\nu}$ determination, to ensure that the deviation due to the neglected fourth order is irrelevant. The bottom panel presents the residuals of the same data with respect to the new ephemeris. The insert gives a histogram of such residuals, with a Gaussian fit and its parameters.

phase φ , frequency ν and its first and second derivatives $\dot{\nu}$ and $\ddot{\nu}$. Therefore, the largest spline order which is possible to employ is $N = 3$. TEMPO2 supports up to 40 such “glitches” in an ephemeris file, but this limitation has no real motivation. The number can be increased at will by modifying a single hard-coded value in the source code of the package. A patch to do so is also available upon request.



B

JOINT PARAMETER DISTRIBUTIONS

In this appendix I report the parameter distributions for the joint *Fermi*–LAT and MAGIC fits of the Geminga spectrum presented in Chapter 6. Distributions have been produced with the Markov-chain Monte-Carlo sampler EMCEE¹. Dimensionless parameters such as the spectral index Γ have been fit in a linear space. For dimensioned parameters, such as the cutoff energy E_{cut} , the units were dropped and the logarithm $\log_{10}(E_{\text{cut}})$ was used as a parameter instead. The probability distribution $f(\mathbf{p})$ of the parameter vector \mathbf{p} was obtained with Bayes rule as:

$$f(\mathbf{p}) = \frac{\mathcal{L}(\mathbf{p}|\mathbf{d})f_0(\mathbf{p})}{g_0(\mathbf{d})}, \quad (\text{B.1})$$

where $\mathcal{L}(\mathbf{p}|\mathbf{d})$ is the likelihood of the parameter vector \mathbf{p} given the data vector \mathbf{d} , $g_0(\mathbf{d})$ is the probability distribution of the data and acts as normalization constant, and $f_0(\mathbf{p})$ represents the prior probability of the parameters. In all cases, a uniform prior distribution $f_0(\mathbf{p}) = k$ has been chosen. The range of such a uniform prior distributions was selected so that the residual tails of $\mathcal{L}(\mathbf{p}, \mathbf{d})$ exceeding it were negligible. This implies that $f(\mathbf{p}) \propto \mathcal{L}(\mathbf{p}, \mathbf{d})$ and the Bayesian procedure is effectively analogous to a standard Likelihood maximization approach. The parameter distributions $f(\mathbf{p})$ are presented in the following sections as *corner plots*. These constitute a two-dimensional matrix of slices of $f(\mathbf{p})$. If the model has n parameters in total, given two of them p_i and p_j , their two-dimensional cross-distribution in the (i, j) position in the corner plot is given by:

$$f_{ij}(p_i, p_j) = \int \dots \int_{\mathbb{R}^{n-2}} f(p_i, p_j, \mathbf{q}) d\mathbf{q}, \quad (\text{B.2})$$

¹ <https://emcee.readthedocs.io/>

where \mathbf{q} is the $(n - 2)$ -dimensional vector of all the remaining parameters, excluded p_i and p_j . The distribution f_{ij} is obviously symmetric in its indices, so that the corner plot can be represented as a triangular matrix. Along the diagonal of the corner plot, the one-dimensional $f_i(p_i)$ projection is represented, with:

$$f_i(p_i) = \int \dots \int_{\mathbb{R}^{n-1}} f(p_i, \mathbf{q}) d\mathbf{q}, \quad (\text{B.3})$$

and in this case \mathbf{q} is obviously $(n - 1)$ -dimensional. The corner plot is a complete representation of $f(\mathbf{p})$, whereas the single parameter distribution f_i are in general not. A confidence interval on a parameter ($\langle p_i \rangle - u_i, \langle p_i \rangle + U_i$) can be derived, but this necessarily ignores correlations among the parameters. In the following plots, a confidence interval was given taking $\langle p_i \rangle$ as the median of the f_i distribution, and the negative and positive uncertainties as the 16% and 84% percentiles, respectively. This choice is justified by the fact that if the distribution f_i is a Gaussian with mean μ and standard deviation σ , the resulting confidence interval is exactly $\mu \pm \sigma$.

Correlation is present among the data points $\mathbf{d} = (\mathbf{x}, \mathbf{y})$ as well, as a result of the unfolding of the instrument response function. For this reason, the log-likelihood function $\log \mathcal{L}(\mathbf{p}, \mathbf{d})$ was defined in a more general representation as:

$$\log \mathcal{L}(\mathbf{p}, \mathbf{d}) = -\frac{1}{2} [\mathbf{y} - a(\mathbf{p}, \mathbf{x})]^T \mathcal{S}^{-1} [\mathbf{y} - a(\mathbf{p}, \mathbf{x})], \quad (\text{B.4})$$

where \mathbf{x} and \mathbf{y} are two m -dimensional column vectors corresponding to the coordinates of the m data points, $a(\mathbf{p}, \mathbf{x})$ is the model functional form depending on the parameters \mathbf{p} and being evaluated on each of the x coordinates, \mathcal{S}^{-1} is the inverse of the $m \times m$ covariance matrix of the data points \mathcal{S} , and $(\cdot)^T$ represents the transpose operator. This is alternatively written, in tensor notation, as:

$$\log \mathcal{L}(\mathbf{p}, \mathbf{d}) = -\frac{1}{2} \{ \mathcal{S}^{-1} \}^i_j [y_i - a(\mathbf{p}, x_i)] [y^j - a(\mathbf{p}, x^j)]. \quad (\text{B.5})$$

The covariance matrix is defined as $\mathcal{S}_{ij} = \mathbb{E}[y_i - \mathbb{E}(y_i)] \cdot \mathbb{E}[y_j - \mathbb{E}(y_j)]$. In practice, it bears the variances σ_i^2 of the y_i values on its diagonal, and the covariances $\text{cov}(y_i, y_j)$ on cross elements. The latter result from the unfolding procedure (cfr. Section 4.8.3). The data vector $\mathbf{d} = (\mathbf{x}, \mathbf{y})$ can be written as a chain $\mathbf{d} = (\mathbf{d}_F, \mathbf{d}_M)$ of the data vectors of *Fermi*-LAT and MAGIC. Measurements of two different instruments are obviously independent, so that \mathcal{S} is a block matrix of the two \mathcal{S}_F and \mathcal{S}_M covariance matrices of *Fermi*-LAT and MAGIC points alone: $\mathcal{S} = \text{block}(\mathcal{S}_F, \mathcal{S}_M)$. The *Fermi*-LAT analysis tools do not provide \mathcal{S}_F as an output, and instead give just the standard deviations $\sigma_{F,i}$ of the spectral energy distribution values $y_{F,i}$. Therefore, \mathcal{S}_F had to be constructed as the diagonal matrix $\mathcal{S}_F = \text{diag}(\sigma_{F1}^2, \sigma_{F2}^2, \dots)$ of such variances. This effectively assumes that the *Fermi*-LAT points are independent among themselves. Such statement is justified by the small energy resolution ε of *Fermi*-LAT in the considered energy range ($\varepsilon \lesssim 10\%$). The MAGIC unfolding procedure, on the other hand, returns the full \mathcal{S}_M in output, so that the much larger energy resolution of MAGIC ($\varepsilon \lesssim 50\%$) was fully taken into account. In Section 6.4.1, I presented the results of the systematic study that was carried on Geminga MAGIC data. This has shown that possible systematic effects of MAGIC are well modeled

as a *rigid* shift of the spectral energy distribution values y_i by an energy-independent scale factor ς . Since the MAGIC spectrum is well represented by a power-law with spectral index Γ , the scale factor ς can be converted in an absolute energy scale mismatch factor ϵ , with $\epsilon = \varsigma^{1/(\Gamma-1)}$. This allows to introduce the scale factor ς as a nuisance parameter in the joint *Fermi*-LAT and MAGIC likelihood function. In this way, possible systematic effects between the measurements of the two instruments can be taken into account by marginalizing the results on ς . The MAGIC spectral energy distribution values y_M scale with ς and their covariance matrix \mathcal{S}_M does with ς^2 . Accordingly, the complete log-likelihood function used for the joint fits can be defined as:

$$\log \mathcal{L}(\mathbf{p}, \mathbf{d}, \varsigma) = -\frac{1}{2} \left\{ \text{block}(\mathcal{S}_F, \varsigma^2 \mathcal{S}_M)^{-1} \right\}_j^i [\mathfrak{S}_i^k y_k - a(\mathbf{p}, x_i)] [\mathfrak{S}_j^l y^l - a(\mathbf{p}, x^j)], \quad (\text{B.6})$$

where the diagonal matrix \mathfrak{S} evaluates to unity on the *Fermi*-LAT points and to ς on MAGIC ones. By defining the deviation vector \mathbf{V} as:

$$\mathbf{V}(\mathbf{p}, \mathbf{d}, \varsigma) = \mathfrak{S} \mathbf{y} - a(\mathbf{p}, \mathbf{x}) = \begin{pmatrix} \mathbf{1} & \\ & \varsigma \end{pmatrix} \begin{pmatrix} \mathbf{y}_F \\ \mathbf{y}_M \end{pmatrix} - a(\mathbf{p}, \mathbf{x}), \quad (\text{B.7})$$

the log-likelihood can be equivalently written in matrix notation as:

$$\log \mathcal{L}(\mathbf{p}, \mathbf{d}, \varsigma) = -\frac{1}{2} \mathbf{V}^T(\mathbf{p}, \mathbf{d}, \varsigma) \begin{pmatrix} \sigma_{F1}^2 & 0 & \dots & \\ 0 & \sigma_{F2}^2 & \dots & \mathbf{0} \\ \vdots & \vdots & \ddots & \\ \mathbf{0} & & & \varsigma^2 \mathcal{S}_M \end{pmatrix}^{-1} \mathbf{V}(\mathbf{p}, \mathbf{d}, \varsigma). \quad (\text{B.8})$$

In practice, it was more convenient to use $\log_{10}(\varsigma)$ as a parameter in the fits. The code sampling the likelihood distribution and building confidence intervals for the parameters is available in the git software repository (cfr. Appendix C). The following table reports the meaning and units of the parameters in the rest of the appendix.

Symbol	Definition	Unit
E_0	Pivot energy for the power-law component	GeV
f_0	Differential flux at E_0 (in absence of a cutoff)	$\text{TeV}^{-1} \text{cm}^{-2} \text{s}^{-1}$
Γ, Γ_1	<i>Positive-defined</i> Spectral index	1
E_{cut}	Cutoff energy	GeV
β	Exponential index <i>or</i> Log-parabola curvature	1

Table B.1: Parameters definitions. The sign of the spectral index Γ used in this appendix is the opposite of the one defined in Equation 1.9 used and elsewhere in the thesis. The values y_i of the spectral energy distribution and the model function $a(\mathbf{p}, \mathbf{x})$ take the units of $\text{TeV cm}^{-2} \text{s}^{-1}$.

B.1 Power-law with a *pure* exponential cutoff

$$a(p, x) = 10^{-6} E_0^2 \cdot 10^{\log_{10}(f_0)} (x/E_0)^{\Gamma+2} \exp \left[-x/10^{\log_{10}(E_{\text{cut}})} \right]$$

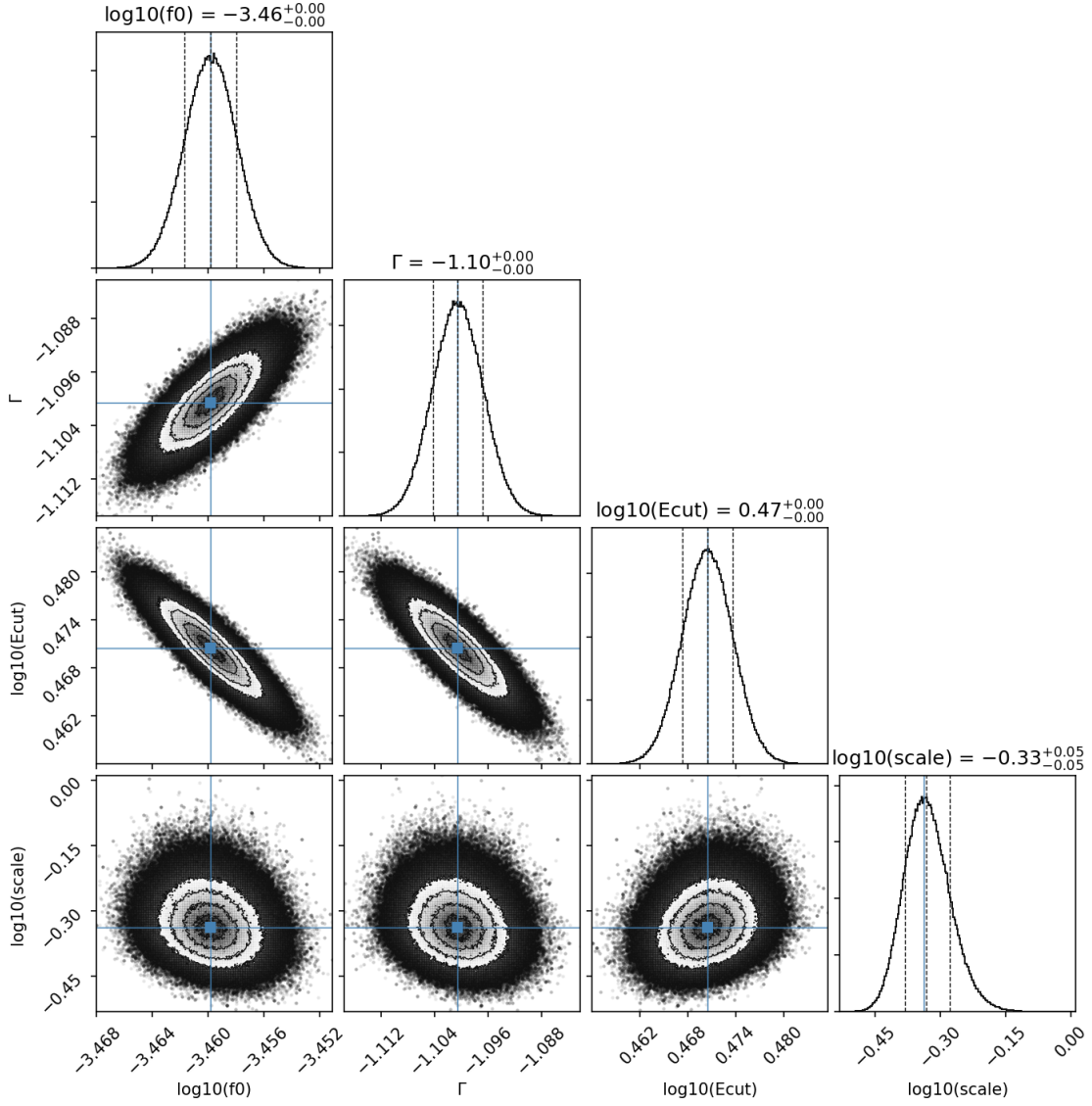


Figure B.1: Corner plot for pure ($\beta = 1$) exponential cutoff power-law function.

A pivot energy $E_0 = 1$ GeV was used. This model is strongly rejected by the observations. The corresponding values of the parameters and their confidence intervals are not statistically meaningful.

B.2 Power-law with a *free* exponential cutoff

$$a(p, x) = 10^{-6} E_0^2 \cdot 10^{\log_{10}(f_0)} (x/E_0)^{\Gamma+2} \exp \left\{ - \left[x/10^{\log_{10}(E_{\text{cut}})} \right]^\beta \right\}$$

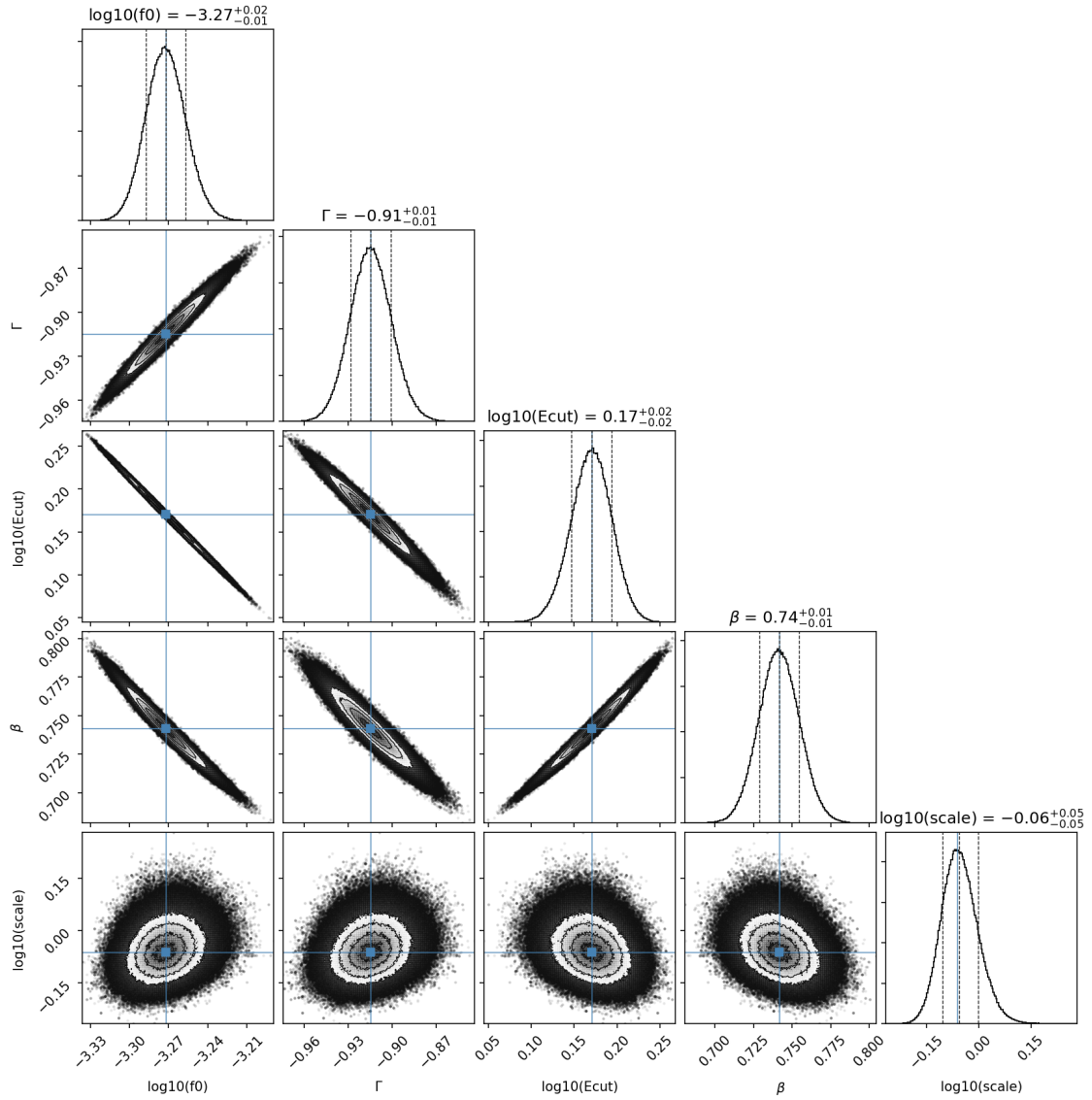


Figure B.2: Corner plot for the free ($\beta > 0$) exponential cutoff power-law function.

A pivot energy $E_0 = 1$ GeV was used. This model is favored over the pure cutoff one, but a tension is present at larger energies (cfr. Section 6.5.1).

B.3 Overlapping power-law

$$a(p, x) = 10^{-6} E_0^2 \cdot 10^{\log_{10}(f_0)} (x/E_0)^{\Gamma+2}$$

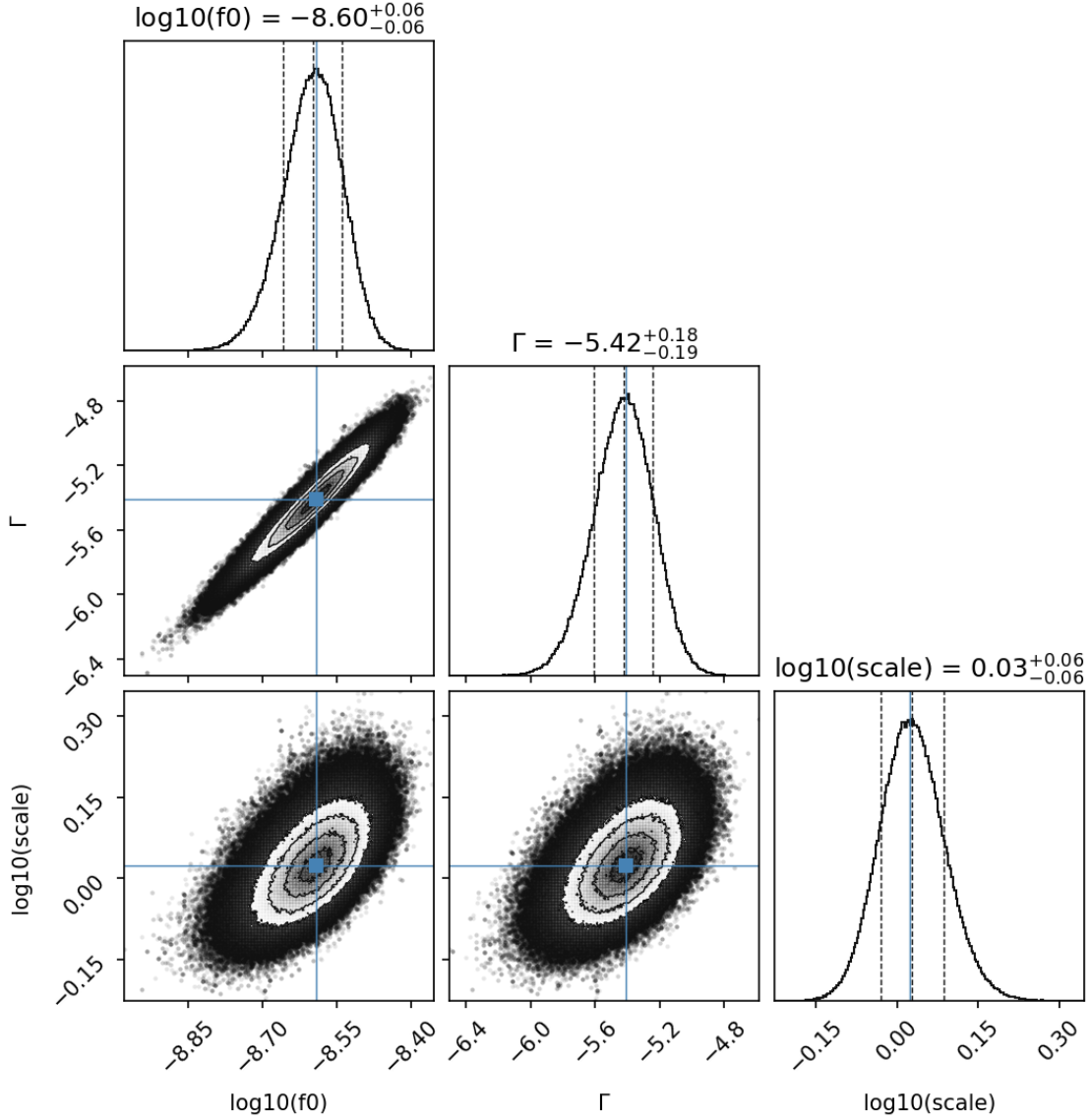


Figure B.3: Corner plot for the power-law function in the overlapping range.

A pivot energy $E_0 = 32.15$ GeV was used, corresponding to the de-correlation energy of MAGIC spectral points. Overlapping energies were defined as those with $E > 12.3$ GeV, the extreme of the last overlapping *Fermi*–LAT point.

B.4 Overlapping log-parabola

$$a(p, x) = 10^{-6} E_0^2 \cdot 10^{\log_{10}(f_0)} (x/E_0)^{2+\Gamma+\beta \cdot \log_{10}(x/E_0)}$$

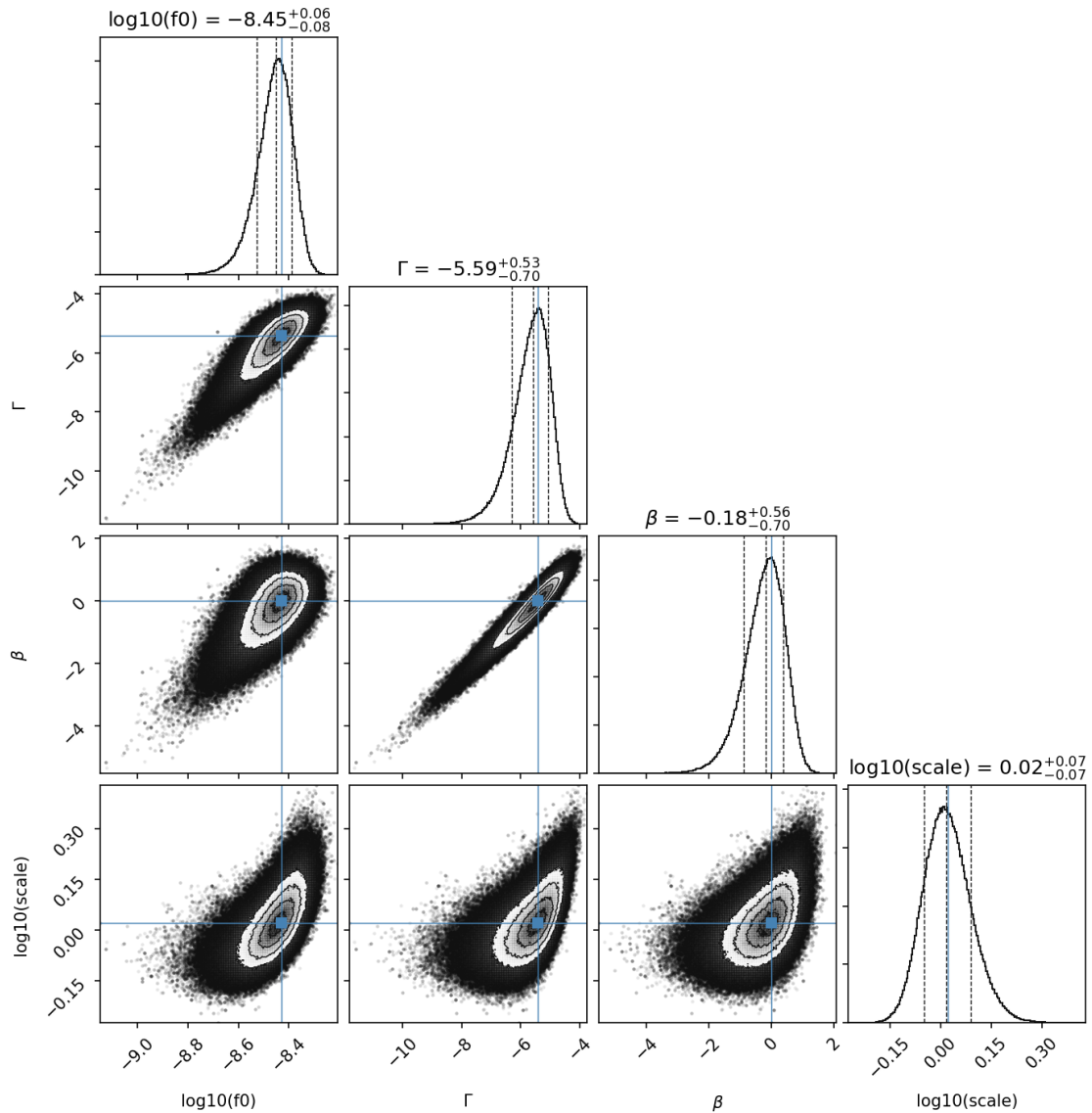


Figure B.4: Corner plot for the log-parabola function in the overlapping range.

A pivot energy $E_0 = 32.15$ GeV was used, corresponding to the de-correlation energy of MAGIC spectral points. Overlapping energies were defined as those with $E > 12.3$ GeV, the extreme of the last overlapping *Fermi*-LAT point. This model is not significantly favored over the simpler power-law one (cfr. Section 6.5.1).

B.5 Composite fit

$$a(p, x) = 10^{-6} \cdot \begin{cases} E_0^2 \cdot 10^{\log_{10}(f_0)} (x/E_0)^{\Gamma+2} \exp \left\{ - \left[x/10^{\log_{10}(E_{\text{cut}})} \right]^\beta \right\} & x < E_{\text{over}} \\ E_{\text{over}}^2 \cdot 10^{\log_{10}(f_0)} (x/E_{\text{over}})^{\Gamma_1+2} & x \geq E_{\text{over}} \end{cases}$$

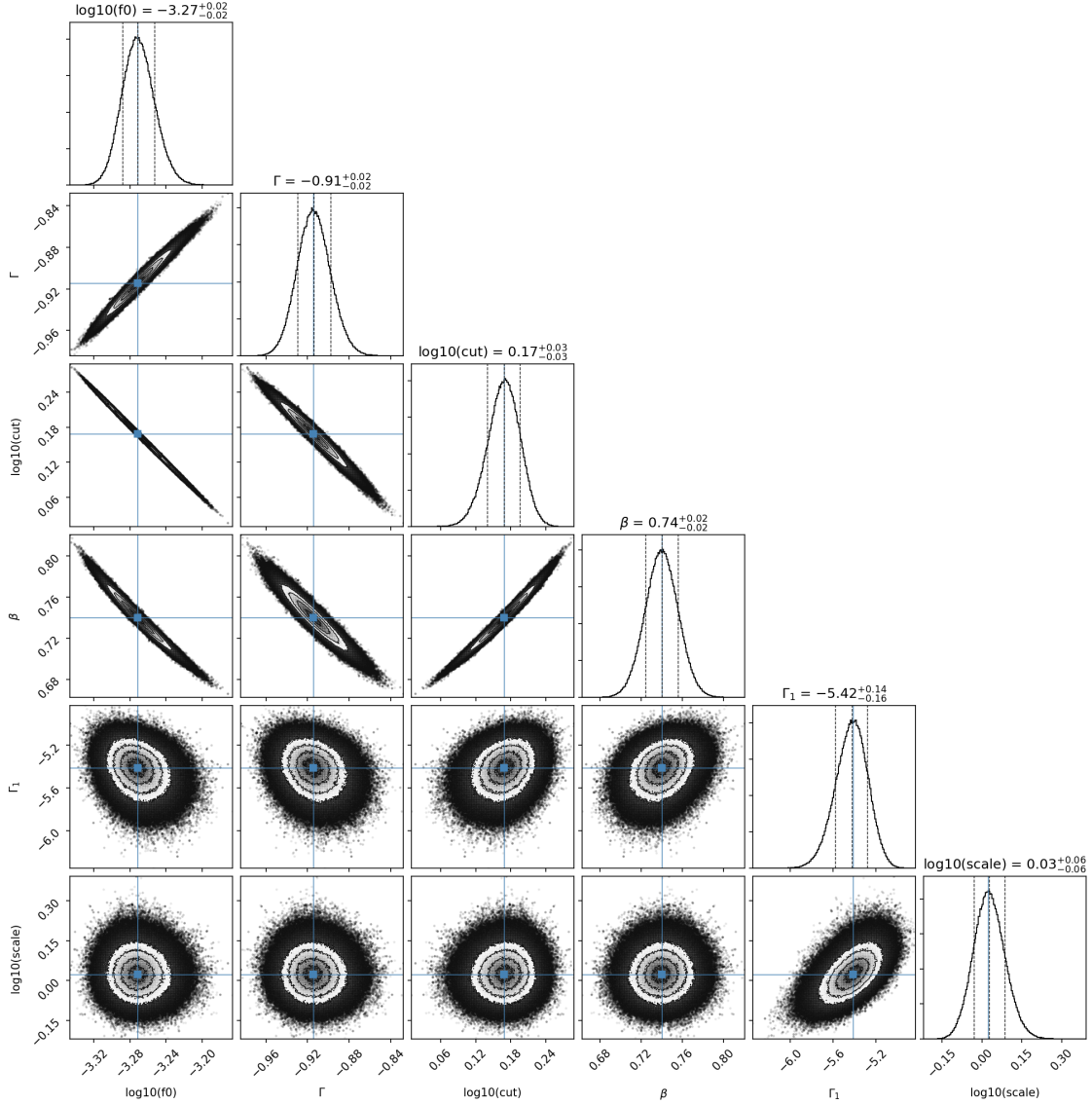


Figure B.5: Corner plot for the composite function.

A pivot energy $E_0 = 1$ GeV was used for the free exponential cutoff power-law function, and the overlapping energy $E_{\text{over}} = 12.3$ GeV was used for the power-law tail. This is the best fitting model, but a likelihood ratio test with the other ones is not possible, as they are not nested sub-cases.



SOFTWARE REPOSITORY

The software that I developed for my doctoral project is freely available in a public git repository. The repository may be accessed at any of these two mirrors:

`https://gitlab.pic.es/ceribell/giosoft.git`

`https://gitlab.mpcdf.mpg.de/gcerib/giosoft`

The original raw data used for my doctoral work, as well as the intermediate and final elaborated stages, are proprietary, and belong to the MAGIC Collaboration (of which I am part). The analysis of MAGIC data requires dedicated tools, which are not available to the general scientific public. The MAGIC Collaboration offers to help external scientists interested in analyzing the data. A request to access the data used for my doctoral project can be made by email at the MAGIC Collaboration contact address:

`contact.magic@mpp.mpg.de`

BIBLIOGRAPHY

Entries with more than ten authors report only the first one. This is also the case for large collaborations such as MAGIC and *Fermi*–LAT. Elements highlighted in **bold** are peer-reviewed publications which I am a corresponding author of (see also the next section).

[Abbott et al. 2017] ABBOTT, B. P. et al.: Multi-messenger Observations of a Binary Neutron Star Merger. In: *Astrophysical Journal, Letters* 848 (2017), October, Nr. 2, p. L12.
URL: <https://ui.adsabs.harvard.edu/abs/2017ApJ...848L..12A>

[Abdalla et al. 2018] ABDALLA, H. et al.: First ground-based measurement of sub-20 GeV to 100 GeV γ -Rays from the Vela pulsar with H.E.S.S. II. In: *Astronomy and Astrophysics* 620 (2018), Dec, p. A66.
URL: <https://ui.adsabs.harvard.edu/abs/2018A&A...620A..66H>

[Abdo et al. 2010a] ABDO, A. A. et al.: The Vela Pulsar: Results from the First Year of Fermi LAT Observations. In: *Astrophysical Journal* 713 (2010), April, Nr. 1, p. 154–165.
URL: <https://ui.adsabs.harvard.edu/abs/2010ApJ...713..154A>

[Abdo et al. 2011] ABDO, A. A. et al.: Gamma-Ray Flares from the Crab Nebula. In: *Science* 331 (2011), February, Nr. 6018, p. 739.
URL: <https://ui.adsabs.harvard.edu/abs/2011Sci...331..739A>

[Abdo et al. 2010b] ABDO, A. A. et al.: The First Fermi Large Area Telescope Catalog of Gamma-ray Pulsars. In: *Astrophysical Journal, Supplement* 187 (2010), April, Nr. 2, p. 460–494.
URL: <https://ui.adsabs.harvard.edu/abs/2010ApJS...187..460A>

[Abdo et al. 2010c] ABDO, A. A. et al.: Fermi Large Area Telescope Observations of the Crab Pulsar And Nebula. In: *Astrophysical Journal* 708 (2010), January, Nr. 2, p. 1254–1267.
URL: <https://ui.adsabs.harvard.edu/abs/2010ApJ...708.1254A>

[Abdo et al. 2010d] ABDO, A. A. et al.: Fermi-LAT Observations of the Geminga Pulsar. In: *Astrophysical Journal* 720 (2010), Sep, Nr. 1, p. 272–283.
URL: <https://ui.adsabs.harvard.edu/abs/2010ApJ...720..272A>

- [Abdo et al. 2013] ABDO, A. A. et al.: The Second Fermi Large Area Telescope Catalog of Gamma-Ray Pulsars. In: *Astrophysical Journal, Supplement* 208 (2013), Oct, Nr. 2, p. 17.
URL: <https://ui.adsabs.harvard.edu/abs/2013ApJS...208...17A>
- [Abdo et al. 2007] ABDO, A. A. et al.: TeV Gamma-Ray Sources from a Survey of the Galactic Plane with Milagro. In: *Astrophysical Journal, Letters* 664 (2007), August, Nr. 2, p. L91–L94.
URL: <https://ui.adsabs.harvard.edu/abs/2007ApJ...664L...91A>
- [Abdollahi et al. 2020] ABDOLLAHI, S. et al.: Fermi Large Area Telescope Fourth Source Catalog. In: *Astrophysical Journal, Supplement* 247 (2020), March, Nr. 1, p. 33.
URL: <https://ui.adsabs.harvard.edu/abs/2020ApJS...247...33A>
- [Abeysekara et al. 2017a] ABEYSEKARA, A. U. et al.: Extended gamma-ray sources around pulsars constrain the origin of the positron flux at Earth. In: *Science* 358 (2017), Nov, Nr. 6365, p. 911–914.
URL: <https://ui.adsabs.harvard.edu/abs/2017Sci...358...911A>
- [Abeysekara et al. 2017b] ABEYSEKARA, A. U. et al.: The 2HWC HAWC Observatory Gamma-Ray Catalog. In: *Astrophysical Journal* 843 (2017), July, Nr. 1, p. 40.
URL: <https://ui.adsabs.harvard.edu/abs/2017ApJ...843...40A>
- [Abeysekara et al. 2019] ABEYSEKARA, A. U. et al.: Measurement of the Crab Nebula Spectrum Past 100 TeV with HAWC. In: *Astrophysical Journal* 881 (2019), August, Nr. 2, p. 134.
URL: <https://ui.adsabs.harvard.edu/abs/2019ApJ...881...134A>
- [Acciari et al. 2020] ACCIARI, V. A. et al.: MAGIC very large zenith angle observations of the Crab Nebula up to 100 TeV. In: *Astronomy and Astrophysics* 635 (2020), March, p. A158.
URL: <https://ui.adsabs.harvard.edu/abs/2020A&A...635A.158M>
- [Acciari et al. 2020] ACCIARI, V. A. et al.: Intensity interferometry with MAGIC. In: TUTHILL, Peter G. (Editor) ; MÉRAND, Antoine (Editor) ; SALLUM, Stephanie (Editor): *Optical and Infrared Interferometry and Imaging VII* Volume 11446 International Society for Optics and Photonics (event), SPIE, 2020, p. 346 – 359.
URL: <https://doi.org/10.1117/12.2561559>
- [Adriani et al. 2009] ADRIANI, O. et al.: An anomalous positron abundance in cosmic rays with energies 1.5-100 GeV. In: *Nature* 458 (2009), April, Nr. 7238, p. 607–609.
URL: <https://ui.adsabs.harvard.edu/abs/2009Natur...458...607A>
- [Aguilar et al. 2013] AGUILAR, M. et al.: First Result from the Alpha Magnetic Spectrometer on the International Space Station: Precision Measurement of the Positron Fraction in Primary Cosmic Rays of 0.5-350 GeV. In: *Physical Review Letters* 110 (2013), April, Nr. 14, p. 141102.
URL: <https://ui.adsabs.harvard.edu/abs/2013PhRvL.110n1102A>

- [Aharonian et al. 2012] AHARONIAN, F. A. ; BOGOVALOV, S. V. ; KHANGULYAN, D.: Abrupt acceleration of a 'cold' ultrarelativistic wind from the Crab pulsar. In: *Nature* 482 (2012), February, Nr. 7386, p. 507–509.
URL: <https://ui.adsabs.harvard.edu/abs/2012Natur.482..507A>
- [Ahnen et al. 2016] AHNEN, M. L. et al.: Search for VHE gamma-ray emission from Geminga pulsar and nebula with the MAGIC telescopes. In: *Astronomy and Astrophysics* 591 (2016), Jun, p. A138.
URL: <https://ui.adsabs.harvard.edu/abs/2016A&A...591A.138A>
- [Albert et al. 2008] ALBERT, J. et al.: VHE γ -Ray Observation of the Crab Nebula and its Pulsar with the MAGIC Telescope. In: *Astrophysical Journal* 674 (2008), February, Nr. 2, p. 1037–1055.
URL: <https://ui.adsabs.harvard.edu/abs/2008ApJ...674.1037A>
- [Aleksić et al. 2012] ALEKSIĆ, J. et al.: Phase-resolved energy spectra of the Crab pulsar in the range of 50–400 GeV measured with the MAGIC telescopes. In: *Astronomy and Astrophysics* 540 (2012), April, p. A69.
URL: <https://ui.adsabs.harvard.edu/abs/2012A&A...540A..69A>
- [Aleksić et al. 2011] ALEKSIĆ, J. et al.: Observations of the Crab Pulsar between 25 and 100 GeV with the MAGIC I Telescope. In: *Astrophysical Journal* 742 (2011), November, Nr. 1, p. 43.
URL: <https://ui.adsabs.harvard.edu/abs/2011ApJ...742...43A>
- [Aleksić et al. 2016a] ALEKSIĆ, J. et al.: The major upgrade of the MAGIC telescopes, Part II: A performance study using observations of the Crab Nebula. In: *Astroparticle Physics* 72 (2016), Jan, p. 76–94.
URL: <https://ui.adsabs.harvard.edu/abs/2016APh....72...76A>
- [Aleksić et al. 2016b] ALEKSIĆ, J. et al.: The major upgrade of the MAGIC telescopes, Part I: The hardware improvements and the commissioning of the system. In: *Astroparticle Physics* 72 (2016), Jan, p. 61–75.
URL: <https://ui.adsabs.harvard.edu/abs/2016APh....72...61A>
- [Aleksić et al. 2014] ALEKSIĆ, J. et al.: Detection of bridge emission above 50 GeV from the Crab pulsar with the MAGIC telescopes. In: *Astronomy and Astrophysics* 565 (2014), May, p. L12.
URL: <https://ui.adsabs.harvard.edu/abs/2014A&A...565L..12A>
- [Aleksić et al. 2015] ALEKSIĆ, J. et al.: Measurement of the Crab Nebula spectrum over three decades in energy with the MAGIC telescopes. In: *Journal of High Energy Astrophysics* 5 (2015), March, p. 30–38.
URL: <https://ui.adsabs.harvard.edu/abs/2015JHEAp...5...30A>
- [Aliu et al. 2008] ALIU, E. et al.: Observation of Pulsed γ -Rays Above 25 GeV from the Crab Pulsar with MAGIC. In: *Science* 322 (2008), Nr. 5905, p. 1221–1224.
URL: <https://science.sciencemag.org/content/322/5905/1221>.
ISSN: 0036-8075

- [Aliu et al. 2015] ALIU, E. et al.: A Search for Pulsations from Geminga above 100 GeV with VERITAS. In: *Astrophysical Journal* 800 (2015), Feb, Nr. 1, p. 61.
URL: <https://ui.adsabs.harvard.edu/abs/2015ApJ...800...61A>
- [Aliu and Wittek 2006] ALIU, E. ; WITTEK, W.: The Unfolding Program in the Standard Analysis Chain. In: *Internal MAGIC-TDAS note 06-01* (2006), April.
URL: <https://magic.mpp.mpg.de/backend/tdas-notes>
- [Allafort et al. 2013] ALLAFORT, A. et al.: PSR J2021+4026 in the Gamma Cygni Region: The First Variable γ -Ray Pulsar Seen by the Fermi LAT. In: *Astrophysical Journal, Letters* 777 (2013), November, Nr. 1, p. L2.
URL: <https://ui.adsabs.harvard.edu/abs/2013ApJ...777L...2A>
- [Amenomori et al. 2019] AMENOMORI, M. et al.: First Detection of Photons with Energy beyond 100 TeV from an Astrophysical Source. In: *Physical Review Letters* 123 (2019), August, Nr. 5, p. 051101.
URL: <https://ui.adsabs.harvard.edu/abs/2019PhRvL.123e1101A>
- [Ansoldi et al. 2016] ANSOLDI, S. et al.: Teraelectronvolt pulsed emission from the Crab Pulsar detected by MAGIC. In: *Astronomy and Astrophysics* 585 (2016), January, p. A133.
URL: <https://ui.adsabs.harvard.edu/abs/2016A&A...585A.133A>
- [Auger et al. 1939] AUGER, Pierre ; EHRENFEST, P. ; MAZE, R. ; DAUDIN, J. ; FRÉON, Robley A.: Extensive Cosmic-Ray Showers. In: *Rev. Mod. Phys.* 11 (1939), Jul, p. 288–291.
URL: <https://link.aps.org/doi/10.1103/RevModPhys.11.288>
- [Backer and Hellings 1986] BACKER, D. C. ; HELTINGS, R. W.: Pulsar timing and general relativity. In: *Annual Review of Astron and Astrophys* 24 (1986), January, p. 537–575.
URL: <https://ui.adsabs.harvard.edu/abs/1986ARA&A...24..537B>
- [Baring 2004] BARING, Matthew G.: High-energy emission from pulsars: the polar cap scenario. In: *Advances in Space Research* 33 (2004), January, Nr. 4, p. 552–560.
URL: <https://ui.adsabs.harvard.edu/abs/2004AdSpR...33..552B>
- [Becerra et al. 2014] BECERRA, J. ; BUEHLER, R. ; HAYS, E.: Fermi LAT detection of enhanced gamma-ray emission from the Crab Nebula region. In: *The Astronomer's Telegram* 6401 (2014), August.
URL: <https://ui.adsabs.harvard.edu/abs/2014ATel.6401....1B>
- [Bennett et al. 1977] BENNETT, K. et al.: COS-B observations of localised high-energy gamma-ray emission from the anticentre region of the galactic disc. In: *Astronomy and Astrophysics* 56 (1977), April, Nr. 3, p. 469–471.
URL: <https://ui.adsabs.harvard.edu/abs/1977A&A....56..469B>
- [Bertero 1989] BERTERO, M.: Linear Inverse and Ill-Posed Problems. In: HAWKES, Peter W. (Editor): *Advances in Electronics and Electron Physics* Volume 75. Academic Press, 1989, p. 1–120.
URL: [https://doi.org/10.1016/S0065-2539\(08\)60946-4](https://doi.org/10.1016/S0065-2539(08)60946-4).
ISSN: 0065-2539

- [Bertsch et al. 1992] BERTSCH, D. L. ; BRAZIER, K. T. S. ; FICHEL, C. E. ; HARTMAN, R. C. ; HUNTER, S. D. ; KANBACH, G. ; KNIFFEN, D. A. ; KWOK, P. W. ; LIN, Y. C. ; MATTOX, J. R.: Pulsed high-energy γ -radiation from Geminga (1E0630+178). In: *Nature* 357 (1992), May, Nr. 6376, p. 306–307.
URL: <https://ui.adsabs.harvard.edu/abs/1992Natur.357..306B>
- [Bignami and Caraveo 1992] BIGNAMI, G. F. ; CARAVEO, P. A.: Geminga: new period, old γ -rays. In: *Nature* 357 (1992), May, Nr. 6376, p. 287.
URL: <https://ui.adsabs.harvard.edu/abs/1992Natur.357..287B>
- [Bignami et al. 1983] BIGNAMI, G. F. ; CARAVEO, P. A. ; LAMB, R. C.: An identification for “GEMINGA” (2CG 195+04) 1E 0630+178 : a unique object in the error box of the high-energy gamma-ray source. In: *Astrophysical Journal, Letters* 272 (1983), Sep, p. L9–L13.
URL: <https://ui.adsabs.harvard.edu/abs/1983ApJ...272L...9B>
- [Bignami et al. 1993] BIGNAMI, G. F. ; CARAVEO, P. A. ; MEREGHETTI, S.: The proper motion of Geminga’s optical counterpart. In: *Nature* 361 (1993), February, Nr. 6414, p. 704–706.
URL: <https://ui.adsabs.harvard.edu/abs/1993Natur.361..704B>
- [Bignami et al. 1988] BIGNAMI, G. F. ; CARAVEO, P. A. ; PAUL, J. A.: The colors of G”, the proposed optical counterpart of Geminga. In: *Astronomy and Astrophysics* 202 (1988), August, p. L1–L4.
URL: <https://ui.adsabs.harvard.edu/abs/1988A&A...202L...1B>
- [Biland et al. 2008] BILAND, A. ; GARCZARCYK, M. ; ANDERHUB, H. ; DANIELYAN, V. ; HAKOBYAN, D. ; LORENZ, E. ; MIRZOYAN, R.: The Active Mirror Control of the MAGIC Telescopes. In: *International Cosmic Ray Conference Volume 3*, IUPAP, January 2008, p. 1353–1356.
URL: <https://ui.adsabs.harvard.edu/abs/2008ICRC....3.1353B>
- [Bionta et al. 1987] BIONTA, R. M. et al.: Observation of a neutrino burst in coincidence with supernova 1987A in the Large Magellanic Cloud. In: *Physical Review Letters* 58 (1987), April, Nr. 14, p. 1494–1496.
URL: <https://ui.adsabs.harvard.edu/abs/1987PhRvL..58.1494B>
- [Bitossi et al. 2016] BITOSSI, Massimiliano ; PAOLETTI, Riccardo ; TESCARO, Diego: Ultra-Fast Sampling and Data Acquisition Using the DRS4 Waveform Digitizer. In: *IEEE Transactions on Nuclear Science* 63 (2016), August, Nr. 4, p. 2309–2316.
URL: <https://ui.adsabs.harvard.edu/abs/2016ITNS...63.2309B>
- [Blanch and Moralejo 2004] BLANCH, O. ; MORALEJO, A.: How to use the Camera Simulation Program 0.7. In: *Internal MAGIC-TDAS note 04-07* (2004), September.
URL: <https://magic.mpp.mpg.de/backend/tdas-notes>
- [Borla Tridon et al. 2009] BORLA TRIDON, D. et al.: Performance of the Camera of the MAGIC II Telescope. In: *arXiv e-prints* (2009), June, p. arXiv:0906.5448.
URL: <https://ui.adsabs.harvard.edu/abs/2009arXiv0906.5448B>
- [Brambilla et al. 2018] BRAMBILLA, Gabriele ; KALAPOTHARAKOS, Constantinos ; TIMOKHIN, Andrey N. ; HARDING, Alice K. ; KAZANAS, Demosthenes: Electron-Positron Pair Flow

- and Current Composition in the Pulsar Magnetosphere. In: *Astrophysical Journal* 858 (2018), May, Nr. 2, p. 81.
URL: <https://ui.adsabs.harvard.edu/abs/2018ApJ...858...81B>
- [Brecher 1978] BRECHER, Kenneth: A Near-Eastern sighting of the supernova explosion of 1054. In: *Nature* 273 (1978), June, Nr. 5665, p. 728–730.
URL: <https://ui.adsabs.harvard.edu/abs/1978Natur.273..728B>
- [Breiman 2001] BREIMAN, LEO: Random Forests. In: *Machine Learning* 45 (2001), January, p. 5–32.
URL: <https://ui.adsabs.harvard.edu/abs/2001MachL...45....5B>
- [Bretz et al. 2009] BRETZ, T. ; DORNER, D. ; WAGNER, R. M. ; SAWALLISCH, P.: The drive system of the major atmospheric gamma-ray imaging Cherenkov telescope. In: *Astroparticle Physics* 31 (2009), March, Nr. 2, p. 92–101.
URL: <https://ui.adsabs.harvard.edu/abs/2009APh....31...92B>
- [Buccheri et al. 1983] BUCCHERI, R. et al.: Search for pulsed γ -ray emission from radio pulsars in the COS-B data. In: *Astronomy and Astrophysics* 128 (1983), Dec, p. 245–251.
URL: <https://ui.adsabs.harvard.edu/abs/1983A&A...128..245B>
- [Buehler et al. 2011] BUEHLER, R. ; D'AMMANDO, F. ; CANNON, A.: Fermi LAT detection of a new enhanced gamma-ray emission from the Crab Nebula region. In: *The Astronomer's Telegram* 3276 (2011), April.
URL: <https://ui.adsabs.harvard.edu/abs/2011ATel.3276....1B>
- [Buehler et al. 2010] BUEHLER, R. ; D'AMMANDO, F. ; HAYS, E.: Fermi LAT confirmation of enhanced gamma-ray emission from the Crab Nebula region. In: *The Astronomer's Telegram* 2861 (2010), September.
URL: <https://ui.adsabs.harvard.edu/abs/2010ATel.2861....1B>
- [Bulgarelli et al. 2018a] BULGARELLI, A. et al.: AGILE confirms enhanced gamma-ray emission from the Crab Nebula. In: *The Astronomer's Telegram* 11415 (2018), March.
URL: <https://ui.adsabs.harvard.edu/abs/2018ATel11415....1B>
- [Bulgarelli et al. 2016] BULGARELLI, A. et al.: Enhanced gamma-ray emission from the Crab Nebula detected by AGILE. In: *The Astronomer's Telegram* 9586 (2016), October.
URL: <https://ui.adsabs.harvard.edu/abs/2016ATel.9586....1B>
- [Bulgarelli et al. 2018b] BULGARELLI, A. et al.: AGILE detection of renewed gamma-ray activity from the Crab Nebula. In: *The Astronomer's Telegram* 12148 (2018), October.
URL: <https://ui.adsabs.harvard.edu/abs/2018ATel12148....1B>
- [Buson et al. 2013] BUSON, Sara ; BUEHLER, Rolf ; HAYS, Elizabeth: Fermi LAT detection of enhanced gamma-ray emission from the Crab Nebula region. In: *The Astronomer's Telegram* 5485 (2013), October.
URL: <https://ui.adsabs.harvard.edu/abs/2013ATel.5485....1B>
- [Caplan and Horowitz 2017] CAPLAN, M. E. ; HOROWITZ, C. J.: Colloquium: Astromaterial science and nuclear pasta. In: *Reviews of Modern Physics* 89 (2017), October, Nr. 4,

- p. 041002.
URL: <https://ui.adsabs.harvard.edu/abs/2017RvMP...89d1002C>
- [Caraveo et al. 2003] CARAVEO, P. A. ; BIGNAMI, G. F. ; DE LUCA, A. ; MEREGHETTI, S. ; PELLIZZONI, A. ; MIGNANI, R. ; TUR, A. ; BECKER, W.: Geminga's Tails: A Pulsar Bow Shock Probing the Interstellar Medium. In: *Science* 301 (2003), September, Nr. 5638, p. 1345–1348.
URL: <https://ui.adsabs.harvard.edu/abs/2003Sci...301.1345C>
- [Caraveo et al. 2004] CARAVEO, P. A. ; DE LUCA, A. ; MEREGHETTI, S. ; PELLIZZONI, A. ; BIGNAMI, G. F.: Phase-Resolved Spectroscopy of Geminga Shows Rotating Hot Spot(s). In: *Science* 305 (2004), July, Nr. 5682, p. 376–380.
URL: <https://ui.adsabs.harvard.edu/abs/2004Sci...305..376C>
- [Caraveo et al. 1996] CARAVEO, Patrizia A. ; BIGNAMI, Giovanni F. ; MIGNANI, Roberto ; TAFF, Laurence G.: Parallax Observations with the Hubble Space Telescope Yield the Distance to Geminga. In: *Astrophysical Journal, Letters* 461 (1996), April, p. L91.
URL: <https://ui.adsabs.harvard.edu/abs/1996ApJ...461L..91C>
- [Cardillo et al. 2018] CARDILLO, M. et al.: AGILE detection of enhanced gamma-ray activity from the Crab Nebula. In: *The Astronomer's Telegram* 12123 (2018), October.
URL: <https://ui.adsabs.harvard.edu/abs/2018ATel12123....1C>
- [Cerutti and Beloborodov 2017] CERUTTI, Benoît ; BELOBORODOV, Andrei M.: Electrodynamics of Pulsar Magnetospheres. In: *Space Science Reviews* 207 (2017), July, Nr. 1-4, p. 111–136.
URL: <https://ui.adsabs.harvard.edu/abs/2017SSRv...207..111C>
- [Cheng et al. 1986] CHENG, K. S. ; HO, C. ; RUDERMAN, M.: Energetic Radiation from Rapidly Spinning Pulsars. I. Outer Magnetosphere Gaps. In: *Astrophysical Journal* 300 (1986), January, p. 500.
URL: <https://ui.adsabs.harvard.edu/abs/1986ApJ...300..500C>
- [Cherenkov 1934] CHERENKOV, P. A.: Видимое свечение чистых жидкостей под действием γ -радиации ("*Visible emission of clean liquids by action of γ radiation*"). In: Доклады Академии Наук СССР 2 (1934), May, Nr. 8, p. 385–389.
URL: <https://ufn.ru/ru/articles/1967/10/n/>
- [Cheung 2016] CHEUNG, C. C.: Fermi-LAT confirmation of enhanced gamma-ray activity from the Crab nebula. In: *The Astronomer's Telegram* 9588 (2016), October.
URL: <https://ui.adsabs.harvard.edu/abs/2016ATel.9588....1C>
- [Cheung 2019] CHEUNG, C. C.: Fermi-LAT detection of enhanced gamma-ray activity from the Crab Nebula in May 2019. In: *The Astronomer's Telegram* 12753 (2019), May.
URL: <https://ui.adsabs.harvard.edu/abs/2019ATel12753....1C>
- [Cheung et al. 2018] CHEUNG, C. C. ; ANGIONI, R. ; BUSON, S. ; VENTERS, T.: Fermi-LAT detection of enhanced gamma-ray activity from the Crab nebula in October 2018. In: *The Astronomer's Telegram* 12095 (2018), October.
URL: <https://ui.adsabs.harvard.edu/abs/2018ATel12095....1C>

- [Clear et al. 1987] CLEAR, J. ; BENNETT, K. ; BUCCHERI, R. ; GRENIER, I. A. ; HERMSEN, W. ; MAYER-HASSELWANDER, H. A. ; SACCO, B.: A detailed analysis of the high energy gamma-ray emission from the Crab pulsar and nebula. In: *Astronomy and Astrophysics* 174 (1987), March, p. 85–94.
URL: <https://ui.adsabs.harvard.edu/abs/1987A&A...174...85C>
- [Coles et al. 2011] COLES, W. ; HOBBS, G. ; CHAMPION, D. J. ; MANCHESTER, R. N. ; VERBIEST, J. P. W.: Pulsar timing analysis in the presence of correlated noise. In: *Monthly Notices of the RAS* 418 (2011), Nov, Nr. 1, p. 561–570.
URL: <https://ui.adsabs.harvard.edu/abs/2011MNRAS.418..561C>
- [Contopoulos et al. 1999] CONTOPOULOS, Ioannis ; KAZANAS, Demosthenes ; FENDT, Christian: The Axisymmetric Pulsar Magnetosphere. In: *Astrophysical Journal* 511 (1999), January, Nr. 1, p. 351–358.
URL: <https://ui.adsabs.harvard.edu/abs/1999ApJ...511..351C>
- [Daugherty and Harding 1996] DAUGHERTY, Joseph K. ; HARDING, Alice K.: Gamma-Ray Pulsars: Emission from Extended Polar CAP Cascades. In: *Astrophysical Journal* 458 (1996), February, p. 278.
URL: <https://ui.adsabs.harvard.edu/abs/1996ApJ...458..278D>
- [Dazzi et al. 2015] DAZZI, F. ; HERRANZ LAZARO, D. ; LOPEZ, M. ; NAKAJIMA, D. ; RODRIGUEZ GARCIA, J. ; SCHWEIZER, T.: Performance studies of the new stereoscopic Sum-Trigger-II of MAGIC after one year of operation. In: *arXiv e-prints* (2015), Aug, p. arXiv:1508.05255.
URL: <https://ui.adsabs.harvard.edu/abs/2015arXiv150805255D>
- [Dazzi et al. 2021] DAZZI, F. et al.: **The Stereoscopic Analog Trigger of the MAGIC Telescopes**. In: *IEEE Transactions on Nuclear Science* 68 (2021), Nr. 7, p. 1473–1486.
URL: <https://doi.org/10.1109/TNS.2021.3079262>
- [De Angelis and Pimenta 2018] DE ANGELIS, Alessandro ; PIMENTA, Mário: *Introduction to Particle and Astroparticle Physics*. Springer Verlag, 2018
URL: <https://ui.adsabs.harvard.edu/abs/2018ipap.book.....D>
- [de Jager and Büsching 2010] DE JAGER, O. C. ; BÜSCHING, I.: The H-test probability distribution revisited: improved sensitivity. In: *Astronomy and Astrophysics* 517 (2010), Jul, p. L9.
URL: <https://ui.adsabs.harvard.edu/abs/2010A&A...517L...9D>
- [de Jager et al. 1986] DE JAGER, O. C. ; RAUBENHEIMER, B. C. ; SWANEPOEL, J. W. H.: Kernel density estimations applied to gamma ray light curves. In: *Astronomy and Astrophysics* 170 (1986), December, Nr. 1, p. 187–196.
URL: <https://ui.adsabs.harvard.edu/abs/1986A&A...170..187D>
- [de Jager et al. 1989] DE JAGER, O. C. ; RAUBENHEIMER, B. C. ; SWANEPOEL, J. W. H.: A powerful test for weak periodic signals with unknown light curve shape in sparse data. In: *Astronomy and Astrophysics* 221 (1989), Aug, p. 180–190.
URL: <https://ui.adsabs.harvard.edu/abs/1989A&A...221..180D>

- [de Naurois et al. 2002] DE NAUROIS, M. et al.: Measurement of the Crab Flux above 60 GeV with the CELESTE Cerenkov Telescope. In: *Astrophysical Journal* 566 (2002), February, Nr. 1, p. 343–357.
URL: <https://ui.adsabs.harvard.edu/abs/2002ApJ...566..343D>
- [Di Mauro et al. 2019] DI MAURO, Mattia ; MANCONI, Silvia ; DONATO, Fiorenza: Detection of a γ -ray halo around Geminga with the Fermi-LAT data and implications for the positron flux. In: *Physical Review D* 100 (2019), December, Nr. 12, p. 123015.
URL: <https://ui.adsabs.harvard.edu/abs/2019PhRvD.100l3015D>
- [Ducati 2002a] DUCATI, J. R.: VizieR Online Data Catalog: Catalogue of Stellar Photometry in Johnson's 11-color system. In: *VizieR Online Data Catalog* (2002), January.
URL: <https://ui.adsabs.harvard.edu/abs/2002yCat..2237....0D>
- [Ducati 2002b] DUCATI, J. R.: VizieR Online Data Catalog: Catalogue of Stellar Photometry in Johnson's 11-color system. In: *VizieR Online Data Catalog* (2002), January.
URL: <https://ui.adsabs.harvard.edu/abs/2002yCat..2237....0D>
- [Duyvendak 1942] DUYVENDAK, J. J. L.: Further Data Bearing on the Identification of the Crab Nebula with the Supernova of 1054 A.D. Part I. The Ancient Oriental Chronicles. In: *Publications of the ASP* 54 (1942), April, Nr. 318, p. 91–94.
URL: <https://ui.adsabs.harvard.edu/abs/1942PASP...54...91D>
- [Edwards et al. 2006] EDWARDS, R. T. ; HOBBS, G. B. ; MANCHESTER, R. N.: TEMPO2, a new pulsar timing package - II. The timing model and precision estimates. In: *Monthly Notices of the RAS* 372 (2006), November, Nr. 4, p. 1549–1574.
URL: <https://ui.adsabs.harvard.edu/abs/2006MNRAS.372.1549E>
- [Espinoza et al. 2011] ESPINOZA, C. M. ; LYNE, A. G. ; STAPPERS, B. W. ; KRAMER, M.: A study of 315 glitches in the rotation of 102 pulsars. In: *Monthly Notices of the RAS* 414 (2011), June, Nr. 2, p. 1679–1704.
URL: <https://ui.adsabs.harvard.edu/abs/2011MNRAS.414.1679E>
- [Faherty et al. 2007] FAHERTY, Jacqueline ; WALTER, Frederick M. ; ANDERSON, Jay: The trigonometric parallax of the neutron star Geminga. In: *Astrophysics and Space Science* 308 (2007), Apr, Nr. 1-4, p. 225–230.
URL: <https://ui.adsabs.harvard.edu/abs/2007Ap&SS.308..225F>
- [Fichtel et al. 1975] FICHTEL, C. E. ; HARTMAN, R. C. ; KNIFFEN, D. A. ; THOMPSON, D. J. ; BIGNAMI, G. F. ; ÖGELMAN, H. ; ÖZEL, M. E. ; TÜMER, T.: High-energy gamma-ray results from the second small astronomy satellite. In: *Astrophysical Journal* 198 (1975), May, p. 163–182.
URL: <https://ui.adsabs.harvard.edu/abs/1975ApJ...198..163F>
- [Fierro et al. 1998] FIERRO, J. M. ; MICHELSON, P. F. ; NOLAN, P. L. ; THOMPSON, D. J.: Phase-resolved Studies of the High-Energy Gamma-Ray Emission from the Crab, Geminga, and VELA Pulsars. In: *Astrophysical Journal* 494 (1998), February, Nr. 2, p. 734–746.
URL: <https://ui.adsabs.harvard.edu/abs/1998ApJ...494..734F>

- [Fomin et al. 1994] FOMIN, V. P. ; STEPANIAN, A. A. ; LAMB, R. C. ; LEWIS, D. A. ; PUNCH, M. ; WEEKES, T. C.: New methods of atmospheric Cherenkov imaging for gamma-ray astronomy. I. The false source method. In: *Astroparticle Physics* 2 (1994), May, Nr. 2, p. 137–150.
URL: <https://ui.adsabs.harvard.edu/abs/1994APh....2..137F>
- [Frank and Tamm 1937] FRANK, I. M. ; ТАММ, И. Е.: Когерентное излучение быстрого электрона в среде (“*Coherent visible radiation of fast electrons passing through matter*”). In: Доклады Академии Наук СССР 14 (1937), Nr. 3, p. 109–114.
URL: <https://ufn.ru/ru/articles/1967/10/o/>.
Translation: https://doi.org/10.1007/978-3-642-74626-0_2
- [García et al. 2014] GARCÍA, J. R. ; DAZZI, F. ; HÄFNER, D. ; HERRANZ, D. ; LÓPEZ, M. ; MARIOTTI, M. ; MIRZOYAN, R. ; NAKAJIMA, D. ; SCHWEIZER, T. ; TESHIMA, M.: Status of the new Sum-Trigger system for the MAGIC telescopes. In: *arXiv e-prints* (2014), Apr, p. arXiv:1404.4219.
URL: <https://ui.adsabs.harvard.edu/abs/2014arXiv1404.4219G>
- [Gasparrini and Buehl 2014] GASPARRINI, D. ; BUEHL, R.: Fermi LAT detection of enhanced gamma-ray emission from the Crab Nebula region. In: *The Astronomer's Telegram* 5971 (2014), March.
URL: <https://ui.adsabs.harvard.edu/abs/2014ATel.5971....1G>
- [Ghosh 2007] GHOSH, Pranab: *Rotation and Accretion Powered Pulsars*. Volume 10. World of Science, 2007
URL: <https://ui.adsabs.harvard.edu/abs/2007rapp.book....G>
- [Gold 1968] GOLD, T.: Rotating Neutron Stars as the Origin of the Pulsating Radio Sources. In: *Nature* 218 (1968), May, Nr. 5143, p. 731–732.
URL: <https://ui.adsabs.harvard.edu/abs/1968Natur.218..731G>
- [Gold 1969] GOLD, Thomas: Rotating Neutron Stars and the Nature of Pulsars. In: *Nature* 221 (1969), January, Nr. 5175, p. 25–27.
URL: <https://ui.adsabs.harvard.edu/abs/1969Natur.221...25G>
- [Goldreich and Julian 1969] GOLDREICH, Peter ; JULIAN, William H.: Pulsar Electrodynamics. In: *Astrophysical Journal* 157 (1969), August, p. 869.
URL: <https://ui.adsabs.harvard.edu/abs/1969ApJ...157..869G>
- [Gray et al. 2003] GRAY, R. O. ; CORBALLY, C. J. ; GARRISON, R. F. ; MCFADDEN, M. T. ; ROBINSON, P. E.: Contributions to the Nearby Stars (NStars) Project: Spectroscopy of Stars Earlier than M0 within 40 Parsecs: The Northern Sample. I. In: *Astronomical Journal* 126 (2003), October, Nr. 4, p. 2048–2059.
URL: <https://ui.adsabs.harvard.edu/abs/2003AJ...126.2048G>
- [Guépin et al. 2020] GUÉPIN, Claire ; CERUTTI, Benoît ; KOTERA, Kumiko: Proton acceleration in pulsar magnetospheres. In: *Astronomy and Astrophysics* 635 (2020), March, p. A138.
URL: <https://ui.adsabs.harvard.edu/abs/2020A&A...635A.138G>

- [Güercinoğlu et al. 2020] GÜERCINOĞLU, E. ; GE, M. Y. ; YUAN, J. P. ; ZHOU, S. Q.: Glitches in four gamma-ray pulsars and inferences on the neutron star structure. In: *arXiv e-prints* (2020), November, p. arXiv:2011.14788.
URL: <https://ui.adsabs.harvard.edu/abs/2020arXiv201114788G>
- [Haefner 2011] HAEFNER, Dennis: New improved Sum-Trigger system for the MAGIC telescopes. In: *International Cosmic Ray Conference Volume 9*, IUPAP, January 2011, p. 251.
URL: <https://ui.adsabs.harvard.edu/abs/2011ICRC....9..251H>
- [Hahn et al. 2018] HAHN, A. ; DETTLAFF, A. ; FINK, D. ; MAZIN, D. ; MIRZOYAN, R. ; TESHIMA, M.: Development of three silicon photomultiplier detector modules for the MAGIC telescopes for a performance comparison to PMTs. In: *Nuclear Instruments and Methods in Physics Research Section A: Accelerators, Spectrometers, Detectors and Associated Equipment* 912 (2018), p. 259–263.
URL: <https://doi.org/10.1016/j.nima.2017.11.071>.
ISSN: 0168-9002
- [Halpern and Ruderman 1993] HALPERN, J. P. ; RUDERMAN, M.: Soft X-Ray Properties of the Geminga Pulsar. In: *Astrophysical Journal* 415 (1993), September, p. 286.
URL: <https://ui.adsabs.harvard.edu/abs/1993ApJ...415..286H>
- [Halpern and Tytler 1988] HALPERN, J. P. ; TYTLER, D.: The Geminga X-Ray Counterpart and a Blue Optical Identification. In: *Astrophysical Journal* 330 (1988), July, p. 201.
URL: <https://ui.adsabs.harvard.edu/abs/1988ApJ...330..201H>
- [Halpern and Wang 1997] HALPERN, J. P. ; WANG, F. Y. H.: A Broadband X-Ray Study of the Geminga Pulsar. In: *Astrophysical Journal* 477 (1997), March, Nr. 2, p. 905–915.
URL: <https://ui.adsabs.harvard.edu/abs/1997ApJ...477..905H>
- [Harding 2007] HARDING, Alice K.: Pulsar High-Energy Emission From the Polar Cap and Slot Gap. In: *arXiv e-prints* (2007), October, p. arXiv:0710.3517.
URL: <https://ui.adsabs.harvard.edu/abs/2007arXiv0710.3517H>
- [Harding et al. 2018] HARDING, Alice K. ; KALAPOTHARAKOS, Constantinos ; BARNARD, Monica ; VENTER, Christo: Multi-TeV Emission from the Vela Pulsar. In: *Astrophysical Journal, Letters* 869 (2018), December, Nr. 1, p. L18.
URL: <https://ui.adsabs.harvard.edu/abs/2018ApJ...869L..18H>
- [Heck et al. 1998] HECK, D. ; KNAPP, J. ; CAPDEVIELLE, J. N. ; SCHATZ, G. ; THOUW, T.: *CORSIKA: a Monte Carlo code to simulate extensive air showers*. Forschungszentrum Karlsruhe, 1998
URL: <https://ui.adsabs.harvard.edu/abs/1998cmcc.book.....H>
- [Hermsen et al. 1977] HERMSEN, W. et al.: New high energy γ -ray sources observed by COS B. In: *Nature* 269 (1977), Nr. 5628, p. 494–495.
URL: <https://doi.org/10.1038/269494a0>.
ISSN: 1476-4687

- [Hewish et al. 1968] HEWISH, A. ; BELL, S. J. ; PILKINGTON, J. D. H. ; SCOTT, P. F. ; COLLINS, R. A.: Observation of a Rapidly Pulsating Radio Source. In: *Nature* 217 (1968), February, Nr. 5130, p. 709–713.
URL: <https://ui.adsabs.harvard.edu/abs/1968Natur.217..709H>
- [Hillas 1985] HILLAS, A. M.: Cerenkov Light Images of EAS Produced by Primary Gamma Rays and by Nuclei. In: *19th International Cosmic Ray Conference (ICRC19)*, Volume 3 Volume 3, IUPAP, August 1985, p. 445.
URL: <https://ui.adsabs.harvard.edu/abs/1985ICRC....3..445H>
- [Hirata et al. 1987] HIRATA, K. et al.: Observation of a neutrino burst from the supernova SN1987A. In: *Physical Review Letters* 58 (1987), April, Nr. 14, p. 1490–1493.
URL: <https://ui.adsabs.harvard.edu/abs/1987PhRvL..58.1490H>
- [Hirotani 2006] HIROTANI, Kouichi: Particle Accelerator in Pulsar Magnetospheres: Super-Goldreich-Julian Current with Ion Emission from the Neutron Star Surface. In: *Astrophysical Journal* 652 (2006), Dec, Nr. 2, p. 1475–1493.
URL: <https://ui.adsabs.harvard.edu/abs/2006ApJ...652.1475H>
- [Hirotani 2008] HIROTANI, Kouichi: Outer-Gap versus Slot-Gap Models for Pulsar High-Energy Emissions: The Case of the Crab Pulsar. In: *Astrophysical Journal, Letters* 688 (2008), November, Nr. 1, p. L25.
URL: <https://ui.adsabs.harvard.edu/abs/2008ApJ...688L..25H>
- [Hirotani 2011] HIROTANI, Kouichi: What Pulsar High-Energy Emission Model Survives? In: *Astrophysics and Space Science Proceedings* 21 (2011), January, p. 117.
URL: <https://ui.adsabs.harvard.edu/abs/2011ASSP...21..117H>
- [Hirotani 2013] HIROTANI, Kouichi: Luminosity Evolution of Gamma-Ray Pulsars. In: *Astrophysical Journal* 766 (2013), Apr, Nr. 2, p. 98.
URL: <https://ui.adsabs.harvard.edu/abs/2013ApJ...766...98H>
- [Hobbs et al. 2004] HOBBS, G. ; LYNE, A. G. ; KRAMER, M. ; MARTIN, C. E. ; JORDAN, C.: Long-term timing observations of 374 pulsars. In: *Monthly Notices of the RAS* 353 (2004), Oct, Nr. 4, p. 1311–1344.
URL: <https://ui.adsabs.harvard.edu/abs/2004MNRAS.353.1311H>
- [Hobbs et al. 2006] HOBBS, G. B. ; EDWARDS, R. T. ; MANCHESTER, R. N.: TEMPO2, a new pulsar-timing package - I. An overview. In: *Monthly Notices of the RAS* 369 (2006), June, Nr. 2, p. 655–672.
URL: <https://ui.adsabs.harvard.edu/abs/2006MNRAS.369..655H>
- [Ishio 2020] ISHIO, Kazuma: *Improvement in the gamma-ray energy reconstruction of MAGIC and impact on the spectral analysis of the first Gamma Ray Burst detected at TeV energies*. Ludwig-Maximilians-Universität München, November 2020
URL: <http://nbn-resolving.de/urn:nbn:de:bvb:19-275991>
- [Jackson et al. 2002] JACKSON, M. S. ; HALPERN, J. P. ; GOTTHELF, E. V. ; MATTOX, J. R.: A High-Energy Study of the Geminga Pulsar. In: *Astrophysical Journal* 578 (2002), October, Nr. 2, p. 935–942.
URL: <https://ui.adsabs.harvard.edu/abs/2002ApJ...578..935J>

- [Kalapotharakos et al. 2018] KALAPOTHARAKOS, Constantinos ; BRAMBILLA, Gabriele ; TIMOKHIN, Andrey ; HARDING, Alice K. ; KAZANAS, Demosthenes: Three-dimensional Kinetic Pulsar Magnetosphere Models: Connecting to Gamma-Ray Observations. In: *Astrophysical Journal* 857 (2018), April, Nr. 1, p. 44.
URL: <https://ui.adsabs.harvard.edu/abs/2018ApJ...857...44K>
- [Kargaltsev et al. 2005] KARGALTSEV, O. Y. ; PAVLOV, G. G. ; ZAVLIN, V. E. ; ROMANI, R. W.: Ultraviolet, X-Ray, and Optical Radiation from the Geminga Pulsar. In: *Astrophysical Journal* 625 (2005), May, Nr. 1, p. 307–323.
URL: <https://ui.adsabs.harvard.edu/abs/2005ApJ...625..307K>
- [Kniffen et al. 1974] KNIFFEN, D. A. ; HARTMAN, R. C. ; THOMPSON, D. J. ; BIGNAMI, G. F. ; FICHTEL, C. E.: Gamma radiation from the Crab Nebula above 35 MeV. In: *Nature* 251 (1974), October, Nr. 5474, p. 397–399.
URL: <https://ui.adsabs.harvard.edu/abs/1974Natur.251..397K>
- [Kuiper et al. 2001] KUIPER, L. ; HERMSEN, W. ; CUSUMANO, G. ; DIEHL, R. ; SCHÖNFELDER, V. ; STRONG, A. ; BENNETT, K. ; MCCONNELL, M. L.: The Crab pulsar in the 0.75–30 MeV range as seen by CGRO COMPTEL. A coherent high-energy picture from soft X-rays up to high-energy gamma-rays. In: *Astronomy and Astrophysics* 378 (2001), November, p. 918–935.
URL: <https://ui.adsabs.harvard.edu/abs/2001A&A...378..918K>
- [Landau and Lifchitz 1969] LANDAU, L. D. ; LIFCHITZ, E. M.: *Physique Théorique*. Volume 8: *Électrodynamique des milieux continus*. Moscow USSR, Editions MIR, 1969 French edition based on the 1959 Russian original.
- [Li and Ma 1983] LI, T. P. ; MA, Y. Q.: Analysis methods for results in gamma-ray astronomy. In: *Astrophysical Journal* 272 (1983), Sep, p. 317–324.
URL: <https://ui.adsabs.harvard.edu/abs/1983ApJ...272..317L>
- [Linden et al. 2017] LINDEN, Tim ; AUCHETTL, Katie ; BRAMANTE, Joseph ; CHOLIS, Ilias ; FANG, Ke ; HOOPER, Dan ; KARWAL, Tanvi ; LI, Shirley W.: Using HAWC to discover invisible pulsars. In: *Physical Review D* 96 (2017), November, Nr. 10, p. 103016.
URL: <https://ui.adsabs.harvard.edu/abs/2017PhRvD...96j3016L>
- [López-Coto et al. 2018] LÓPEZ-COTO, R. ; PARSONS, R. D. ; HINTON, J. A. ; GIACINTI, G.: Undiscovered Pulsar in the Local Bubble as an Explanation of the Local High Energy Cosmic Ray All-Electron Spectrum. In: *Physical Review Letters* 121 (2018), December, Nr. 25, p. 251106.
URL: <https://ui.adsabs.harvard.edu/abs/2018PhRvL.121y1106L>
- [Lovell et al. 1968] LOVELACE, R. V. E. ; SUTTON, J. M. ; CRAFT, H. D.: Pulsar NP 0532 Near Crab Nebula. In: *IAU Circulars* 2113 (1968), November, p. 1.
URL: <https://ui.adsabs.harvard.edu/abs/1968IAUC.2113....1L>
- [Lucarelli et al. 2018] LUCARELLI, F. et al.: Ongoing episode of enhanced gamma-ray emission from the Crab Nebula detected by AGILE. In: *The Astronomer's Telegram* 12105 (2018), October.
URL: <https://ui.adsabs.harvard.edu/abs/2018ATel12105....1L>

- [Lyne et al. 1993] LYNE, A. G. ; PRITCHARD, R. S. ; GRAHAM SMITH, F.: 23 years of Crab pulsar rotational history. In: *Monthly Notices of the RAS* 265 (1993), December, p. 1003–1012.
URL: <https://ui.adsabs.harvard.edu/abs/1993MNRAS.265.1003L>
- [Lyutikov 2013] LYUTIKOV, Maxim: Inverse Compton model of pulsar high-energy emission. In: *Monthly Notices of the RAS* 431 (2013), May, Nr. 3, p. 2580–2589.
URL: <https://ui.adsabs.harvard.edu/abs/2013MNRAS.431.2580L>
- [MAGIC Collaboration et al. 2020] MAGIC COLLABORATION et al.: **Detection of the Geminga pulsar with MAGIC hints at a power-law tail emission beyond 15 GeV.** In: *Astronomy and Astrophysics* 643 (2020), November, Nr. L14, p. 6.
URL: <https://ui.adsabs.harvard.edu/abs/2020A&A...643L..14M>
- [Manchester et al. 2005] MANCHESTER, R. N. ; HOBBS, G. B. ; TEOH, A. ; HOBBS, M.: The Australia Telescope National Facility Pulsar Catalogue. In: *Astronomical Journal* 129 (2005), April, Nr. 4, p. 1993–2006.
URL: <https://ui.adsabs.harvard.edu/abs/2005AJ....129.1993M>
- [Manconi et al. 2020] MANCONI, Silvia ; DI MAURO, Mattia ; DONATO, Fiorenza: Contribution of pulsars to cosmic-ray positrons in light of recent observation of inverse-Compton halos. In: *Physical Review D* 102 (2020), July, Nr. 2, p. 023015.
URL: <https://ui.adsabs.harvard.edu/abs/2020PhRvD.102b3015M>
- [Mattox et al. 1992] MATTOX, J. R. ; BERTSCH, D. L. ; FICHEL, C. E. ; HARTMAN, R. C. ; KNIFFEN, D. A. ; THOMPSON, D. J.: SAS 2 Observation of Pulsed High-Energy Gamma Radiation from Geminga. In: *Astrophysical Journal, Letters* 401 (1992), December, p. L23.
URL: <https://ui.adsabs.harvard.edu/abs/1992ApJ...401L..23M>
- [Mayer-Hasselwander et al. 1994] MAYER-HASSELWANDER, H. A. et al.: High-Energy Gamma Radiation from Geminga Observed by EGRET. In: *Astrophysical Journal* 421 (1994), January, p. 276.
URL: <https://ui.adsabs.harvard.edu/abs/1994ApJ...421..276M>
- [Meyer et al. 2010] MEYER, M. ; HORNS, D. ; ZEHLIN, H. S.: The Crab Nebula as a standard candle in very high-energy astrophysics. In: *Astronomy and Astrophysics* 523 (2010), November, p. A2.
URL: <https://ui.adsabs.harvard.edu/abs/2010A&A...523A...2M>
- [Mirzoyan 1997] MIRZOYAN, R.: On the Calibration Accuracy of Light Sensors in Atmospheric Cherenkov Fluorescence and Neutrino Experiments. In: *International Cosmic Ray Conference Volume 7, IUPAP*, January 1997, p. 265.
URL: <https://ui.adsabs.harvard.edu/abs/1997ICRC....7..265M>
- [Mochol and Petri 2015] MOCHOL, I. ; PETRI, J.: Very high energy emission as a probe of relativistic magnetic reconnection in pulsar winds. In: *Monthly Notices of the RAS* 449 (2015), April, p. L51–L55.
URL: <https://ui.adsabs.harvard.edu/abs/2015MNRAS.449L..51M>

- [Mochol 2017] MOCHOL, Iwona: *Pulsar Striped Winds*. Volume 446. p. 135. In: TORRES, Diego F. (Editor): *Modelling Pulsar Wind Nebulae* Volume 446, Springer Verlag, 2017, URL: <https://ui.adsabs.harvard.edu/abs/2017ASSL..446..135M>
- [Moralejo 2003] MORALEJO, A.: The Reflector Simulation Program v.0.6. In: *Internal MAGIC-TDAS note* 02-11 (2003), January. URL: <https://magic.mpp.mpg.de/backend/tdas-notes>
- [Mori et al. 2014] MORI, Kaya et al.: A Broadband X-Ray Study of the Geminga Pulsar with NuSTAR and XMM-Newton. In: *Astrophysical Journal* 793 (2014), October, Nr. 2, p. 88. URL: <https://ui.adsabs.harvard.edu/abs/2014ApJ...793...88M>
- [Munar-Adrover et al. 2016] MUNAR-ADROVER, P. et al.: New episode of enhanced gamma-ray emission from the Crab Nebula detected by AGILE. In: *The Astronomer's Telegram* 9617 (2016), October. URL: <https://ui.adsabs.harvard.edu/abs/2016ATel.9617....1M>
- [Nakajima et al. 2013] NAKAJIMA, D. ; FINK, D. ; HOSE, J. ; MIRZOYAN, R. ; PANEQUE, D. ; SAITO, K. ; SCHWEIZER, T. ; TESHIMA, M. ; TOYAMA, T. ; WETTESKIND, H.: New Imaging Camera for the MAGIC-I Telescope. In: *International Cosmic Ray Conference* Volume 33, IUPAP, January 2013, p. 3044. URL: <https://ui.adsabs.harvard.edu/abs/2013ICRC...33.3044N>
- [Nolan et al. 1993] NOLAN, P. L. et al.: Observations of the Crab Pulsar and Nebula by the EGRET Telescope on the Compton Gamma-Ray Observatory. In: *Astrophysical Journal* 409 (1993), June, p. 697. URL: <https://ui.adsabs.harvard.edu/abs/1993ApJ...409..697N>
- [Ojha et al. 2012] OJHA, Roopesh ; BUEHLER, Rolf ; HAYS, Elizabeth ; DUTKA, Michael: Fermi LAT detection of enhanced gamma-ray emission from the Crab Nebula region. In: *The Astronomer's Telegram* 4239 (2012), July. URL: <https://ui.adsabs.harvard.edu/abs/2012ATel.4239....10>
- [Ojha et al. 2013] OJHA, Roopesh ; HAYS, Elizabeth ; BUEHLER, Rolf ; DUTKA, Michael: Fermi LAT detection of a new gamma-ray flare from the Crab Nebula region. In: *The Astronomer's Telegram* 4855 (2013), March. URL: <https://ui.adsabs.harvard.edu/abs/2013ATel.4855....10>
- [Osmanov and Rieger 2017] OSMANOV, Z. ; RIEGER, F. M.: Pulsed VHE emission from the Crab Pulsar in the context of magnetocentrifugal particle acceleration. In: *Monthly Notices of the RAS* 464 (2017), January, Nr. 2, p. 1347–1352. URL: <https://ui.adsabs.harvard.edu/abs/2017MNRAS.464.1347O>
- [Osmanov and Rieger 2019] OSMANOV, Z. ; RIEGER, F. M.: Rotationally driven VHE emission from the Vela pulsar. In: *Astronomy and Astrophysics* 627 (2019), July, p. A22. URL: <https://ui.adsabs.harvard.edu/abs/2019A&A...627A..22O>
- [Paoletti et al. 2007] PAOLETTI, R. ; CECCHI, R. ; CORTI, Daniele ; DAZZI, F. ; MARIOTTI, Mosè ; PEGNA, Raffaello ; TURINI, Nicola: The trigger system of the MAGIC telescope.

- In: *Nuclear Science, IEEE Transactions on* 54 (2007), 05, p. 404 – 409.
 URL: <https://doi.org/10.1109/TNS.2007.892649>
- [Pellizzoni et al. 2009] PELLIZZONI, A. et al.: High-Resolution Timing Observations of Spin-Powered Pulsars with the AGILE Gamma-Ray Telescope. In: *Astrophysical Journal* 691 (2009), February, Nr. 2, p. 1618–1633.
 URL: <https://ui.adsabs.harvard.edu/abs/2009ApJ...691.1618P>
- [Pétri 2016] PÉTRI, Jérôme: Theory of pulsar magnetosphere and wind. In: *Journal of Plasma Physics* 82 (2016), October, Nr. 5, p. 635820502.
 URL: <https://ui.adsabs.harvard.edu/abs/2016JPh...82e6302P>
- [Portocarrero and Arqueros 1998] PORTOCARRERO, C. E. ; ARQUEROS, F.: On the Cherenkov light produced at several observatory altitudes by extensive air showers in the energy range 0.01-10 TeV. In: *Journal of Physics G Nuclear Physics* 24 (1998), January, Nr. 1, p. 235–253.
 URL: <https://ui.adsabs.harvard.edu/abs/1998JPhG...24..235P>
- [Posselt et al. 2017] POSSELT, B. ; PAVLOV, G. G. ; SLANE, P. O. ; ROMANI, R. ; BUCCIANINI, N. ; BYKOV, A. M. ; KARGALTSEV, O. ; WEISSKOPF, M. C. ; NG, C. Y.: Geminga’s Puzzling Pulsar Wind Nebula. In: *Astrophysical Journal* 835 (2017), January, Nr. 1, p. 66.
 URL: <https://ui.adsabs.harvard.edu/abs/2017ApJ...835...66P>
- [Recchia et al. 2021] RECCHIA, Sarah ; DI MAURO, Mattia ; AHARONIAN, Felix A. ; DONATO, Fiorenza ; GABICI, Stefano ; MANCONI, Silvia: Does the Geminga γ -ray halo imply slow diffusion around pulsars? In: *arXiv e-prints* (2021), June, p. arXiv:2106.02275
- [Rissi et al. 2008] RISSI, M. ; OTTE, N. ; SCHWEIZER, T. ; SHAYDUK, M.: A new trigger provides a lower energy threshold for the MAGIC Cherenkov telescope. In: *2008 IEEE Nuclear Science Symposium Conference Record, IUPAP, 2008*, p. 1472–1475.
 URL: <https://doi.org/10.1109/NSSMIC.2008.4774693>
- [Romani 1996] ROMANI, Roger W.: Gamma-Ray Pulsars: Radiation Processes in the Outer Magnetosphere. In: *Astrophysical Journal* 470 (1996), October, p. 469.
 URL: <https://ui.adsabs.harvard.edu/abs/1996ApJ...470..469R>
- [Rossi and Greisen 1941] ROSSI, Bruno ; GREISEN, Kenneth: Cosmic-Ray Theory. In: *Reviews of Modern Physics* 13 (1941), October, Nr. 4, p. 240–309.
 URL: <https://ui.adsabs.harvard.edu/abs/1941RvMP...13..240R>
- [Rossi 1934] ROSSI, Bruno B.: Misure sulla distribuzione angolare d’intensità della radiazione penetrante all’Asmara (“*Measurements on the angular distribution of the penetrating radiation intensity in Asmara*”). In: *Supplemento a «La Ricerca Scientifica»* 1 (1934), Nr. III, p. 579–589. Courtesy of the geo-science department library of the University of Padua.
- [Ruderman and Sutherland 1975] RUDERMAN, M. A. ; SUTHERLAND, P. G.: Theory of pulsars: polar gaps, sparks, and coherent microwave radiation. In: *Astrophysical Journal* 196 (1975), February, p. 51–72.
 URL: <https://ui.adsabs.harvard.edu/abs/1975ApJ...196...51R>

- [Saito and Sitarek 2009] SAITO, T. ; SITAREK, J.: Improvement of the θ^2 analysis by using the Random Forest method in the DISP estimation. In: *Internal MAGIC-TDAS note 09-01* (2009), May.
URL: <https://magic.mpp.mpg.de/backend/tdas-notes>
- [Schmelling 1994] SCHMELLING, Michael: The method of reduced cross-entropy A general approach to unfold probability distributions. In: *Nuclear Instruments and Methods in Physics Research A* 340 (1994), February, Nr. 2, p. 400–412.
URL: <https://ui.adsabs.harvard.edu/abs/1994NIMPA.340..400S>
- [Shapiro 1964] SHAPIRO, Irwin I.: Fourth Test of General Relativity. In: *Physical Review Letters* 13 (1964), December, Nr. 26, p. 789–791.
URL: <https://ui.adsabs.harvard.edu/abs/1964PhRvL..13..789S>
- [Shapiro et al. 1971] SHAPIRO, Irwin I. ; ASH, Michael E. ; INGALLS, Richard P. ; SMITH, William B. ; CAMPBELL, Donald B. ; DYCE, Rolf B. ; JURGENS, Raymond F. ; PETTENGILL, Gordon H.: Fourth Test of General Relativity: New Radar Result. In: *Physical Review Letters* 26 (1971), May, Nr. 18, p. 1132–1135.
URL: <https://ui.adsabs.harvard.edu/abs/1971PhRvL..26.1132S>
- [Shaw et al. 2018] SHAW, B. et al.: The largest glitch observed in the Crab pulsar. In: *Monthly Notices of the RAS* 478 (2018), August, Nr. 3, p. 3832–3840.
URL: <https://ui.adsabs.harvard.edu/abs/2018MNRAS.478.3832S>
- [Shayduk 2013] SHAYDUK, Maxim: Optimized next-neighbor image cleaning method for Cherenkov Telescopes. In: *arXiv e-prints* (2013), Jul, p. arXiv:1307.4939.
URL: <https://ui.adsabs.harvard.edu/abs/2013arXiv1307.4939S>
- [Shearer et al. 1998] SHEARER, A. et al.: Possible pulsed optical emission from Geminga. In: *Astronomy and Astrophysics* 335 (1998), July, p. L21–L24.
URL: <https://ui.adsabs.harvard.edu/abs/1998A&A...335L..21S>
- [Shibanov et al. 2006] SHIBANOV, Y. A. ; ZHARIKOV, S. V. ; KOMAROVA, V. N. ; KAWAI, N. ; URATA, Y. ; KOPTSEVICH, A. B. ; SOKOLOV, V. V. ; SHIBATA, S. ; SHIBAZAKI, N.: Subaru optical observations of the two middle-aged pulsars PSR B0656+14 and Geminga. In: *Astronomy and Astrophysics* 448 (2006), March, Nr. 1, p. 313–326.
URL: <https://ui.adsabs.harvard.edu/abs/2006A&A...448..313S>
- [Shibata et al. 2019] SHIBATA, Masaru ; ZHOU, Enping ; KIUCHI, Kenta ; FUJIBAYASHI, Sho: Constraint on the maximum mass of neutron stars using GW170817 event. In: *Physical Review D* 100 (2019), July, Nr. 2, p. 023015.
URL: <https://ui.adsabs.harvard.edu/abs/2019PhRvD.100b3015S>
- [Sitarek et al. 2013] SITAREK, Julian ; GAUG, Markus ; MAZIN, Daniel ; PAOLETTI, Riccardo ; TESCARO, Diego: Analysis techniques and performance of the Domino Ring Sampler version 4 based readout for the MAGIC telescopes. In: *Nuclear Instruments and Methods in Physics Research A* 723 (2013), September, p. 109–120.
URL: <https://ui.adsabs.harvard.edu/abs/2013NIMPA.723..109S>

- [Slettebak 1982] SLETTEBAK, A.: Spectral types and rotational velocities of the brighter Be stars and A-F type shell stars. In: *Astrophysical Journal, Supplement* 50 (1982), September, p. 55–83.
URL: <https://ui.adsabs.harvard.edu/abs/1982ApJS...50...55S>
- [Sobczynska 2002] SOB CZYNSKA, D.: Mmcs from CORSIKA 6.014. In: *Internal MAGIC-TDAS note* 02-10 (2002), July.
URL: <https://magic.mpp.mpg.de/backend/tdas-notes>
- [Sobczyńska 2003] SOB CZYŃSKA, D.: Characteristics of a few GeV γ showers. In: *Internal MAGIC-TDAS note* 03-05 (2003), May.
URL: <https://magic.mpp.mpg.de/backend/tdas-notes>
- [Spir-Jacob et al. 2019] SPIR-JACOB, M. ; DJANNATI-ATAÏ, A. ; MOHRMANN, L. ; GIAVITTO, G. ; KHELIFI, B. ; RUDAK, B. ; VENTER, C. ; ZANIN, R.: Detection of sub-100 GeV gamma-ray pulsations from PSR B1706-44 with H.E.S.S. (2019), August.
URL: <https://arxiv.org/abs/1908.06464>
- [Spoelstra and Hermsen 1984] SPOELSTRA, T. A. T. ; HERMSEN, W.: Radio observations at 21 CM wavelength in the direction of Geminga. In: *Astronomy and Astrophysics* 135 (1984), June, p. 135–140.
URL: <https://ui.adsabs.harvard.edu/abs/1984A&A...135..135S>
- [Striani et al. 2011] STRIANI, E. et al.: AGILE monitoring of the strongly variable gamma-ray emission from the Crab Nebula. In: *The Astronomer's Telegram* 3286 (2011), April.
URL: <https://ui.adsabs.harvard.edu/abs/2011ATel.3286....1S>
- [Striani et al. 2013a] STRIANI, E. et al.: Enhanced gamma-ray emission from the Crab Nebula region detected by AGILE. In: *The Astronomer's Telegram* 4856 (2013), March.
URL: <https://ui.adsabs.harvard.edu/abs/2013ATel.4856....1S>
- [Striani et al. 2013b] STRIANI, E. et al.: Variable Gamma-Ray Emission from the Crab Nebula: Short Flares and Long “Waves”. In: *Astrophysical Journal* 765 (2013), March, Nr. 1, p. 52.
URL: <https://ui.adsabs.harvard.edu/abs/2013ApJ...765...52S>
- [Sturrock 1971] STURROCK, P. A.: A Model of Pulsars. In: *Astrophysical Journal* 164 (1971), March, p. 529.
URL: <https://ui.adsabs.harvard.edu/abs/1971ApJ...164..529S>
- [Sudoh et al. 2019] SUDOH, Takahiro ; LINDEN, Tim ; BEACOM, John F.: TeV halos are everywhere: Prospects for new discoveries. In: *Physical Review D* 100 (2019), August, Nr. 4, p. 043016.
URL: <https://ui.adsabs.harvard.edu/abs/2019PhRvD.100d3016S>
- [Tavani et al. 2011a] TAVANI, M. et al.: AGILE monitoring of the enhanced gamma-ray emission from the Crab Nebula region. In: *The Astronomer's Telegram* 3282 (2011), April.
URL: <https://ui.adsabs.harvard.edu/abs/2011ATel.3282....1T>

- [Tavani et al. 2011b] TAVANI, M. et al.: Discovery of Powerful Gamma-Ray Flares from the Crab Nebula. In: *Science* 331 (2011), February, Nr. 6018, p. 736.
URL: <https://ui.adsabs.harvard.edu/abs/2011Sci...331..736T>
- [Tavani et al. 2010] TAVANI, M. et al.: AGILE detection of enhanced gamma-ray emission from the Crab Nebula region. In: *The Astronomer's Telegram* 2855 (2010), September.
URL: <https://ui.adsabs.harvard.edu/abs/2010ATel.2855....1T>
- [Tescaro 2012] TESCARO, D.: The upgraded readout system of the MAGIC telescopes. In: *2012 IEEE Nuclear Science Symposium and Medical Imaging Conference Record (NSS/MIC)*, IEEE, 2012, p. 1901–1904.
URL: <https://ieeexplore.ieee.org/document/6551440/>
- [Thompson et al. 1977] THOMPSON, D. J. ; FICHEL, C. E. ; HARTMAN, R. C. ; KNIFFEN, D. A. ; LAMB, R. C.: Final SAS-2 gamma-ray results on sources in the galactic anticenter region. In: *Astrophysical Journal* 213 (1977), April, p. 252–262.
URL: <https://ui.adsabs.harvard.edu/abs/1977ApJ...213..252T>
- [Tikhonov 1963] ТИХОНОВ, Andrei N.: О решении некорректно поставленных задач и методе регуляризации (“*On the solution of ill-posed problems and the method of regularization*”). In: Доклады Академии Наук СССР 151 (1963), Nr. 3, p. 501–504.
URL: <http://mi.mathnet.ru/dan28329>
- [Trimble 1973] TRIMBLE, Virginia: The Distance to the Crab Nebula and NP 0532. In: *Publications of the ASP* 85 (1973), October, Nr. 507, p. 579.
URL: <https://ui.adsabs.harvard.edu/abs/1973PASP...85..579T>
- [Valverde et al. 2018] VALVERDE, Janeth ; OJHA, Roopesh ; BUEHL, Rolf: Fermi-LAT detection of enhanced gamma-ray activity from the Crab nebula. In: *The Astronomer's Telegram* 11412 (2018), March.
URL: <https://ui.adsabs.harvard.edu/abs/2018ATel11412....1V>
- [van Scherpenberg et al. 2019] VAN SCHERPENBERG, J. ; MIRZOYAN, R. ; VOVK, I. ; PERESANO, M. ; ZARIC, D. ; ТЕМНИКОВ, P. ; GODINOVIĆ, N. ; BESENRIEDER, J.: Searching for Variability of the Crab Nebula Flux at TeV Energies using MAGIC Very Large Zenith Angle Observations. In: *36th International Cosmic Ray Conference (ICRC2019) Volume 36*, IUPAP, July 2019, p. 812.
URL: <https://ui.adsabs.harvard.edu/abs/2019ICRC...36..812V>
- [Vaughan et al. 2003] VAUGHAN, S. ; EDELSON, R. ; WARWICK, R. S. ; UTTLEY, P.: On characterizing the variability properties of X-ray light curves from active galaxies. In: *Monthly Notices of the RAS* 345 (2003), November, Nr. 4, p. 1271–1284.
URL: <https://ui.adsabs.harvard.edu/abs/2003MNRAS.345.1271V>
- [VERITAS Collaboration et al. 2011] VERITAS COLLABORATION et al.: Detection of Pulsed Gamma Rays Above 100 GeV from the Crab Pulsar. In: *Science* 334 (2011), October, Nr. 6052, p. 69.
URL: <https://ui.adsabs.harvard.edu/abs/2011Sci...334...69V>

- [Verrecchia et al. 2013a] VERRECCHIA, F. et al.: After a gamma-ray flare, AGILE detects the Crab Nebula returning to the normal flux level. In: *The Astronomer's Telegram* 5506 (2013), October.
URL: <https://ui.adsabs.harvard.edu/abs/2013ATel.5506....1V>
- [Verrecchia et al. 2013b] VERRECCHIA, F. et al.: Sustained high-flux emission above 100 MeV from the Crab Nebula source. In: *The Astronomer's Telegram* 4867 (2013), March.
URL: <https://ui.adsabs.harvard.edu/abs/2013ATel.4867....1V>
- [Wagner 2006] WAGNER, Robert M.: *Measurement of Very High Energy Gamma-Ray Emission from Four Blazars Using the MAGIC Telescope and a Comparative Blazar Study*. Technische Universität München, November 2006
URL: <http://publications.mppmu.mpg.de/2006/MPP-2006-245/FullText.pdf>
- [Weekes et al. 1989] WEEKES, T. C. et al.: Observation of TeV Gamma Rays from the Crab Nebula Using the Atmospheric Cerenkov Imaging Technique. In: *Astrophysical Journal* 342 (1989), July, p. 379.
URL: <https://ui.adsabs.harvard.edu/abs/1989ApJ...342..379W>
- [Will et al. 2019] WILL, M. ; MIRZOYAN, R. ; VAN SCHERPENBERG, J. ; GARCZARCYK, M.: Novel Back-coated Glass Mirrors for the MAGIC Telescopes. In: *36th International Cosmic Ray Conference (ICRC2019)* Volume 36, IUPAP, July 2019, p. 823.
URL: <https://ui.adsabs.harvard.edu/abs/2019ICRC...36..823W>
- [Wittek 2002] WITTEK, W.: Determination of the effective observation time. In: *Internal MAGIC-TDAS note 02-02* (2002), February.
URL: <https://magic.mpp.mpg.de/backend/tdas-notes>
- [Wittek 2006] WITTEK, W.: Unfolding. In: *Internal MAGIC-TDAS note 05-05* (2006), April.
URL: <https://magic.mpp.mpg.de/backend/tdas-notes>
- [Wood et al. 2017] WOOD, M. ; CAPUTO, R. ; CHARLES, E. ; DI MAURO, M. ; MAGILL, J. ; PERKINS, J. S. ; FERMI-LAT COLLABORATION: Fermipy: An open-source Python package for analysis of Fermi-LAT Data. In: *35th International Cosmic Ray Conference (ICRC2017)* Volume 301, IUPAP, January 2017, p. 824.
URL: <https://ui.adsabs.harvard.edu/abs/2017ICRC...35..824W>
- [Yeung 2020] YEUNG, Paul K. H.: Inferring the origins of the pulsed γ -ray emission from the Crab pulsar with ten-year Fermi-LAT data. In: *Astronomy and Astrophysics* 640 (2020), August, p. A43.
URL: <https://ui.adsabs.harvard.edu/abs/2020A&A...640A..43Y>
- [Zanin et al. 2013] ZANIN, Roberta et al.: MARS, the MAGIC analysis and reconstruction software. In: *Proceedings of the 33rd International Cosmic Ray Conference (ICRC2013): Rio de Janeiro, Brazil, July 2-9, 2013*, IUPAP, 2013, p. 0773.
URL: <http://inspirehep.net/record/1412925>

LIST OF PUBLICATIONS RELATED TO MY DOCTORAL PROJECT

These peer-reviewed publications are based on or include a large part of my doctoral work, and I am a corresponding author of them. All publications of the MAGIC Collaboration are signed by all of its members, in strict alphabetical order, with external collaborators listed at the end. Primary roles are acknowledged by the corresponding authorship. I have not used or discussed these publications to obtain my previous academic degrees.

DAZZI, F.; SCHWEIZER, T.; CERIBELLA, G.; CORTI, D.; DETTLAFF, A.; GARCIA, J. R.; HÄFNER, D.; HERRANZ, D.; LÓPEZ-MOYA, M.; MARIOTTI, M.; MAIER, R.; METZ, S.; MIRZOYAN, R.; NAKAJIMA, D.; SAITO, T.; SHAYDUK, M.; SITAREK, J.; STROM, D.; TESHIMA, M.; TRAN, S.; WILL, M.

The Stereoscopic Analog Trigger of the MAGIC Telescopes.

In: *IEEE Transactions on Nuclear Science* 68 (2021), July, Nr. 7, pp. 1473-1486.

URL: <https://ieeexplore.ieee.org/document/9427568>

DOI: 10.1109/TNS.2021.3079262

MAGIC COLLABORATION: ACCIARI, V. A.; ANSOLDI, S.; ANTONELLI, L. A.; ARBET ENGELS, A.; ASANO, K.; BAACK, D.; BABIĆ, A.; BAQUERO, A.; BARRES DE ALMEIDA, U.; BARRIO, J. A.; BECERRA GONZÁLEZ, J.; BEDNAREK, W.; BELLIZZI, L.; BERNARDINI, E.; BERNARDOS, M.; BERTI, A.; BESENRIEDER, J.; BHATTACHARYYA, W.; BIGONGIARI, C.; BILAND, A.; BLANCH, O.; BONNOLI, G.; BOŠNJAK, Ž.; Busetto, G.; CAROSI, R.; CERIBELLA, G.; CERRUTI, M.; CHAI, Y.; CHILINGARIAN, A.; CIKOTA, S.; COLAK, S. M.; COLOMBO, E.; CONTRERAS, J. L.; CORTINA, J.; COVINO, S.; D'AMICO, G.; D'ELIA, V.; DA VELA, P.; DAZZI, F.; DE ANGELIS, A.; DE LOTTO, B.; DELFINO, M.; DELGADO, J.; DELGADO MENDEZ, C.; DEPAOLI, D.; DI GIROLAMO, T.; DI PIERRO, F.; DI VENERE, L.; DO SOUTO ESPÍNEIRA, E.; DOMINIS PRESTER, D.; DONINI, A.; DORNER, D.; DORO, M.; ELSAESSER, D.; FALLAH RAMAZANI, V.; FATTORINI, A.; FERRARA, G.; FOFFANO, L.; FONSECA, M. V.; FONT, L.; FRUCK, C.; FUKAMI, S.; GARCÍA LÓPEZ, R. J.; GARCZARCZYK, M.; GASPARYAN, S.; GAUG, M.; GIGLIETTO, N.; GIORDANO, F.; GLIWNY, P.; GODINOVIĆ, N.; GREEN, J. G.; GREEN, D.; HADASCH, D.; HAHN, A.; HECKMANN, L.; HERRERA, J.; HOANG, J.; HRUPEC, D.; HÜTTEN, M.; INADA, T.; INOUE, S.; ISHIO, K.; IWAMURA, Y.; JORMANAINEN, J.; JOUVIN, L.; KAJIWARA, Y.; KARJALAINEN, M.; KERSZBERG, D.; KOBAYASHI, Y.; KUBO, H.; KUSHIDA, J.; LAMAISTRA, A.; LELAS, D.; LEONE, F.; LINDFORS, E.; LOMBARDI, S.; LONGO, F.; LÓPEZ-COTO, R.; LÓPEZ-MOYA, M.; LÓPEZ-ORAMAS, A.; LOPORCHIO, S.; MACHADO DE OLIVEIRA FRAGA, B.; MAGGIO, C.; MAJUMDAR, P.; MAKARIEV, M.;

MALLAMACI, M.; MANEVA, G.; MANGANARO, M.; MANNHEIM, K.; MARASCHI, L.; MARIOTTI, M.; MARTÍNEZ, M.; MAZIN, D.; MENDER, S.; MIĆANOVIĆ, S.; MICELI, D.; MIENER, T.; MINEV, M.; MIRANDA, J. M.; MIRZOYAN, R.; MOLINA, E.; MORALEJO, A.; MORCUENDE, D.; MORENO, V.; MORETTI, E.; MUNAR-ADROVER, P.; NEUSTROEV, V.; NIGRO, C.; NILSSON, K.; NINCI, D.; NISHIJIMA, K.; NODA, K.; NOZAKI, S.; OHTANI, Y.; OKA, T.; OTERO-SANTOS, J.; PALATIELLO, M.; PANEQUE, D.; PAOLETTI, R.; PAREDES, J. M.; PAVLETIĆ, L.; PEÑIL, P.; PERENNES, C.; PERSIC, M.; PRADA MORONI, P. G.; PRANDINI, E.; PRIYADARSHI, C.; PULJAK, I.; RHODE, W.; RIBÓ, M.; RICO, J.; RIGHI, C.; RUGLIANCICH, A.; SAHA, L.; SAHAKYAN, N.; SAITO, T.; SAKURAI, S.; SATALECKA, K.; SATURNI, F. G.; SCHLEICHER, B.; SCHMIDT, K.; SCHWEIZER, T.; SITAREK, J.; ŠNIDARIĆ, I.; SOBCZYNSKA, D.; SPOLON, A.; STAMERRA, A.; STROM, D.; STRZYS, M.; SUDA, Y.; SURIĆ, T.; TAKAHASHI, M.; TAVECCHIO, F.; TEMNIKOV, P.; TERZIĆ, T.; TESHIMA, M.; TORRES-ALBÀ, N.; TOSTI, L.; TRUZZI, S.; TUTONE, A.; VAN SCHERPENBERG, J.; VANZO, G.; VAZQUEZ ACOSTA, M.; VENTURA, S.; VERGUILOV, V.; VIGORITO, C. F.; VITALE, V.; VOVK, I.; WILL, M.; ZARIĆ, D.; HIROTANI, K.; SAZ PARKINSON, P. M.

Detection of the Geminga pulsar with MAGIC hints at a power-law tail emission beyond 15 GeV.

In: *Astronomy and Astrophysics* 643 (2020), November, Nr. L14, p. 6.

URL: <https://ui.adsabs.harvard.edu/abs/2020A&A...643L..14M>

DOI: 10.1051/0004-6361/202039131



LIST OF FIGURES

1.1	Scheme of the interior of a neutron star	14
1.2	Goldreich-Julian potentials and fields in the near zone close to the pulsar .	15
1.3	Scheme of the pulsar magnetosphere in the near and wind zones	18
1.4	Sample curvature radiation spectra	21
1.5	Possible regions of particle acceleration in the inner magnetosphere	24
1.6	Scheme of the striped pulsar wind	25
1.7	Sample phase diagrams	27
1.8	Pulsar $P - \dot{P}$ diagram	30
1.9	Composite images of the Crab pulsar and nebula	32
1.10	Variation of the Crab pulsar pulse profile in a broad energy range	34
1.11	Broad-band spectral energy distribution of the Crab nebula	36
1.12	<i>Fermi</i> -LAT flares of the Crab nebula	37
1.13	Historical results on the Geminga gamma-ray emission	39
1.14	Geminga phaseograms in X and gamma rays	41
1.15	Images of the (non pulsed) extended emission of Geminga	43
2.1	Typical atmosphere profile	46
2.2	Electromagnetic shower longitudinal profiles	47
2.3	Number of Cherenkov photons for vertical showers	49
2.4	Radial Cherenkov photon density, for a vertically incident shower	49
2.5	MAGIC differential sensitivity plot	51
2.6	Picture of the MAGIC Telescopes	52
2.7	Close-up picture of some MAGIC-I mirrors	54
2.8	Close-up view of the MAGIC-I camera	55
2.9	Layout of the macro-cells of the Sum-Trigger-II	59
2.10	Scheme of the operating principle of the Sum-Trigger-II	60
2.11	Photograph of a clip-board	61
3.1	Sample rate scan for the Sum-Trigger-II attenuation and delay values	64
3.2	Flowchart of the Sum-Trigger-II calibration procedure	66
3.3	Delay-induced attenuation in the signals on the Sum-Trigger-II clip-boards	67
3.4	Sum-Trigger-II pixel amplitude and delay distribution, after calibration . .	68
3.5	Variation of the Sum-Trigger-II amplitude and delay spread	69
3.6	Sketch of the front cabling of the two Sum-Trigger-II astro-boards	71

4.1	Flow-chart of the data analysis process	74
4.2	Sample DRS4-digitized waveform with spike-removal and signal extraction	76
4.3	Image of a real Cherenkov light event	77
4.4	Nearest neighbor groups of order 2, 3 and 4.	79
4.5	Scheme of the MaTaJu cleaning procedure with data of a real event.	81
4.6	Analysis threshold and effective area for the standard and MaTaJu cleaning	83
4.7	Hillas parametrization of an event in both MAGIC cameras	84
4.8	Scheme of the stereoscopic event reconstruction	85
4.9	Approximate field of view of the MAGIC Telescopes around the Crab pulsar	87
4.10	Approximate field of view of the MAGIC Telescopes around Geminga . . .	88
4.11	Distributions of notable Hillas parameters affected by starlight	89
4.12	Surviving pedestals in Geminga data versus the exclusion circle radius . .	90
4.13	Sketch of the variables listed in Table 4.2	91
4.14	Comparison of hadronness distributions for gamma and cosmic rays . . .	93
4.15	Sketch of the DISP method for a 50 GeV simulated gamma	95
4.16	Evolution of the MAGIC point spread function versus energy	96
4.17	Energy migration matrix for the look-up table estimation method	97
4.18	Migration of events for steep power-law spectra	98
4.19	Energy dependent hadronness and θ^2 cuts	103
4.20	Background estimation strategies for wobble observations of a point source	105
4.21	Phaseograms of <i>Fermi</i> -LAT Geminga data	107
4.22	Effective area as a function of the true event energy	109
4.23	Energy threshold plot for the full analysis chain	112
4.24	Energy threshold variation with the zenith distance and spectral shape . .	113
4.25	Relative dispersion of the effective area caused by a low-statistic Monte-Carlo	115
4.26	Comparison between migration matrices, large vs. small statistics	116
4.27	Scheme for the selection of the source-tailored Monte-Carlo bins	117
5.1	Overview of the Crab pulsar observations	120
5.2	Nightly observability window of the Crab pulsar	121
5.3	Phaseogram of the Crab pulsar, overview	125
5.4	Energy development of the Crab pulsar phaseogram	126
5.5	Crab pulsar P1/P2 height ratio and pulse widths	127
5.6	Spectra of the P1 and P2 components of the Crab pulsar emission	128
5.7	Analysis thresholds for the Crab pulsar P1 and P2	130
5.8	MAGIC and <i>Fermi</i> -LAT spectra of the Crab pulsar and nebula	132
5.9	Cumulative energy scan in the significance of the Crab pulsed emission .	133
5.10	Long term lightcurve of the Crab pulsar, on a nightly base	134
5.11	Long term lightcurve of the Crab pulsar, on a fortnightly base	135
5.12	Long term lightcurve of the Crab pulsar, on a monthly base	136
5.13	Simulated excess variance distributions for stable pulsar emission	139
5.14	Models considered for the variability Monte-Carlo study	140
5.15	Excess variance distributions for simulated fortnightly lightcurves	141
5.16	Probability density functions of the flux increase	142
6.1	Overview of the Geminga pulsar observations	146
6.2	Count and test statistic maps for the <i>Fermi</i> -LAT Geminga analysis	150

6.3	Phaseogram of the Geminga pulsar, overview	152
6.4	$P - \dot{P}$ diagram with known and new very-high-energy pulsars	153
6.5	Morphological analysis of the Geminga phaseogram	154
6.6	MAGIC spectrum of Geminga	155
6.7	Analysis threshold for the MAGIC Geminga data	157
6.8	Validation of the lowest energy spectral points	158
6.9	Geminga spectrum with joint <i>Fermi</i> -LAT and MAGIC points	161
6.10	Geminga spectral fits in the <i>Fermi</i> -LAT and MAGIC overlapping region	163
6.11	Geminga spectral fits for a composite model	165
6.12	Theoretical models of the Geminga P2 emission	166
6.13	Theoretical models of the Geminga P2 emission, hard X-ray component	167
A.1	Effects of phase drift due to a non-refined ephemeris	178
A.2	Two dimensional scans of the Z_{10}^2 test statistics in the $(\nu, \dot{\nu})$ space	181
A.3	Phase stack for the Boomerang pulsar (PSR J2229+6114)	182
A.4	Segmented ephemeris for the Geminga pulsar	185
B.1	Corner plot for pure ($\beta = 1$) exponential cutoff power-law function.	190
B.2	Corner plot for the free ($\beta > 0$) exponential cutoff power-law function.	191
B.3	Corner plot for the power-law function in the overlapping range.	192
B.4	Corner plot for the log-parabola function in the overlapping range.	193
B.5	Corner plot for the composite function.	194

LIST OF TABLES

1.1	List of the Crab nebula flares	36
4.1	Galactic-field optimized MaTaJu cleaning parameters	82
4.2	Star exclusion circles for different pointings	91
4.3	Signal and background regions for the Geminga pulsar	106
4.4	List of the Monte-Carlo simulations for pulsar analysis	114
5.1	Summary of the Crab pulsar and nebula observations	122
5.2	Spectral parameters for the MAGIC Crab observations	129
5.3	Spectral points for the Crab P1 observations	129
5.4	Spectral points for the Crab P2 observations	129
5.5	Variability tests on Crab pulsar data	137
5.6	Empirical limits on systematic energy scale variation	138
5.7	Parameters for the lightcurve simulations	139
6.1	Summary of the Geminga observations	148
6.2	Spectral parameters for the MAGIC Geminga observations	156
6.3	Spectral points for the Geminga P2 observations	156
6.4	Systematic variation due to the energy mismatch	158
6.5	Parameters for the exponentially cutoff power law fits	160
6.6	Parameters for the overlapping range log parabola and power-law fits	163
6.7	Parameters for the composite model fit	164
6.8	Very high energy gamma-ray pulsar comparison	169
6.9	Summary of the joint <i>Fermi</i> -LAT and MAGIC Geminga fits	171
B.1	Spectral parameter definitions	189

ACKNOWLEDGMENTS

In this journey through pulsars and very-high-energy gamma rays, I have met many mentors and friends that helped, supported, encouraged, and inspired me. I attempt to properly credit them in this final message, and apologize if my entangled memory fails me in the process.

First, I want to sincerely thank the entire MAGIC group at the Max Planck Institute for Physics in Munich. I came as a scared foreigner, with the awe of a wayfarer approaching a sacred place. I found a fantastic company of wonderful people, where differences of language, culture, and view rapidly fall in front of a smile. It is an exceptional privilege to have working colleagues that I can also consider friends of mine. It was extraordinary useful to be able to discuss informally about science and life with anybody.

I deeply thank Prof. Masahiro Teshima for the continuous support and trust across the years, during which he never turned down a single question of mine. I was honored to be invited as a tutor to the ICRR Spring School in Japan, and to get a feeling of his country full of wonders.

Dr. Razmik Mirzoyan was a mentor along the entire path, and instilled me the fascination for gamma-ray astronomy. I sincerely thank him for the scientific ideas and marvelous conversations that he gifted me in his office. They made me feel as if we were wandering in the ancient $\Lambda\acute{\upsilon}\kappa\epsilon\iota\omicron\nu$.

Dr. David Paneque was my ultra-relativistic supervisor. Whenever I asked for five minutes of his time, I was always rewarded with hours of suggestions, comments, and new ideas. I suspect that his time-transcending availability originates from a couple of fully-functional miniature active galactic nuclei, hidden in his drawer.

Dr. Thomas Schweizer, the initiator of the Sum-Trigger-II project, was the first to note my pulsar presentation during the PhD admission round. In a time in which meeting the advisor on Skype seemed to be futuristic and eccentric, he was my remote supervisor and guide into the MAGIC Collaboration.

Dr. Béla Majorovits, the official supervisor for the Technical University of Munich, has never refused me a meeting or a chat, even in very busy times. I very much appreciated his availability and help.

My sincere gratitude goes to all the present and past post-doc researchers of the group, and in particular to Dr. Giacomo D'Amico, Dr. David Green, Dr. Moritz Hütten, Dr. Derek Strom, Dr. Yusuke Suda, Dr. Ievgen Vovk, and Dr. Martin Will. Each of them, with their background knowledge and experience, helped me find my way into science. In the same way, I thank all my student friends in the group: Yating Chai, Alexander Hahn, Lea Heckmann, Dr. Kazuma Ishio, Marine Pihet, Jezabel Rodriguez García, Felix Schmuckermeier, Dr. Marcel Strzys, Juliane van Scherpenberg. It is their passion and determination that pushes everyday the progress of our discipline. My friendship with Toni Dettlaff, grown out of hours of astrophotography in La Palma, has been the best gift of my technical activity on the Sum-Trigger-II. I feel very obliged to the former secretary of the group, Sybille Rodriguez, and to the present one, Diana Werner, who helped me in the gloomy time of early 2020. Their precious work, as for other non-scientific workers of the institute, often gets unnoticed, but ultimately makes the wheel go round.

MAGIC is a fantastic example of a scientific collaboration where cooperation and friendship win over competition and individualism. I thank all of its members for the exceptional opportunities that I was given, for the extremely high quality of the scientific research, and for the many memorable moments during (and after) the meetings and conferences. In particular, I wish to acknowledge the help and support of Dr. Victor Acciari (IFAE/IAC), Prof. Marcos López-Moya (UCM), Dr. Francesco Dazzi (CTAO Bologna), Prof. Mosè Mariotti and Dr. Rubén Lopez-Coto (Padova), Dr. Julian Sitarek and Dr. Dorota Sobczyńska (Łódź), Prof. Narek Sahakyan and Mher Khachatryan (Yerevan), Dr. Biswajit Banerjee (Saha Institute), Prof. Daniel Mazin, Prof. Takayuki Saito, Dr. Daniela Hadasch, Yuki Iwamura (ICRR Tokyo). Outside MAGIC, my gratitude goes also to Prof. Kouichi Hirotani (Academia Sinica).

In the end, I want to thank Lucia and Giulio, and also Maria, Gina, Toni, and Giovanni, because their actions shaped everything as it is.

